

Synthesis, characterization and performance evaluation of advanced carbon materials for CO_2 capture application

By

Mengbin Li

Faculty of Engineering

University of Nottingham

A thesis submitted to the University of Nottingham for the degree of Doctor of Philosophy

Jul 2023

Abstract

The synthesis of sustainable functional carbon materials has received increasing interest due to the soaring demand and wide-ranging applications, particularly within the evolving landscape of future energy and chemical industries. These industries are currently undergoing a dramatic transformation towards achieving net-zero emissions by 2050. Over the past two decades, there has been significant development in utilizing biomass, notably forestry residue, as a non-fossil renewable replacement feedstock to produce both classical and advanced carbon materials. However, concerns about sustainability and environment/climate benefits are growing due to deforestation primarily driven by excessive exploitation of forest resources for carbon materials and bioenergy production. Therefore, there is a pressing need, and indeed a desire, to explore and utilise other naturally abundant and more renewable biomass feedstock for sustainable carbon materials manufacturing with improved whole life cycle benefits. This PhD research project examines the use of more sustainable biomass and non-biomass wastes for manufacturing functional carbon materials through a simple and low-energy chemical activation process. The examined materials include kraft lignin waste, eucalyptus wood, cellulose, and plastic polyvinyl chloride wastes. Among various potential energy-related applications, the performance of the prepared carbon materials for CO_2 capture applications was evaluated due to the recognized desirable characteristics of carbon materials for CO_2 adsorption, including cost-effectiveness, rapid adsorption kinetics, moderate heat of adsorption, and exceptional thermo-oxidative stability.

The research demonstrates that the bio-carbon materials derived from kraft lignin (KL) waste, through an integrated carbonization-activation process, exhibited well-developed ultra-microporous structures with predominant pore sizes generally well below 1 nm. Additionally, a pre-oxidation treatment was employed to tailor the structure and surface chemistry of kraft lignin, aiming to increase the carbon yield and optimize the pore structure of activated carbons. The results showed that

distinctive hierarchical ultra-micro/mesoporous structures with narrow bimodal pore size distributions were observed in the pre-oxidized lignin prepared under mild activation conditions. The best performing KL carbon achieved a fully reversible record high CO_2 adsorption capacity of 2.01 mmol/g, with an exceptional CO_2/N_2 selectivity of 33 at 25 ^oC and 15 kPa CO_2, despite its modest surface area of just 878 m^2/g and total pore volume of 0.372 cm^3/g. Further examination of carbon samples by correlation between their CO_2 adsorption capacities and critical pore volume revealed that up to 50% of the total CO_2 uptake at low CO_2 patrial pressures was attributable to the unique strongly polarizing surface chemistry. Characterization by XRD and XRF demonstrated that such unique surface chemistry appears to be induced by the intercalated potassium in the form of extra-framework cations during KOH activation.

Activated carbon materials derived from eucalyptus wood were prepared using a methodology involving hydrothermal carbonization coupled with KOH activation in this study. Characterisations showed that these carbons were marked by a high level of ultra-microporosity and a strongly polarizing surface. The evaluation of CO_2 adsorption behavior indicated that the carbons prepared under mild activation conditions (600 ^oC, KOH/hydrochar mass ratio of 2) using the HTC char produced at 220 ^oC possessed an exceedingly high CO_2 uptake of 1.91 mmol/g at 25 ^oC and 15 kPa with slightly higher CO_2/N_2 selectivity (35) compared to those carbons derived from KL. The outstanding CO_2 adsorption performance at low CO_2 partial pressures was found to be the highest ever reported for bio-carbons prepared using HTC hydrochar, thanks to their high ultra-micropore (<0.40 nm) volume (0.160 cm^3/g) and distinctive surface chemistry dominated by the enhanced formation of extra- framework potassium cations. Moreover, under the same activation conditions, carbons prepared from HTC hydrochar were found to have a 20% higher CO_2 adsorption capacity than those prepared without HTC pre-treatment, indicating the great efficacy of HTC in tailoring the biomass precursor in favour of the formation of ultra-microporosity during the KOH chemical activation. The phenomenon is presumably attributed to the denser and more ordered texture

structures of the Eucalyptus hydrochar formed as a result of the dehydration, decarboxylation, condensation and potential aromatisation reactions that can occur during hydrothermal carbonization.

The use of polyvinyl chloride (PVC) plastic wastes to prepare advanced carbon materials has also been successfully achieved through hydrothermal co-carbonization (co-HTC) with biomass, coupled with chemical activation. The research demonstrates that, due to a synergistic effect, the hydrothermal co-processing of PVC and biomass wastes significantly improved the efficiency of the PVC dechlorination, leading to the formation of high-quality co-hydrochars precursor for the production of carbon materials. The results showed that the dechlorination efficiency could be increased by 50% when PVC was co-processed with kraft lignin waste at a mild HTC temperature of 220 ^{o}C. Meanwhile, by controlling the synthetic conditions such as HTC temperature, activation temperature and KOH/hydrochar mass ratio, the carbon materials prepared from using co-hydrochars exhibited rarely seen large ultra-micropore volumes (i.d. < 0.40 nm) of up to 0.171 cm^3/g, which is 61% higher than that of PVC-derived carbons prepared under the same conditions. Adsorption characterisations demonstrate that the ultra-microporous PVC/biomass-derived carbon materials gave rise to CO_2 uptake capacities of up to 2.00 mmol/g at 15 kPa CO_2 and 25 ^{o}C, which are significantly higher compared to those of many “designer” carbon materials prepared from using pristine woody biomass and polymeric precursor materials.

Our findings clearly demonstrated that exceptional CO_2 adsorption performance can be achieved using low-cost waste materials derived carbons prepared through chemical activation coupled with designated pre-treatment protocols (pre-oxidation, hydrothermal carbonization and co-carbonization). The CO_2 uptake capacities of carbons derived from kraft lignin, eucalyptus wood and PVC/biomass wastes can reach up to 2.01, 1.91 and 2.00 mmol/g at 15 kPa CO2 and 25 ^{o}C, respectively, which outperform most of biomass derived activated carbons developed so far. The outcomes of the PhD research bode extremely well for the promising use of

abundantly available non-forestry biomass and hard-to-process plastic wastes as more sustainable feedstock to produce high-value functional carbon materials with greater environmental/climate and economic benefits.

Acknowledgements

I would like to express my sincere gratitude and appreciation to all those who have contributed to the completion of this PhD thesis. Without their support, guidance, and encouragement, this achievement would not have been possible.

First and foremost, I am deeply indebted to my supervisor, Prof Chenggong Sun, for offering me this PhD opportunity to pursue my academic ideals. His expertise, invaluable guidance and mentorship have been instrumental in shaping my research and academic development. Though he has recently departed from the University, I would like to extend my heartfelt wishes for his future endeavours.

I would also like to express appreciation to Prof Hao Liu and Prof Colin Snape for their help and unwavering support, and special thanks to Dr. Xin Liu for his advice, patience and constructive comments in many discussions on my experimental work and thesis.

I would like to acknowledge Dr. Lee Stevens for his technical assistance in the laboratory and helpful discussion in sample characterization. I also appreciate Dr. Robin Irons for his valuable advice on my academic progress year by year. I would thank Dr. Sabrin Samad and Mr. Nigel Neate for teaching me to use SEM and EDS, Ms Teresa Needham for assistance of XRF and Dr. Hannah Constantin for support with XRD measurements. I also wish to express my appreciation to the laboratory technicians, Adrian Quinn and Christopher Powell for their technical support and assistance in resolving everyday lab issues.

I would also like to say thanks to my colleagues and friends, Dr. Wei Li, Dr. Shaobo Wang, Dr. Suleiman Sani, Dr. Ahmed Ibrahim, Umar Musa, Dr. Clement Uguna, Mohammed Alamo, Kun Du, Dr. Fengtian Bai, Xu Yang and Xiaoya Zhu for their help in the past four years.

Finally, I am especially grateful to my parents for their unconditional support and my deepest gratitude goes to my wife for her incredible sacrifices and unwavering support throughout my PhD journey.

Content

Abstract…….. I
Acknowledgement……...IV
Content……..V
List of Figures……..IX
List of Tables……..……XV
List of Abbreviations…….. VI
Chapter 1 GENERAL INTRODUCTION 1
Chapter 2 LITERATURE REVIEW 7
2.1 CO_2 capture technologies 8
2.1.1 Oxy-fuel combustion technologies 9
2.1.2 Pre-combustion technologies 10
2.1.3 Post-combustion technologies 11
2.2 Carbon based sorbents for CO_2 capture 21
2.2.1 Precursors for carbon materials 21
2.2.2 Pre-treatment of precursor feedstock for activated carbon materials 24
2.2.3 Preparation of activated carbons 36
2.3 CO_2 adsorption performance of carbon materials for carbon capture 49
2.3.1 Effect of surface textural properties of carbons 50
2.3.2 Effect of surface chemistry 54
2.3.2.1 Oxygen containing groups 54
2.3.2.2 Nitrogen containing groups 55
2.3.2.3 Metal-doping carbon materials 57
2.4 Aims and objectives 59
Chapter 3 EXPERIMENTAL METHODOLOGIES 60
3.1 Preparation of carbon materials 61
3.1.1. Preparation of Kraft lignin-derived activated carbon 62

3.1.2. Preparation of Eucalyptus carbons 64
3.1.4. Preparation of PVC and PVC/biomass carbons 66
3.2 Characterization 70
3.2.1 Textural properties 70
3.2.2 Physicochemical characteristics 79
3.2.3 Morphology 81
3.2.4 Composition analysis 81
3.2.5 Surface chemistry 82
3.3 Evaluation of carbon materials for CO_2 adsorption 83
3.3.1 CO_2 adsorption isotherms 83
3.3.2 Dynamic CO_2 adsorption capacity 83
3.3.3 Heat of adsorption 84
3.4 Repeatability and reproductivity 86
3.4.1 Repeatability of measurements 86
3.4.2 Reproductivity of samples 88
Chapter 4 SYNTHESIS AND CHARACTERIZATION OF ADVANCED FUNCTIONAL BIO-CARBON MATERIALS FROM KRAFT LIGNIN WASTE WITH ENHANCED CO_2-ADSORPTIVE PROPERTIES 90
4.1 Introduction 91
4.2 Results and discussion 95
4.2.1 Physicochemical properties of KL and OKL precursors 95
4.2.2 Textural properties of kraft lignin-derived carbons 98
4.2.3 Morphology of kraft lignin-derived carbons 104
4.2.4 CO_2 adsorption properties of kraft lignin-derived carbons 106
4.2.5 Role of textural properties and surface chemistry in CO_2 adsorption 113
4.2.6 Heat of CO_2 adsorption 120
4.3 Conclusion 125

Chapter 5 Hydrothermal Carbonization and Hydrochar-based functional carbon materials 126

5.1 Introduction 127

5.2 Results and discussion 128

5.2.1 Physicochemical properties of biomass and hydrochars 128

5.2.2 Textural properties of EU-derived activated carbons 132

5.2.3 Morphology of EU-derived hydrochar and EUHC carbons 137

5.2.4 CO_2 adsorption properties of EUHC-derived carbons 140

5.2.5 Role of textural properties and surface chemistry in CO_2 adsorption 147

5.2.6 Heat of CO_2 adsorption 152

5.2.7 CO_2/N_2 selectivity 154

5.3 Conclusion 155

Chapter 6 FUNCTIONAL CARBON MATERIALS FROM HYDROTHERMAL CO-CARBONIZATION OF BIOMASS AND POLYVINYL CHLORIDE PLASTIC WASTE AND PERFORMANCE EVALUATION FOR CO_2 ADSORPTION 156

6.1 Introduction 157

6.2 Results and discussion 158

6.2.1 Physicochemical properties of precursors and hydrochar 158

6.2.2 Textural properties of activated carbons 167

6.2.3 Morphology of hydrochar and activated carbons 177

6.2.4 CO_2 adsorption properties of PVC-derived carbons prepared via HTC 180

6.2.5 Role of textural properties and surface chemistry in CO_2 adsorption 187

6.2.6 Heat of CO_2 adsorption 194

6.3 Conclusion 196

Chapter 7 CONCLUSION AND FUTURE RESEARCH 198

7.1 General discussion 199

7.1.1 Effect of pre-treatment on the physiochemical properties of carbon precursors derived from different raw feedstocks 199

7.1.2 Effect of activation conditions and carbon precursors on the textural properties of activated carbon samples 201

7.2 Conclusions 208

7.3 Future work 211

7.3.1 Advanced characterization of chemical properties of hydrochar ... 211

7.3.2 Advanced characterization of potassium intercalated in carbon ... 211

7.3.3 Improvement in preparation of PVC/biomass co-hydrochar derived carbon 212

7.3.4 The effect of water vapor and gas impurities on CO_2 capture performance of carbon materials 212

References 214

Appendix A 248

Appendix B 251

List of Figures

Figure 1.1 Global energy consumption and CO_2 emissions by scenario, 2000-2040 (World Energy Outlook 2022) 3

Figure 2.1 (a) Oxy-fuel combustion technologies, (b) Pre-combustion technologies, (c) Post-combustion technologies……..9

Figure 2.2 General composition of biomass feedstock 23

Figure 2.3 Illustration for the temperature dependence of hydrothermal biomass transformation. Freezing point (fp), boiling point (bp) and critical point (cp) (Moller et al., 2011)..... 27

Figure 2.4 The mechanisms of HTC and evolution pathways of lignocellulosic biowastes (Zhuang et al., 2019) 29

Figure 2.5 Hydrothermal decomposition mechanism of PC in subcritical water (Zhao et al., 2018b) 30

Figure 2.6 Reaction pathway of PVC decomposition in the HTC process reproduced from reference (Nagai et al., 2007)..... 32

Figure 2.7 Trends of oxygenated functional groups and temperature with variations of other parameters reproduced from reference (Jain et al., 2016) 34

Figure 2.8 Surface oxygen-containing groups on carbon and their decomposition by TPD reproduced from reference (Shen et al., 2008)..... 48

Figure 2.9 The curves of sorption potential energy in different-sized micropores (Zhang et al., 2013a) 51

Figure 2.10 Types of N surface functional groups: (a) pyrrole, (b) primary amine, (c) secondary amine, (d) pyridine, (e) imine, (f) tertiary amine, (g) nitro, (h) nitroso,

(i) amide, (j) pyridone, (k) pyridine-N-oxide, and (l) quaternary nitrogen (Ma et al., 2018) 55

Figure 3.1 Horizontal tube furnace……..62

Figure 3.2 Hydrothermal carbonization reactor (a) and fluidized sand bath (b) .. 64

Figure 3.3 Parr high-pressure hydrothermal reactor (a) and hydraulic press (b) 68

Figure 3.4 Classification of N_2 adsorption isotherms (Thommes et al., 2015) 72

Figure 3.5 Classification of hysteresis loops (Thommes et al., 2015)..... 75

Figure 3.6 LECO CHN 628 series elemental analyzer 79

Figure 3.7 TA Instruments Q500 Thermogravimetric analyzer 80

Figure 4.1 (a) Schematic depiction of the location and structure of lignin in the lignocellulosic biomass; (b) three primary monomers of the lignin (Zakzeski et al., 2010)…….92

Figure 4.2 Five typical bonding patterns in lignin matrix structure (Zakzeski et al., 2010) 93

Figure 4.3 Thermal decomposition behaviour of KL and OKL precursors 96

Figure 4.4 FT-IR spectra of KL, OKL, KLK-1–600 and OKLK-1–600..... 98

Figure 4.5 N_2 adsorption isotherms obtained at - 196 ^{o}C for KLK carbons (a) (b) and OKLK carbons (c) (d)..... 100

Figure 4.6 NLDFT pore size distributions for KLK carbons (a) and OKLK carbons (b) 104

Figure 4.7 SEM images of carbon samples: KLK–1–600 (a, b), OKLK–1–600 (c,d), KLK–1–700 (e, f) and OKLK–1–700 (g, h)..... 105

Figure 4.8 CO_2 adsorption isotherms for KLK carbons at (a) 0 ^oC (b) 25 ^oC and OKLK carbons at (c) 0 ^oC (d) 25 ^oC 107

Figure 4.9 CO_2 adsorption capacity of the Kraft lignin-derived carbons against other biomass-derived carbons at 25 ^oC and 15 kPa 109

Figure 4.10 Dynamic CO_2 adsorption curve (a) and cyclic adsorption/desorption performance (b) of KLK–1–600 under simulated flue gas conditions containing 15% CO2 in N2. Adsorption temperature: 25 ^oC; Desorption temperature: 120 ^oC .. 112

Figure 4.11 Relationship between CO_2 uptake and ultra-micropore volume of KL carbons (a) ≤0.48nm, 15 kPa CO_2 and 0 ^oC; (b)≤0.44 nm, 15 kPa CO_2 and 25 ^oC; (c) ≤1nm, 100 kPa CO_2 and 0 ^oC; (d) ≤0.55nm, 100 kPa CO_2 and 25 ^oC 116

Figure 4.12 XRD patterns of KLK-1-600 carbon (a) and SEM-EDX element mapping of KLK-1-600 118

Figure 4.13 Relationship between CO_2 uptake and the density of intercalated potassium in the KLK and OKLK carbons 120

Figure 4.14 Isosteric heat of CO_2 adsorption calculated from the adsorption isotherms at 0 and 25 ^oC for (a) KLK carbons; (b) OKLK carbons 122

Figure 5.1 Van Krevelen diagram of raw EU and hydrochars at different carbonization temperatures……..….130

Figure 5.2 FT-IR spectra of raw EU and the hydrochars prepared at different HTC temperatures 132

Figure 5.3 N_2 sorption isotherms obtained at - 196 ^oC for EU and EUHC derived carbon samples prepared at different HTC temperatures and activation conditions 133

Figure 5.4 Pore size distributions for EUHC samples from KOH activation with different activation temperature and KOH/EUHC mass ratios 136

Figure 5.5 SEM images of hydrochars prepared under different HTC temperature: (a)(b) hydrochar prepared at 220 ^{o}C; (c)(d) hydrochar prepared at 260 ^{o}C 137

Figure 5.6 SEM images of EUHC26 and EUHC26-derived carbons prepared under different KOH activation protocols: (a)(b) EUHC22-1-600; (c) (d) EUHC22-2-700; (e)(f) EUHC26-1-600; (g)(h) EUHC26-2-700. 139

Figure 5.7 Representative XRD patterns of EUHC22-1-600 and EUHC26-1-600 140

Figure 5.8 CO_2 adsorption isotherms EUHC22-derived carbons at (a) 0 ^{o}C (c) 25 ^{o}C and EUHC26-derived carbons at (b) 0 ^{o}C (d) 25 ^{o}C 142

Figure 5.9 CO_2 adsorption curve and cyclic performance of selected samples (flue gases: 15% CO_2 + 85% N_2; adsorption temperature: 25^{o}C; desorption temperature: 120^{o}C) 145

Figure 5.10 Relationship between CO_2 uptake and ultra-micropore volume of the EUHC-derived carbons: (a) 100 kPa CO_2 and 0 ^{o}C; (b) 100 kPa CO_2 and 25 ^{o}C; (c) 15 kPa CO_2 and 0 ^{o}C; (d) 15 kPa CO_2 and 25 ^{o}C..... 149

Figure 5.11 Relationship between CO_2 uptake and the density of intercalated potassium in the EUHC carbons..... 151

Figure 5.12 Isosteric heat of CO_2 adsorption calculated from the adsorption isotherms at 0 and 25 ^{o}C: (a) EUHC22 carbons; (b) EUHC26 carbons..... 153

Figure 6.1 Yield of hydrochar derived from different feedstocks under different HTC temperature……...160

Figure 6.2 The Van Krevelen diagram of feedstocks and hydrochar samples.. 163

Figure 6.3 Dechlorination efficiency of PVC through HTC and co-HTC with biomass materials at different HTC temperatures 165

Figure 6.4 FT-IR spectra of feedstocks and hydrochar samples 167

Figure 6.5 N2 adsorption isotherms obtained at -196 °C for activated carbons derived from PVC under different HTC and activation conditions: (a) PHC24 carbons; (b) PHC26 carbons 168

Figure 6.6 N2 adsorption isotherms obtained at -196 °C for activated carbons derived from biomass and PVC under different HTC and activation conditions: (a) CEPHC24 carbons; (b) CEPHC26 carbons; (c) KLPHC24 and KLPHC26 carbons 170

Figure 6.7 Pore size distributions (PSDs) of PVC-derived carbons via different HTC temperatures：(a) samples prepared at HTC temperature of 240 °C; (b) samples prepared at HTC temperature of 260 °C..... 171

Figure 6.8 Pore size distributions (PSDs) of CEPHC and KLPHC-derived carbons; (a) CEPHC24 carbons; (b) CEPHC26 carbons; (c) KLPHC carbons..... 177

Figure 6.9 SEM images of hydrochars; (a) PHC22; (b) PHC24; (c) PHC26; (d) CEPHC22; (e) CEPHC24; (f) CEPHC26; (g) KLPHC22; (h) KLPHC24; (i) KLPHC26 178

Figure 6.10 SEM images of hydrochars derived carbons; (a) PHC24-1-600; (b) PHC24-1-700; (c) PHC26-1-700; (d) CEPHC24-1-600; (e) CEPHC24-1-700; (f) CEPHC26-1-700; (d) KLPHC24-1-600; (e) KLPHC24-1-700; (f) KLPHC26-1-700 179

Figure 6.11 CO_2 adsorption profiles of PHC24-derived carbons at: (a) 0 °C (b) 25 °C and PHC26-derived carbons at (c) 0 °C (d) 25 °C. 182

Figure 6.12 CO_2 adsorption profiles of CEPHC24- and KLPHC24-derived carbons at: (a) 0 °C (b) 25 °C and PHC26-derived carbons at (c) 0 °C (d) 25 °C..... 186

Figure 6.13 Relationship between CO_2 uptake and ultra-micropore volume of the CEPHC and KLPHC-derived carbons: (a) 100 kPa CO_2 and 0 ^oC; (b) 100 kPa CO_2 and 25 ^oC; (c) 15 kPa CO_2 and 0 ^oC; (d) 15 kPa CO_2 and 25 ^oC..... 190

Figure 6.14 SEM images of potassium mapping: (a) PHC24-1-700, (b) CEPHC24-1-700, (c) KLPHC24-1-700..... 193

Figure 6.15 XRD pattern of selected carbon samples 194

Figure 6.16 (a) Fitted isosteric adsorption heat at a CO_2 uptake level of 0.01 mmol/g for all the carbon samples; (b) Fitted isosteric adsorption heat of selected carbon samples as a function of absolute CO_2 loading using dual-site Langmuir model..... 196

Figure 7.1 Relationship between CO_2 uptake and ultra-micropore volume of carbons at 25 ^oC and 15 kPa CO_2: (a) kraft lignin derived carbon; (b) eucalyptus derived carbon via HTC; (c) PVC/cellulose and PVC/kraft lignin derived carbon via co-HTC……..….206

List of Tables

Table 2.1 CO_2 adsorption capacity of chemically activated carbons 53

Table 3.1 Synthesis conditions for KL-derived activated carbons……..63

Table 3.2 Synthesis conditions for eucalyptus-derived hydrochars 65

Table 3.3 Synthesis conditions for eucalyptus-derived activated carbons prepared via hydrothermal carbonization..... 66

Table 3.4 Synthesis conditions for PVC and PVC/biomass hydrochars 67

Table 3.5 Synthesis conditions for PVC/biomass-derived activated carbons via HTC 69

Table 3.6 The ultimate analysis of precursors and hydrochar samples 87

Table 3.7 Textural properties of sample CEPHC24-2-700 (repeated 3 times) ... 88

Table 3.8 CO_2 adsorption capacity of sample CEPHC24-2-700 (repeated 3 times) 88

Table 3.9 Textural properties of sample OKLK-2-600 89

Table 3.10 CO_2 adsorption capacities of selected samples at 25 ^oC and 15 kPa by TGA 89

Table 4.1 Physicochemical properties of KL and OKL precursors…….95

Table 4.2 Carbon yield of KLK and OKLK carbons prepared in different integrated carbonization-activation conditions..... 96

Table 4.3 Surface textural properties of Kraft lignin-derived carbons 102

Table 4.4 CO_2 uptake capacities of KLK and OKLK carbons at different partial pressures and adsorption temperatures 108

Table 4.5 Chemical analysis by XRF of KLK and OKLK carbons 119

Table 4.6 Dual-Langmuir Fitting results..... 123

Table 4.7 CO_2 uptake at 25 ^oC, 15 kPa CO_2 capacity and IAST CO_2/N_2 selectivity 124
Table 5.1 Physicochemical properties of raw EU and derived hydrochar……129
Table 5.2 Textural properties of prepared carbon samples 134
Table 5.3 CO_2 adsorption capacity of EU- and EUHC-derived carbons 144
Table 5.4 CO_2 adsorption capacity of biomass-derived activated carbon via hydrothermal carbonization 146
Table 5.5 Chemical analysis by XRF of EUHC carbons 151
Table 5.6 CO_2 uptake at 25 ^oC, 15 kPa CO_2 capacity and IAST CO_2/N_2 selectivity 154
Table 6.1 Proximate analysis of precursor materials and hydrochar samples 159
Table 6.2 XRF and Ultimate analysis of raw materials and hydrochar samples 162
Table 6.3 Specific surface areas, pore structure parameters of activated carbon derived from PVC hydrochars via different HTC temperatures 172
Table 6.4 Specific surface areas, pore structure parameters of activated carbon derived from blended PVC/CE and PVC/KL via co-HTC at different conditions 173
Table 6.5 CO_2 adsorption capacity of PHC-derived carbons 183
Table 6.6 CO_2 adsorption capacity of CEPHC- and KLPHC-derived carbons .. 187
Table 6.7 Chemical analysis by XRF of CEPHC and KLPHC carbons 192
Table 7.1 Physiochemical properties of raw materials and their derived samples after different pre-treatment methods……200
Table 7.2 Textural properties and CO_2 adsorption capacities of selected carbon samples from using different precursors 202
Table 7.3 The CO_2 adsorption capacity of prepared carbons at flue gas conditions compared to the literature 204

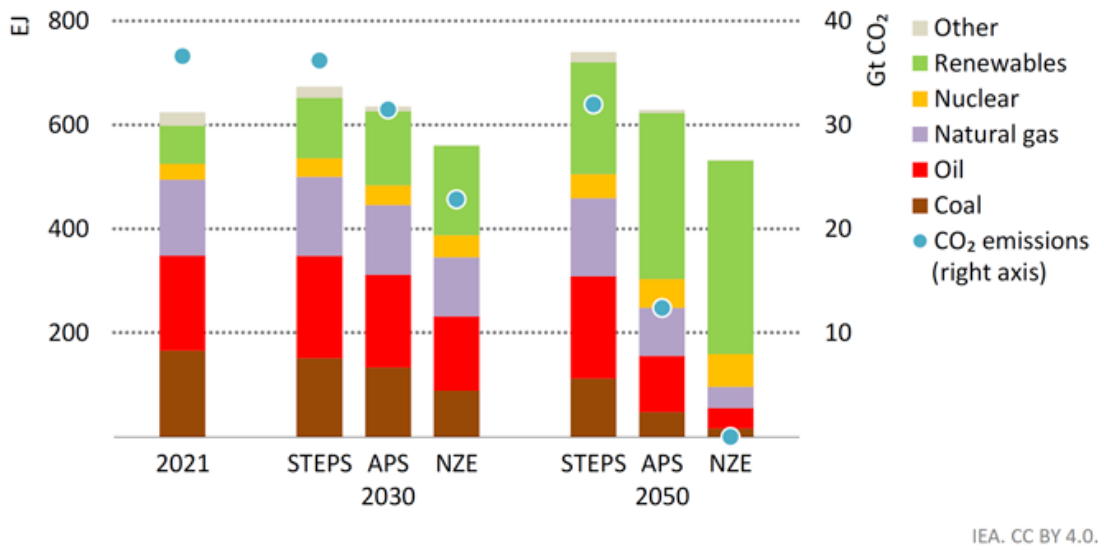
List of Abbreviations

BET	Brunauer–Emmett–Teller
BP	British Petroleum
CCS	Carbon Capture and Storage
CE	Cellulose
DE	Dechlorination Efficiency
DSL	Dual-Site Langmuir
EDS	Energy Dispersive X-Ray Spectroscopy
EU	Eucalyptus Wood
FT-IR	Fourier Transform Infrared
HTC	Hydrothermal Carbonization
IAST	Ideal Adsorption Solution Theory
IGCC	Integrated Gasification Combined Cycles
IUPAC	International Union of Pure And Applied Chemistry
KL	Kraft Lignin
MEA	Monoethanolamine
MOFs	Metal Organic Frameworks
NLDFT	Non-Local Density Function Theory
NMR	^{13}C Solid-State Nuclear Magnetic Resonance
OFGs	Oxygenated Functional Groups
OKL	Pre-Oxidized Kraft Lignin
PSD	Pore Size Distribution
PVC	Polyvinyl Chloride
SBET	Specific Surface Area
SEM	Scanning Electron Microscopy
TGA	Thermogravimetric Analyzer
TPD	Temperature-Programmed Desorption
XRD	X-Ray Diffraction
XRF	X-Ray Fluorescence Spectroscopy

Chapter 1

GENERAL INTRODUCTION

The world is facing unprecedented challenges in tackling the crisis of climate change, which occurs directly as a result of soaring energy demand and excessive fossil energy consumption due to socio-economic development and a growing global population (Shukla, 2022). The climate emergency means that essentially all industrial, business and domestic sectors need to be drastically and radically decarbonised towards net zero by 2050. Despite the tremendous efforts since since the United Nations Framework Convention on Climate Change signed in 1992, global energy-related CO_2 emissions have still been increased by over 60%, reaching the highest ever level of 36.8 Gt per annum in 2022 (IEA, 2023). Whereas the 2023 report by UN's Intergovernmental Panel on Climate Change states that the CO_2 emissions must be reduced by 48% by 2030 relative to the 2019 levels and reach net-zero by around 2050 to meet the Paris Agreement goal of limiting temperature rise to 1.5 ^{o}C by the end of this century (IPCC, 2023). According to the latest IEA's report, fossil fuels including coal, natural gas, and oil, account for 82% of the world's primary energy consumption in 2021 and will still remain the dominant source of energy in foreseeable futures despite the rapid growth in renewable energy (Figure 1.1) (IEA, 2022). Given the continual dominance of fossil energy in the foreseeable future, industrial and direct air CO_2 capture and storage (CCS) has been broadly recognized as one of the essential technologies that must be developed and deployed to deliver the climate change target, irrespective of other energy measures, such as energy efficiency and transitions to renewable energy (Bui et al., 2018, IEA, 2022).



Notes: EJ = exajoule; Gt CO_2 = gigatonnes of carbon dioxide; STEPS = Stated Policies Scenario; APS = Announced Pledges Scenario; NZE = Net Zero Emissions by 2050 Scenario.

Figure 1.1 Global energy consumption and CO_2 emissions by scenario (World Energy Outlook 2022)

CCS involves the capture of CO_2 from large stationary emission sources (e.g. coal-fired power plants, petroleum refineries, and large industrial facilities), along with the subsequent compression and transportation of captured CO_2 to a site where it can be injected into deep geological formations for permanent storage (IEA, 2022). Technically, CCS technologies can be commonly classified into post-combustion, pre-combustion, and oxy-fuel combustion, where post-combustion technologies offer great advantages over the other two options in terms of being applied in the large amounts of existing power plants, such as features of flexibility and easy to be integrated without further modifications (Petrescu et al., 2017, Patrón and Ricardez-Sandoval, 2022). However, the high cost of CCS has been identified as the major challenge preventing the widespread adoption of this technology, with the CO_2 capture technology constituting the most energetically demanding, accounting for about 70–80% of the total cost of CCS (Leung et al., 2014). Of all

post-combustion technologies, chemical absorption based on amine scrubbing has been considered the most technologically mature approach to capture CO_2 from flue gases of fossil fuel-fired power plants, while the technology is still facing many challenges such as high energy penalty, potential amine degradation and equipment corrosion (Vitillo et al., 2017). Therefore, numerous research studies have been devoted to developing next-generation carbon capture technologies that can achieve high CO_2 capture efficiencies while minimizing energy consumption (Siegelman et al., 2021, Hu et al., 2020, Ding et al., 2019).

Among various CO_2 capture technologies currently under development, adsorption-based carbon capture or solid adsorbent looping technology has been considered a technology with great promise for deployment, due to its great process efficiency, reduced energy consumption, lower capital and operational costs, and smaller plant footprints (Lee and Park, 2015). A wide array of solid adsorbents has therefore been investigated, including zeolites, amine-functionalized adsorbents, covalent organic frameworks (COFs), metal organic frameworks (MOFs) and porous carbon materials (Cheung and Hedin, 2014, Foo et al., 2017, Tian and Zhu, 2020, Liao et al., 2016, Guo et al., 2020). However, the technology deployment continues to face significant performance barriers, particularly in terms of the cost and lifetime performance of the sorbent materials. Zeolites are widely used as adsorbents for gas separation, which can achieve high CO_2 uptake of up to 4.2 mmol/g at a typical flue gas condition (25 ^oC and 15 kPa CO_2), while the actual CO_2 adsorption performance can be seriously impaired due to their low tolerance to moisture present in the flue gas (Bae et al., 2013, Chao et al., 2021). Metal-organic frameworks (MOFs) have been investigated recently as promising materials for CO_2 capture owing to their large surface area and unprecedented chemical and structural tunability, which together can facilitate the adsorption strength of CO_2 at low pressure, with the highest level of CO_2 adsorption capacity of 5.30 mmol/g can be reached at 15 kPa and 40 ^oC (Verdegaal et al., 2016). However, the materials still suffer from low water resistance and complex and cost-prohibitive synthesis processes, which can limit their scalability and

commercialization (Younas et al., 2020b). Amine-functionalized adsorbents are considered as upgraded alternatives of amine scrubbing for CO_2 capture in post-combustion scenarios, providing lower heat adsorption compared to aqueous amine solution. Notwithstanding, their fragile multi-cycle stability due to the amine degradation caused by the undesired side reactions of active amine with flue gas impurities (e.g., O_2, SO_x and NO_x) still needs to be improved in the scale-up operation. (Hack et al., 2022).

Activated carbons are a class of adsorbent materials that have been widely used across various industries. Thanks to their widespread availability and affordability, exceptional thermal and chemical durability, low energy demands for regeneration, rapid adsorption kinetics, and adaptability for surface modification, activated carbons have received considerable attention as CO_2 adsorbents in recent years (Boujibar et al., 2018, Li and Xiao, 2019, Kim et al., 2020a, Liu et al., 2020c). Differing from MOFs and zeolites, the hydrophobic nature of activated carbons prevents the materials from decomposition or reduced capacity in the humid environment, whilst the adsorption of CO_2 primarily relies on the Van der Waals interaction between CO_2 and carbon allows relatively low regeneration energy (Samanta et al., 2012). However, the primary challenge in utilizing carbon materials for post-combustion carbon capture lies in developing highly efficient activated carbons that not only offer cost-effectiveness but also possess high CO_2 adsorption capacities. To date, there has been significant research effort dedicated to improving the CO_2 adsorption capacity of activated carbons by either enhancing the ultra-microporosity or modulating favourable surface chemistries, while with only the materials produced from using well-designed carbon precursors or sophisticated synthetic protocols that exhibited comparable CO_2 uptake capacity (Ashourirad et al., 2015, Wang et al., 2020b).

In this context, we aim to develop high efficient CO_2-capturing carbon adsorbents derived from low-cost and easily accessible precursors through easy and sustainable synthetic routes in this PhD project, which helps build a feasible scheme for the industrial application of carbon materials in the future. Firstly, two

abundant and low-cost biomass wastes (kraft lignin and eucalyptus wood) were selected as the precursors to prepare carbon adsorbents through an integrated carbonization-activation route and a two-stage method of hydrothermal carbonization and chemical activation, respectively. Kraft lignin is a carbon-rich precursor that is produced as a byproduct of the kraft pulping process, with a scale of 10 million tons of production per year worldwide (Bajwa et al., 2019). Eucalyptus wood is one of the most important hardwood resources in global pulp and paper production with attractive properties of rapid growth and high density, which has great potential as a feedstock of carbon materials (Ren et al., 2020). In addition, polyvinyl chloride (PVC) wastes as easily accessible materials were employed to produce activated carbons through hydrothermal carbonization with biomass wastes (cellulose and kraft lignin) coupled with chemical activation. As for PVC materials, it is one of the most prevalent plastics commodities mainly destined for packaging applications, with global production reaching about 60 million tons annually (Correa et al., 2019). The results showed that the prepared carbon samples exhibited excellent CO_2 adsorption performance in typical flue gas conditions, which outperformed most of the carbon materials developed so far and was even higher than many MOFs and zeolites. Throughout the characterization and fitting analysis, the compelling high CO_2 uptake capacity is attributable to the exceptionally high ultra-microporosity and the unique surface chemistry modified by intercalated alkaline metals.

Chapter 2

LITERATURE REVIEW

Given that the world continues to rely heavily on fossil fuels, it is crucial to have an effective technology to capture CO_2 from industrial emission sources. Carbon capture and storage (CCS), which involves the separation of CO_2 from large point sources (e.g. coal-fired power plants) followed by the transportation of captured CO_2 to a designated storage location, has been recognized as one of the most practical approaches in meeting global climate targets. However, the deployment of large commercial scale CCS has been falling short of projected progress despite the fact that there are currently 196 CCS projects at various stages around the world (Bui et al., 2018, Alex Zapantis, 2022). One of the main obstacles that prevent a widespread rollout of CCS technology is the stubbornly high cost from the CO_2 capturing stage, which constitutes the most energetically demanding, accounting for about 70–80% of the total cost of CCS (Leung et al., 2014, Durmaz, 2018). Therefore, it is imperative to develop the next-generation CO_2 capture technologies from the perspective of high CO_2 adsorption efficiency and economic feasibility. This chapter will provide a comprehensive review of a wide range of CO_2 capture technologies, including those currently utilized in industry and those in development. Among all the techniques, adsorption by using carbon-based sorbents as a promising post-combustion capture approach was emphatically discussed in terms of their preparation and adsorption mechanisms.

2.1 CO_2 capture technologies

Depending upon the configuration of different fossil fuel power plants, CO_2 capture can be implemented through three main technological means, namely, oxy-fuel combustion capture, pre-combustion capture and post-combustion capture. The schematic diagrams of the three technologies are shown in Figure 2.1.

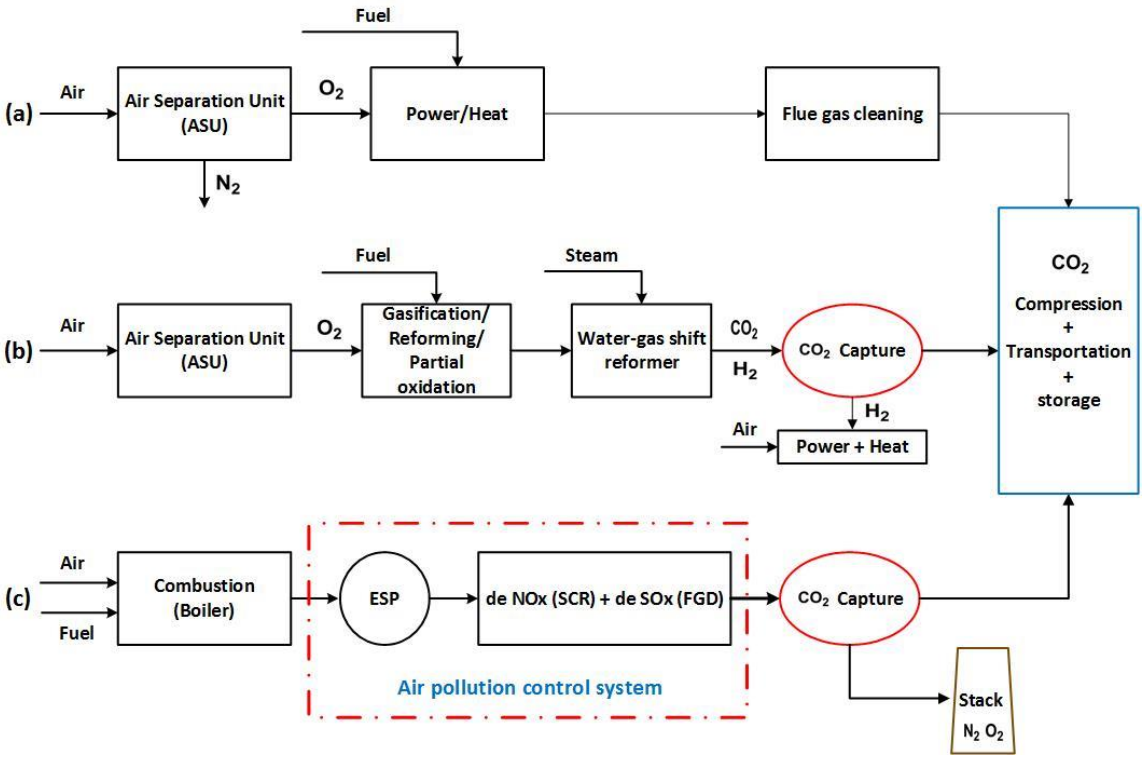


Figure 2.1 (a) Oxy-fuel combustion technologies, (b) Pre-combustion technologies, (c) Post-combustion technologies

2.1.1 Oxy-fuel combustion technologies

In the oxy-fuel combustion process, pure oxygen or enriched oxygen produced from the membrane or cryogenic air separation is performed as the medium of fossil fuel combustion instead of air. As a consequence, the flue gas generated from combustion process is mainly composed of high purity CO_2 and H_2O, with a CO_2 concentration of over 80% can be achieved, which facilitates the subsequent CO_2 separation through easier purification techniques such as flash and distillation (Koohestanian and Shahraki, 2021, Yadav and Mondal, 2022). The advantages of oxy-fuel combustion include high CO_2 purity, reduced NO_x emissions, and lower gas volumes. However, these benefits are at the expense of an energy-intensive air separation unit (ASU), which results in a high capital cost and energy penalty. In addition, the flue gas pre-treatment systems, e.g. flue gas desulphurization and electrostatic precipitator are still required to remove the residual sulphur dioxide

and particulates in the exhaust gases to produce CO_2 to ensure the flue gas stream is pure enough for sequestration. Despite numerous pilot and demonstration projects of oxy-fuel combustion have been operated successfully worldwide, the high energy consumption and cost associated with oxygen production must be addressed by developing new air separation technologies before its larger commercial deployment (Faber et al., 2011, Komaki et al., 2014, Nemitallah et al., 2017, Sher et al., 2018).

2.1.2 Pre-combustion technologies

Pre-combustion carbon capture is defined as a process in which CO_2 is separated from fossil fuels or biomass fuels prior to the combustion. The technology is typically applied in gasification and natural gas power plants where the fuel (biomass, coal, and natural gas) reacts with oxygen or air (Equation 2.1) and/or steam (Equation 2.2) to generate synthesis gas (syngas) composed principally of carbon monoxide and hydrogen. The syngas is then subjected to the water gas shift reformer wherein the carbon monoxide is reacted with steam to give CO_2 and more hydrogen (Equation 2.3). The high concentration and high pressure of CO_2 (i.e. 15–60% by volume, dry basis) can then be separated via physical or chemical absorption, resulting in hydrogen-enriched fuel which can be utilized for various power generation applications (i.e. gas boiler, gas turbine, fuel cell, etc.) (Metz et al., 2005, Jansen et al., 2015, Theo et al., 2016).

Partial oxidation: $$C_xH_y + x/2\ O_2 \leftrightarrow xCO + (y/2)H_2 \quad (2.1)$$

Steam reforming: $$C_xH_y + xH_2O \leftrightarrow xCO + (\ x + y/2)H_2 \quad (2.2)$$

Water-gas shift: $$CO + H_2O \leftrightarrow\ CO_2 + H_2 \quad (2.3)$$

Apart from the production of clean carbon-free fuel (i.e. hydrogen under pressure) from carbon fuel, pre-combustion capture has many other advantages such as producing CO_2 at elevated pressure that requires a lower energy demand for carbon separation and compression operation as well as easy integration with

existing infrastructures (Jansen et al., 2015, Olabi et al., 2022). The current development and demonstration focus of pre-combustion capture is on Integrated Gasification Combined Cycles (IGCC) plants due to its greater compatibility with pre-combustion capture compared to Natural Gas Combined Cycle (NGCC) system where post-combustion capture is more applicable from an economic point of view (Kanniche et al., 2010b). However, despite the pre-combustion in IGCC being on the verge of commercialization, this system is still handicapped by the high investment and retrofit cost and low availability (Kanniche et al., 2010a).

2.1.3 Post-combustion technologies

Post-combustion capture refers to the separation of CO_2 from the flue gas after the fossil fuel has been combusted. In the post-combustion process, the hot flue gas will cool down and the gas streams will undergo a pre-treatment scheme where the selective catalytic reduction (SCR), electrostatic precipitator (ESP) and flue gas desulphurization (FGD) are configured to remove the nitrogen oxides, particulate matter, and sulphur oxides, respectively, prior to the capturing system (Rashidi and Yusup, 2016). At this point, the flue gas is maintained at a temperature in the range of 50–60 ^{o}C and near atmospheric pressure and represents between 10-15% by volume of CO_2 concentration (Hornbostel et al., 2013). Based on the principles of the capture process, the post-combustion capture offers the greatest promise among all the three capture technologies as it can be easily retrofitted to the existing large point sources such as fossil fuel power plants, petroleum refineries and cement manufacturing facilities, where a large fraction of anthropogenic CO_2 comes from nowadays (Osman et al., 2021). Nevertheless, the low flue gas pressure (~1 atm) and low partial pressure of CO_2 in post-combustion gas streams still pose the major challenges in the separation stage (i.e. CO_2 capture) which constitutes the most energy-intensive units of carbon capture system, accounting for about 70–80% of the total cost of CCS (Leung et al., 2014). Hence, a variety of separation technologies for CO_2 post-combustion capture from flue gas streams have been investigated and developed

to reduce energy consumption and lower cost. In terms of the mechanism, current CO_2 separation technologies can be categorized as chemical absorption, membrane separation, cryogenic distillation, microalgal bio-fixation and adsorption using solid sorbent materials.

2.1.3.1 Chemical absorption technologies

Chemical absorption using amine-based solvents, often referred to as 'amine scrubbing', is considered as the most developed technology currently for post-combustion CO_2 capture and is expected to be available commercially within the next decade (Liang et al., 2015). A wide range of amines have been investigated for CO_2 capture such as monoethanolamine (MEA), diethanolamine (DEA), tri-ethanolamine (TEA), N-methyl-diethanolamine (MDEA) and 2-amino-2-methyl-1-propanol (AMP), with MEA is so far the most studied and suitable solvent due to its high reactivity, fast kinetics and low cost (El Hadri et al., 2017, Xiao et al., 2016, Khalifa et al., 2022). During the absorption process, the flue gas stream is counter-currently contacted with the aqueous amine solution in a packed absorber column, which is operated at a low temperature (around 40–60 ^oC) and atmospheric pressure. The CO_2 in the flue gas is absorbed through the following reaction by using MEA (Equation 2.4), where the MEA reacts with CO_2 to form carbamate $RNHCOO^-$ (Blauwhoff et al., 1984).

$$2RNH_2 + CO_2 \leftrightarrow RNHCOO^- + RNH_3^+ \quad (2.4)$$

Afterwards, the CO_2-rich amine solution flows from the bottom of the absorber and passes through a regenerator unit for regeneration. Considering the strong C-N chemical bond formed between CO_2 molecules and amine functionalities, a regeneration temperature of 100-140 ^oC is normally required to liberate CO_2 from the amine solution. The hot lean amine solvent is then cooled down to 40–60 ^oC and is recycled into the absorption column for further CO_2 removal (Wilberforce et al., 2021). According to the available literature, an amine-based regenerative chemical absorption process can achieve much high capture efficacy of up to 98%

(Rashidi and Yusup, 2016). However, the major drawback of amine scrubbing is the large energy consumption for the regeneration of amine solvent, which can be as high as 70-80% of the overall CO_2 capture cost (Nwaoha et al., 2017). In addition, this technique also suffers from the corrosion of equipment by the absorber during carbon capture, which can lead to the reduction of process efficiency and an increase in maintenance costs. Moreover, the degradation of amine compounds either through oxidative or thermal degradation can lead to their accumulate in the solvent phase and result in poor CO_2 absorption capacity and kinetic rate (Meng et al., 2022). Other potential impacts on the ecosystem arising from the evaporation of a large portion of the amine-based chemicals also need to be addressed (Ogungbenro et al., 2017).

2.1.3.2 Membrane separation technologies

The application of membrane technology in CO_2 abatement is a relatively novel approach but has been extensively developed since the last decade because of its low capital cost, low energy penalty and operational simplicity compared to other competitive technique routes (Vakharia et al., 2018). Membranes form semi-permeable barriers to separate compounds by various mechanisms (solution/diffusion, adsorption/diffusion, molecular sieve and ionic transport). Based on the different nature of materials applied, the membrane can be either organic (polymeric), inorganic (carbon, zeolite, ceramic or metallic) or mixed matrix derived. With regards to CO_2 capture, the gas stream containing CO_2 at elevated pressure passes through the membrane separator to the permeate side at low pressure on a positive pressure difference (i.e., driving force) (Mukherjee et al., 2019). The membrane separation performance relies on the permeability and selectivity of the membrane as well as the diffusivity of gas molecules in the membrane and the gradient in partial pressures of gases. Hence, the gas stream with a relatively higher CO_2 initial pressure (well above 20%) is generally recommended for membrane technology to achieve higher separation efficiency. Given that the low CO_2 pressure in the post-combustion flue gas results in less

drive force that will inhibit the separation performance, an alternative solution could be the utilization of multistage membrane systems (Chao et al., 2021).

2.1.3.3 Cryogenic separation

Cryogenic separation is another potential pathway for CO_2 capture via a physical distillation process in which the CO_2 component of the flue gas stream is separated by condensation. In the cryogenic separation process, the CO_2 is condensed from a gas stream at a very low temperature of −56.6 ^oC. One advantage of the cryogenic CO_2 distillation approach is the CO_2 can be captured in a liquid form, which makes it easier to store CO_2 underground without any consumption of water and corrosion issues (Liu et al., 2021). However, cryogenic separation processes operated at low temperatures often require high pressures to maintain the CO_2 in a liquid state, which could be a challenge to the efficiency of the process in terms of managing the pressure and temperature conditions. Additionally, considering the presence of a large number of impurities in the flue gas and the reduction in pressure of CO_2 from the post-combustion exhaust, this physical process is more applicable for the treatment of flue gas with a high concentration of CO_2, especially for oxyfuel-combustion (Mukherjee et al., 2019).

2.1.3.4 Bio-fixation

Bio-fixation of flue gas by culturing microalgae appears as a new effort to reduce the CO_2 concentration in the atmosphere. According to the mechanism involved in the process of microalgae photosynthesis, the atmospheric CO_2 and CO_2 from flue gases can be utilized for their growth. Microalgae are regarded as fast-growing microorganisms with a relatively high CO_2 bio-fixation rate of 10–15 times more than terrestrial plants. Additionally, the accumulation of large quantities of lipids and carbohydrates inside the cells of certain microalgae strains can be further extracted for biodiesel production (Singh et al., 2019). This clean and sustainable

technology is especially suited for post-combustion carbon capture because CO_2 released from power plants can be fed directly into the microalgae culture without purification, where the flue gas components other than CO_2 such as oxides of sulphur and nitrogen with heavy metals can be effectively utilized as nutrients for microalgae cultivation. However, the heavy requirement of inorganic nutrients sources and intensive energy in cultivating suitable microalgal species for sequestration of CO_2 from actual combustion flue gas may limit the development of this technology in large-scale production (Zhao and Su, 2014, Singh et al., 2019).

2.1.3.5 Adsorption

Compared to other technologies, adsorption using solid materials has gained increasing attention in recent years and is considered as an effective option for CO_2 separation due to its advantages such as high CO_2 adsorption capacity at ambient conditions, low regeneration cost, long-term stability, fast kinetics and ease of handling over a relatively wide range of temperatures and pressure (Rashidi and Yusup, 2016, Ünveren et al., 2017, Modak and Jana, 2019). In the post-combustion capture through the adsorption process, CO_2 molecules are selectively separated from a gas mixture by either chemisorption or physisorption based on the nature of the bonding between the adsorbate and the solid surface. Chemisorption is achieved by the formation of chemical bonds with the adsorbent, whereas physisorption involves CO_2 adsorption on the adsorbent matrix surface by weak intermolecular forces. Upon equilibrium, the solid adsorbent is then regenerated by reducing the pressure or increasing the operating temperature, to discharge the adsorbed CO_2 from the adsorbent surface and be reused for the next adsorption cycle (Liu et al., 2014). The adsorption system becomes attractive since it can reduce the total energy consumption in the regeneration process, owing to the lower heat capacity of the sorbent, as well as reducing the maintenance requirements with reduced secondary waste generation (Mukherjee et al., 2019). A variety of solid sorbents have been developed for CO_2 capture in the post-combustion separation process, ranging from materials that separate CO_2

mainly by physical adsorption, such as zeolite, MOFs and activated carbons, to adsorbents with specific functional groups, for example, amine-functionalized adsorbents, targeted to achieve chemical reaction with CO_2. However, the success of such an approach for CO_2 capture from flue gas will depend on several imperative factors from both economical and operational perspectives, such as:

1. High CO_2 adsorption capacity: The equilibrium adsorption capacity of an adsorbent, which refers to the amount of CO_2 adsorbed at the thermodynamic equilibrium, determines the capital cost of the capture system. The high CO_2 adsorption capacity enables the reduction of adsorbent quantity used and the size of process equipment, therefore reducing the capital cost as well as the energy penalty. In this framework, a target working capacity of solid materials would be suggested to approach or greater than 3 mmol/g to be competitive with the existing amine scrubbing system (Drage et al., 2012, Samanta et al., 2012).
2. Adsorption kinetics: CO_2 adsorption kinetics control the cycle time of a dynamic adsorption system. Sorbents with fast CO_2 adsorption kinetics provide a fast CO_2 breakthrough curve, which contributes to the high efficiency and economical operation of the multiple adsorption-desorption cycles, whereas the slow kinetics expand breakthrough time, thus potentially impacting the amount of sorbent required (Raganati et al., 2019).
3. The heat of adsorption: A proper adsorbent should be characterized by mild conditions for regeneration to reduce the cost of the capture system. The heat of adsorption is an important parameter to indicate the energy required for regeneration and the surface affinity of an adsorbent toward CO_2. The optimal heat of adsorption for the selected adsorbents should be moderate because too high a heat of adsorption will give rise to increased energy requirement for sorbent regeneration whilst too low a heat of adsorption stands for unacceptably low CO_2 uptake at typical flue gas temperatures and CO_2 partial pressures (Sethia and Sayari, 2015). The heat of adsorption

is substantially different with regard to physisorbents (20–50 kJ mol^{-1}) and chemisorbents (60–100 kJ mol^{-1}) (Samanta et al., 2012).

4. CO_2 selectivity: The CO_2 selectivity is defined as the ratio of CO_2 uptake capacity to that of other components (e.g. mainly N_2) present in the flue gas stream at a given flue gas conditions, which directly affects the purity of captured CO_2 and in turn impacts the transportation and sequestration of CO_2 as well as the cost of CO_2 storage. Thus, high CO_2 selectivity over other components present in the flue gas is essential for a proper adsorbent (Raganati et al., 2021).
5. Chemical and mechanical/thermal stability: The presence of impurities like SO_x, NO_x and moisture in the flue gas will reduce the CO_2 adsorption capacity of adsorbents during multi-cycle operations. Specific operating and handling conditions, such as high flow rate of flue gas, vibration and temperature fluctuation will also impact the integration of adsorbents. A proper adsorbent should possess good regenerability and stability for the efficient CO_2 capture process (Choi et al., 2021).

Amine-functionalized adsorbents are produced by incorporating amine species into solid porous materials, taking advantage of both the porous structure of solid adsorbents and the acidic gas affinity of amine compounds. Compared to the aqueous amine solvents, the amine-functionalized materials have the benefit of lower regeneration energy consumption due to the low heat capacities of solid supports. A broad range of porous materials including mesoporous silicas, zeolites, metal-organic frameworks (MOFs) and activated carbons have been used as substrates to load amine sources for CO_2 capture from flue gas (Jiao et al., 2016, Cheng et al., 2019, Yu et al., 2017, Wang et al., 2017). Regarding the loading of amine sources on support materials, the preparation methods of amine-functionalized adsorbents can be classified into three types, namely wet impregnation, grafting and direct synthesis, based on the amine sources and the bonding styles between the amine sources and the supports (Hu et al., 2020). Wet

impregnation refers to the organic amine species being loaded into pores and on the surface of support materials through weak, non-covalent interactions, which gives rise to sorbents with high amine content and easy in preparation. The immobilized amino groups could react with CO_2 to produce carbamates through the formation of zwitterionic intermediates, likewise to the absorption of CO_2 with primary and secondary amines (Chiang and Juang, 2017). Wang et al. (2013) developed a mesoporous carbon-based PEI-loaded sorbent, with the highest CO_2 adsorption capacity achieved 4.82 mmol/g at a low CO_2 partial pressure of 15 kPa. However, as there is no substantial chemical bond between the dispersed amines and the supports, the as-obtained adsorbents have similar thermal degradation issues with the origins of the amines (Wang et al., 2017). On the contrary, amine grafting refers to a chemical process in which the amine-containing silanes are tethered to the support surface through a covalent bond, leading to high thermal stability and a high CO_2 diffusion rate of the sorbent. Whereas the amine-grafted adsorbents mainly suffer from relatively low CO_2 uptake and sophisticated synthesis (Chen et al., 2017). Direct synthesis involves the covalent incorporation of amine-containing precursors in situ into the porous materials, which eliminates the need for additional modification steps, resulting in a more cost-effective production process. However, the synthesized materials often have a problem achieving a homogeneous distribution of amine functional groups throughout the substrates due to the straightforward one-step method, which may result in poor adsorption performance and reduced capacity (Lin et al., 2023). In general, the CO_2 capacities of amine derived absorbents are mainly determined by the characteristics of basic groups contained within the materials, rather than the porosity and textural structure of substrates. Amine functionalized adsorbents are overall promising materials for post-combustion CO_2 capture owing to the preferable affinity to CO_2, excellent CO_2 capture selectivity and lower energy requirement for sorbent regeneration but still need to overcome the stability problem in the cyclic CO_2 adsorption–desorption runs (Zhao et al., 2021a, Hack et al., 2022).

Zeolite, which are crystalline aluminosilicates composed of aluminium, silicon, oxygen, and exchangeable cations (Ca^{2+}, Mg^{2+}, Na^{+}, K^{+}, etc.) with a particularly ordered microporous structure, have been widely studied as CO_2 adsorbents for post-combustion process (Cheung and Hedin, 2014, Chao et al., 2021). These naturally occurring or synthesized microporous materials have a framework of interconnecting channels or cages formed by the covalent oxides of Al and Si providing a porous structure with uniform pore sizes of 0.5–1.2 nm that favours adsorbing CO_2 molecules (Lee and Park, 2015). Moreover, the existence of cations in the silicate framework, such as Na^{+} and Li^{+}, induces a negative charge and therefore creates a strong electric field that can strongly interact with gases possessing a high dipole or quadrupole, like CO_2, and the electrostatic interaction can be enhanced by altering the Si/Al ratio (Sun et al., 2019). Due to the favourable CO_2 adsorption properties, zeolites have received extensive attention and shown promising results for the separation of CO_2 from flue gas streams. Zeolite 13X is considered a benchmark CO_2 adsorbent owing to its preferable porous structure for CO_2 capture. It was reported that Zeolite 13 have a high equilibrium selectivity for CO_2 and featured a high CO_2 uptake of up to 2.2 mmol/g at 25 ^{o}C and 15 kPa (Lee et al., 2002). On the other hand, the modification by exchanging the cations with various metal ions has been further investigated to improve the CO_2 adsorption performance since the interaction of CO_2 molecules with the electric field created by the charge-compensating cations also largely influences the CO_2 adsorptive properties. For example, Moura et al. (2016) measured the CO_2 adsorption capacities for cation-exchanged samples of zeolite 13X and found that the adsorption capacity decreased in the order Li > Na > Ba> Fe, with the Li-exchanged zeolite exhibited the highest CO_2 uptake of 3 mmol/g at 25 ^{o}C and 15 kPa. However, the main drawbacks are their strong hydrophilic nature, resulting in low tolerance to water and low CO_2 selectivity. Consequently, their CO_2 adsorption capacity can be drastically decreased due to the occupation of CO_2 adsorption sites by the preferential adsorption of the polar H_2O, SO_x, NO_x and H_2S molecules to the cations (Bui et al., 2018). Furthermore, to fully recover the adsorption capacity of the zeolite, the energy and time-intensive temperature swing approach

needs to be employed due to the strong affinity between CO_2 molecules and the surface of zeolites. (Spigarelli and Kawatra, 2013).

Metal–organic frameworks (MOFs) are another family of porous crystalline adsorbents which can be obtained via the self-assembly of metal ions and organic ligands. Since their inception in the late 1990s (Li et al., 1998, Li et al., 1999), MOFs have been recognized as emerging materials for CO_2 adsorption and capture applications due to their large surface areas, high porosity and chemical tunability (Aniruddha et al., 2020). The interior surface area of MOFs can vary from hundreds to a current record of 7839 $m^2 g^{-1}$ (Honicke et al., 2018), with the pore size ranging from angstroms to nanometres. The phenomenal textural properties offer MOFs materials a potentially high CO_2 storage capacity, especially at higher pressures (Li et al., 2020c). Yaghi's group prepared the MOF-77 with an excellent high surface area of 4500 m^2/g and showed a remarkable CO_2 adsorption capacity of 33.5 mmol/g at 35 bar and 25 ^oC which is far greater than that of any other porous material reported, whereas only 0.8 mmol/g of uptake capacity was observed at atmospheric pressure (1 bar and 25 ^oC) (Millward and Yaghi, 2005). It was believed that rather than surface area and pore volume determining the adsorption capacity, the enhanced interactions between the framework (e.g. open metal sites and functional groups) and CO_2 molecules are in the more dominant role in defining the CO_2 adsorption performance at lower pressures (Ding et al., 2019). On the basis of MOFs' chemical tunability and compatibility, the strengths of the interactions can be enhanced by tailoring the chemical and physical properties of frameworks via the distinct incorporation of appropriate metal nodes and organic linkers. Mg-MOF-74 with a high density of available open Mg^{2+} sites in the framework exhibited a high CO_2 adsorption capacity of 5.30 mmol/g at a CO_2 partial pressure of 15 kPa and 40 ^oC (Verdegaal et al., 2016). Wen et al. (2019) developed Ni-based UTSA-120 with adjusted pore size (4.6 Å) and dual functional groups ($SiF6^{2-}$ and tetrazine) on pore surfaces has a high CO_2 uptake of up to 3.56 mmol/g at 15 kPa and 23 ^oC. However, one of the major issues that limit the carbon capture application of MOFs is their chemical instability, which enables the

competitive adsorption between CO_2 and flue gas components like water, NO_X and SO_X and thus not only reduces the adsorption and selectivity of MOFs but also causes framework destruction (Younas et al., 2020a, Raganati et al., 2021). In addition, the cost of MOFs is still exorbitant compared to that of conventional adsorbents like zeolites and activated carbon, which is largely attributed to the lack of scale-up production routes developed for MOFs (Mahajan and Lahtinen, 2022).

2.2 Carbon based sorbents for CO_2 capture

Carbon-based sorbents represent a class of carbonaceous materials comprising activated carbons, carbon nanotubes, fullerenes, graphene, and carbon nanofibers, with activated carbons have received enormous attention for CO_2 capture in the post-combustion process due to their mature synthesis technology and developed porous structures (Raganati et al., 2021). In comparison to the above-mentioned solid adsorbent materials being used in post-combustion carbon capture, activated carbons possess several advantages, such as easy availability, high moisture tolerance, ease in surface chemistry modification, excellent chemical stability and reversibility, and low regeneration energy requirement, aside from their low cost (Ben-Mansour et al., 2016, Mukherjee et al., 2019). In this section, the mechanisms of activated carbon preparation including precursor materials, pre-treatment and activation pathways as well as the CO_2 adsorption on activated carbons will be reviewed and discussed.

2.2.1 Precursors for carbon materials

Activated carbons, in a broad sense, refer to a wide range of amorphous carbonaceous materials that possess high porosity and surface area, which are obtained from the thermal treatment of a variety of carbon-rich materials under different conditions. The adsorption capacity and quality of activated carbon can be significantly dependent on the source of the precursors. The precursors for the preparation of activated carbon gravitate toward the non-expensive sources with low ash and substantial volatile matter due to the evolution of contained volatile

matter during the thermal treatment will benefit the formation of porous structures in activated carbons (Herawan et al., 2013, Rashidi and Yusup, 2016). A wide range of raw materials or precursors ranging from biomass, coal, and petroleum pitch to waste materials from industrial processes have been explored to prepare activated carbons. Coal is the most commonly used precursor, mainly because of its low cost and abundance. However, considering environmental sustainability, the paradigm should shift toward renewable resources, such as biomass or any carbon-rich waste for activated carbon production (Danish and Ahmad, 2018). Waste materials have significant contributing properties to produce activated carbon mainly with their economic and environmental natures. In addition, converting wastes to value-added sorbent materials is also a promising approach to reduce the large quantities of disposals to landfills. Activated carbon can be prepared from a variety of waste materials, which are normally categorised as conventional wastes (from agriculture and wood industry) and non-conventional wastes (from municipal and industrial activities) (Dias et al., 2007).

2.2.1.1 Forestry and Agricultural wastes

The conventional waste materials for activated carbon production are mainly biomass wastes from the discards or by-products in agriculture and the wood industry, such as the shells and/or stones of fruits, wastes resulting from the production of cereals, various seed wastes, woody wastes, and forest residues. It is estimated that approximately 100 billion metric tons of biomass are produced globally per annum, with only 3% of these being cultivated, harvested and utilized including for both first-generation (food sources) and second-generation (non-food-based sources) biofuels (Sheldon, 2014). In terms of the compositions in typical biomass, as shown in Figure 2.2, the largest fraction is cellulose, which accounts for 30-50 wt% of biomass, hemicellulose shares 20-35 wt% of biomass, lignin offers up 15-20 wt% of biomass whilst the remaining 15-20 wt% includes proteins, fats, extractives and ash content (Mood et al., 2013). These compounds are strongly intermeshed and chemically bonded through either non-covalent

forces or covalent linkage (Saidur et al., 2011). Due to the large abundance, renewability and low ash content, different types of biomass materials such as rice husk, olive stones, sawdust, coconut shell and sunflower seed shell have been investigated for the synthesis of activated carbon for CO_2 sequestration (Liu et al., 2017, Chen et al., 2016, Quan et al., 2020, Deng et al., 2015, Calvo-Munoz et al., 2016). These materials are not only inexpensive and can be easily synthesized but also offer high CO_2 adsorption capacities at both low- and high-pressure regimes.

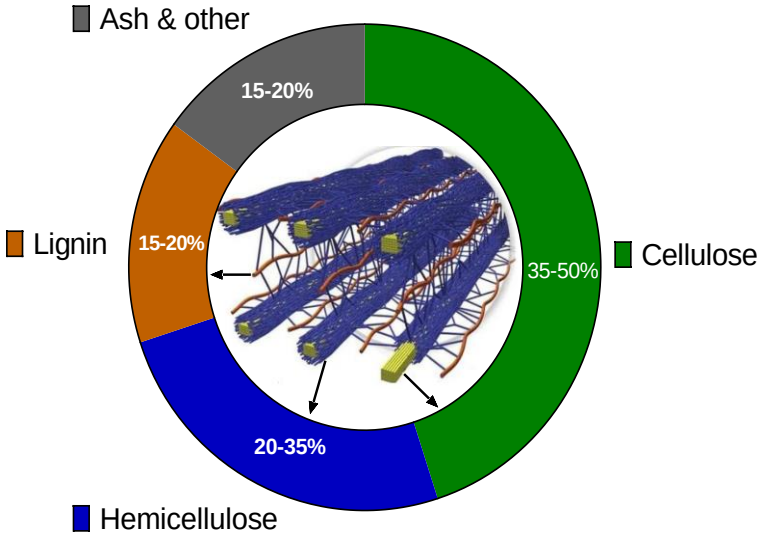


Figure 2.2 General composition of biomass feedstock

2.2.1.2 Municipal and industrial wastes

Non-conventional wastes are generally from widespread municipal and industrial activities, which by their nature are difficult or poorly effective to be regenerated into other materials with most of them ending up in incineration plants or landfills. The valorisation of such non-conventional waste as carbon sources for the production of activated carbon will provide two-fold advantages in reducing the amounts of waste materials and developing low-cost adsorbents. Therefore, a wide variety of such wastes have been explored recently to prepare activated carbon, ranging from plastic wastes, such as polyethylene terephthalate (PET) and polyvinyl chloride (PVC), to industrial wastes like fly ash and polymeric residues

from factories as well as other wastes such as tires and sewage sludge (Wang et al., 2020c, Liu et al., 2022, Dindi et al., 2019, Tang et al., 2017, Li et al., 2022a, Wei et al., 2016). However, there are still several challenges or limitations from using such wastes for the production of activated carbon for CO_2 capture. For example, waste PVC can produce a significant amount of benzoic acid and hydrochloride acid during the pyrolysis process, which results in severe corrosion problems to the equipment (Papari et al., 2021). Other concerns include the relatively low CO_2 adsorption capacities of activated fly ash carbon and the potential release of hazardous heavy metals during the use of sludge-derived carbon (Dindi et al., 2019, Chen et al., 2002).

2.2.2 Pre-treatment of precursor feedstock for activated carbon materials

As previously stated, valorisation of various underutilized waste materials can be achieved by the production of activated carbons. These carbon-based materials are usually converted to activated carbons through a series of preliminary steps prior to activation depending on the nature of precursors, which aims to modify the physical and chemical properties of the precursor materials to improve their suitability for use in the production of activated carbon. The common pre-treatment technologies usually include pre-oxidation treatment and carbonization through either pyrolysis or hydrothermal carbonization (HTC) (Liu et al., 2010a, Anca-Couce, 2016, MacDermid-Watts et al., 2021). Pre-oxidation treatment is a promising method to tailor the structure and surface chemistry of precursor materials and further increase carbon yield and improve the pore structure of activated carbons (Jin et al., 2020). Among those oxidation methods, impregnation of strong acids, such as nitric acid, is most extensively used in biochar modification (Li and Li, 2019). However, this method may suffer from secondary pollution due to long rinsing steps and high corrosivity. In comparison, air oxidation is considered to be more economical, simple, environmentally friendly and mild, which is often used to increase the carbon yield and promote the porosity development of activated carbons (Liu et al., 2010a, Ruiz et al., 2006). Chars formed during the

carbonization process are an important aspect to extend the successful high-value-added activated carbons. Two principle carbonization processes, namely pyrolysis and hydrothermal carbonization (HTC) have been recognized as effective pre-treatments to convert raw materials into higher energy-density chars. Pyrolysis is a traditional thermochemical conversion process which refers to the thermal degradation of carbonaceous materials in an inert atmosphere over a wide temperature range (300 to 600 ^{o}C), forming solid char, a gaseous mixture of CO, CO_2, H_2O, H_2 and short-chain hydrocarbons (Anca-Couce, 2016). Another process called hydrothermal carbonization (HTC) involves the conversion of precursor materials into carbon-rich products in a hot, pressurized, aqueous environment (Malghani et al., 2013). Compared to pyrolysis, hydrothermal carbonization is characterized by a more mild and environmentally friendly thermochemical process by only involving water as the solvent, with the temperature typically ranging from 180 to 250 ^{o}C (MacDermid-Watts et al., 2021).

2.2.2.1 Hydrothermal treatment to upgrade the feedstock for carbon materials

HTC has received growing attention in the past few decades as an alternative to pyrolysis due to its simplicity and ability to endow hydrochar with homogeneous chemical and morphology characteristics and a plentiful amount of oxygenated functional groups (OFGs), making them effective precursors for the production of chemically activated carbon (Wen et al., 2017). Moreover, this technology can not only be applied for carbonizing wet biomass but also for feedstock with a small particle size (Correa et al., 2018). By taking advantage of these, from simple monosaccharides and oligosaccharides to complex lignocellulose biomass and polymeric plastic wastes have been effectively employed as HTC starting materials in many reports (Sevilla and Fuertes, 2011, Zhang et al., 2019c, Hao et al., 2013, Zhao et al., 2018c). Using hydrothermal carbonization in preparing hydrochar has several important advantages compared to pyrolysis: (1) relatively low

carbonization temperature – typically in the range of 180^{o}C - 250^{o}C, resulting in lower energy consumption and reduced greenhouse gas emissions; (2) carbonization takes place in the water phase therefore allowing the direct utilization of wet biomass, which can effectively reduce the energy requirement for pre-drying biomass prior to pyrolysis; (3) the occurrence of hydrolysis and dehydration reaction during the HTC bestows the carbonized products enriched with a high content of oxygen-containing functional groups which can be effectively exploited in post chemical activation strategies; (4) greater flexibility in feedstock - HTC can process a wide range of feedstocks, including agricultural waste, forestry residues, municipal solid waste, and wastewater sludge, with preferential physicochemical properties can be obtained through the synergistic carbonization of two or more feedstocks via co-HTC; (5) HTC generates less greenhouse gas emissions compared to pyrolysis, making it a more environmentally friendly option (Titirici et al., 2012, Bardhan et al., 2021). Overall, the significant operational and environmental benefits associated with this process have led to the recent exploration of waste stream valorisation (Berge et al., 2011, Lin et al., 2017, Lin et al., 2020). The successful hydrothermal carbonization of wastes has the potential not only to convert waste materials to value-added products but also substantially reduce fugitive greenhouse gas emissions from current treatment/management processes (e.g. municipal solid waste (MSW) landfills, compost (including N_2O) and incineration facilities) (Lu et al., 2012).

2.2.2.2 Mechanisms of hydrothermal carbonization

The mechanism of hydrothermal carbonization (HTC) can vary with the precursor materials being processed. The composition and structure of the precursor material can have a significant impact on the reaction pathways and mechanisms involved in HTC.

HTC of biomass wastes As the most integral part of biomass wastes, lignocellulosic biomass (cellulose, hemicelluloses and lignin), with its high initial

oxygen content (40-50 wt.%), is a preferred precursor for the production of well-defined functional carbonaceous materials via HTC (Unur, 2013). HTC can physiochemically transform the solid biomass into value-added products (i.e., hydrochar) at a comparatively low temperature (180–250 ^{o}C) and saturated pressure (2–10 MPa) (Funke and Ziegler, 2010, Jain et al., 2016). In the HTC process, water is commonly used as a catalyst that facilitates hydrolysis and cleavage of lignocellulosic biomass due to its high ionization constant under high temperatures (Jain et al., 2016). Substantially, the nature of the conversion process is a function of the reaction temperature, with the products in different states of matter being formed at all temperatures. However, the extent of the respective main product formation shifts from solid (at low temperature) via liquid (medium temperature) to gaseous (at high temperature) products, with an increasing process temperature augmenting the thermal energy and thus allowing the reactions to take place at increasing rates (Moller et al., 2011). The temperature influence on the final products of hydrothermal biomass transformation is shown in Figure 2.3.

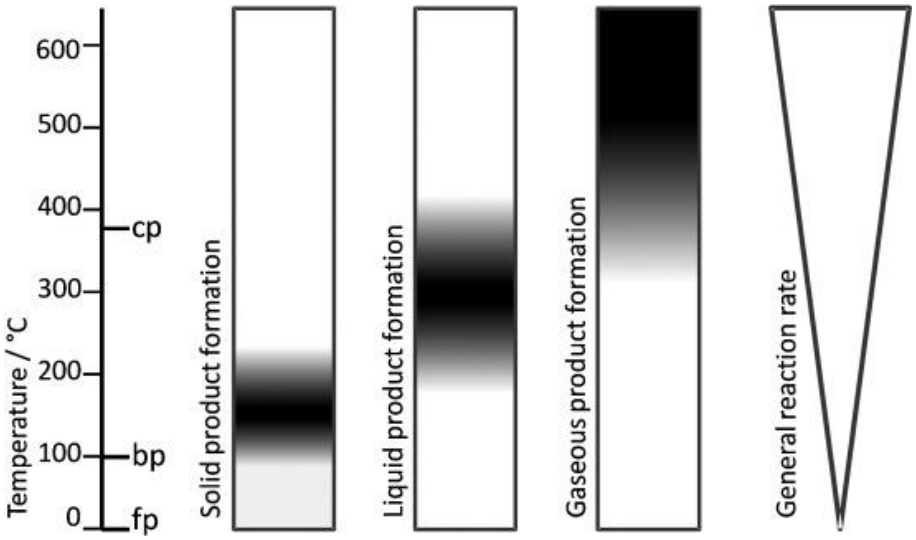


Figure 2.3 Illustration for the temperature dependence of hydrothermal biomass transformation. Freezing point (fp), boiling point (bp) and critical point (cp) (Moller et al., 2011)

In terms of the mechanism of the formation of hydrochar products from lignocellulosic biomass, the hemicellulose is initially depolymerized at 180 ^{o}C to polysaccharides (e.g. glucuronoxylan and galactoglucomannan) which continue hydrolyze to generate monosaccharide units including hexoses (glucose, mannose and galactose) and pentoses (xylose and arabinose), with glucose subsequently isomerizes to form fructose (Shen, 2020). The reactions with increasing temperature then give rise to the diversification of hydrothermal products such as the organic acids, aldehyde compounds and soluble intermediates (e.g. furans, 5-hydroxymethylfurfural and furfurals) as a result of acid-catalysed dehydration and fragmentation reactions (i.e., ring opening and C-C bond breaking) of monosaccharides (Titirici et al., 2008, Baccile et al., 2014, Shen, 2020). Likewise, the monosaccharide derived from cellulose undergoes a similar pathway to that of hemicellulose, albeit the hydrolysis temperature of cellulose is higher. The subsequent predominant reactions shift from hydrolysis toward condensation and polymerization, where the intermediates with significant reactivity begin to form cyclopentanone, furanone derivatives or even monocyclic aromatics via ring condensation and intermolecular dehydration. Subsequently, the aromatized molecules are further polymerized and aromatized to form aromatic clusters (Zhuang et al., 2019). As the concentration of aromatics in the aqueous phase reaches its threshold value, a burst of nucleation process takes place and large amounts of aromatic clusters are concurrently accumulated (Kang et al., 2012). Under the auspices of residence time, hydrochars with abundant aromatic structures are finally formed via the surface diffusion of aromatic clusters. The mechanisms of HTC and evolution pathways of lignocellulosic biowastes are presented in Figure 2.4. Unlike the carbohydrate structures of cellulose and hemicellulose, lignin is a polymer with substantial aromatic structures. During its hydrothermal process, the polyaromatic hydrochar is preferentially produced via a solid-solid conversion from the non-dissolved parts of lignin, whereas the residual lignin (namely dissolved lignin) is first hydrolyzed to an aqueous phase above 210 ^{o}C followed by a series of homogeneous reactions (Dinjus et al., 2011). Phenolic compounds and methoxylated benzenes are the primary products from

the secondary hydrolysis of aromatic oligomers, which subsequently undergo polymerization as part of aromatic clusters via intermolecular dehydration and thereby expanding the carbon nucleus (Shen et al., 2017, Zhuang et al., 2019).

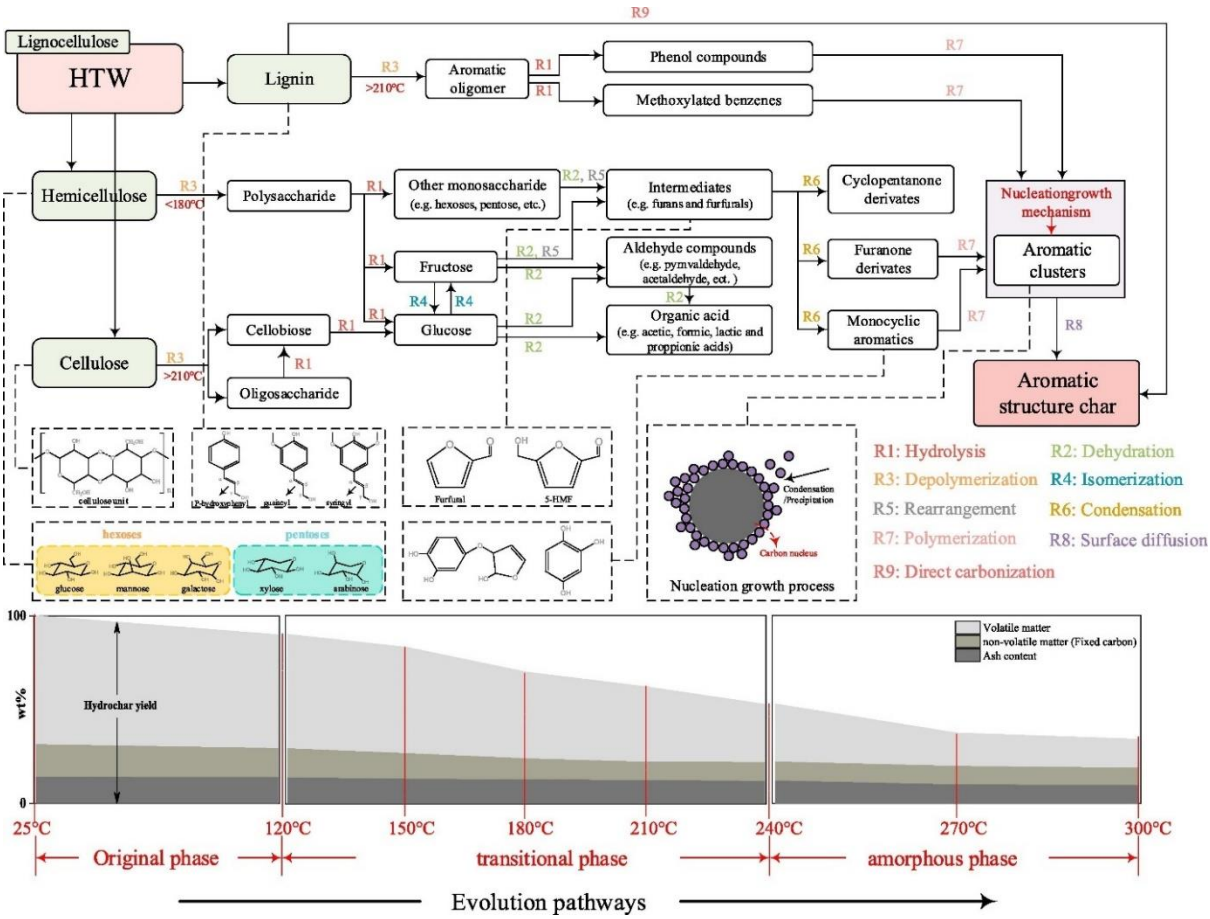


Figure 2.4 The mechanisms of HTC and evolution pathways of lignocellulosic biowastes (Zhuang et al., 2019)

HTC of Plastic wastes The management of plastic wastes poses a significant challenge due to their poor degradability, leading to severe environmental problems. Plastic wastes with low moisture and oxygen contents have been commonly disposed of by thermochemical processing at higher temperatures, releasing hazardous gases that have a high risk to the environment and human/animal health. Hydrothermal treatment of these plastic wastes offers a sustainable and cost-effective solution to remove the toxic substances (e.g. toxic

halogenated dibenzodioxins and dibenzofurans from the PVC combustion), with the generated hydrochar can be utilized for the production of clean solid fuel or advance carbon materials (Shen, 2020). However, the mechanisms of different plastic wastes from municipal and industrial activities through hydrothermal carbonization treatment can be complicated and varied with the specific constitution. Many studies have investigated the HTC pathways of different kinds of plastics (Zhao et al., 2018b, Zhao et al., 2018c, Poerschmann et al., 2015).

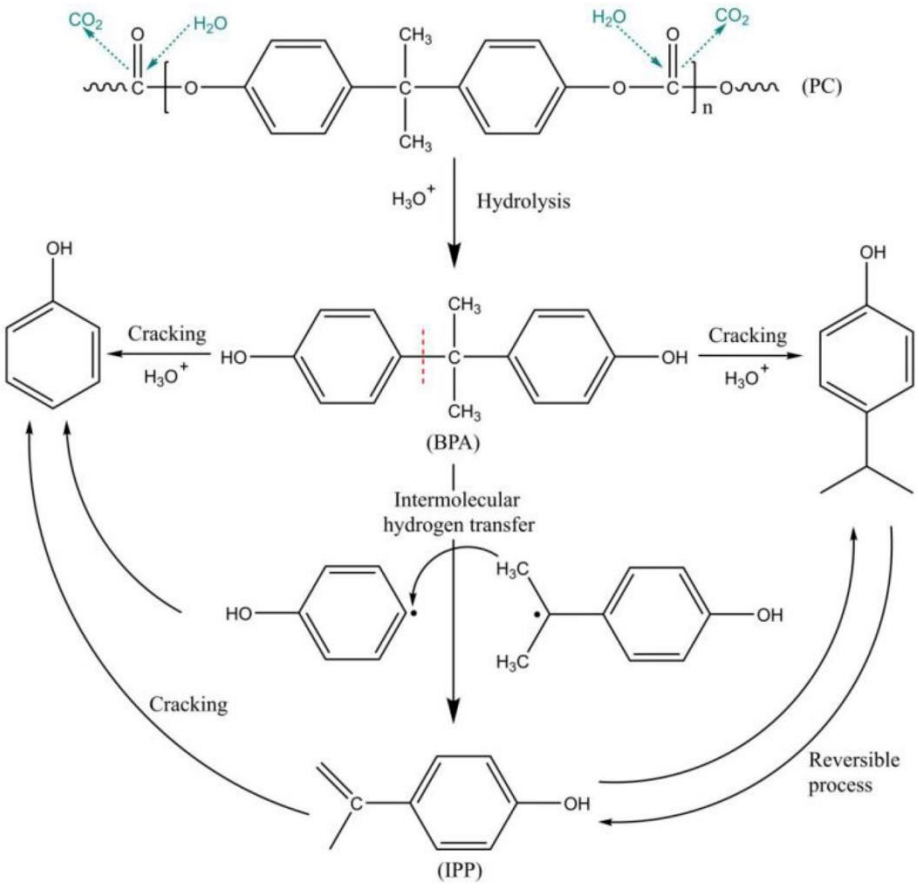


Figure 2.5 Hydrothermal decomposition mechanism of PC in subcritical water (Zhao et al., 2018b)

For example, the hydrothermal decomposition mechanism of polycarbonate (PC) is illustrated in Figure 2.5. In the initial stages, the depolymerization of PC is accomplished by the decomposition of carbonic ester bonds through hydrolysis.

As increasing the temperature above 200 ^{o}C, a large number of native hydronium and hydroxyl ions presented in water participate in the reaction and combine with the groups of missing electrons to form bisphenol A (BPA). Subsequently, the C–C bond on the main chain of BPA is broken by the energy from the reaction system, and the intermediate product is combined with hydrogen proton to form phenol, with 3-(1-methylethyl)-phenol, on the other hand, is produced by the same cleavage mechanism of BPA. Simultaneously, the intermediate products of cracking the BPA can generate p-isopropenylphenol (IPP) via intermolecular hydrogen transfer. The hydrogenation and cracking of IPP extend the pathway to generate 3-(1-methylethyl)-phenol and phenol. Deep and intense cracking will reduce hydroxyl groups to generate phenyl substances. The formation of 4-Methyl-2-phenylphenol is derived from the combination of phenols and phenyl.

Dechlorination of PVC wastes can be achieved under hydrothermal conditions. Generally, during the HTC process of PVC wastes, the thermal dechlorination of PVC mostly follows a free radical mechanism (Starnes, 2012). The reaction starts with the generation of free radicals and chloroallylic structures characterized by low thermal stabilities. A subsequent HCl elimination leads to the formation of polyene, which is a non-free radical reaction mechanism (Starnes and Ge, 2004, Shen et al., 2017). Clearly, conjugated double bonds can be created by a “zipper” mechanism: once a double bond has formed, the allylic chlorine atom on the C-atom adjacent to the double bond splits off HCl forming two double bonds in the process, which in turn activates adjacent chlorine to propagate the dehydrochlorination process. In aqueous suspensions, it is assumed that the PVC can be degraded via ionic chain reactions and cracking. Beyond that, nucleophilic substitution with water as the nucleophile proceeds to generate alcohols, diols, and polyols. Reactive polyenes, as well as diol/polyol structures, are regarded as precursors of aromatic compounds and oxygen-functionalized low molecular weight compounds. Temperatures below 450 ^{o}C and high water densities in favour of OH-nucleophilic substitution with water acting as a role of nucleophilic agent

(Nagai et al., 2007). The reaction pathway of PVC decomposition in the HTC process is illustrated in Figure 2.6.

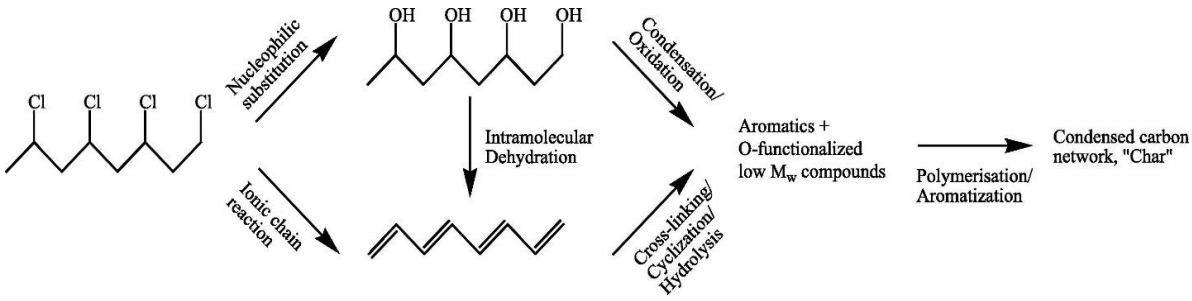


Figure 2.6 Reaction pathway of PVC decomposition in the HTC process reproduced from reference (Nagai et al., 2007).

2.2.2.3 Factors governing hydrothermal treatment

The production and quality of hydrochars from HTC depend upon several process parameters: reaction temperature, reaction time, substrate concentration and pH. The effects of each process parameter are further discussed in the following sections.

Hydrothermal temperature The hydrothermal temperature is suggested as the key parameter for the HTC process. Higher temperature results in extensive dehydration and an increase in the degree of condensation of the hydrochar whereas lower temperature leads to a lower rate of reaction and dominant formation of solid products (Jain et al., 2016). Sevilla and Fuertes (2019b). observed the emergence of C=O (carbonyl, carboxyl, quinone or ester) and oxygen in hydrochar in the form of OH under hydrothermal carbonization of cellulose at ⩾220 ^{o}C, which gave rise to a decrease in the O/C and H/C atomic ratios with an increase in the temperature of hydrothermal carbonization from 230 to 250 ^{o}C. Nevertheless, the cellulose that was hydrothermally treated below 210 ^{o}C showed FT-IR features similar to those of the raw cellulose, indicating no chemical transformation occurred. Hydrothermal carbonization of starch likewise

resulted in a decrease in O/C and H/C ratio with the increase in temperature from 180 to 200 ^{o}C (Sevilla and Fuertes, 2009a). Falco et al. (2011) compared the chemical structural differences between cellulose, glucose and lignocellulosic biomass-derived hydrochar. The ^{13}C solid-state nuclear magnetic resonance (NMR) showed the presence of cellulose signals in rye straw-derived hydrochar prepared at up to 200 ^{o}C whereas no signals were observed at 200 ^{o}C for glucose- and cellulose-derived hydrochars. This difference was attributed to the presence of lignin in rye straw, which bestows the stabilization of cellulose against the decomposition of its crystalline structure at lower temperatures. Kang et al (2012). investigated the effect of hydrothermal carbonization temperature (225, 245 and 265 ^{o}C) on the formation of OFGs of d-xylose, cellulose, lignin and lignocellulosic biomass (woodmeal). A reduction in OFGs and OH groups was observed with an increase in temperature for all the starting materials except lignin. However, a small increase in OFGs in the case of lignin was observed from 225 to 245 ^{o}C due to the high temperature required for the hydrolysis of lignin. Notwithstanding the impact of HTC temperature on the growth of OFGs contents, this content is also simultaneously dependent on the type of starting materials, residence time and substrate concentrations used. According to the current literature, lignocellulosic biomass upon treatment at higher hydrothermal temperatures can yield high OFGs contents even at relatively (a) lower residence times because of higher reaction rate and thus easy hydrolysis, (b) higher substrate concentrations due to the easy hydrolysis of higher concentration of biomass and (c) higher lignin content because of higher reaction severity and its easier disintegration into smaller constituents. Trends of oxygenated functional groups against temperature with variations of other parameters are shown in Figure 2.7.

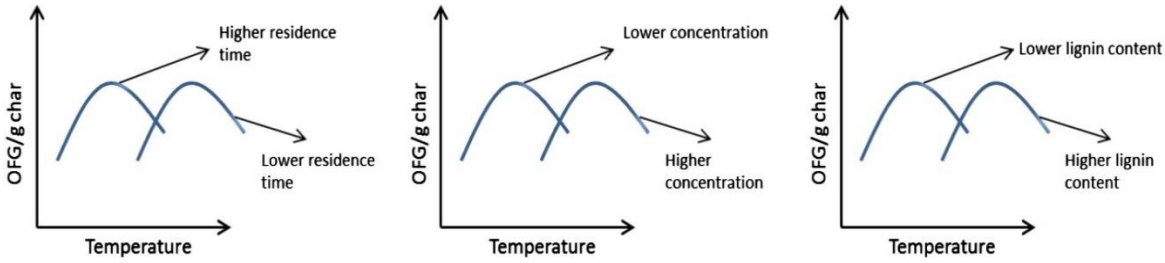


Figure 2.7 Trends of oxygenated functional groups and temperature with variations of other parameters reproduced from reference (Jain et al., 2016)

In terms of the effect of HTC temperature on the yield of hydrochar products, Hoekman et al. (2011) reported a decrease in hydrochar yield for lignocellulosic biomass (mixture of Jeffrey pine and White fir) with an increase in hydrothermal temperature from 215 to 255 ^{o}C which remained constant up to 295 ^{o}C. However, a small increase in yield was reported for cellulose-derived hydrochar when the temperature was increased from 230 to 250 ^{o}C (Sevilla and Fuertes, 2009b). The different variation of yield with temperature is presumably due to the combined effect induced by other parameters such as reaction time and substrate concentration.

Reaction time is another important factor in determining the extent of hydrothermal reaction as well as the quality of final hydrochars. The longer reaction time usually results in highly condensed hydrochar products due to excessive polymerization. Zhang et al. (2014) reported an increasing –C=O and –COOH groups in sewage sludge-derived hydrochar with an increase in residence time from 1 to 24 h at 190 ^{o}C and 1 to 12 h at 260 ^{o}C, respectively. In addition, less condensed products (high O/C and H/C atomic ratios) were observed due to a lesser extent of hydrolysis and polymerization during shorter reaction times (Zhang et al., 2014). However, the longer reaction time appeared to have little impact on the –COO/N-C=O of the hydrochars prepared at 250 ^{o}C at 3 and 20 h (Cao et al., 2013). This indicates the complex dependency of OFGs upon temperature, time, concentration and type of starting materials. A similar synergistic effect can be also found in the variation of hydrochar yield. Typically, a longer reaction time leads to

a decrease in the yield of hydrochar, while increase in the residence time can also result in a higher yield of hydrochar with the involvement of other conditions (temperature and biomass concentration) due to a higher extent of polymerization of dissolved fragments in the liquid phase which finally leads to the production of insoluble solids (Jain et al., 2016).

Substrate concentration The substrate concentration referred to the reactant-to-water ratio which is less studied but imposes an impact on the properties of hydrochars. Knezevic et al. (2009) reported that a high primary concentration of glucose delivered the hydroxymethylfurfural that promptly formed some polymerization reactions. Moreover, an increased concentration of cellulose leads to a decreased yield of hydrochar and the solid product shows comparatively high H/C and O/C ratios as reported by Sevilla et al (Sevilla and Fuertes, 2009b). Their outcomes demonstrate that the inadequate hydrolysis procedure prompts the development of a few monomers, which produce the precursors for condensation or polymerization.

pH A drop in pH or an increase in acidity of an aqueous medium is usually found during hydrothermal carbonization, due to the formation of carbonic and organic acid. Normally, the hydrothermal procedure is considered to be auto catalytic for the development of organic acids like lactic acid, levulinic acid and formic acid from the biomass, thus leading to a drop in pH. Organic acids act as a crucial transitional throughout the hydrothermal reaction succession to catalyse bio-macromolecule decomposition and the development of hydrochar (Khan et al., 2019). Therefore, the addition of acidic compounds as a catalyst during the hydrothermal reaction process is considered to be beneficial to the growth of protons that cause a high ionic strength, altering the pathway of reaction or accelerating the rate of reaction to accomplish the anticipated hydrochars (MacDermid-Watts et al., 2021). Lu et al. (2014) studied the effect of acid (H_2SO_4 and HCl) at concentrations as low as 0.0001 N on the hydrothermal reaction of cellulose. The results showed that the presence of acids improves the hydrolysis and dehydration process, which increases the carbonization level at a certain residence time and reduces the

oxygen content in hydrochar. The outcomes also demonstrated that CO_2 production by acidic additives improved the decarboxylation of organic acid decomposition (Lu et al., 2014). Moreover, Reza et al. (2015) conducted the hydrothermal carbonization of wheat straw using feed water with a pH of 2–12 prepared by means of potassium hydroxide and acetic acid and found that hydrochars produced with acidic feedwater had a larger surface area and pore volume than that produced with basic feedwater. All these results emphasize the addition of acids accelerates the hydrolysis process and also decomposition by means of improving the intermediary products, comprising the production of organic acids and the decarboxylation meant for CO_2 production.

Overall, it is concluded that the properties of hydrochar resulting from various concentrations heavily depend on the type of precursor and HTC condition.

2.2.3 Preparation of activated carbons

Activated carbon can be prepared with either physical or chemical activation approaches, with the involved carbonization step being performed either separately in a two-stage process or integrated into a single-stage process. The physical activation process is usually carried out at high temperatures in the range of 800–1200 ^oC with the presence of an oxidizing agent, such as steam, CO_2, air or a mixture of them. Physical activation is usually considered a clean and eco-friendly production process, due to the avoidance of solid and aqueous waste streams. Nevertheless, physical activation surfers from major disadvantages, including the requirement of high activation temperatures, long processing time, low carbon yield, and poorly defined pore structures and specific surface areas (Heidarinejad et al., 2020). Chemical activation involves an impregnation step where the material either in its raw or carbonized form is mixed with a chemical and then subjected to the activation process at much milder temperatures ranging from 450 to 850 ^oC (Gao et al., 2020). Compared to physical activation, chemical activation benefits from its shorter processing time, lower activation temperature

required, more controllable pore structure development, and higher obtainable specific surface areas, despite the drawbacks of process corrosion and the post-activation washing process required (Rambabu et al., 2015, Singh et al., 2023). In addition, chemical activation has been demonstrated to be an effective means to produce activated carbons with suitable textural properties dominated by fine micropores (<1nm) and favourable surface chemistry for gas adsorption in a gas separation process (Coromina et al., 2016, Manya et al., 2018). Furthermore, the activating agents play decisive roles in determining the formation of pores or surface chemistry during the activation process, which will be elucidated in detail in terms of their activation mechanisms.

2.2.3.1 Methodologies and mechanisms of chemical activation

Various chemicals are employed as activating agents in the preparation of activated carbon, which can be divided into three main categories namely alkali, acidic and salt mediums (Rashidi and Yusup, 2016). The commonly used alkali activating agents include alkali hydroxides (KOH and NaOH) and alkali carbonate (K_2CO_3 and Na_2CO_3). The acidic activating agents usually involve H_3PO_4 and H_2SO_4, whereas $ZnCl_2$ is a representative salt medium in preparing activated carbon materials.

KOH In terms of KOH activation, the global reaction generally consists of several simultaneous/consecutive reactions that can be divided into two stages depending on the activation temperature: the reactions between carbon and KOH below 700 ^oC and the reactions related to K_2CO_3 at temperatures higher than 700 ^oC. At the first stage when the activation temperature is lower than 700 ^oC, KOH first dehydrates to form K_2O (Reaction 2.5) and water which are then consumed by carbon via a two-step reaction to produce CO_2, CO, and H_2 (Reaction 2.6 and 2.7), with K_2CO_3 is subsequently formed through the reaction between K_2O and CO_2 (Reaction 2.8).

$$2KOH \rightarrow K_2O + H_2O \quad (2.5)$$

$$C + H_2O \rightarrow CO + H_2 \quad (2.6)$$

$$CO + H_2O \rightarrow CO_2 + H_2 \quad (2.7)$$

$$CO_2 + K_2O \rightarrow K_2CO_3 \quad (2.8)$$

In the second stage when the activation temperature is higher than 700 ^oC, the as-formed K_2CO_3 decomposes to K_2O and CO_2 (Reaction 2.9) and simultaneously reacts with the carbon to form more gaseous species (e.g. CO) (Reaction 2.10). The produced CO_2 is then reduced at a high temperature by carbon to generate CO (Reaction 2.11). K_2O continuously react with carbon to form free metallic potassium (Reaction 2.12) which can be further intercalated into the carbon lattice and enlarge the surface area of activated carbon (Li et al., 2017b, Liu et al., 2015b).

$$K_2CO_3 \rightarrow K_2O+CO_2 \quad (2.9)$$

$$K_2CO_3 + C \rightarrow K_2O + 2CO \quad (2.10)$$

$$CO_2 + C \rightarrow 2CO \quad (2.11)$$

$$C + K_2O \rightarrow 2K + CO \quad (2.12)$$

The potassium compounds will be subsequently washed out using water or acid after activation is completed, while the expanded carbon lattice still remains, which causes porosity and yields high surface area carbon (Marsh et al., 1984).

NaOH The mechanism of NaOH activation is similar to that of KOH activation. The proposed activation process starts with the formation of carbonate at activation temperature below 700 ^oC (Reaction 2.13) followed by the decomposition of Na_2CO_3 at high temperature (normally >800 ^oC) releasing CO, CO_2, H_2 gases (Reaction 2.14 and 2.15) (Liu et al., 2015b). As a result, the graphite layers can be destructed and separated through the redox reactions of sodium hydroxide and thereby give rise to the expansion of pores. Furthermore, the reactions between active intermediates and carbon surface cause the evolution of H_2, CO_2 and CO, which enables the development of porosity (Foo and Hameed, 2012).

$$6NaOH + 2C \rightarrow 2Na + 2Na_2CO_3 + 3H_2 \quad (2.13)$$

$$Na_2CO_3 \rightarrow Na_2O + CO_2 \quad (2.14)$$

$$2Na + CO_2 \rightarrow Na_2O + CO \quad (2.15)$$

In chemical activation with alkali hydroxides, sodium hydroxide is cheaper, more environmentally friendly and less harmful than potassium hydroxide (Heidarinejad et al., 2020). However, activation with potassium hydroxide has been demonstrated in many studies that can give a better result than sodium hydroxide in terms of surface area and micropore volumes (Fierro et al., 2007, Muniandy et al., 2014, Toprak and Kopac, 2017). The differences found between KOH and NaOH, regarding their activating behaviour, can be explained by the different intercalation abilities of K^+ and Na^+ depending on the structural order of the pristine material. Metallic potassium produced during redox reactions can be intercalated between the graphene layers of the carbon crystalline, independently of the structural order of the material (the higher the structural order, the better intercalation), being responsible for the separation and degradation of the graphitic layers and thus for the development of microporosity. On the contrary, sodium is only able to be intercalated in structural-disordered materials (Raymundo-Pinero et al., 2005). In addition, KOH has a stronger dehydrating and oxidising action than NaOH for activating precursors, which can be reflected by its lower starting temperature of activation (Lillo-Rodenas et al., 2003).

Alkali carbonates Compared to alkali hydroxide, alkali carbonates such as K_2CO_3 and Na_2CO_3 are milder basic compounds, less toxic and corrosive, which is also the main reaction product during alkali hydroxide activation and has been widely investigated as more environmentally friendly activating agents for the production of activated carbon (Sevilla et al., 2021). The porogenic action of alkali carbonate is based on a redox reaction with carbon, in which the alkali carbonate oxidizes the carbon skeleton to CO yielding porosity in the carbon residue (Reaction 2.16) (Hayashi et al., 2002). Simultaneously, the produced metallic K/Na may intercalate

between the graphene layers to cause swelling and the disruption of the carbon microstructure, which thereby generates additional porosity.

$$M_2CO_3 + 2C \rightarrow 2M + 3CO \quad (2.16)$$

When the activation temperature is higher than 850 ^oC, alkali carbonate slowly decomposes to metal oxide and CO_2 (Reaction 2.17), with the former being reduced by carbon to metallic K/Na (Reaction 2.18) etching additional carbon atoms, and the latter can react with carbon creating new pores or enlarging the existing ones (Reaction 2.19) (Sevilla and Fuertes, 2013, Sevilla and Fuertes, 2016).

$$M_2CO_3 \rightarrow M_2O + CO_2 \quad (2.17)$$

$$M_2O + C \rightarrow 2M + CO \quad (2.18)$$

$$C + CO_2 \rightarrow 2CO \quad (2.19)$$

In the end, the inorganic matter remaining in the solid material after the activation is unreacted metal (or a hydrated phase owing to the contact with ambient air), which is normally removed by washing with diluted acid. Despite the similar activation mechanism of different alkali carbonates, the radius of the cation has a significant effect on the porosity and specific surface area of precursors. Okada's group examined the performance of various activating agents Li_2CO_3, Na_2CO_3, K_2CO_3, Rb_2CO_3 and Cs_2CO_3 on the same materials at the activation temperature of 800 ^oC for 2 h and at the mass ratio of 1 and found the pore volume and surface area increased with the increase of the radii of cation (Li < Na < K <<Rb< Cs) (Okada et al., 2003). The thermal stability of the alkali carbonate was also found to affect the quality of produced carbon, with the lower thermal stability of the activating agent having a greater effect of activation on the evolution of porosity and surface area, which can be explained by the reaction 2.17 and 2.18. Consequently, alkali carbonate activation stands out for allowing higher activation yields and preserving the particle morphology of the precursor, but pore development achieved in the produced activated carbon is normally lower than that achieved through KOH activation (Sevilla et al., 2021).

Inorganic acid In addition to the alkali activating agents, acidic groups such as H_3PO_4 and H_2SO_4 are widely used in the activation of various lignocellulosic precursors (Yakout and El-Deen, 2016, Ogungbenro et al., 2020). In the case of H_3PO_4 activation, H_3PO_4 may act as an acid catalyst to promote bond cleavage, hydrolysis, dehydration and redistribution of biopolymers in lignocellulosic materials. With the presence of H_3PO_4, hetero elements such as hydrogen and oxygen are removed in the form of water vapour which serves as a physical activating agent, promoting the formation of more pores (Danish and Ahmad, 2018). In the meantime, the reaction of phosphoric acid with the active carbon-based precursor leads to the formation of products in the form of particles or volatile substances, creating new pores and enlarging the existing pores occurred at the sites previously occupied by these substances (de Yuso et al., 2014). In addition, H_3PO_4 molecules could be converted into polyphosphoric acid $H_{n+2}P_nO_{3n+1}$ in various chain lengths (Reaction 2.20) (Zhang et al., 2020, Liu et al., 2012a).

$$nH_3PO_4 \rightarrow H_{n+2}P_nO_{3n+1} + (n-1)\ H_2O \qquad (2.20)$$

The polyphosphoric acid with strong corrosivity along with H_3PO_4 acid can interact with the functional organic component of the wood to form a phosphate linkage such as phosphate and polyphosphate esters that connect and cross-link in biopolymers. The pores are generated due to the formation of these linkages which expand the biomass structure. However, these larger polyphosphate compounds fill a wide range of pore sizes resulting in the creation of larger-sized mesopores which may not favour the adsorption of CO_2 with a small molecular size (Danish and Ahmad, 2018).

H_2SO_4 acting as an extremely strong dehydrating and oxidizing agent, has also been commonly used for the production of activated carbon. The activation mechanism can be interpreted by the reaction between H_2SO_4 and organic compounds (such as carbohydrates and other organic materials), removing water and breaking down organic precursors into carbon elements (Reaction 2.21) (Olivares-Marin et al., 2012). The incorporation of H_2SO_4 acid into the interior char

matrix may retard the formation of tars and promote the introduction of oxygen functionalities (Reaction 2.22) Therefore, H_2SO_4 activation induces the formation of stable C–O complexes, which accounts for the internal porosities.

$$C_nH_{2n}O_n + H_2SO_4 \rightarrow nC + H_2SO_4 \cdot nH_2O \quad (2.21)$$

$$2H_2SO_4 + C \rightarrow 2SO_2 + CO_2 + 2H_2O \quad (2.22)$$

However, due to the strong oxidative nature of H_2SO_4, such activation behaviour usually leads to the generation of large and medium porosity on the surface of the activated carbon and relatively low carbon yield (Ahmad et al., 2021).

$ZnCl_2$ as a representative neutral salt medium is also extensively applied to produce activated carbon. Due to its ability to interact with nonbonding electrons of oxygen atoms in precursors to form Zn-O complexes, $ZnCl_2$ is often used to activate oxygen-enriched precursors such as lignocellulosic and cellulosic precursors (Heidarinejad et al., 2020). During the activation process, $ZnCl_2$ eliminates hydrogen and oxygen atoms in the form of water from the precursor structure based on its dehydrating function. Meanwhile, as a Lewis acid, $ZnCl_2$ also contributes to the aromatization by facilitating molecular hydrogen deformation from the hydro-aromatic structure of precursors and therefore leaving some active sites on adjacent molecules that can undergo aromatization (polymerization) reactions (Gundogdu et al., 2013, Alothman et al., 2011). As a result of these reactions, the volatile molecules are stabilized, and the carbon yield is increased. It is also reported by Saka (2012) that the $ZnCl_2$ activation induces an electrolytic action termed as “swelling” in the molecular structure of cellulose, which results in the breaking of lateral bonds in the cellulose molecules and leads to an increase in “inter” and “intra” miscellaneous voids. After the removal of the activating agent by the subsequent washing process, the matrix generated leaves behind a considerable number of pores, which makes it possible to produce a greater porous structure and surface area in activated carbons.

2.2.3.2 Process factors of chemical activation governing the surface chemistry and textural properties of carbon materials

Apart from the activating agent, other parameters that influence the textural properties and surface chemistry of activated carbon via chemical activation include activation temperature, impregnation ratio, activation time, precursor constituents and surface functionalities (Abd et al., 2021).

Activation temperature Activation temperature is one of the significant parameters that influence the creation of porosity and enlargement of surface area in activated carbon. Typically, activated carbons that possess the desired properties are generally produced at an activation temperature within the suitable range. An excessively high activation temperature may decrease the specific surface area and carbon yield because of the excessive transformation of cross-linked substances in the solid phase to volatile matters in the gas phase (Liang et al., 2020). Whereas a low activation temperature cannot provide enough activation energy to initiate the reactions between different activating agents and carbon, which results in a poor structure in the activated carbon (Nayak et al., 2017). Generally speaking, the optimal activation temperature by using alkali hydroxide and alkali carbonate is normally in the range of 700-800 ^{o}C, and the favourable activation temperature using acidic activating agents is usually in the range of 400–500 ^{o}C (Gao et al., 2020). However, these temperature ranges can vary depending on factors such as the specific activating agent and the precursor material being activated. Okman et al. (2014) studied the influence of activation temperature on the activation of grape seed using either K_2CO_3 or KOH. The experimental results showed that the optimal activation temperature for obtaining the highest surface areas was 800 ^{o}C for both K_2CO_3 and KOH. Many researchers have proposed that, when the activation temperature exceeded the boiling point of potassium (762 ^{o}C), KOH was reduced to free metallic potassium which can be intercalated into the carbon matrix and widen the spaces between carbon layers, enhancing the development of specific surface areas and pore volumes (Li et al., 2017b, Brito et al., 2018). As for the activation by using acidic activating agents, the favourable

activation temperature is usually in the range of 400-500 ^{o}C due to the lower decomposition temperature of acids such as phosphorous compounds (Li et al., 2015b). According to the study by Prahas et al. (2008), well-developed pores were produced for activated carbons prepared from jackfruit peel using H_3PO_4 at activation temperatures of 450 and 550 ^{o}C, while carbons produced at a temperature of 350 ^{o}C were non-porous materials. In addition, the carbon yield was found to decrease with the increasing temperature due to the enhanced evolution of volatile products at elevated temperatures. Yorgun and Yildiz (2015) prepared activated carbon samples by using H_3PO_4 at different activation temperatures (300–600 ^{o}C) and impregnation ratios (1–4) and found the BET surface area and total pore volume of the activated carbons increased with increasing carbonization temperature from 300 to 400 ^{o}C but decreased in temperature from 400 to 600 ^{o}C.

Based on the mechanism of $ZnCl_2$ activation illustrated above, the optimized activation temperature by using $ZnCl_2$ depends not only on the reaction but also on the melting point and boiling point. $ZnCl_2$ has a low melting point of 283–293 ^{o}C allowing better contact with the carbon surface above a 500 ^{o}C activation temperature. However, if the activation temperature is over its boiling point (732^{o}C), $ZnCl_2$ as the template will evaporate, which will influence the surface area and porosity of the final product. Li et al (2020a). observed that the activated carbon prepared with a 3:1 mass ratio of $ZnCl_2$/polypyrrole at 600 ^{o}C showed the highest micropore area and percentage of micropore volume of 1105 m_2/g and 86.26%, respectively. However, the pore properties of prepared activated carbon diminished owing to the heat shrinkage as the temperature rises up to 700 ^{o}C (Li et al., 2020a).

Impregnation ratio The impregnation ratio is defined as the weight ratio between the activating agent and precursor, which affects the porosity and textural structure of activated carbon in a similar variation trend as activation temperature does. Generally, within an optimum range, the increase in the impregnation ratio is beneficial to the development of porosity and specific areas. However, an

excessive increase in the impregnation ratio is unfavourable, which can destroy the pore wall during the activation process, resulting in the merging and erosion of existing pores, thereby reducing the specific surface area (Zhu et al., 2021). Arvind and Hara prepared the activated carbon by using $ZnCl_2$ as the activating agent and varied the impregnation ratio of $ZnCl_2$ and raw material (Euryale ferox) from 1 to 2.5. The BET surface area and total pore volume of the prepared activated carbon increased and reached the maximum values of 2869 m^2/g and 1.96 cm^3/g, respectively, with an increase in the impregnation ratio from 1 to 2. As the impregnation ratio increased to 2.5, more carbon burn-off occurred, resulting in a lower yield value and micropores widening into mesopores (Kumar and Jena, 2015). Li et al studied the effect of the KOH/precursor ratio on gulfweed-derived activated carbon, the results showed that the surface area and pore volume grow from 2227 to 3362 m^2/g and from 1.64 to 3.08 cm^3/g with the increase of impregnation ratio from 3 to 4, respectively. However, both specific surface area and pore volume decreased when the impregnation ratio was beyond 4 (Li et al., 2017b). The excess amount of activating agent not only consumes the carbon atoms on the active sites but also consumes the carbon atoms on the lattice surface. In that way, some micropores will be ablated exceedingly and pore volume will decrease.

Activation time The activation time refers to the duration time at a certain activation temperature, which is also an important factor affecting the pore structure and yield of activated carbon. In general, the longer the reaction time, the greater the degree of reaction between the activating agent and the precursor material, gradually widening the pore size of activated carbon, leading to a higher carbon burn-off (Danish and Ahmad, 2018). However, an excessive activation time results in the destruction of micropores and a decrease in the specific surface area due to the collapse and widening of pores. Therefore, an appropriate activation time should be selected for optimizing the pore size distribution of mesopores and micropores. Xu et al. (2014b) prepared the activated carbon from reedy grass leaves by chemical activation with H_3PO_4. The results suggested that increasing

the activation duration from 1–2 h increased the BET surface area and micropore volume. However, the increase in the activation duration from 2 to 5 h led to a lower BET and micropore volume, which is attributed to the enlargement or even collapse of the micropores under the longer duration of activation time (Xu et al., 2014b). Similar results were found by Bagheri and Abedi (2009) that activated carbons prepared through chemical activation of corn cob precursor, using potassium hydroxide as the chemical agent, achieved the highest BET surface area of 1320 m^2/g at 1 h of activation time. However, the BET surface area decreased when prolonged the activation time to 2 h (Bagheri and Abedi, 2009).

It has been found in many other research studies that an activation time of 1-2 hours is typically the optimal range for producing activated carbon with appropriate porosity and specific surface area (Acikyildiz et al., 2014, Kumar and Jena, 2016).

The effect of precursor It has been proven that the pore structures of activated carbon depend not only on the preparation conditions of activation steps but also on the initial nature and structure of the raw materials. In principle, raw material containing a high carbon content, high volatile content, and lower ash content can be considered as an appropriate precursor for producing high-quality activated carbon from the point of view of industrial analysis. From the perspective of elemental analysis, higher contents of carbon, hydrogen, and oxygen and lower contents of other inorganic impurities indicate a high potential for preparing activated carbon with optimum textural properties. As aforementioned, lignocellulosic biomass mainly consists of three basic structural components: hemicellulose, cellulose, and lignin. Many studies have shown that raw materials with a larger proportion of lignin can produce activated carbon with higher micropore density, while raw materials with a higher percentage of cellulose can produce activated carbon with a mixture of pores with a wide pore size range (Cagnon et al., 2009, Correa et al., 2017a, Tiryaki et al., 2014).

Surface functional groups In addition to the influence of precursor reactivity on the porosity of activated carbons, surface functional group content in the precursor is another important indicator of the effectiveness of chemical activation (Jain et

al., 2016). During chemical activation, some of the functional groups are removed in the form of gas while others transform from heat-liable forms into relatively stable groups at a high temperature up to 900 ^{o}C, affecting the development of textural properties and surface chemistry in the prepared carbon materials. Besides, the activation reactions resulting from alkali metals on the surface of carbon precursors are accompanied by oxidation-reduction reactions that can lead to porosity promotion via KOH surface etching and such redox reactions are affected by the surface characteristics of activated carbon (e.g. electron donors) (Kim et al., 2019). Therefore, it is of great importance to understand the behaviour of the surface functional groups during the activation or preparation processes and thus optimize the process conditions by the use of appropriate pre-treatment processes.

Shafeeyan et al. (2010) proposed thermal decomposition behaviours of different types of oxygen functional groups (OFGs) incorporated into the carbonaceous material. Specifically, high temperature treatment >700 ^{o}C like KOH activation under an inert atmosphere was able to decompose the acidic oxygen-containing functional groups (e.g. carboxylic, anhydrides and lactones) to carbon dioxide. Other weakly acidic functionalities (such as carbonyl, phenol and quinone) decompose at elevated temperatures to carbon monoxide, with the majority of OFGs on a carbon surface can be decomposed at 800–1000 ^{o}C (Shafeeyan et al., 2010). Surface oxygen-containing groups on carbon and their decomposition by temperature-programmed desorption (TPD) are shown in Figure 2.8. Moreover, radical and open pores are observed and formed as OFGs at the carbon surface are volatilized through heat treatment. At this point, as CO_2 is formed for quinones and carboxyl groups, the carbon bond is removed and open pore formation is not easy, whereas as CO is formed for the carbonyl groups and ketones, open pores are formed more easily (Kim et al., 2019).

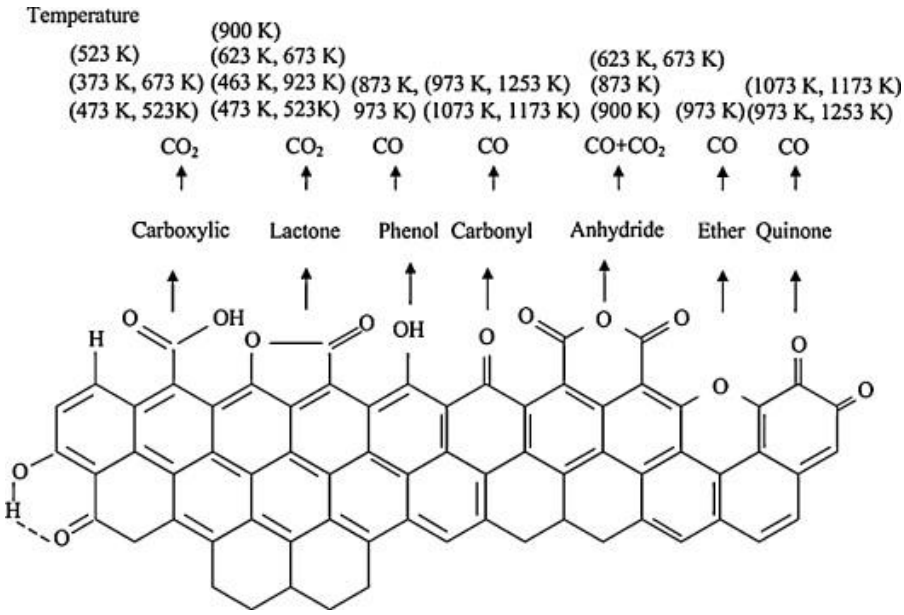


Figure 2.8 Surface oxygen-containing groups on carbon and their decomposition by TPD reproduced from reference (Shen et al., 2008)

The introduction of oxygen-bearing functional groups in precursor materials can be achieved by either pre-oxidation treatment or hydrothermal carbonization as illustrated in the previous section (section 2.2.2) to promote the pore forming in the activated carbon. Li et al. (2010b) applied air pre-oxidation on phenolic resin-based activated carbon spheres before activation, the yield increased from 51 to 58%, and the S_{BET} increased from 1196 to 1897 m^2/g. Jin et al. (2020) developed a stillage-derived activated carbon via the air pre-oxidation treatment and results showed that the optimized carbon sample exhibited high yield (55.5%), large surface area (762.9 m^2/g) and pore volume (0.444 cm^3/g), which significantly exceeded carbon produced without pre-oxidation treatment. Yu et al. (2019) lucubrated the reaction mechanism between KOH and hydrochar enriched with OFGs which can serve as useful electron donors during KOH activation. The activation of hydrochar by KOH could be triggered by the reaction between KOH and OFGs on the hydrochar surface at 200–300 ^oC (reaction 2.23) followed by redox reactions at 400–500 ^oC (reaction 2.24 and 2.25). The as-formed K_2CO_3 will follow the reactions 2.9 to 2.12 as illustrated in the previous section (2.2.3.1) to

contribute to the further development of porosity. As a result, the obtained porous carbon derived from sucrose-based hydrochar possessed a large specific surface area (2604 m^2/g) and microporous surface area (1318 m^2/g).

$$-COOH + KOH \rightarrow -COOK + H_2O \quad (2.23)$$

$$-COOK + KOH \rightarrow K_2CO_3 + 1/2H_2 \quad (2.24)$$

$$-CH_2 + 4KOH \rightarrow K_2CO_3 + K_2O + 3H_2 \quad (2.25)$$

Other operating parameters such as the methods of mixing of activating agents and the type of flow gas in activation will also affect the quality of chemically activated carbon to different extents.

2.3 CO_2 adsorption performance of carbon materials for carbon capture

The chemically activated carbons have been widely acknowledged as promising adsorbents for CO_2 capture due to their high surface area and well-developed porosity. Theoretically, the CO_2 adsorption performance of activated carbons is highly dependent on their structures and properties. For example, activated carbon with higher surface area and pore volume can provide a greater potential for the interaction between the carbon surface and CO_2 molecules, and the presence of appropriate porous structures in the activated carbon is also significant for the diffusion of CO_2. However, the CO_2 adsorption capacity of activated carbon in general, particularly at flue gas conditions, cannot compete with that of MOFs and zeolites. This is because MOFs and zeolites have not only well-defined pore structures and high surface area but also strong surface affinity to CO_2 molecules. From this perspective, exploring the potential to increase the interaction between the carbon surface and CO_2 molecules is essential aside from the textural properties (Zhao et al., 2018a). As for activated carbon, their controlling factors on CO_2 adsorption, which can be classified into two categories, namely those related to 1) surface texture, and 2) surface chemistry, will be discussed in detail.

2.3.1 Effect of surface textural properties of carbons

By definition, adsorption is a process in which a substance enriches on the surface of an adsorbent, where the mass transfer will take place in the form of molecular diffusion. In specific, CO_2 molecules are mostly adsorbed via an internal mass transfer through the macro- and micropores inter-connected network (intra-particle diffusion) in the activated carbon (W John Thomas and Crittenden, 1998). In the gas phase adsorption, macropore adsorption can be neglected whilst microporosity diffusion is dominant. The micropores formed by the activation process are localised, allowing van der Waals forces to overlap. As a result, strong electrostatic attraction is formed between activated carbon and CO_2, promoting physisorption (Subramaniam et al., 2020).

Gas adsorption in pores depends on the potential energy resulting from the interaction between a gas molecule and the whole pore structure, which is significantly affected by the pore shape and pore width (Lowell et al., 2006). Zhang et al investigated the distribution of adsorption potential along with the vertical section of parallel pore walls (Zhang et al., 2013a). As shown in Figure 2.9, the slit width is the distance between two adjacent graphite layers, d is half of the slit width and the r_0 value (the effective collision distance of CO_2 with carbon surface) is equal to the sum of molecule radius of CO_2 and interlayer spacing of graphite planes. It can be clearly observed that the potential energy curve exhibits two minima for the large slit width, while these minima coalesce giving a single minimum of increasing depth and sharpening curvature until at $d/r_0 = 1.0$ due to the entire superposition of the van der Wall force derived from the two adjacent walls of slit pores. The results indicate that the absolute value of interaction potential reaches the maximum when the slit width is equal to the dimension of the CO_2 molecule. The point from double minima of adsorption potential merge into a single minimum can be considered as the critical stage, where the pore width at this critical state is about 0.54 nm (Powl and Everett, 1976, Zhang et al., 2013b). For the micropores larger than 0.54 nm, the adsorption potential significantly

decreases due to the much lower superposition extent of the sorption potential, leading to the weak interaction between CO_2 and carbon adsorbent.

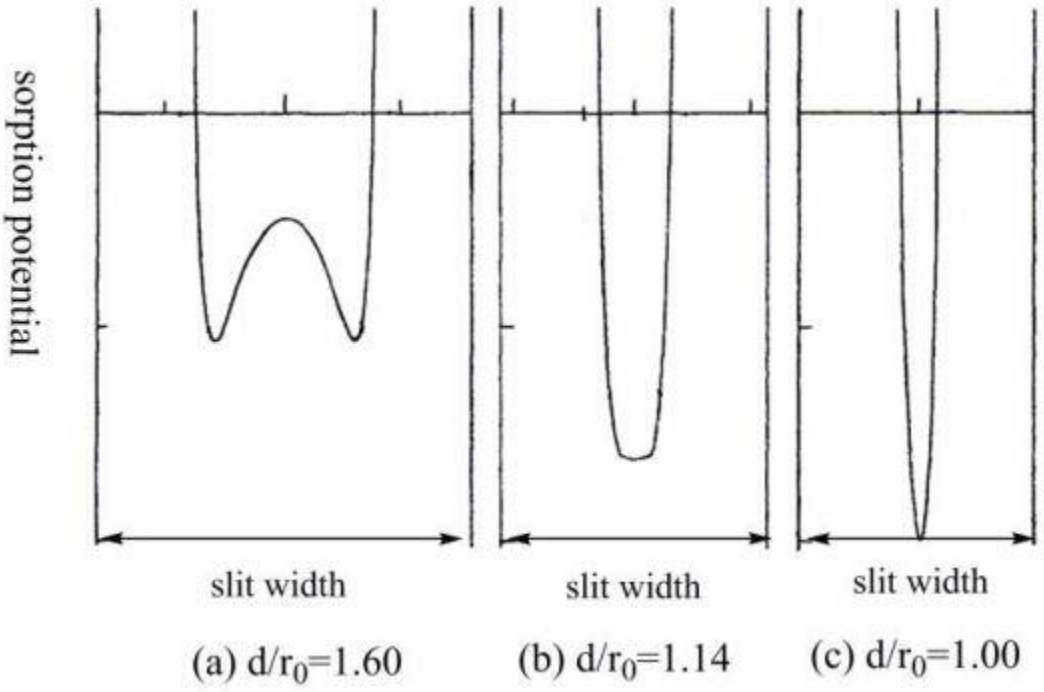


Figure 2.9 The curves of sorption potential energy in different-sized micropores (Zhang et al., 2013a)

However, due to the weak interaction force created by the Van der Waals force, adsorption on activated carbons is very sensitive to CO_2 partial pressure and temperature. The adsorption capacity is drastically decreased with the decreasing CO_2 partial pressure or increasing adsorption temperature. As aforementioned, typical flue gas from the post-combustion process contains relatively low CO_2 partial pressure of 10-15% and more than 70% nitrogen at atmospheric pressure and temperature in the range of 50–60 ^oC, which therefore poses a major challenge for effective CO_2 adsorption by activated carbon. Much effort has been devoted to improving the CO_2 adsorption performance of activated carbon in post-combustion scenarios. From many research studies, micropores smaller than 0.57 nm were manifested to determine the CO_2 capture capacity under post-combustion

conditions (Serafin et al., 2017, Deng et al., 2015, Liu et al., 2018, Liu et al., 2019). In particular, Serafin et al. demonstrated that the total volume of pores with a diameter of 0.57 nm or less in the prepared pomegranate peels derived activated carbon was mainly contributing to the CO_2 adsorption at flue gas conditions (Serafin et al., 2017). Deng et al. (2015) prepared the activated carbon by using peanut shell as the precursor and found the optimal activated carbons were obtained at a low KOH/carbon ratio of about 1. The results showed that the carbon possessed higher CO_2 uptake of 1.46 mmol/g at 25 ^oC and 0.15 bar due to the higher volume of micropores in the range of 0.30-0.44 nm, despite its lower surface area and micropore volume (Deng et al., 2015). Liu et al. (2018) developed an ultra-microporous activated carbon from inexpensive and widely available biomass (i.e., glucose) for efficient CO_2 capture via hydrothermal carbonization. The prepared carbon materials showed a high CO_2 sorption capacity of 1.33 mmol/g at 25 ^oC under 0.15 bar, which is mainly attributed to the abundant presence of ultra-micropores around 0.57 nm and well-developed ultra-microporosity. Moreover, Liu et al. (2019) prepared novel hierarchical ultra-micro/mesoporous bio-carbons using the vastly available renewable agricultural waste of rice husk and found that carbon with the highest volume of ultra-micropores pores (≤0.44 nm) achieved the highest adsorption capacity of 1.90 mmol/g at 15 kPa CO_2 and 25 ^oC. Referring to the recent work, the wider utilization of KOH as the activating agent for the synthesis of activated carbon is in favour of the development of highly ultra-microporous structure and preferable CO_2 adsorption of produced activated carbon in the post-combustion scenario. Besides, the KOH activation process requires lower energy consumption as compared to water vapour, aside from imposing less environmental impact when compared to other chemical activators such as $ZnCl_2$ and H_3PO_4 (Rashidi and Yusup, 2016). The recent work for post-combustion CO_2 capture by using chemically activated carbon is summarised in Table 2.1.

Table 2.1 CO_2 adsorption capacity of chemically activated carbons

Precursor	Activator	S_{BET} (m^2/g)	V_{total} (cm^3/g)	CO_2 adsorption capacity (mmol/g)				Ref.
				15 kPa		100 kPa		
				0°C	25°C	0°C	25°C	
Glucose	KOH	923	0.5	2.45	1.58	5.91	3.37	(Zhang et al., 2019c)
Rice husk	KOH	1025	0.43	2.96	2.00	5.91	4.75	(Liu et al., 2017)
	K_2CO_3	944	0.60	2.30		4.80		
Coffee ground	KOH	1624	0.66	2.20	1.40	7.55	4.42	(Travis et al., 2015)
Cellulose	KOH	2370	1.08		1.40	5.8	3.5	(Sevilla and Fuertes, 2011)
Starch		2190	1.01		1.35	5.6	3.5	
Eucalyptus		1260	0.62		1.15	6.1	4.8	
Lignin	KOH	2779	1.39	2.58	1.65	8.56	5.48	(Saha et al., 2017)
Bamboo	KOH			2.43	1.43	5.3	4.0	(Wei et al., 2012)
Lumpy bracket	KOH	1968	1.14	-	1.67	7.14	4.62	(Serafin et al., 2019)
Palm shells	KOH	770	0.35	2.6	1.7	5.4	3.9	(Ello et al., 2013b)
Pine nut shell	KOH	1486	0.64/	3.3	2.0	7.7	5.0	(Deng et al., 2014)
Peanut shell	KOH	956	0.43	2.6	1.54	5.23	4.03	(Deng et al., 2015)
Sunflower seed shell	KOH	1790	0.77	2.5	1.46	7.06	4.61	
Empty fruit bunch	KOH	2510	1.05	1.84	1.32	5.23	3.71	(Parshetti et al.,2015)
Peanuts	KOH	1354	0.55	2.57	1.30	6.51	4.07	(Hong et al., 2020)
Lotus stalk	KOH	1105	0.53	1.96	1.21	5.11	3.65	(Yang et al., 2020)
Water caltrop shell	KOH	2129	0.91	2.10	1.50	5.06	3.97	(Zhao et al., 2021b)
Cotton stalk	KOH/Alum	2695		2.69	1.60	5.40	3.91	(Pramanik et al., 2021)
Pomegranate peels	KOH	585	0.28	2.25	1.25	6.03	4.11	(Serafin et al., 2017)
Carrot peels	KOH	1379	0.58	2.0	1.13	5.64	4.18	
Fern leaves		1593	0.74	1.25	0.80	4.52	4.12	
Rice husk	KOH	1041	0.53	2.42	1.55	6.24	4.16	(Li et al., 2015a)
Coffee ground	K2CO3	1692	0.71	2.32	1.20	7.18	3.65	(Kim et al., 2020b)
Sugarcane bagasse	H_3PO_4	873	1.06		1.25		2.65	(Guo et al., 2020)
	NaOH	1149	1.73	2.16	1.5	5.50	4.28	
Date	KOH	2367	1.15	1.80	0.92	6.40	4.36	(Li et al., 2019)

2.3.2 Effect of surface chemistry

In addition to the implication of ultra-microporosity for CO_2 adsorption, the surface chemistry of the activated carbon is also important to ensure a specific interaction between the activated carbon and CO_2 in the flue gas mixture. The surface chemistry of the activated carbon is governed by the heteroatoms such as oxygen, nitrogen and metals, controlled by the nature of raw precursors as well as the activation conditions.

2.3.2.1 Oxygen containing groups

Oxygen-containing functionalities formed during oxidative treatments can induce an acidic character and therefore impart electron-acceptor properties to the adsorbents' surface (Vagner et al., 2003). Generally, acidic groups such as carboxylic, carbonyl, lactonic and phenolic groups can be formed at relatively low temperatures with oxidative treatment by using HNO_3, H_2O_2, H_3PO_4 or H_2SO_4 (Rajapaksha et al., 2016). Plaza et al. (2013) reported that the oxygen functionalities introduced in the phenolic resin carbon through nitric acid oxidation increased the CO_2 adsorption capacity at 25 ^oC and 1 bar by up to 26% despite their predominant acidic nature. The results showed that the carboxylic acids presented in liquid-phase oxidised samples gave rise to strong Lewis acid–Lewis base interactions with the CO_2 molecule. Increases in oxygen functionalities can also be achieved in the form of surface basicity by introducing functional groups such as hydroxyl or carbonyl groups. The basicity of the -OH group is often reported and is frequently shown to positively impact the adsorption of CO_2 (Liu and Wilcox, 2012). Liu and Wilcox (2012) investigated that -OH and carbonyl groups affect CO_2 adsorption due to their high electron densities. The interactions between -OH groups and CO_2 can also be described by the potential of electron donation to CO_2 as a result of the high electrostatic potential. Moreover, -OH groups have been shown to affect CO_2 adsorption through H-bond interactions (Ma et al., 2018).

2.3.2.2 Nitrogen containing groups

Due to the acidic nature of CO_2 (weak Lewis acid), increasing the basicity of the sorbent surface has been proven to improve the interaction between the adsorbents and CO_2 (Chiang and Juang, 2017). The introduction of nitrogen-containing groups has been extensively demonstrated as an effective approach to increase the surface basicity of adsorbents. Figure 2.10 shows the types of N functional groups on the surface of the activated carbons. The basic nature of N functional groups can effectively enhance the surface affinity towards CO_2, and thus higher adsorption enthalpy and CO_2 selectivity can be obtained. The nitrogen modified carbon is usually synthesized through two strategies: post-treatment through heat treatment with nitrogen containing reagents (such as NH_3, nitric acid, and amines) and activation with nitrogen containing precursors.

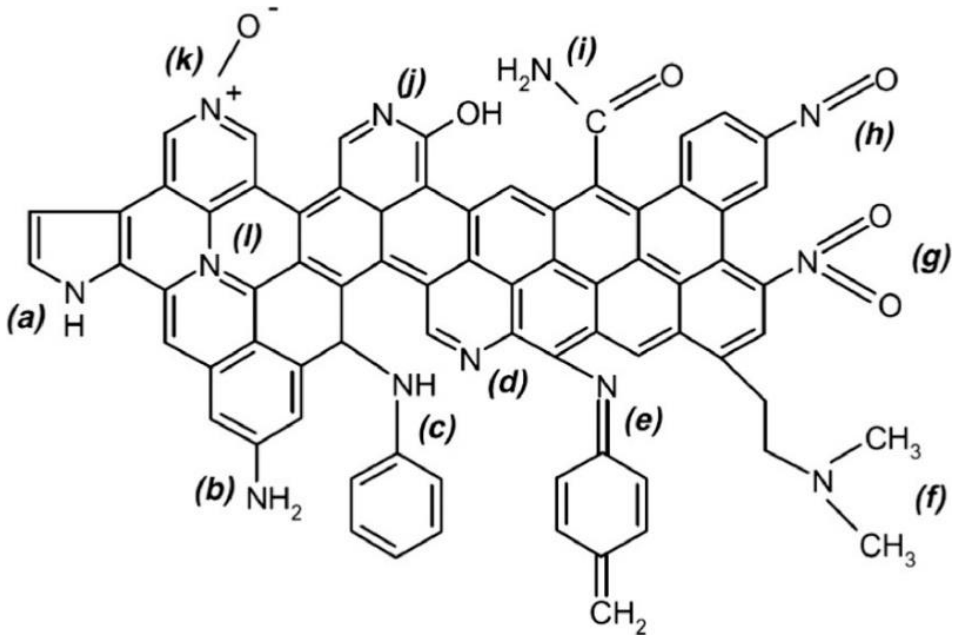


Figure 2.10 Types of N surface functional groups: (a) pyrrole, (b) primary amine, (c) secondary amine, (d) pyridine, (e) imine, (f) tertiary amine, (g) nitro, (h) nitroso, (i) amide, (j) pyridone, (k) pyridine-N-oxide, and (l) quaternary nitrogen (Ma et al., 2018)

The post-treatment, often referred to as the amination process, usually involves heating the pristine activated carbons to elevated temperatures (200–1000 ^{o}C) in NH_3 atmosphere before cooling to ambient temperature under inert gas flow (Zhang et al., 2016c, Zhang et al., 2016a). During the heating process, NH_3 decomposes into free radicals such as NH_2, NH, atomic hydrogen and nitrogen, which will react with carbon surfaces to form nitrogen functionalities such as pyridinic, pyrrolic, and quaternary N_2 (Pevida et al., 2008b). The basic sites generated from the nitrogen-containing groups are often those with the lone pair of electrons in an SP^3 orbital, which has sufficient binding energies for CO_2 (Adelodun et al., 2015). For example, Lim et al described that the Lewis acid-base interaction between pyridinic-N and CO_2 was triggered by the lone pair electron donation of the N-atom to the C-atom of CO_2 (Lim et al., 2016). According to the report from Sun et al. (2016), unlike the electrostatic interaction between pyridinic- and pyrrolic-N and CO_2, the interaction for the quaternary-N is through dispersion interaction, which leads to the lower binding energies of quaternary-N with CO_2 than those of pyridinic- and pyrrolic-N. Saha et al. (2017) synthesized nitrogen-doped and hierarchical porous carbons from lignin precursors by KOH and NH_3 activation. The results revealed that the nitrogen introduced is predominantly pyridinic, amino and pyrrolic/pyridonic type of functionality, with the porous carbon with the highest nitrogen content demonstrating the best CO_2 selectivity. However, the process still needs to overcome many obstacles such as limited improvement in CO_2 uptake and time-consuming synthesis steps involving the use of corrosive reagents.

Activated carbons prepared from nitrogen containing precursors can provide an alternative solution for CO_2 adsorption improvement. Nitrogen-containing precursors such as polyamide, melamine-formaldehyde resin, and various natural products, including chitin and chitosan, can be used to prepare nitrogen-containing activated carbons. Many studies have suggested that incorporating nitrogen functionalities can enhance both the CO_2 uptake and the heat of adsorption (Pevida et al., 2008a, Sanchez-Sanchez et al., 2014, Rehman and Park, 2020).

Pevida et al. (2008a) investigated the effect of nitrogen functional groups on CO_2 adsorption using melamine–formaldehyde resins derived carbons. It was found that carbon samples prepared at lower temperatures possessed a favourable chemistry, which dominated the CO_2 adsorption, while the loss of triazine and outer edge nitrogen functional groups as pyrolysis temperature increased and the increasing proportion of tertiary nitrogen reduced the surface affinity of the carbons to CO_2. It is because the nitrogen at the edge of graphene layers has the greatest effect of producing higher electron mobility and lowering the electron work function of the carbon-gas interface, leading to a higher activity towards CO_2. Sanchez-Sanchez et al. (2014) investigated the influence of different nitrogen functional groups like pyridinic, pyrrolic and quaternary N on CO_2 adsorption using polyamide. The rank of importance of different groups was reported as pyrrolic > pyridinic > quaternary N. However, one potential limitation is that nitrogen-containing precursors can be more expensive and difficult to obtain compared to traditional biomass precursors.

2.3.2.3 Metal-doping carbon materials

The incorporation of metallic additives into the carbon matrix is another technology to enhance the interaction between CO_2 and the carbon surface to increase CO_2 uptake, which has drawn great attention recently. Metallic additives usually in the form of metal oxides act as the electron donor in activated carbon that can improve the surface basicity.

It is well known that potassium can be intercalated into the carbon lattice in the form of surface potassium oxide groups via KOH activation to enhance the surface interaction with CO_2 molecules, especially at low CO_2 partial pressure (Liu et al., 2015a, Li et al., 2022b, Liu et al., 2017). Liu et al. (2017) reported that up to 50% of the total CO_2 uptake of rice husk-derived carbon at 25 ^oC and 15 kPa CO_2 was attributed to the unique surface chemistry modified by potassium intercalation. The results highly suggested that the significantly enhanced surface CO_2 affinity is

closely associated with the solid-state electrostatic effects created by the extra framework cations due to alkali intercalation, a phenomenon that is usually observed in MOFs and zeolites materials (Liu et al., 2012b, Bae et al., 2013).

Other metals such as alkaline earth metals (i.e. Mg, Ca) and transition metals (i.e. Cu, Co, Ni, Fe, Cr) have also been widely investigated to improve the surface chemistry and adsorptive performance of activated carbons (Lahijani et al., 2018, Shahkarami et al., 2016, Hosseini et al., 2015). Lahijani et al. (2018) examined the CO_2 adsorption capacities of metal-incorporated biochar at ambient conditions. The results showed that the incorporation of basic metal sites into the biochar skeleton enhanced the adsorption of acidic CO_2 gas onto the metalized biochar in the sequence of Mg > Al > Fe > Ni > Ca > raw biochar > Na. Hosseini et al. (2015) prepared the adsorbent by impregnation two metals Cu and Zn on the surface of the nitric acid modified activated carbon. The results revealed that the CO_2 adsorption capacity of modified activated carbon (20% of metal loading) at 15 kPa CO_2 and 30 ^oC is 48% higher than that of unmodified activated carbon. It is suggested that the oxygen atoms in the CO_2 molecules will contact and chemisorbed onto the cationic Cu^{2+} and Zn^{2+} on the carbon support, and a shorter distance between the cations and CO_2 adsorbates will favour the adsorption process due to lesser adsorption energy.

2.4 Aims and objectives

The challenges encountered for activated carbon materials nowadays lie in the optimization of carbon footprint and cost reduction while simultaneously enhancing their CO_2 adsorption performance, particularly at low CO_2 partial pressure. The paradigm of carbon preparation should shift from using traditional resources to renewable resources, with the employment of appropriate pre-treatment and activation processes to achieve the objective of attaining high CO_2 adsorption performance. The proposed PhD research aims to valorise underutilized biomass and plastic wastes for high-value advanced functional carbon materials through different pre-treatment approaches followed by chemical activation using alkaline hydroxide as an activating agent, with the CO_2 adsorption performance of synthesized activated carbons to be highly improved to achieve the target of post-combustion carbon capture in power plants. To the best of our knowledge, no investigation has been conducted to use either biomass wastes or hydrochar from hydrothermal co-carbonization (co-HTC) of biomass and PVC wastes as precursor materials to produce activated carbons for CO_2 capture. The specific objectives of this research project extend to the following parts:

1) To investigate a variety of biomass and plastic wastes as precursors to develop novel CO_2 carbon-based adsorbents with high adsorption capacity and high CO_2/N_2 selectivity at simulated flue gas conditions.
2) To explore the efficacy of different pre-treatment methods including pre-oxidation and hydrothermal carbonization on tuning the textural properties and surface chemistry of carbon materials prepared through chemical activation.
3) To identify the role of surface texture and surface chemistry on CO_2 adsorption capacity at varying temperatures and pressures to elucidate the fundamentals that govern the performance of CO_2 adsorption on porous carbons.
4) To evaluate the utilization of hydrothermal carbonization treatment as a sustainable and environmentally-friendly route for the valorisation of biomass and hazardous end-of-life plastic and the potential to use the obtained hydrochars as precursors to produce efficient CO_2 adsorbents.

Chapter 3

EXPERIMENTAL METHODOLOGIES

This chapter presents the experimental methodologies involved in this PhD research project, which includes the general sample preparation, characterization of samples and CO_2 adsorption measurements. Characterization of samples including textural properties, physicochemical characteristics, morphology, composition and surface chemistry was also involved in this chapter. In addition, the CO_2 adsorption performance of prepared activated carbon samples was evaluated by using volumetric and thermogravimetric analysis.

3.1 Preparation of carbon materials

Activated carbons were prepared from using different biomass wastes and plastic wastes as precursors through different carbonization and activation routes: (1) Kraft lignin was selected as a renewable and cost-effective carbon source precursor to prepare activated carbons via an integrated one-step carbonization-activation method, with the experimental parameters like carbonization-activation temperature and mass ratio designed based on the references (Liu et al., 2017, Li et al., 2022b), (2) Eucalyptus wood waste was chosen as the abundant biomass precursor to produce activated carbons via hydrothermal carbonization followed by KOH activation process, with the experimental parameters like hydrothermal carbonization temperature, biomass concentration, activation temperature and mass ratio designed referring to the references (Musa et al., 2022, Sevilla and Fuertes, 2011, Li et al., 2022b), (3) Cellulose and polyvinyl chloride (PVC) wastes were employed to prepared activated carbons via co-hydrothermal carbonization followed by KOH activation protocols, with the experimental conditions like hydrothermal carbonization temperature, biomass concentration, activation temperature and mass ratio designed according to the references (Yao and Ma, 2018, Ma et al., 2019b, Xue et al., 2022b, Li et al., 2022b). The labels of the prepared samples, along with their synthetic conditions, are summarized in Appendix A.

3.1.1. Preparation of Kraft lignin-derived activated carbon

The Kraft lignin (KL) and potassium hydroxide (KOH) were purchased from Sigma-Aldrich and used as received. One gram of dried KL sample was firstly mixed with 20 ml KOH solution via wet impregnation at a pre-set KL/KOH mass ratio (1:1) overnight. The mixture was then dried in an oven at 105 ^{o}C for 24 h and collected for use after cooled down to ambient temperature. The integrated carbonization and activation were carried out in a horizontal tube furnace where the alkali impregnated KL sample was loaded in a crucible and placed into the central heated area of the furnace (Figure 3.1). The sample was then heated up to the desired different temperatures (600 ^{o}C, 700 ^{o}C and 800 ^{o}C) at a heating rate of 5 ^{o}C /min in a flow of nitrogen (1 L/min). The sample mixture was kept at a given temperature for 1 h before it was cooled down to ambient temperature. The mixture was then washed thoroughly with deionized water until the pH reached neutral. The rinsed carbon sample was then dried at 105 ^{o}C in an oven to obtain the final activated carbon.

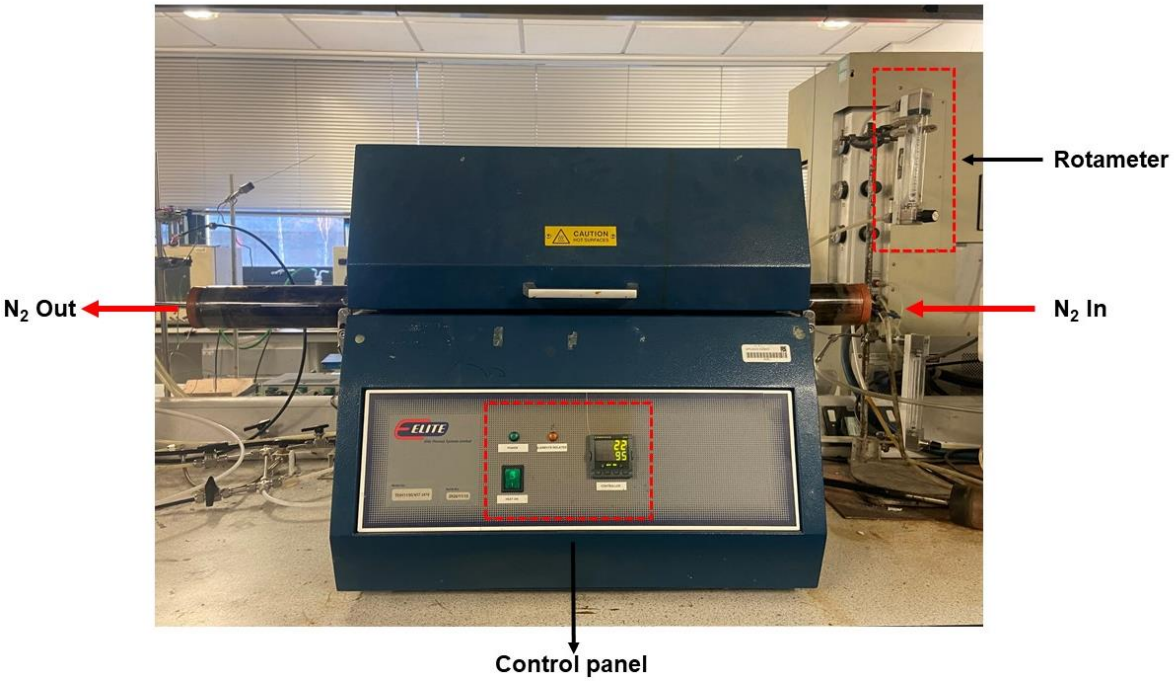


Figure 3.1 Horizontal tube furnace

Pre-oxidation: The intervention of oxidation treatment of carbon precursor prior to the carbonization-activation protocol is a well-established approach to accelerate the activation process and further contribute to the porosity evolution of the obtained activated carbons (Zhang et al., 2022, Liu et al., 2022). In this study, the pre-oxidation treatment was employed on the Kraft lignin before the integrated carbonization-activation treatment. The general procedure was as follows: a certain amount of KL was loaded in a crucible and placed into the central heated area of the furnace. The temperature was then increased from ambient to 200 ^{o}C for 6 h in a controlled airflow of 50 ml/min. The sample was collected after the temperature was cooled down to room temperature and stored for the next step of treatment. The pre-oxidized KL sample for the subsequent carbonization-activation treatment was denoted as OKL.

The carbons obtained from KOH activation under different technical conditions are labelled as KLK–x–y and OKLK–x–y, respectively, where x denotes the KOH/KL mass ratio and y stands for the activation temperature. The selected synthesis conditions are presented in Table 3.1

Table 3.1 Synthesis conditions for KL-derived activated carbons

Sample	Activation temperature (^{o}C)	KOH/KL mass ratio
KLK-1-600	600	1
KLK-1-700	700	1
KLK-1-800	800	1
KLK-2-600	600	2
KLK-2-700	700	2
OKLK-1-600	600	1
OKLK-1-700	700	1
OKLK-1-800	800	1
OKLK-2-600	600	2
OKLK-2-700	700	2

3.1.2. Preparation of Eucalyptus carbons

1) Hydrothermal carbonization: HTC experiments were conducted in a Parr 4740 series reactor with 75ml capacity. Figure 3.2 (a) shows the empty reactor before coupling and Figure 3.2 (b) shows the setup of the sand bath for the HTC experiment.

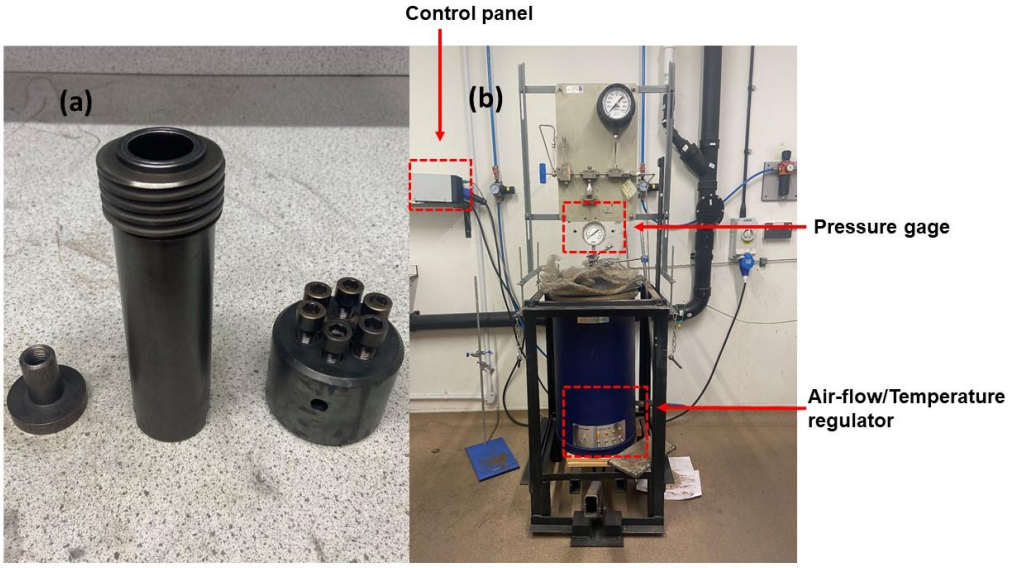


Figure 3.2 Hydrothermal carbonization reactor (a) and fluidized sand bath (b)

Firstly, the collected EU was thoroughly washed with clean water to remove sand, dried at 80 ^{o}C for 6 h in an oven, and then cut into small pieces of 3-6 mm diameters using using a cutting mill. About 6 g of EU biomass and 30 g of deionized water were charged into the reactor for each HTC run (biomass-water ratio of 1:5). The reactor was then closed and purged with nitrogen gas to eradicate the oxygen in the system. After that, the reactor was pressurized with 1 bar of N_2 to create an inert atmosphere in each experiment. The reactor was then lowered into a fluidized sand bath to start the experiment. The temperature of each experimental run was monitored using an additional K-type thermocouple connected externally to a computer that records the temperature every 10 s. The autoclave was heated up to the required temperature (220 ^{o}C and 260 ^{o}C) in a fluidized sand bath and the

reaction was allowed to run for a residence time of 3 h. At the end of each experiment, the reactor was removed from the sand bath and allowed to cool to room temperature. The solid-liquid mixture was then separated by vacuum filtration through a pre-weighted filter paper (0.45 μm). The primary solid products were washed with deionized water and recovered as hydrochars (designated as EUHC). The hydrochar samples were dried in an oven at 105 ^{o}C for 16 h. The samples were collected after the temperature was cooled down to room temperature and stored for the next step of treatment. Table 3.2 shows the synthesis conditions for eucalyptus-derived hydrochars.

Table 3.2 Synthesis conditions for eucalyptus-derived hydrochars

Sample	Hydrothermal temperature (^{o}C)
EUHC22	220
EUHC26	260

2) KOH activation: Firstly, the dried hydrochar samples were mixed with KOH solution via wet impregnation at a pre-set KOH/EUHC mass ratio of 1:1 and 2:1 overnight and dehydrated in an oven at 105 ^{o}C for 24 h. The hydrochar samples were collected for use after being cooled down to ambient temperature. The activation protocols for all the alkali impregnated EUHC samples were carried out by an electric horizontal furnace at different desired temperatures (600 ^{o}C and 700 ^{o}C) at an unvarying heating rate of 5 ^{o}C/min in a flow of nitrogen (1 L/min) for 1 h. The chemically activated EUHC hydrochar products were cooled down to ambient temperature and washed thoroughly with deionized water until the pH reached neutral. The rinsed samples were dried at 105 ^{o}C in an oven for 24 h. The obtained activated samples were labelled in the form of EUHCx-y-z, where x, y, and z represent the hydrothermal carbonization temperature divided by 10, KOH/EU mass ratio and activation temperature, respectively. Table 3.3 shows the synthesis

conditions for eucalyptus-derived activated carbons prepared via hydrothermal carbonization.

Table 3.3 Synthesis conditions for eucalyptus-derived activated carbons prepared via hydrothermal carbonization

Sample	Activation temperature (°C)	KOH/EUHC mass ratio
EU-1-600	600	1
EUHC22-1-600	600	1
EUHC22-1-700	700	1
EUHC22-2-600	600	2
EUHC22-2-700	700	2
EUHC26-1-600	600	1
EUHC26-1-700	700	1
EUHC26-2-600	600	2
EUHC26-2-700	700	2

3.1.4. Preparation of PVC and PVC/biomass carbons

1) Hydrothermal carbonization: 10g of used PVC pipes were firstly cut into small stripes and other biomass precursors such as cellulose (CE) and KL were used as received. The HTC experiment of cellulose, KL, PVC and their mixture was carried out by using a 2-liter hydrothermal reactor (Model 4520, Parr Instrument) (Figure 3.3a). 20g PVC and 20g solid mixture (10g cellulose and 10g PVC; 10g KL and 10g PVC) were dissolved in 500 ml distilled water at a mass ratio of 1:25, respectively, and then fed to the HTC reactor. The reactor was heated up to the desired temperatures (220, 240 and 260 °C) at a heating rate of ~4 °C/min and maintained for a designated residence time (6 h). The stirring speed was set to 300 rpm throughout the hydrothermal reaction process. After the reaction was completed, the reactor was cooled down to room temperature naturally. The solid-liquid mixture was then separated by vacuum filtration through a pre-weighted filter

paper (0.45 μm). The primary solid products were washed with deionized water and recovered as hydrochars (designated as PHC, CEPHC and KLPHC). The hydrochar samples were dried in an oven at 105 ^{o}C for 16 h and collected after the temperature was cooled down to room temperature. The hydrochar samples were marked as PHCx, CEPHCx and KLPHCx, where x denotes the hydrothermal carbonization temperature divided by 10. Table 3.4 shows the Synthesis conditions for PVC and PVC/biomass hydrochars.

Table 3.4 Synthesis conditions for PVC and PVC/biomass hydrochars

Sample	Precursor	Hydrothermal temperature (^{o}C)
PHC22	PVC	220
PHC24	PVC	240
PHC26	PVC	260
CEPHC22	PVC/cellulose	220
CEPHC24	PVC/cellulose	240
CEPHC26	PVC/cellulose	260
KLPHC22	PVC/kraft lignin	220
KLPHC24	PVC/kraft lignin	240
KLPHC26	PVC/kraft lignin	260

2) Pre-compaction: The compaction treatment on the produced hydrochar and co-hydrochar prior to activation treatment was employed to obtain the homogeneous precursor composite for effective activation. It was found that the introduction of compaction could effectively reduce the inter-particle voids and increase the contact between the particles of the activating agents and carbon precursor, thereby enhancing activation efficacy and leading to further developed porosity, particularly in the range of fine micropores (<0.6 nm) (Liu et al., 2019). In this study, the hydrochar samples were mixed with KOH solution via wet impregnation at a pre-set KOH/hydrochar mass ratio of 1:1 and 2:1 overnight and dehydrated in an

oven at 105 ^{o}C for 24 h. The dried samples were then ground into powder for pellet pressing. Thereafter, the ground samples were compressed into 1.5 mm thick pellets by using a 13-mm diameter pellet die under 7 tons of maximum load with the help of a hydraulic press (Figure 3.3b).

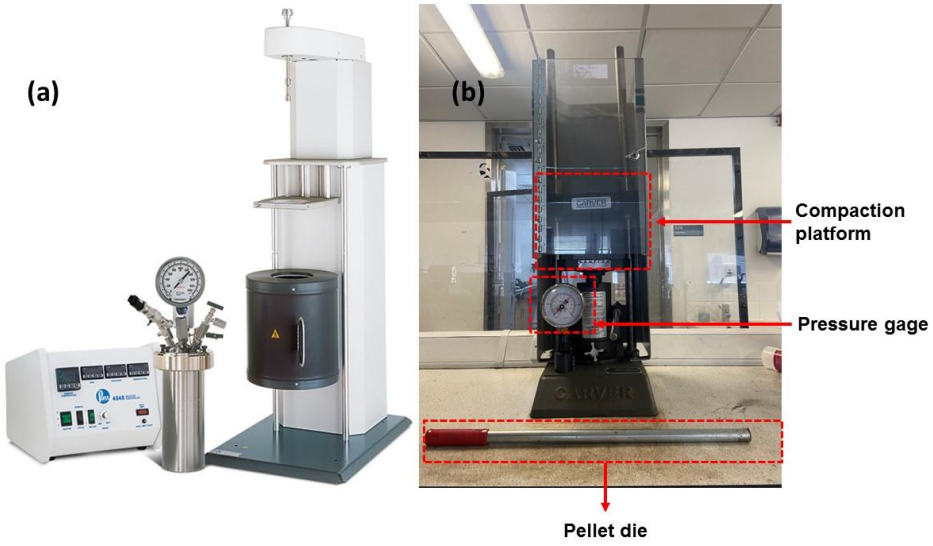


Figure 3.3 Parr high-pressure hydrothermal reactor (a) and hydraulic press (b)

3) KOH activation: The activation process was carried out by an electric horizontal furnace at different desired temperatures (600 ^{o}C, 700 ^{o}C and 800 ^{o}C) at a consistent heating rate of 5 ^{o}C/min in a flow of nitrogen (1 L/min) for 1 h. After the reaction was completed and cooled down to room temperature, the activated carbon samples were collected and washed with deionized water until the pH became neutral. The rinsed samples were dried at 105 ^{o}C in an oven for 24 h. The obtained activated samples were labelled in the form of PHCx-y-z, CEPHCx-y-z and KLPHCx-y-z, where x represents the hydrothermal carbonization temperature divided by 10, y indicates the KOH/HC mass ratio and z denotes the activation temperature. The synthesis conditions for biomass/PVC-derived activated carbons are listed in Table 3.5. Given that the hydrochars obtained at the lower HTC temperature of 220 ^{o}C were still reluctant to be ground into powder due to the large

proportion of crosslinking chlorine remained, only hydrochars prepared at 240 and 260 ^{o}C will be used for KOH activation after homogeneous compaction treatment.

Table 3.5 Synthesis conditions for PVC/biomass-derived activated carbons via HTC

Sample	Activation temperature (^{o}C)	KOH/EUHC mass ratio
PHC24-1-600	600	1
PHC24-1-700	700	1
PHC24-1-800	800	1
PHC24-2-600	600	2
PHC24-2-600	700	2
PHC26-1-600	600	1
PHC26-1-700	700	1
PHC26-1-800	800	1
PHC26-2-600	600	2
PHC26-2-700	700	2
CEPHC24-1-600	600	1
CEPHC24-1-700	700	1
CEPHC24-1-800	800	1
CEPHC24-2-600	600	2
CEPHC24-2-700	700	2
CEPHC26-1-600	600	1
CEPHC26-1-700	700	1
CEPHC26-1-800	800	1
CEPHC26-2-600	600	2
CEPHC26-2-700	700	2
KLPHC22-1-600	600	1
KLPHC22-1-700	700	1
KLPHC26-1-600	600	1
KLPHC26-1-700	700	1

3.2 Characterization

3.2.1 Textural properties

Gas adsorption is a widely accepted methodology for determining the textural properties of porous materials. The application of this method is based on a physisorption phenomenon characterized by the adsorption/desorption of gas molecules on the solid surface to obtain the equilibrium adsorption capacity of gas as a function of pressure, which allows the calculation of specific surface area, pore volume and pore size distribution by using different theoretical models.

In this study, the Micromeritics ASAP 2420 analyzer was employed to characterize the textural properties of all the samples. The surface areas (S_{BET}) were determined using the Brunauer–Emmett–Teller (BET) method based on N_2 adsorption isotherms at −196 ^oC in the relative pressure range of 0.01– 0.1. The pore volume/pore size distribution (PSD) was determined via the non-local density function theory (NLDFT) method using the combination of CO_2 adsorption isotherms at 0 ^oC with N_2 adsorption isotherm at −196 ^oC.

3.2.1.1 Classification of N_2 physisorption isotherms

For physisorption, the adsorption mechanisms in different pores vary with their pore size. According to the IUPAC (International Union of Pure and Applied Chemistry) recommendation, pores with widths less than 2 nm, between 2 nm and 50 nm, and exceeding 50 nm are classified as micropores, mesopores and macropores, respectively (Sing, 1985). For micropores (< 2nm), the adsorption process is dominated by the micropore filling which occurs in a continuous way. The filling of narrow micropore of approximate width < 0.7 nm takes place at low relative pressure ($p/p^o < 0.01$) via the strong adsorption potential derived from the enhanced adsorbent-adsorbate interactions caused by the overlap of the adsorption forces, whereas the filling of the wide micropores (i.e. supermicropores) is determined by a cooperative mechanism including both adsorbent-adsorbate and adsorbate-adsorbate interactions in a range of higher relative pressure (p/p^o

= 0.01–0.15) (Thommes et al., 2015). The adsorption behaviour in mesopores (2-50 nm) depends not only on the adsorbent-adsorbate interactions but also significantly on the attractive adsorbate-adsorbate interactions, which leads to the occurrence of multilayer adsorption and capillary condensation. Capillary (or pore) condensation represents a phenomenon whereby a gas condenses to a liquid-like phase in a pore at a pressure (p) less than the saturation pressure (p_o) of the gas (Thommes et al., 2015). The capillary condensation occurs at high relative pressure (p/p^o >0.4) and is very often accompanied by hysteresis which is observed in single pores as well as in pore networks. As for macropores (>50 nm), the phenomenon of capillary condensation does not exist due to the abundance of space between the pore walls and the adsorbate that limits their interaction. The macropores are only considered as transportation paths.

The specific surface areas and pore size analysis of porous materials are usually obtained from the adsorption isotherm which is defined as the amount adsorbed as a function of the equilibrium relative pressure (p/p^o) at a constant temperature. Given the pore structures in different porous materials vary greatly, their adsorption isotherms exhibit many different shapes. IUPAC first grouped the majority of adsorption isotherms into six types in 1985 and recently refined the classification of adsorption isotherms as shown in Figure 3.4 (Sing, 1985, Thommes et al., 2015).

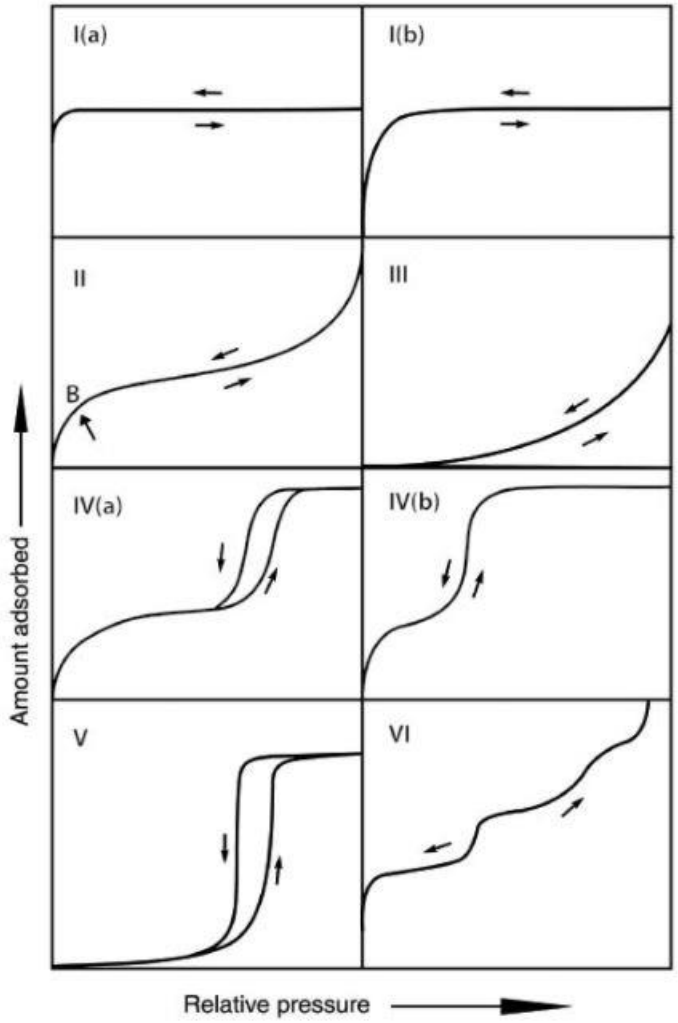


Figure 3.4 Classification of N_2 adsorption isotherms (Thommes et al., 2015)

Type I isotherms are normally observed with microporous solids having relatively small external surfaces (e.g. some activated carbons, molecular sieve zeolites and certain porous oxides). It can be found in Figure 3.4 that, for both Type I(a) and Type I(b) isotherms, a sharp uptake occurs at low relative pressure, followed by a plateau at high relative pressure. In addition, Type I(a) isotherms possess a steeper uptake at very low relative pressure due to the enhanced adsorbent-adsorbate interactions in narrow micropores, which are given by microporous materials having mainly narrow micropores. Type I(b) isotherms are normally

found in materials with broader pore size distributions including wider micropores and possibly narrow mesopores.

Type II isotherms are typically found in nonporous or macroporous adsorbents, which present a gradual increasing uptake with increasing relative pressure, indicating unrestricted monolayer-multilayer adsorption occurs. The transition point marked as point B in Type II isotherms corresponds to the completion of monolayer coverage and the onset of multilayer adsorption. The ever-growing uptake up to high relative pressure implies that the thickness of the adsorbed multilayer increases indefinitely at the saturation pressure ($p/p^o = 1$).

Type III isotherms are also indicative of nonporous or macroporous materials and only occur when the adsorbent-adsorbate interactions become much weaker than the intermolecular force of adsorbate. Unlike Type II isotherms, Type III isotherms have no Point B and therefore no identifiable monolayer formation, which leads to the finite adsorbed amount when the pressure reaches saturated.

Type IV isotherms are often given by porous materials with mesoporous or microporous structures. In this case, the initial monolayer-multilayer adsorption takes the same path as the corresponding part of Type II isotherms, followed by a plateau of variable length up to the saturation pressure ($p/p^o = 1$). To be specific, the hysteresis loop emerges at a high relative pressure ($p/p^o > 0.4$) in Type IV(a) isotherms, which is associated with the capillary condensation in large mesopores. In contrast to Type IV(a) isotherms, Type IV(b) isotherms are found in materials with conical and cylindrical mesopores of smaller widths, with the isotherms being completely reversible.

Type V isotherms are observed for water adsorption on hydrophobic microporous and mesoporous adsorbents. At lower relative pressure regions, the Type V isotherms are very similar to that of Type III isotherms due to the relatively weak adsorbent-adsorbate interactions. At a higher relative pressure range, the isotherms turn into Type IV-like isotherms with a hysteresis loop, which is associated with the presence of mesopores.

Type VI isotherms are usually given by the materials with a highly uniform nonporous surface, showing stepwise layer-by-layer adsorption isotherms (e.g. adsorption of krypton at low temperature on graphitized carbon blacks).

3.2.1.2 Types of hysteresis loops

It is noteworthy that certain Type V and Type VI isotherms given by the mesoporous adsorbents are accompanied by hysteresis which are generally associated with capillary condensation. The formation of hysteresis can be attributed to either metastability of the adsorbed multilayers or network effects, leading to many different shapes of hysteresis loops. As shown in Figure 3.5, six characteristic types of hysteresis loop are identified and extended by IUPAC in 2015 based on the original IUPAC classification of 1985 (Sing, 1985, Thommes et al., 2015).

Type H1 loop is usually observed in porous materials possessing uniform mesopores in a narrow range, for instance in templated silicas, some controlled pore glasses and ordered mesoporous carbons. The steep uptake with a narrow loop is clearly indicative of delayed condensation on the adsorption branch.

The hysteresis loop of Type H2 is given by adsorbents containing complex pore structures in which network effects are significant. The formation of Type H2(a) loops, which is characterized by the very steep desorption branch, is mainly attributed either to pore-blocking/percolation in a narrow range of pore necks or to cavitation-induced evaporation. Type H2(a) hysteresis loops have been found in materials such as silica gel, porous glasses and ordered mesoporous materials. A similar mechanism of desorption applies to the materials (e.g. mesocellular silica foams) with Type H2(b) hysteresis loop, while the more gradual desorption branch indicates the size distribution of neck widths is much larger, which allows the adsorbed in the pores to desorbed before narrow necks empty. A similar adsorption branch as in Type II isotherms and the lower limit of the desorption branch located at the cavitation-induced relative pressure are characteristic

features of Type H3 hysteresis loop that can be found in non-rigid aggregates of plate-like particles (e.g. certain clays).

The Type H4 loop, which is characterized by the more pronounced uptake at low relative pressure being associated with the filling of micropores, is often found in mesoporous zeolites and micro-mesoporous carbons.

The Type H5 hysteresis loop represents a very rare and distinctive form associated with certain pore structures containing both open and partially blocked mesopores (e.g. plugged hexagonal templated silicas).

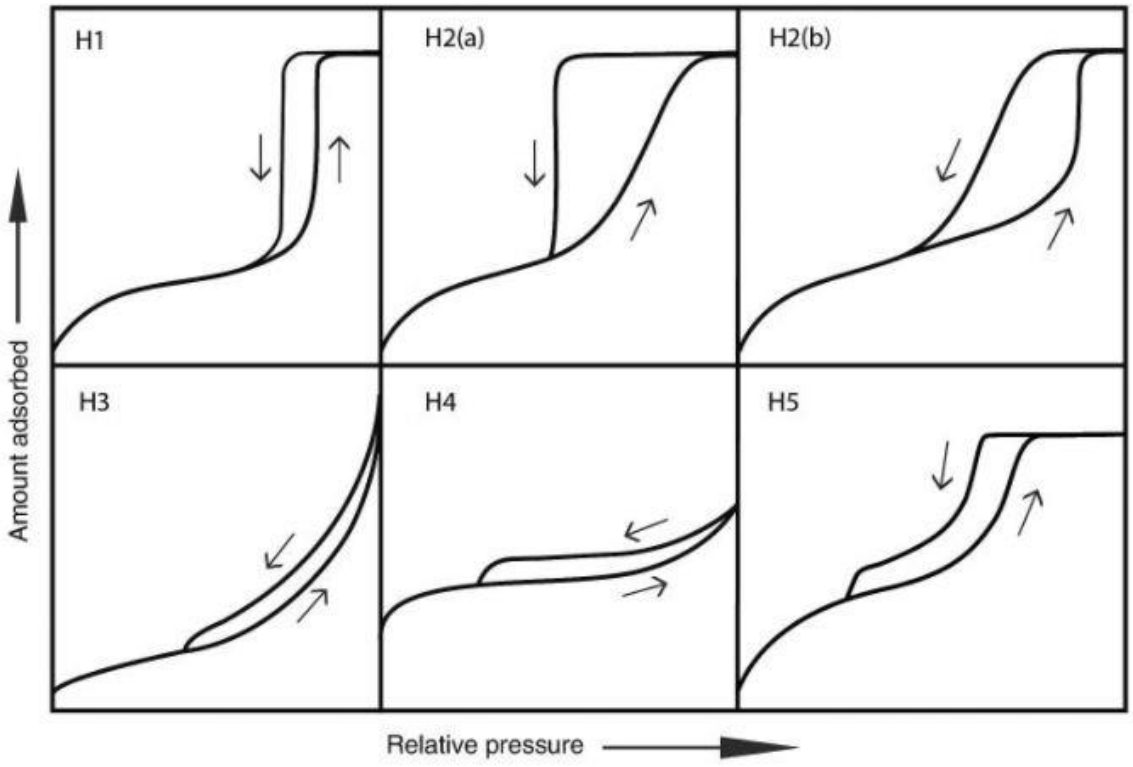


Figure 3.5 Classification of hysteresis loops (Thommes et al., 2015)

3.2.1.3 Assessment of surface area

The Brunauer–Emmett–Teller (BET) method is the most widely used procedure to evaluate the surface area of porous solid materials (Brunauer et al., 1938).

Compared to other adsorption methods like Langmuir adsorption theory which only considers monolayer adsorption (Type I isotherms), the BET model which extends to multilayer adsorption (Type II, IV and V isotherms) is more applicable for the measurement of the specific surface area of adsorbents having composite isotherms. The BET theory is based on the following assumptions:

1. Adsorption occurs on a uniform surface and the adsorption energies of all molecules are identical.
2. The adsorption of gas molecules on materials takes place in multilayers, with interactions only existing between adjacent layers in the vertical direction.
3. The lateral interaction between adsorbate molecules is negligible.
4. There is no steric limitation to the thickness of the multilayer.
5. The enthalpy of adsorption of physical adsorption of each layer is equal to the liquefaction energy of the materials except for the first layer where the enthalpy of adsorption is greater than the liquefaction energy.

Therefore, the resulting BET equation can be described as Equation 3.1

$$\frac{p/p_{\mathrm{o}}}{n(1-p/\mathrm{po})} = \frac{1}{n_m C} + \frac{C-1}{n_m C}(P/P\mathrm{o}) \qquad \text{Equation 3.1}$$

Where n is the specific adsorption capacity at the relative pressure p/p^o, n_m is the specific monolayer capacity and C is an empirical number.

Equation 3.1 is an adsorption isotherm, which can be plotted as a straight line with $(p/p^o)/n\ (1–p/p^o)$ on the y-axis and p/p^o on the x-axis in the range of $0.05 < p/p^o < 0.35$. Thus, the total surface area and the specific surface area could be calculated by using Equation 3.2 and Equation 3.3.

$$S_{total} = n_m L \frac{\sigma}{m} \qquad \text{Equation 3.2}$$

$$S_{BET} = \frac{S_{total}}{a} \qquad \text{Equation 3.3}$$

Where S_{total} is the total specific area, S_{BET} is the specific surface area, m is molar volume of the adsorbate gas, L is the Avogadro's number (6.02 x 10^{23}), σ is the cross-sectional area occupied by each molecule (0.162 nm^2 for nitrogen molecule and 0.142 nm^2 for argon molecule) and a is the mass of the adsorbent.

3.2.1.4 Assessment of porosity

The total pore volume (V_{total}) is derived from the amount of gas adsorbed at a relative pressure close to unity ($p/p^o \approx 1$), by assuming that the pores are fully occupied with liquid adsorbate according to Gurvisch Law. The volume of nitrogen adsorbed (V_{ads}) can be converted to the volume of liquid nitrogen (V_{total}) contained in the pores using following Equation 3.4.

$$V_{total} = \frac{P_a V_{ads} V_m}{RT} \qquad \text{Equation 3.4}$$

Where P_a is the ambient pressure, V_m is the molar volume of the liquid nitrogen (34.7 cm^3/mol), and R is the universal gas constant.

Pore size distribution (PSD) means the distribution of pore volume versus pore size, which can be determined by employing the appropriate model that is applicable to the shape and structure of the pores. Classic macroscopic theories such as Dubinin-Radushkevich (DR) and Dubinin-Astakhov (DA) methods yield size distribution in the micropore range, whereas other semi-empirical models like Horvath-Kavazoe (HK) and Saito-Foley (SF) models are suitable for microporous materials with a predominance of ether slit-lite pores or cylindrical pores (Lowell et al., 2006, Thommes and Cychosz, 2014). The Barrett-Joyner-Halenda (BJH) model could be used to calculate the mesopore size. Although these methods have been often used for pore size calculation, they are still subjected to inadequate descriptions for the whole range of pore size distributions and different pore shapes, leading to an underestimation of pore sizes. Thus, density functional theory (DFT), which is based on the fundamental principles of statistical mechanics, is developed to describe the configuration of the adsorbed phase at the molecular level as well as provide a more reliable approach to pore size analysis over the

complete nanopore range (Landers et al., 2013). However, adsorbate-adsorbate interactions are not accounted for in the DFT model. In order to yield an explicit pore size distribution, the Non-local density functional theory (NLDFT) method, which describes the behaviour of fluid in pores from a molecular level as well as correlating the properties of adsorbate with their adsorption behaviour in pores with different pore size, is employed in this study (Landers et al., 2013, Thommes and Cychosz, 2014, Lowell et al., 2006). The relation between isotherms determined by this microscopic approach and the experimental isotherms on porous materials can be interpreted in terms of a Generalized Adsorption Isotherm (GAI) equation as follows (Equation 3.5):

$$\mathrm{N}(p/po) = \int_{W_{min}}^{W_{max}} N(p/po, W) f(W) dW \qquad \text{Equation 3.5}$$

Where N(p/p^o) is the experimental adsorption isotherm data, N(p/p^o, w) is the isotherm on a single pore of width W, W_{max} and W_{min} are the maximum and minimum pore width, respectively, f(w) is the pore size distribution function. This equation can be solved numerically via a fast non-negative least square algorithm (Landers et al., 2013). In this study, the SAIEUS (Solution of Adsorption Integral Equation Using Splines) program was used in the ASAP 2420 system to calculate the pore size distribution (PSD) of prepared carbon materials via adsorption isotherms using an NLDFT model based on the following critical elements. A Kernel was used to describe the adsorption isotherms as a function of the pore size and pressure; a regularization method using non-negativity constraints combined with optimally minimizing the second derivative of the calculated distribution via the L-curve method was also employed. In addition, given that the molecular dynamic diameter of CO_2 (0.33 nm) is smaller than that of N_2 (0.364 nm), which allows more adequate diffusion of CO_2 molecules into ultra-micropores, the PSDs of ultra-micropores is usually calculated by applying the data of CO_2 adsorption isotherm at 0 ^{o}C to the NLDFT method. Therefore, the PSDs in the ultra-micropore to mesopore region can be obtained in this study via the NLDFT method using the combination of CO_2 adsorption isotherms at 0 ^{o}C with N_2 adsorption isotherm at 196 ^{o}C.

3.2.2 Physicochemical characteristics

Physicochemical properties for each biomass and PVC precursor and their derived hydrochars are characterized by using Ultimate analysis (C,H,O,N) and Proximate analysis (moisture, ash, volatile matter and fixed carbon).

3.2.2.1 Ultimate analysis

Ultimate analysis was carried out to determine the carbon, hydrogen, oxygen and nitrogen contents of the raw precursor materials and hydrochar samples by using a LECO CHN 628 series elemental analyzer as shown in Figure 3.6. Approx. 150 mg pre-weighed sample was encapsulated and then loaded into the appropriate position on the sample carouse, which transferred the sample into a ceramic crucible inside the furnace. The sample was burned in the pure oxygen environment in the furnace at 1050 oC for rapid and complete combustion. The contents of C and H present in the sample are quantitatively determined by the detection of their combustion gases (CO_2 and H_2O) through a non-dispersive infrared sensor, with the proportion of N determined by the analysis of NO_x via a temperature-conductive sensor. The oxygen content is calculated by subtracting the content of C, H, N and ash. Blank correction and calibration are recommended to be performed prior to the analysis according to the instrument operation and instruction manual.



Figure 3.6 LECO CHN 628 series elemental analyzer

3.2.2.1 Proximate analysis

Proximate analysis gives the composition of the substance in terms of gross components including moisture (M), volatile matter (VM), ash (ASH), and fixed carbon (FC). In this study, the proximate analysis was carried out in observance of ISO 687, ISO 562 and ISO 1170 for moisture at 105 ^{o}C, volatile matter at 900 ^{o}C and ash at 815 ^{o}C, respectively, using a TA Instruments Q500 Thermogravimetric analyzer as shown in Figure 3.7. The fixed-carbon content was determined by subtracting the sum of the weight percent value of moisture, volatile matter and ash from 100%. Thermogravimetric analysis is a thermal analysis method that measures the change in physical and chemical properties of materials with increasing temperature or isothermally with increasing time in a specified atmosphere. The operating temperature for the Q500 ranges from ambient to 1000 ^{o}C, with the isothermal temperature accuracy of $\pm$1^{o}C and isothermal temperature precision of $\pm$0.1^{o}C, the heating rate is controlled within the range of 0.01 to 100 ^{o}C/min.



Figure 3.7 TA Instruments Q500 Thermogravimetric analyzer

3.2.3 Morphology

Scanning electron microscopy (SEM) is an electron imaging technique used to characterize the morphology and microstructure of solid materials. In general, a finely focused electron beam with high energy levels of typically 0.1–30 keV is emitted from an electron gun fitted with a tungsten filament cathode and scanned across the sample. The electron signals generated (including secondary electrons and backscattered electrons) due to the interaction between accelerated electrons and the sample surface are then amplified and detected to produce an image of the surface of the sample. The secondary electrons with relatively low energy can effectively show the morphology of samples while backscattered electrons with higher energy determine the contrast between areas with different chemical compositions. Through the calculation of the X-ray signals, the composition of samples can be carried out qualitatively or semi-quantitatively by Energy-Dispersive X-Ray Spectroscopy (EDS). In this project, the morphology and composition of the prepared hydrochar and activated carbon samples were characterized using an FEI Quanta 600 MLA and a JEOL 7000F Field Emission Gun Scanning Electron Microscope (FEG-SEM). Compared to thermionic tungsten filaments, Field Emission Gun (FEG) SEM uses a high-brightness electron beam with a high spatial resolution and therefore more suitable for imaging features on the nanoscale.

3.2.4 Composition analysis

Similar to the aforementioned EDS, X-ray fluorescence spectroscopy (XRF) uses the interaction of X-rays with a material to determine its elemental composition. In the typical XRF analysis, the sample surface is excited by the primary X-ray beam produced by an Rh target leading to holes generated on inner electron shells; the electrons from outer shells fill the holes during relaxation resulting in the emission of X-ray fluorescence characteristic of sample element. The intensity of the energy measured is proportional to the abundance of the element in the sample. EDX detection limit is typically at 0.1% level, whereas XRF usually detects elements at ppm level. Another major difference between XRF and EDS is in the signal

collection mechanism where EDS uses a Si (Li) detector and XRF uses analytical crystal to differentiate X-rays coming off of the sample surface that makes XRF peak resolution better than that of EDX (Nasrazadani and Hassani, 2016). A Bruker S8 Tiger X-ray fluorescence (XRF) spectroscopy was used to quantitatively evaluate the elemental compositions of the manufactured activated carbons in this study. X-ray diffraction (XRD) is a non-destructive technique for characterizing the microcrystalline structure of activated carbons. X-ray diffraction peaks are produced by constructive interference of a monochromatic beam of X-rays scattered at specific angles from each set of lattice planes in a sample. The peak intensities are determined by the distribution of atoms within the lattice. Given each peak in a diffractogram results from a corresponding d-spacing, the sample structure can be identified by comparing the d-spacing with standard reference patterns. Consequently, the X-ray diffraction pattern is the fingerprint of periodic atomic arrangements in a given material (Bunaciu et al., 2015). A Bruker D8 Advance X-ray diffractometer (XRD) was employed to explore the crystalline phases present in prepared carbons.

3.2.5 Surface chemistry

Fourier Transform Infrared (FT-IR) Spectroscopy is a technique used in determining an infrared spectrum of transmission or absorption of materials, including their functional groups, as well as possible molecular bonds between chemical compounds. In theory, the infrared beam passes via an interferometer where the spectral coding occurs. The beam recombines in various path lengths in the interferometer to produce an interferogram. The resulting interferogram is then transferred from the sample surface, where specific energy frequencies are absorbed. Depending on the infrared absorption in the range of 4000-400 cm^{-1}, different functional groups prevailing in the samples can be determined through spectrum data in the automated software of spectroscopy (Undavalli et al., 2021). In this study, Fourier Transform Infrared (FT-IR) spectra of the raw materials and hydrochar samples were recorded within the frequency range of 4000-500 cm^{-1} using a Bruker Tensor 27 Fourier-transform infrared (FT-IR) spectrometer. Another

important signal generated as the incident electron beam interacts with the sample is the characteristic X-ray signal, which is used to determine the elemental composition of small or larger areas of the sample. Based on the calculations of the X-ray signals, the composition of samples can be analyzed qualitatively or semi-quantitatively using an energy-dispersive X-ray Spectroscopy (EDX) system (Goldstein et al., 2017).

3.3 Evaluation of carbon materials for CO_2 adsorption

The CO_2 adsorption performance of prepared samples was evaluated in terms of their static and dynamic CO_2 adsorption capacities, CO_2/N_2 selectivity, the heat of adsorption and CO_2 adsorption reversibility.

3.3.1 CO_2 adsorption isotherms

The CO_2 equilibrium adsorption capacity is measured through a static volumetric method by using a Micromeritics ASAP 2420 analyzer to obtain the CO_2 adsorption isotherms of samples at 0 ^oC and 25 ^oC at varying relative pressures.

3.3.2 Dynamic CO_2 adsorption capacity

The dynamic CO_2 adsorption characteristics of the samples were analyzed using a TA Instruments Q500 Thermogravimetric analyzer as shown in Figure 3.7. The CO_2 adsorption capacities of produced samples are analyzed by following the procedures: (1) The sample (~20 mg) was first dried at 150 ^oC in a flow of nitrogen (100 ml/min) for 30 min before it was cooled down to 25 ^oC for CO_2 adsorption; (2) The gas flow was then switched from N_2 to a simulated flue gas (15% CO_2 in N_2) at a flow rate of 100 mL/min to initiate the CO_2 adsorption test; (3) The sample was held for minimum 60 min until the adsorption reached equilibrium at a given temperature and CO_2 partial pressure; (4) the sample was then heated up to 120 ^oC and held at this temperature until the desorption was completed. In addition, a continuous adsorption-desorption cyclic test of up to 50 cycles for the selected

samples was also carried out by TGA Q500 to evaluate their adsorption reversibility.

3.3.3 Heat of adsorption

Isosteric heat of adsorption is an important parameter to indicate the binding strength of adsorbate molecules and adsorbent lattice atoms. In this study, the heat of adsorption was calculated by the integral adsorption heat values (Q_{int}) from the isosteric heat of adsorption, which is given by Equation 3.6:

$$Q_{int} = \frac{1}{n}\int_0^n Q_{st}\,dn \qquad \text{Equation 3.6}$$

Where n is the equilibrium CO_2 adsorption capacity, Q_{st} is the isosteric heat of adsorption, which can be calculated by the Clausius-Clapeyron equation (Equation 3.7) by using adsorption data at different temperatures (Saha et al., 2011):

$$Q_{st} = R\left[\frac{\partial \mathrm{lnP}}{\partial \mathrm{In}(1/T)}\right]_q \qquad \text{Equation 3.7}$$

Where R is the ideal gas constant and q is the CO_2 adsorption capacity at pressure P and temperature T. A plot of lnP versus ln(1/T) gives a straight line with a slope of Q_{st}.

In this study, Dual-site Langmuir (DSL) model was used to fit the CO_2 adsorption isotherms to obtain all parameters required for the Clausius-Clapeyron equation.

Langmuir model: The Langmuir model is commonly used to describe the equilibrium between adsorbate and adsorbent system at a constant temperature based on the assumptions as follows (Langmuir, 1918, Masel, 1996):

1. The surface containing the adsorption sites of the immobile state is perfectly flat with no corrugations.
2. Only one gaseous molecule can be adsorbed by each site (monolayer coverage only).
3. No interactions between adsorbate molecules on adjacent sites.
4. The adsorption sites are identical and energetically equivalent.

Therefore, the Langmuir equation is described by the following Equation 3.8:

$$q = q_m(\frac{bp}{1+bp}) \quad \text{Equation 3.8}$$

Where q is the amount of CO_2 adsorbed per unit mass of adsorbent (mmol/g), q_m is the equilibrium adsorption capacity, p is the equilibrium pressure, and B is the Langmuir constant.

Dual-Site Langmuir (DSL) model: Given the heterogeneity of the prepared samples induced by the potassium intercalation, the Langmuir model is not suitable since it only describes the adsorption process that occurs at particular homogeneous sites on the surface of the adsorbent. The dual-site Langmuir mode (DSL), which assumes that there are two kinds of adsorption sites with different adsorption energies, is more applicable to predict the CO_2 adsorption behavior on heterogeneous surfaces of adsorbent samples prepared in this study. On heterogeneous surfaces, the adsorption energy of each site varies with the surface chemistry and structure. Therefore, the gas will be adsorbed on the most favourable sites followed by less favourable sites. In this work, the adsorption isotherms data were fitted in dual-site Langmuir model equations using Origin. All the fittings corresponded to adjusted R^2 values exceeding 0.999.

The mathematical form of DSL model is as follows (Equation 3.9) :

$$q = q_a + q_b = \frac{q_{ma}b_a p}{1+b_a p} + \frac{q_{mb}b_b p}{1+b_b p} \quad \text{Equation 3.9}$$

Where the subscripts a and b represent two different adsorption sites, q_{ma} and q_{mb} are the equilibrium adsorbed amount for site a and site b, respectively, and b_a and b_b are constants.

The selective CO_2 adsorption over N_2 is also critical for adsorbents in terms of CO_2 capture in the flue gas. In this work, the CO_2/N_2 selectivity of selected carbon samples was investigated using the ideal adsorption solution theory (IAST) that has been employed as an effective model to evaluate the CO_2/N_2 selectivity of sorbent materials (Sethia and Sayari, 2015, Li et al., 2016). The IAST selectivity

for the CO_2:N_2 (15%:85%) gas mixture was calculated using the following Equation 3.10:

$$S = \frac{q_1/q_2}{p_1/p_2} \quad \text{Equation 3.10}$$

Where S is the selectivity, q_1 and q_2 represent the amount adsorbed of CO_2 and N_2, and p_1 and p_2 represent the partial pressure of CO_2 and N_2, respectively.

3.4 Repeatability and reproductivity

The repeatability and reproductivity of prepared samples are very important parameters to show the reliability of the measurement methods and the preparation methods. Due to time constraints with facilities, only specific samples were selected for repetition to conduct error analysis.

3.4.1 Repeatability of measurements

Repeatability refers to the agreement degree between multiple measurements of the same sample, which indicates the precision and consistency of the measurement method. In this project, all the instruments were calibrated following the standard procedures before the characterization of prepared samples to avoid systematic errors. The elemental analysis of all the precursor materials and their derived hydrochar samples were repeated three times (Table 3.6), with the results including differences shown in Chapter 5 and Chapter 6. The textural properties and CO_2 adsorption performance of selected samples (CEPHC24-2-700) were repeated three times. As shown in Table 3.7, the maximum difference of BET surface area was only 5 m^2/g and total pore volume, micropore volume and ultra-micropore (<0.7 nm) volume gave a difference of 0.003, 0.002 and 0.008 cm^3/g, respectively. The CO_2 adsorption capacities of sample CEPHC24-2-700 under different conditions after three times measurements were listed in Table 3.8, which showed great consistency, with no difference overrun 0.029. The test results demonstrated that the measurement of samples was stable and reliable.

Table 3.6 The ultimate analysis of precursors and hydrochar samples

Sample	Batch	C	H	N
KL	1	62.58	5.36	0.46
	2	62.66	5.53	0.45
	3	62.41	5.52	0.44
OKL	1	60.42	3.35	0.57
	2	60.89	3.28	0.63
	3	60.55	3.31	0.59
EU	1	49.27	5.90	0.28
	2	49.24	5.92	0.31
	3	49.30	5.91	0.29
EUHC22	1	60.70	5.38	0.41
	2	60.82	5.24	0.43
	3	60.76	5.32	0.42
EUHC26	1	69.34	4.97	0.46
	2	69.59	5.02	0.50
	3	69.41	4.98	0.47
PVC	1	22.91	4.21	0.07
	2	22.99	4.38	0.05
	3	22.94	4.27	0.06
CE	1	42.68	6.25	0.18
	2	42.94	6.48	0.09
	3	42.76	6.39	0.12
PHC22	1	44.85	5.87	0.18
	2	45.15	6.14	0.18
	3	44.92	6.03	0.18
PHC24	1	66.57	6.36	0.20
	2	67.87	6.82	0.20
	3	67.34	6.45	0.20
PHC26	1	75.52	6.43	0.30
	2	75.82	6.57	0.26
	3	75.65	6.51	0.29
CEPHC22	1	54.09	6.04	0.41
	2	54.72	6.31	0.22
	3	54.57	6.29	0.27
CEPHC24	1	71.96	6.21	0.35
	2	71.70	6.30	0.31
	3	71.82	6.28	0.32
CEPHC26	1	75.52	6.44	0.26
	2	75.87	6.57	0.30
	3	75.72	6.48	0.29
KLPHC22	1	67.95	5.90	0.40
	2	67.47	6.18	0.44
	3	67.84	6.02	0.38
KLPHC24	1	71.08	5.71	0.44
	2	71.41	5.62	0.44
	3	71.22	5.65	0.44
KLPHC26	1	72.76	5.56	0.41
	2	72.14	5.35	0.47
	3	72.31	5.54	0.43

Table 3.7 Textural properties of sample CEPHC24-2-700 (repeated 3 times)

Test NO.	S_{BET} (m^2/g)	V_{total} (cm^3/g)	V_{micro} (cm^3/g)	$V_{micro<0.7nm}$ (cm^3/g)
1	885	0.360	0.320	0.285
2	875	0.366	0.317	0.270
3	877	0.362	0.317	0.277
	879± 5	0.363± 0.003	0.318± 0.002	0.277± 0.008

Table 3.8 CO_2 adsorption capacity of sample CEPHC24-2-700 (repeated 3 times)

Test NO.	CO_2 adsorption capacity (mmol/g)			
	0 °C		25 °C	
	15 kPa	100 kPa	15 kPa	100 kPa
1	2.82	5.44	1.69	3.93
2	2.87	5.43	1.70	3.90
3	2.87	5.44	1.70	3.92
	2.85± 0.029	5.44± 0.006	1.70± 0.006	3.92± 0.015

3.4.2 Reproductivity of samples

In addition to repeatability, reproductivity is an important parameter to assess the reliability and consistency of sample preparation methods. Two batches of the kraft lignin derived carbon OKLK-2-600 were prepared. As can be found in Table 3.9, the textural properties of both samples were similar, with the difference in surface area being only 51 m^2/g and the volume of total pore, micropore and ultra-micropore were nearly identical. In addition, three batches of different precursor materials derived carbons (KLK-1-600, EUHC22-1-600 and CEPHC24-) were prepared, with their CO_2 adsorption capacities at 25 °C and 15 kPa measured by TGA were presented in Table 3.10. The results gave a difference of 0.06, 0.06 and

0.05 for KLK-600, EUHC22-1-600 and CEPHC24-1-700, respectively. The results proved that the preparation method was reliable.

Table 3.9 Textural properties of sample OKLK-2-600

Sample	S_{BET} (m^2/g)	V_{total} (cm^3/g)	V_{micro} (cm^3/g)	$V_{micro<0.7nm}$ (cm^3/g)
Batch 1	957	0.399	0.352	0.264
Batch 2	1008	0.403	0.365	0.272

Table 3.10 CO_2 adsorption capacities of selected samples at 25 ^oC and 15 kPa by TGA

Sample	Batch 1	Batch 2	Batch 3	
KLK-1-600	2.17	2.12	2.05	2.06± 0.06
EUHC22-1-600	2.06	1.99	2.11	2.05± 0.06
CEPHC24-1-700	2.21	2.16	2.26	2.21± 0.05

Chapter 4

SYNTHESIS AND CHARACTERIZATION OF ADVANCED FUNCTIONAL BIO-CARBON MATERIALS FROM KRAFT LIGNIN WASTE WITH ENHANCED CO_2-ADSORPTIVE PROPERTIES

4.1 Introduction

To date, a variety of studies have established that activated carbons with high ultra-microporosity and modulated surface chemistries usually have enhanced affinity to CO_2 under typical operational conditions, with reported highest CO_2 uptakes being generally in the range of 1.8–2.0 mmol/g at 25 ^oC and 15 kPa (Liu et al., 2017, Deng et al., 2014, Liu et al., 2018). Activated carbons with high microporosity especially ultra-microporosity with pore diameters smaller than 0.5 nm have been demonstrated to be most favourable for CO_2 capture at ambient temperature and low CO_2 partial pressures (Presser et al., 2011, Sevilla et al., 2013). It was also found that the surface modification with basic nitrogen functionalities via either heat treatment with N-containing gases or co-carbonization of N-containing precursors can enhance the surface affinity of carbon materials to CO_2, with the latter being widely recognized as the more effective way to increase CO_2 uptake capacity (Zhao et al., 2018, Pang et al., 2021). However, the activated carbons in possession of either favourable ultra-microporosity and/or favourable surface chemistries are usually subjected to tedious and costly synthesis protocols involving the use of various chemical reagents and well-designed carbon precursors (Ashourirad et al., 2015, Liu et al., 2015, Wang et al., 2013). Therefore, the preparation of high-efficient CO_2-capturing carbon adsorbents should be ideally based on easily available, low-cost and renewable feedstock through relatively easy synthetic routes, which can help reduce not only the cost but also the carbon footprint of the materials manufacturing. Due to its fast-growing production, rich aromatic structure, and high carbon content, kraft lignin has received increasing attention to be the precursor for the production of activated carbon materials (Li et al., 2014, Correa et al., 2017b, Brazil et al., 2022). The following sections will describe the behaviour of kraft lignin in terms of its structure, origination and utilisation as a precursor of CO_2 sorbent material.

Lignin, in addition to cellulose and hemicellulose, is one of the three primary components of the lignocellulosic biomass, which constitutes 15-20% of the typical dry lignocellulosic biomass by weight (Azadi et al., 2013). Lignin is a complex three-dimensional amorphous macromolecule composed of phenylpropane derivates connected by carbon-carbon bonds and ether bonds (Andlar et al., 2018). As found in a typical lignocellulosic biomass, lignin fills the spaces between cellulose and hemicellulose, acting like concrete to crosslink the lignocellulose matrix together and reinforce the system. The biosynthesis of lignin typically involves the copolymerization of three primary monomers, i.e., p-coumaryl alcohol, coniferyl alcohol, and sinapyl alcohol by random phenol radical-radical coupling reactions (Zakzeski et al., 2010). Figure 4.1 represents the schematic depiction of lignin in lignocellulosic biomass and three monolignols of lignin.

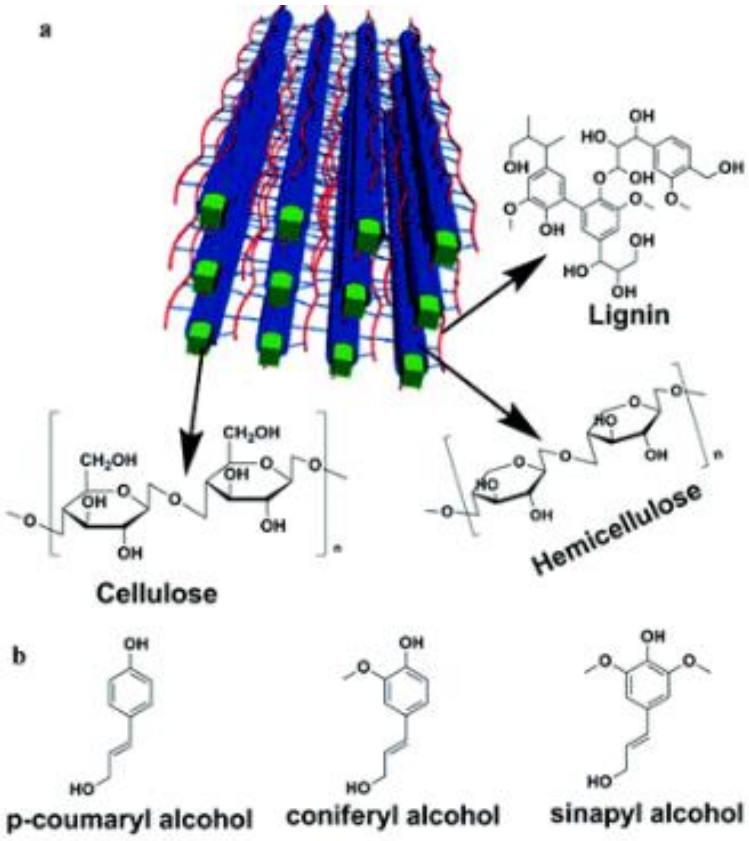


Figure 4.1 (a) Schematic depiction of the location and structure of lignin in the lignocellulosic biomass; (b) three primary monomers of the lignin (Zakzeski et al., 2010)

In terms of interunit bonding patterns, the most frequent coupling linkages are β-O-4-aryl ether bonds. Other major linkage patterns involve β-5 phenylcoumaran bonds, β–β′ pinoresinol, diphenyl ether 4-O-5′, and β-1′ diphenyl methane linkages, which are depicted in Figure 4.2. Although the proportions of these linkages may vary significantly in various woods and plants (Zakzeski et al., 2010). Compared to the polysaccharide components (e.g. cellulose and hemicelluloses) in the lignocellulosic biomass, lignin contains more aromatics, which brings many possibilities for its valorisation. Structural elucidation studies of lignin so far have indicated that 50% of its components are aromatic hydrocarbons (Xu et al., 2014a).

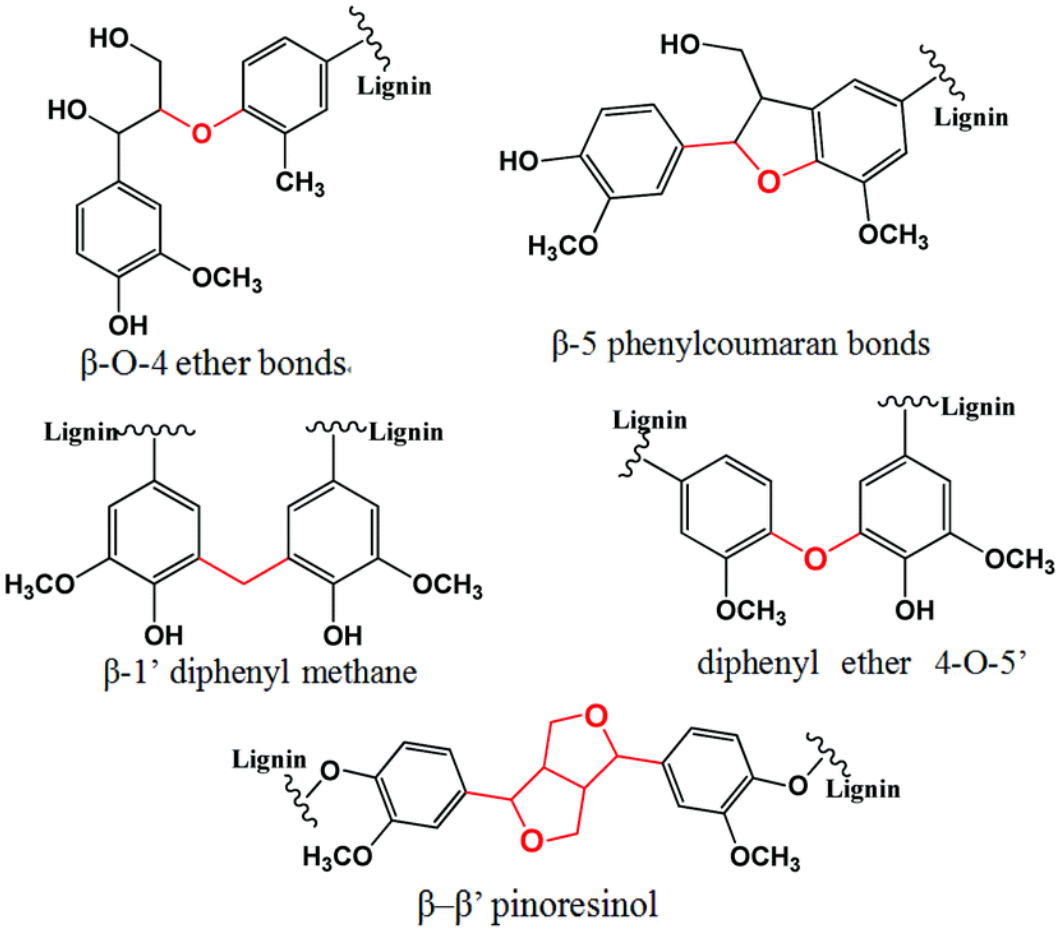


Figure 4.2 Five typical bonding patterns in lignin matrix structure (Zakzeski et al., 2010)

Approximately 100 million tons of lignin are produced per year mainly as industrial by-products of pulp and paper manufactories, which include lignosulfonate, kraft lignin (KL), soda lignin, hydrolysis lignin and organosolv lignin. Despite that lignosulfonate dominates the production of lignin, their applications are consolidated and limited to surfactants, bonding agents, dispersants, and concrete admixtures, with the market being forecasted to grow at only 1% CAGR (Dessbesell et al., 2020). As the second largest source of produced lignin, kraft lignin has great potential in terms of its valorisation shifting from low-price application (e.g. bioenergy generation) to high-value chemicals and materials market (Ľudmila et al., 2015). Li et al. prepared the activated carbons with a maximum surface area of 2763 m^2/g and pore volume of 1.32 cm^3/g by using kraft lignin wastes via a one-step mixing activation method (Li et al., 2014). Correa et al. produced kraft lignin-derived activated carbons via KOH activation, with the largest BET surface area of 2548 m^2/g obtained for carbon prepared with a char-to-KOH mass ratio of 1:4 at 600^oC for 2 h (Correa et al., 2017b). Recently, Brazil et al successfully developed activated carbons from kraft lignin impregnated with H_3PO_4 using microwave pyrolysis (Brazil et al., 2022). The results indicated that the highest acid: lignin weight ratio (4:1) favoured higher values of surface area (1055 m^2/g) and pore volume (0.76 cm^3/g). However, to the best of our knowledge, no investigation has ever been carried out to prepare alkali-intercalated ultramicroporous materials from using kraft lignin as the precursor for CO_2 adsorption. In this chapter, activated carbons using kraft lignin as a renewable and cost-effective carbon source precursor through a facile integrated one-step carbonization-activation route were prepared and evaluated in terms of their textural properties and CO_2 adsorption performance.

4.2 Results and discussion

4.2.1 Physicochemical properties of KL and OKL precursors

The physicochemical properties of KL and OKL are shown in Table 4.1. In terms of the proximate analysis results, the raw KL exhibited 58.60 wt % of VM and 35.28 wt % of FC. While the pre-oxidation treatment of KL gave rise to an increase in the FC (45.00 wt %) and a decrease in the VM (49.83 wt %) of OKL.

Table 4.1 Physicochemical properties of KL and OKL precursors

Precursor	Proximate analysis (wt %)				Ultimate analysis (wt %, dry basis)			
	Moist.	Fixed carbon	Volatile matter	Ash	C	H	N	O(diff.)
KL	3.29	35.28	58.60	2.31	62.55± 0.13	5.28± 0.10	0.45± 0.01	29.41± 0.15
OKL	2.72	45.00	49.83	2.45	60.67± 0.21	3.30± 0.05	0.60± 0.03	32.98± 0.06

The thermal decomposition characteristics of KL with/without pre-oxidation treatment were characterized by using thermogravimetric analysis (TGA) and the results are shown in Figure 4.3. It was found that the thermal decomposition of KL and OKL occurred over a broad temperature range from approximately 150 ^{o}C to 900 ^{o}C, which can be divided into two stages: the release of volatiles between 150-450 ^{o}C and the decomposition and condensation of aromatic rings above 450 ^{o}C. This is consistent with the pyrolysis of Lignoboost® lignin and alkali lignin reported in previous studies (Brebu et al., 2013, Ma et al., 2016). The solid residue from the pyrolysis of KL was 37.6 wt %. In contrast, pre-oxidation treatment of KL resulted in an increase of solid product yield to 47.5 wt % at 900 ^{o}C. Given the 9.6 wt % weight loss of KL during pre-oxidation, the overall carbon yield is about 43.0 wt %, which is 15% higher than the yield obtained from the direct carbonization of the

raw KL. Accordingly, as shown in Table 4.2, generally higher carbon yields were obtained for activated carbons prepared with pre-oxidation treatment under the same activation conditions.

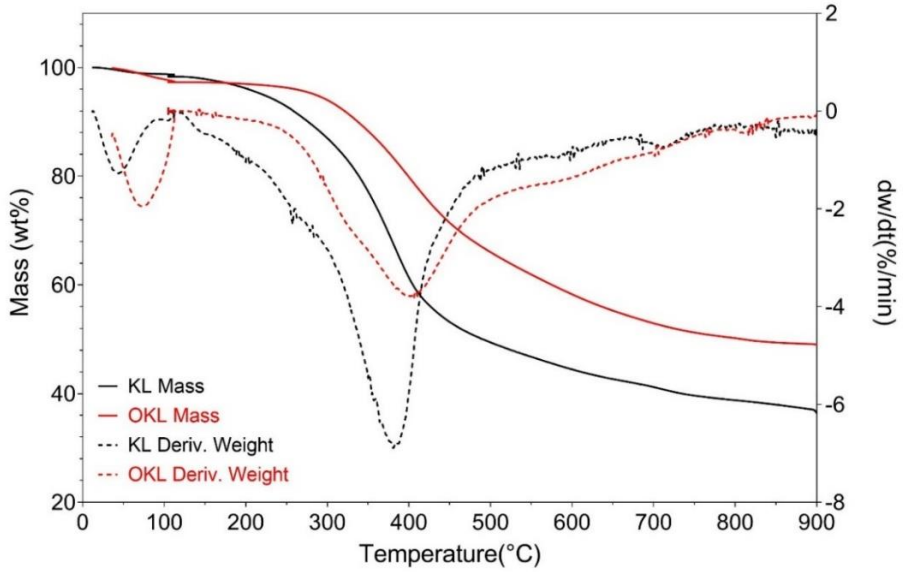


Figure 4.3 Thermal decomposition behaviour of KL and OKL precursors

Table 4.2 Carbon yield of KLK and OKLK carbons prepared in different integrated carbonization-activation conditions

Sample	Carbon yield (wt.%)
KLK-1-600	55.2
KLK-1-700	48.5
KLK-1-800	33.7
KLK-2-600	47.6
KLK-2-700	42.6
KLK-2-800	31.6
OKLK-1-600	57.6
OKLK-1-700	44.4
OKLK-1-800	38.3
OKLK-2-600	48.7
OKLK-2-700	43.4

The ultimate analysis results show that the KL contains 62.55% carbon, 5.28% hydrogen, 29.41% oxygen (diff.) and 0.45% nitrogen, whereas OKL possesses 60.67% carbon, 3.30% hydrogen, 32.98% oxygen (diff.) and 0.60% nitrogen. Figure 4.4 shows Fourier transform infrared spectroscopy (FTIR) spectra for the KL and OKL precursors and their derived activated carbons. It is evident that the pre-oxidation treatment resulted in a significant decrease in the abundance of -OH groups of alcoholic, phenolic hydroxyl and methyl units in the lignin, as can be seen from the decrease in peak intensities of -OH stretching (3351 cm^{-1}) and C-H stretching (2935 cm^{-1}). Other noticeable differences due to pre-oxidation treatment include the drastically reduced intensity of the peaks at 1512 cm^{-1}, 1265 cm^{-1}, and 1126 cm^{-1}, which are attributable to the conversion of monomeric aromatic, syringyl and guaiacyl ring structures, respectively. The results indicated that the condensation reactions of the aromatic structures and the oxidation of alkyl groups lead to the formation of carbonyl and carboxyl structures during the pre-oxidation process of KL. The FTIR results were also found to be consistent with the significantly higher oxygen content (32.98 wt %) obtained for the OKL precursor than for the KL (29.41 wt %) as mentioned above. In terms of the KL-derived corresponding activated carbons, the FTIR spectra shows that the presence of the C–OH, C–O, C=O, and alkyl groups in the carbons were all reduced or eliminated due to the thermo-chemical reactions during the carbonization/activation process, which involves the decomposition of carbonyl and carboxyl structures during the reactions of the carbon with KOH/K_2O and cogenerated water (steam).

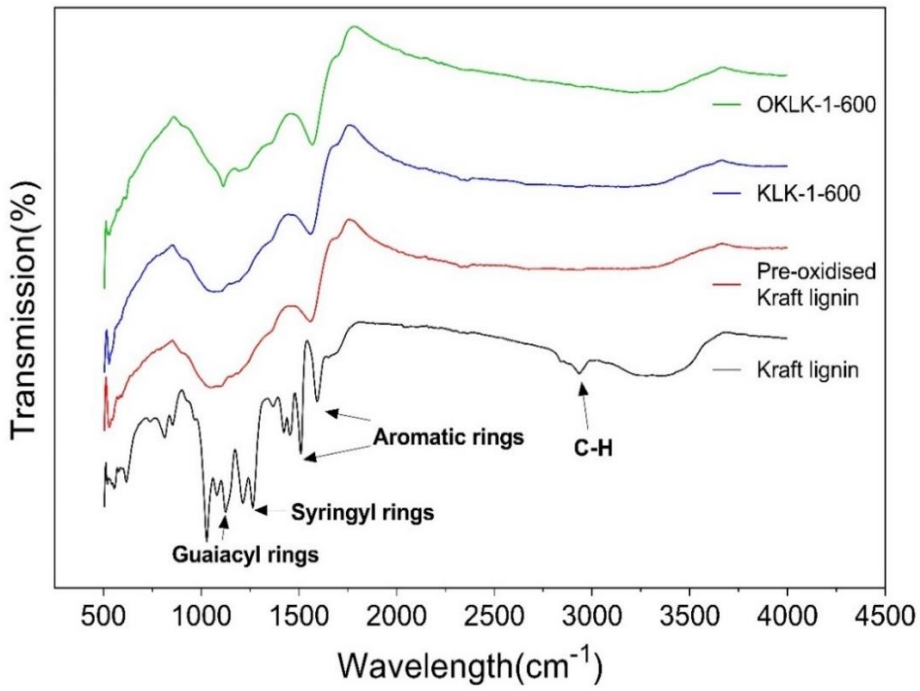


Figure 4.4 FT-IR spectra of KL, OKL, KLK-1–600 and OKLK-1–600

4.2.2 Textural properties of kraft lignin-derived carbons

The N_2 isotherms of the KL- and OKL-derived carbons prepared at different activation temperatures ranging from 600 to 800 ^oC and with KOH/KL ratios varying from 1 to 2 by mass were presented in Figure 4.5. The isotherms show that all the prepared activated carbons possess a steep and large N_2 uptake at relative pressures of well below 0.1, with the highest N_2 adsorption capacity of KLK-2–800 being 23 mmol/g, indicating the extraordinary prevalence of micro or ultra-microporosity of the carbon materials. It can be found that the activated carbons prepared with the lower KOH/KL mass ratio of 1 all showed type IV adsorption isotherms characterised by the presence of hysteresis loops in relatively higher pressure regions according to the IUPAC classification, which indicates the development of ink bottle-shaped mesoporous structures that increased with increasing carbonization/activation temperatures used (Figure 4.5(a,c)) (Thommes et al., 2015). In sharp contrast, as shown in Figure 4.5(b,d), the carbons prepared from using the higher KOH/KL ratio of 2:1 by mass were

found to exhibit type I N_2 adsorption isotherms with sharp and large N_2 uptake at relative pressures below 0.1, followed by a horizontal plateau at high relative pressures, which suggests the prominent ultra-microporous nature of the carbon materials. The disappearance of the hysteresis loop with increasing KOH/KL ratio implies the collapse of mesoporous structures due to the increased severity of KOH activation (Li et al., 2017c, Cuong et al., 2019).

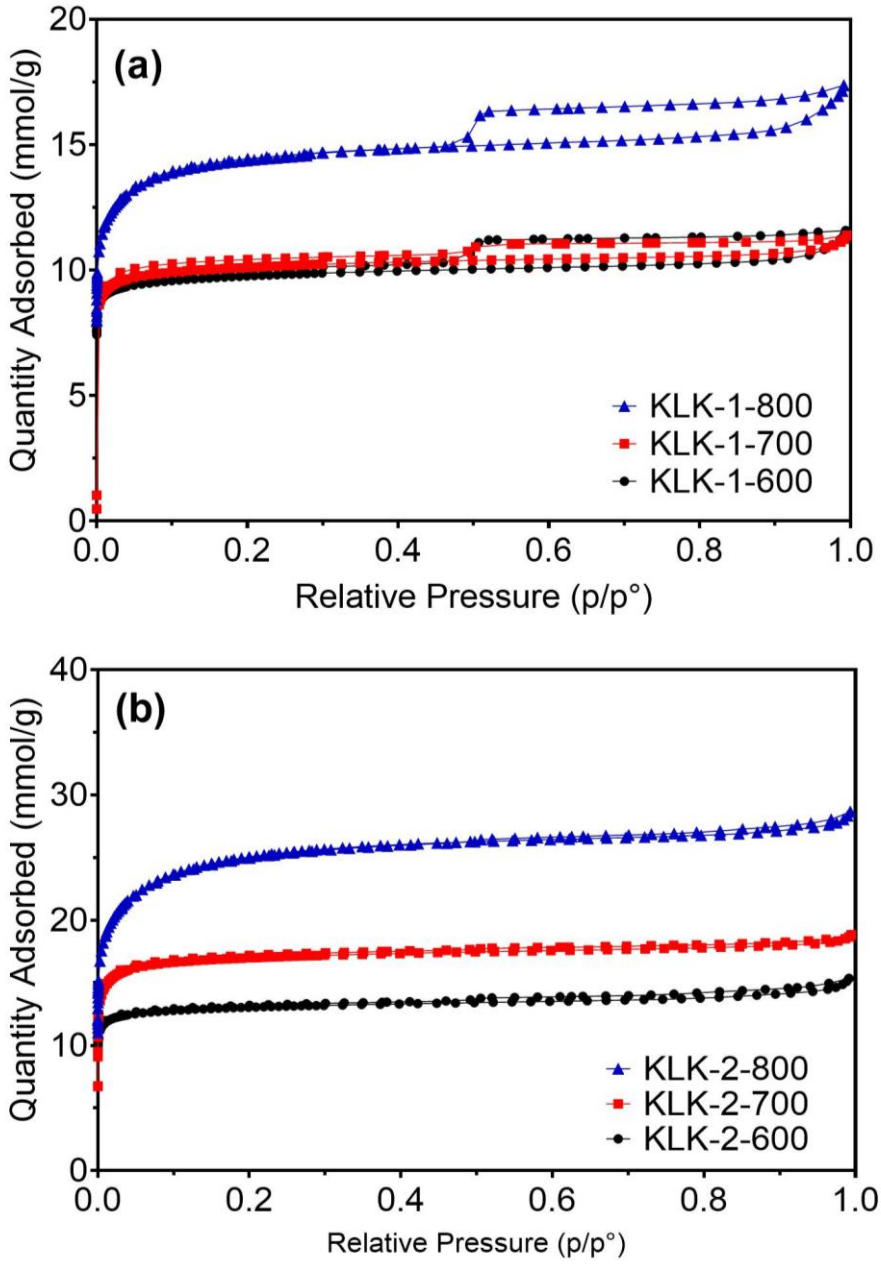


Figure 4.5 N_2 adsorption isotherms obtained at -196 ^oC for KLK carbons (a) (b) and OKLK carbons (c) (d).

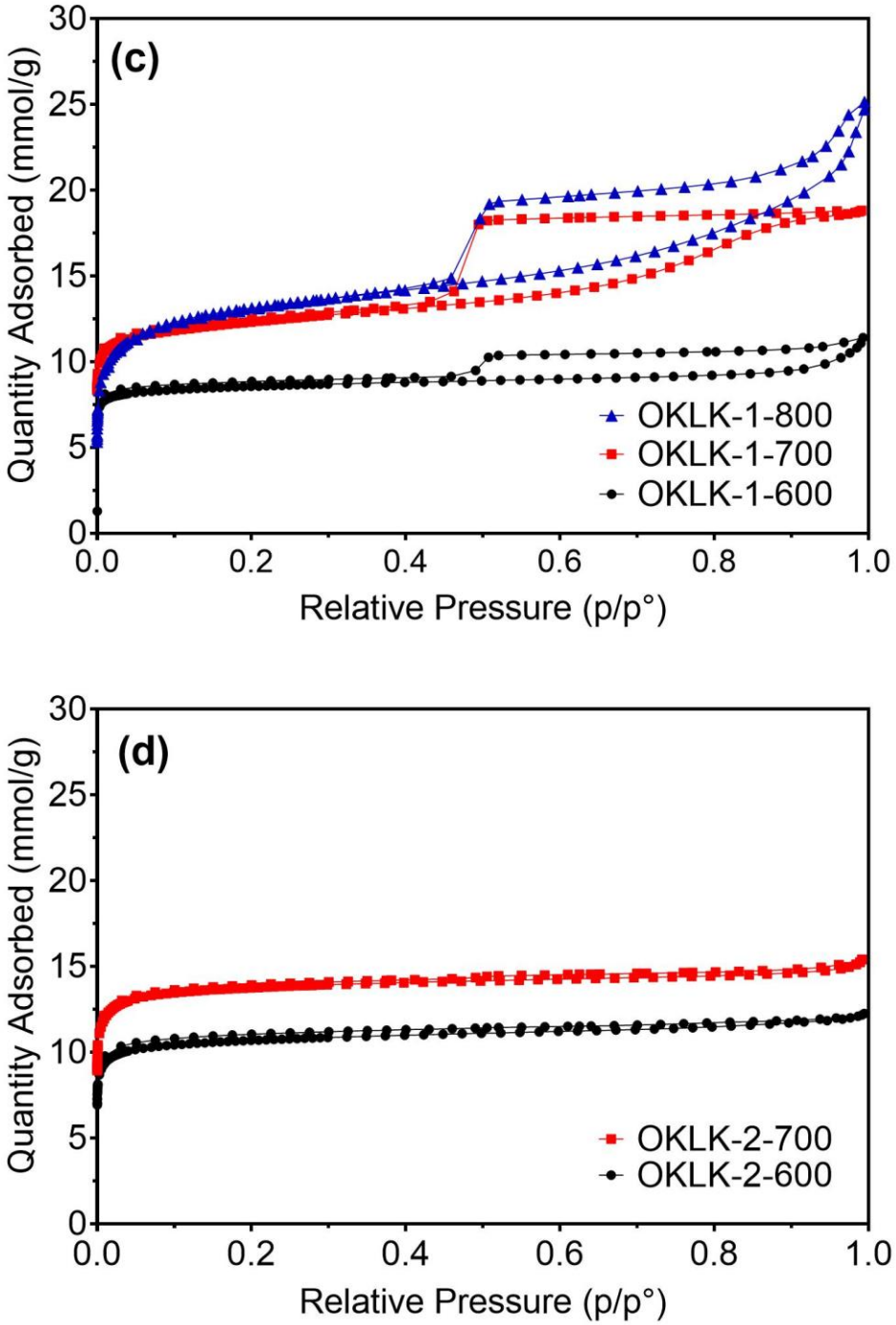


Figure 4.5 N_2 adsorption isotherms obtained at -196 ºC for KLK carbons (a) (b) and OKLK carbons (c) (d)

The overall textural properties of all the prepared carbon samples are given in Table 4.3. It is evident that the textural properties of the prepared activated carbons were affected by the activation temperature, KOH/KL mass ratio and the pre-oxidation treatment. At a given KOH/KL mass ratio of 1, the BET surface area and total pore volume of the KLK carbons increased substantially from 878 m^2/g and 0.372 cm^3/g to 1255 m^2/g and 0.554 cm^3/g, respectively, as the temperature for the integrated carbonization/activation increased from 600^o to 800 ^oC. Additionally, a large increase in BET surface area and pore volume with increasing KOH/KL ratios was also observed for KL–derived carbons at a given activation temperature. It is found that for the KLK carbons, an increase in KOH/KL ratio from 1 to 2 at a carbonization/activation temperature of 800 ^oC gave rise to a 70% increase in BET surface area from 1255 to 2121 m^2/g, while the total pore volume was increased by 63% from 0.554 to 0.903 cm^3/g. A similar trend was observed for the OKLK carbons, while the OKLK carbons were found to have overall lower surface areas compared to the KLK carbons prepared under similar conditions, with the highest surface area of 1240 m^2/g obtained for the OKL–derived carbon (OKLK–2–700) prepared at 700 ^oC with a KOH/KL ratio of 2, which is significantly lower than the 1528 m^2/g obtained for the pristine KL–derived carbon (KLK–2–700). It is also noticed that the total pore volume of OKLK carbons is generally lower than that of KLK carbons prepared under similar conditions except for OKLK–1–700 and OKLK–1–800 which possess higher total pore volumes of 0.618 and 0.785 cm^3/g compared to 0.364 and 0.554 cm^3/g for KLK–1–700 and KLK–1–800, indicating the impact of pre-oxidation treatment.

Table 4.3 Surface textural properties of Kraft lignin-derived carbons

Sample	S_{BET}, m^2/g	V_{total}, cm^3/g	V_{micro}, cm^3/g	$V_{micro<0.7\ nm}$, cm^3/g	V_{micro}/V_{total}	$V_{micro<0.7nm}/V_{micro}$
KLK-1-600	878	0.372	0.320	0.278	86%	87%
KLK-1-700	916	0.364	0.331	0.303	91%	92%
KLK-1-800	1255	0.554	0.466	0.275	84%	59%
KLK-2-600	1180	0.494	0.428	0.354	87%	83%
KLK-2-700	1528	0.598	0.557	0.377	93%	68%
KLK-2-800	2121	0.903	0.792	0.347	88%	44%
OKLK-1-600	770	0.366	0.279	0.238	76%	85%
OKLK-1-700	1073	0.618	0.366	0.277	59%	76%
OKLK-1-800	1109	0.785	0.397	0.195	51%	49%
OKLK-2-600	957	0.399	0.352	0.264	88%	75%
OKLK-2-700	1240	0.492	0.450	0.322	91%	72%

Figure 4.7 shows the pore size distribution calculated by using a non-local density functional theory (NLDFT) model by a combinative analysis of N_2 and CO_2 adsorption isotherms for KLK and OKLK carbons. It can be seen that the microporous structures of all prepared carbon excluding OKLK–1–700 and OKLK–1–800 carbons are extremely dominated by the ultra-micropores with pore diameters centred at 0.37 nm, 0.53 nm and 1.1 nm, with the relative significance of the ultra-microporosity affected by the activation temperature and/or the KOH/KL ratios used. As shown in Figure 4.7 and Table 4.3, an increase in KOH/KL mass ratio and/or activation temperature led to decreased volumes of the 0.37 nm pores and increased volumes of the larger pores of 0.53 and 1.1 nm. Particularly important for gas separation applications, it is noteworthy that all the KLK carbons are predominantly microporous with micropore volume accounting for up to 93%

of total pore volume. More specifically, higher microporosity was observed for KLK carbons especially those prepared with higher KOH/KL ratios of 2 whereas KLK carbons with lower KOH/KL ratio of 1 possessed higher ultra-microporosity with up to 92% of the microporosity composed of ultra-micropores with diameters smaller than 0.7 nm. In comparison, however, the OKLK carbons prepared at the low KOH/KL ratio of 1 were found significantly more mesoporous, with mesoporosity accounting for up to 50% of the total porosity. This pore widening effect observed for the OKLK carbons is highly suggestive of a combinative effect of the etching effect of pre-oxidation on the inner structure of the KL precursor and the decomposition of the formed oxygen-bearing functional groups (e.g. ketones, phenols and possibly carboxylic acids) during the integrated carbonization and KOH activation process (Shang et al., 2018, Liu et al., 2015b).

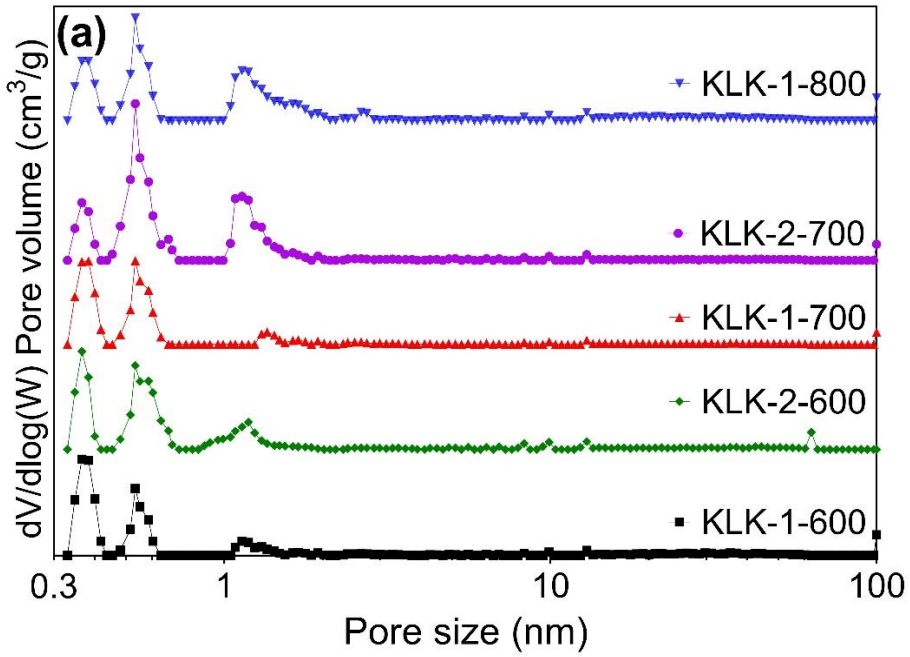


Figure 4.6 NLDFT pore size distributions for KLK carbons (a) and OKLK carbons (b)

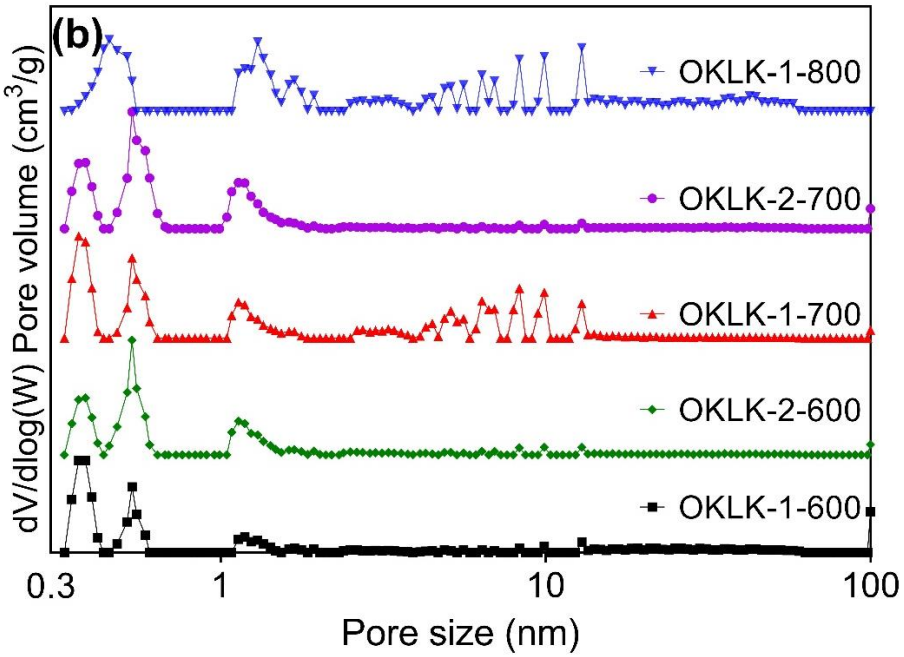


Figure 4.7 NLDFT pore size distributions for KLK carbons (a) and OKLK carbons (b)

4.2.3 Morphology of kraft lignin-derived carbons

Figure 4.8 elucidates the morphology of the KLK and OKLK carbons revealed by FEG-SEM. The images show that all the carbon samples exhibit highly porous textures in the carbon matrix with widely distributed irregular but inter-connected cavities. As the activation temperature was increased from 600 to 700 ^{o}C, the macro-structures of both KLK and OKLK carbons became notably widened with apparent cracks created due to the more severe carbon-consuming activities. However, compared to the KLK carbon (Figure 4.8 (a, b, e, f)), the OKLK carbons prepared under the same activation conditions appeared to have a less rigid and more amorphous macrotexture (Figure 4.8 (c, d, g, h)). This phenomenon is presumably due to the pre-oxidation treatment that prevented the thermal cross-linking of the lignin during the carbonization process from forming a rigid three-dimensional carbon network (Leng et al., 2021).

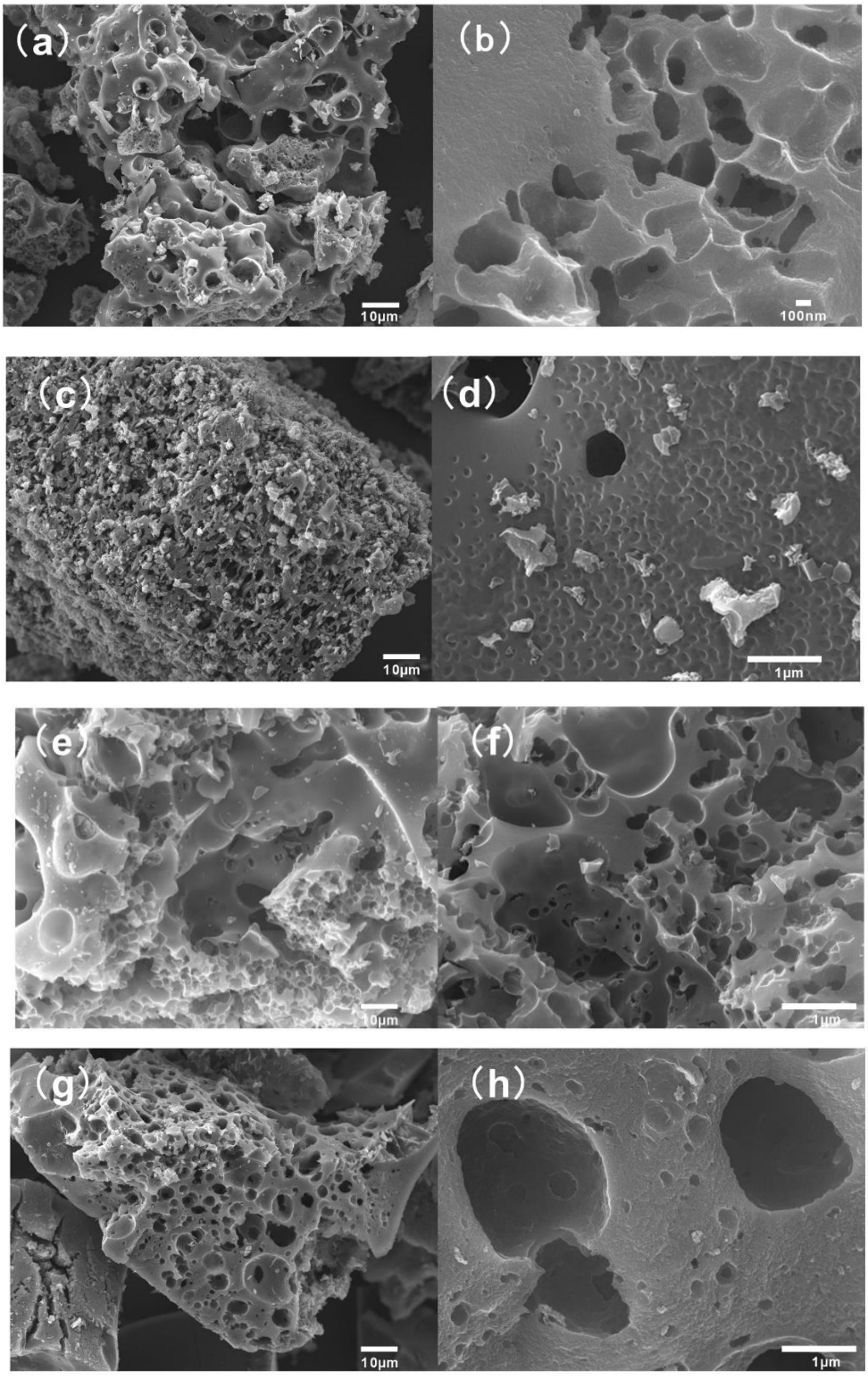


Figure 4.8 SEM images of carbon samples: KLK–1–600 (a, b), OKLK–1–600 (c,d), KLK–1–700 (e, f) and OKLK–1–700 (g, h)

4.2.4 CO_2 adsorption properties of kraft lignin-derived carbons

The prepared activated carbons were evaluated for their performance in CO_2 adsorption at different relative CO_2 pressures. Figure 4.9 presents the CO_2 adsorption isotherms of KLK and OKLK carbons at 0 and 25 ^oC, while Table 4.4 shows the CO_2 uptake capacity at selected CO_2 partial pressures.

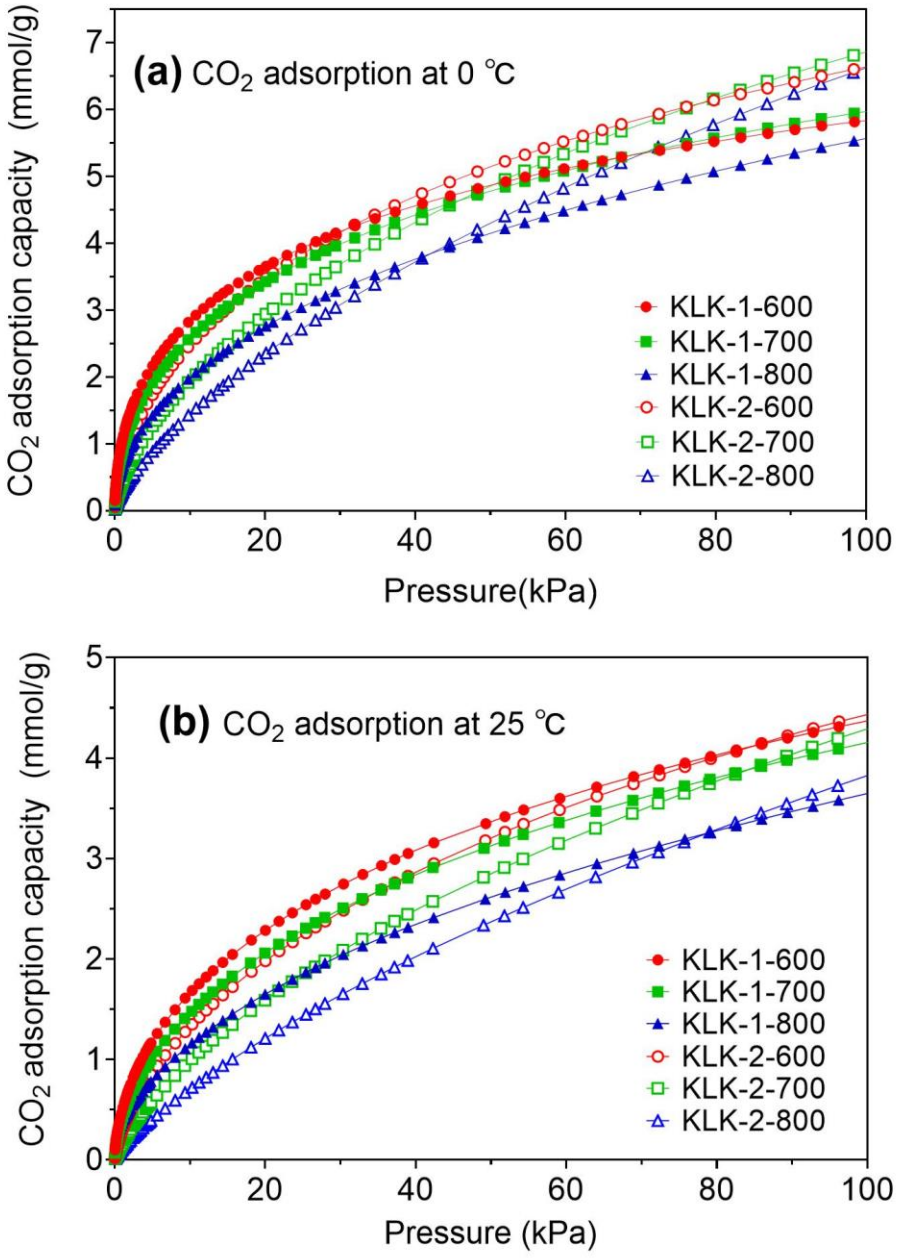


Figure 4.8 CO_2 adsorption isotherms for KLK carbons at (a) 0 ^oC (b) 25 ^oC and OKLK carbons at (c) 0 ^oC (d) 25 ^oC

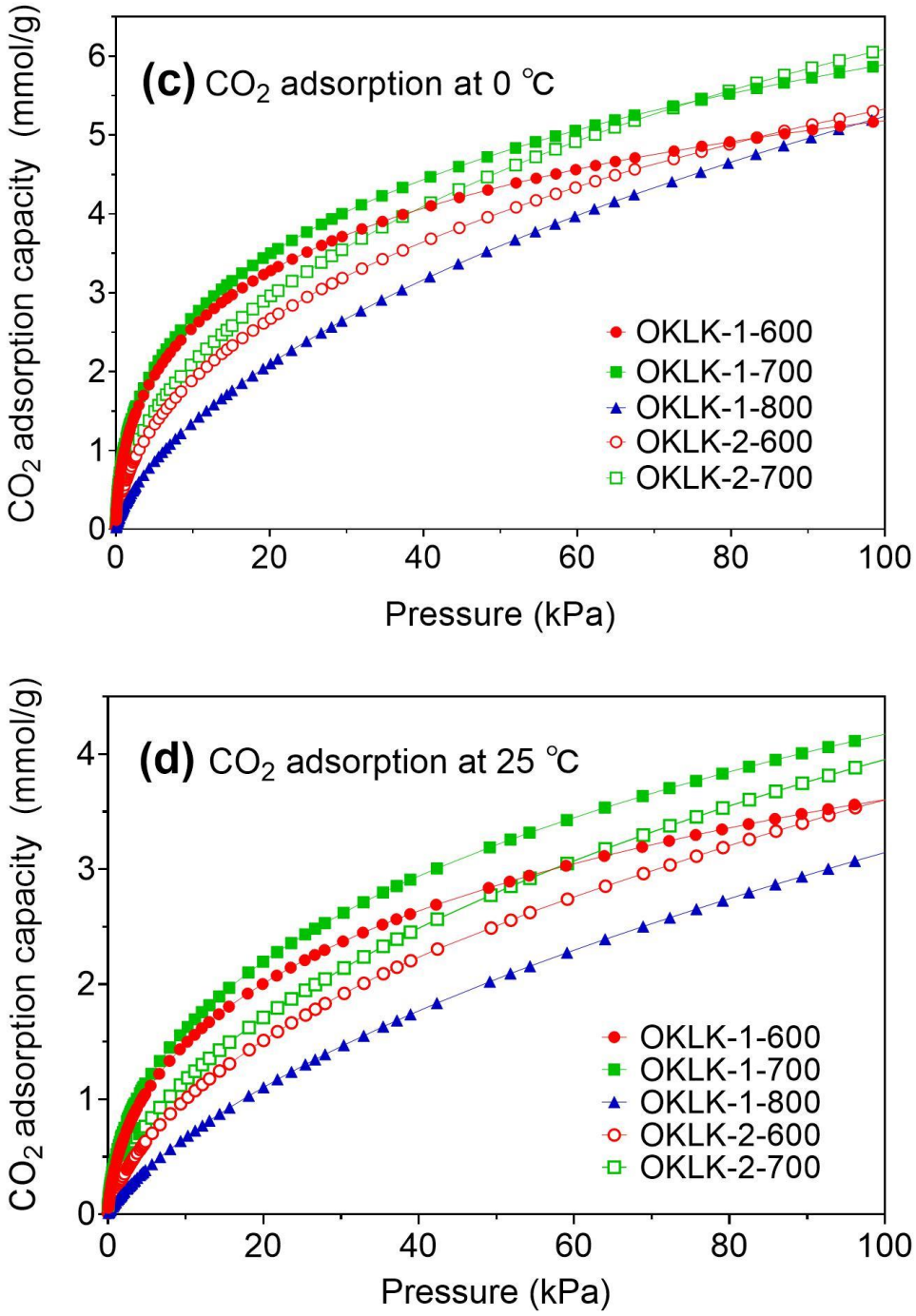


Figure 4.9 CO_2 adsorption isotherms for KLK carbons at (a) 0 ºC (b) 25 ºC and OKLK carbons at (c) 0 ºC (d) 25 ºC

Table 4.4 CO_2 uptake capacities of KLK and OKLK carbons at different partial pressures and adsorption temperatures

Sample	CO_2 uptake capacity, mmol-CO_2/g-ads			
	0 ^oC		25 ^oC	
	15 kPa	100 kPa	15 kPa	100 kPa
KLK-1-600	3.29	5.84	2.01	4.34
KLK-1-700	3.05	5.95	1.79	4.16
KLK-1-800	2.41	5.55	1.42	3.61
KLK-2-600	3.03	6.63	1.68	4.43
KLK-2-700	2.48	6.86	1.31	4.30
KLK-2-800	1.92	6.62	0.97	3.82
OKLK-1-600	2.97	5.17	1.78	3.61
OKLK-1-700	3.15	5.85	1.93	4.17
OKLK-1-800	1.75	5.24	0.90	3.15
OKLK-2-600	2.32	5.34	1.27	3.56
OKLK-2-700	2.57	6.09	1.46	3.95

It was found that all the prepared kraft lignin-derived carbon materials showed superior CO_2 adsorption performance despite the facile preparation methodologies. At a CO_2 partial pressure of 15 kPa, the best-performing carbon (KLK–1–600) was found to be capable of achieving exceedingly high CO_2 uptake capacities of 3.29 mmol/g at 0 ^oC and 2.01 mmol/g at 25 ^oC. Whereas, at 100 kPa CO_2, the CO_2 adsorption capacity reached 6.86 mmol/g at 0 ^oC and 4.30 mmol/g at 25 ^oC (KLK–2–700), respectively. An examination of the literature reveals that particularly at

low CO_2 partial pressures, the CO_2 adsorption performance of the carbons derived from kraft lignin was along the highest ever reported for carbons prepared from using other biomass feedstock (Figure 4.10) (Ello et al., 2013a, Serafin et al., 2019, Saha et al., 2017, Pramanik et al., 2021, Kim et al., 2020b, Deng et al., 2015, Wei et al., 2012, Tian et al., 2018, Rao et al., 2019, Serafin et al., 2017, Yang et al., 2020, Zhang et al., 2016a).

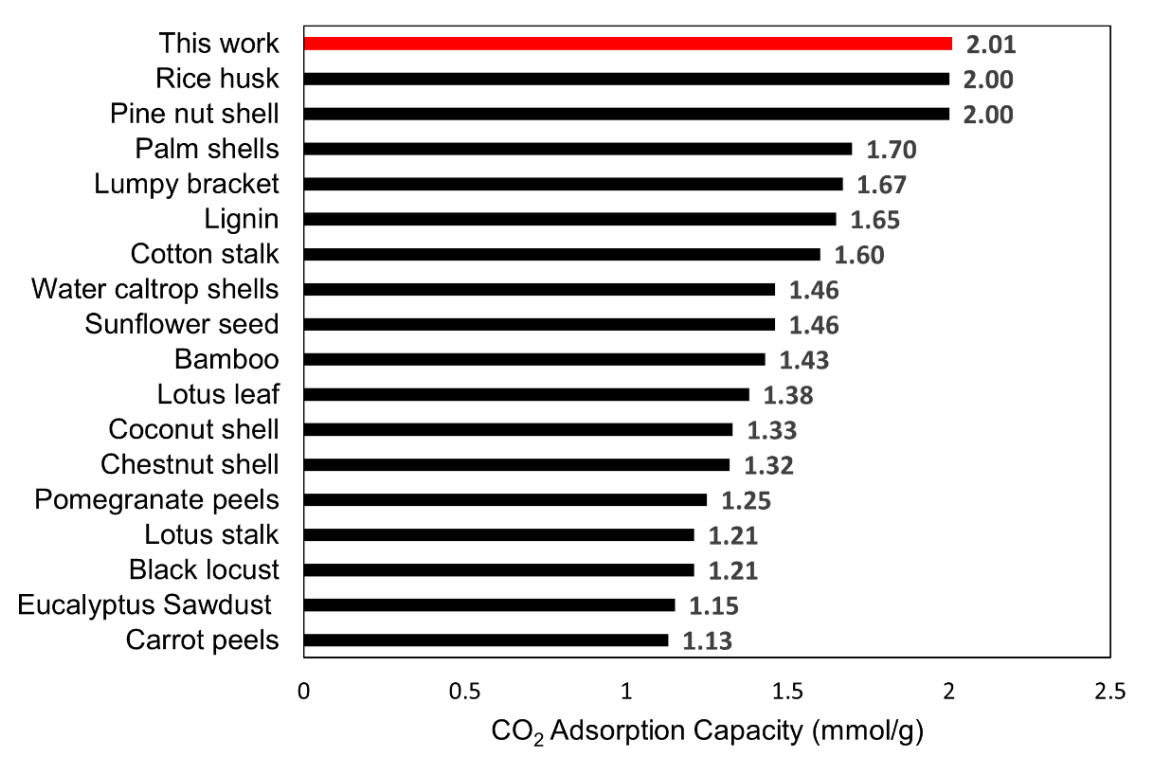


Figure 4.10 CO_2 adsorption capacity of the Kraft lignin-derived carbons against other biomass-derived carbons at 25 ^oC and 15 kPa

As shown in Figure 4.9 and Table 4.4, the CO_2 uptake of the activated carbons varied remarkably with the carbonization/activation conditions. In general, it appears that an increase in KOH/KL ratio and/or carbonization/activation temperature led to decreased CO_2 capacity and adsorption rate at low CO_2 partial pressures. It was found in Figure 4.9 (a, b) that in terms of KLK carbons, KLK–1–600 prepared under the mildest conditions possesses the highest CO_2 capacity at

15 kPa CO_2 among all the carbons, which reached 3.29 mmol/g at 0 ^oC and 2.01 mmol/g at 25 ^oC, respectively. As the activation temperature was increased from 600^o to 800 ^oC for KOH/KL ratio 1:1 by mass, the CO_2 capacity of KLK carbons at 15 kPa CO_2 was decreased by 25% from 3.29 to 2.41 mmol/g at 0 ^oC, and by 30% from 2.01 to 1.42 mmol/g at 25 ^oC, respectively. Similar decreases in CO_2 capacity at low CO_2 pressure were also observed with increasing KOH/KL ratio used at a given activation temperature. For instance, at the given activation temperature of 700 ^oC, an increase in KOH/KL ratio from 1 to 2 led to ca. 20% decrease in CO_2 capacity at 0 ^oC, from 3.05 (KLK–1–700) to 2.48 mmol/g (KLK–2–700), and ca. 35% decrease from 1.79 to 1.31 mmol/g at 25 ^oC, respectively. The results indicate that an increase in activation temperature and/or KOH/KL ratio always leads to a disproportionately larger decrease in CO_2 capacity at higher adsorption temperatures. Correspondingly, it was foreseeable that the carbons prepared at 800 ^oC and a KOH/KL ratio of 2 were found to have much lower CO_2 adsorption capacities at low CO_2 partial pressures, with the carbon KLK–2–800 showing the lowest capacity at 15 kPa CO_2 despite its highest surface area and pore volume as shown in Table 4.3. On the other hand, it appears that an increase in the amount of KOH used in activation favours CO_2 uptake at higher CO_2 partial pressures for the KLK carbons. At a CO_2 partial pressure of 100 kPa, the KLK–2–700 carbon was found to give the highest rarely obtainable CO_2 capacity of 6.86 mmol/g at 0 ^oC. Whereas, at the higher adsorption temperature of 25 ^oC, KLK–2–600 was instead found to have the highest capacity of 4.43 mmol/g. This suggests that the KLK carbons prepared at lower activation temperatures have higher strength of interaction between CO_2 molecules and the adsorption sites, compared to the carbons prepared at higher carbonization/activation temperatures.

Figure 4.9 (c, d) shows the CO_2 adsorption isotherms measured at 0 and 25 ^oC for the OKLK carbons. The variation of CO_2 adsorption of the carbon materials with activation temperatures and KOH/KL ratio was overall found to follow the same trends as those observed for the KLK carbons. However, the results reveal that the carbons derived from the pre-oxidised KL generally exhibited considerably

lower CO_2 capacities than the carbons prepared from using the non-preoxidised KL under the same adsorption conditions. Among all the OKLK carbons, the OKLK–1–700 carbon achieved the highest capacity of 3.15 at 0 ^oC and 1.93 mmol/g at 25 ^oC in 15 KPa CO_2, respectively, being similar to those obtained for the KLK–1–600 carbon under the same adsorption conditions, as shown in Figure 4.9 (a, b). In general, the measurements of CO_2 adsorption isotherms at different adsorption temperatures demonstrate that mild activation conditions, which are typically characterised by using low activation temperature (600 ^oC) with a low KOH/KL ratio (≤2), particularly favour CO_2 adsorption of the carbons at low CO_2 partial pressures. In contrast, the use of relatively higher activation temperatures and/or KOH/KL ratios favours CO_2 adsorption of the Kraft lignin-derived carbons at high CO_2 partial pressures. Taken with the textural properties as shown in Table 4.3 and Figure 4.5, the CO_2 adsorption characteristics also indicate that the CO_2 adsorption at low partial pressures appears to be predominantly dependent on the abundance of ultra-micropores, compared to CO_2 adsorption at higher partial pressures where the total micropore volumes appeared to be more important in determining CO_2 capacity. The rarely obtainable high CO_2 uptake capacity at low partial pressures suggests that the combined carbonization-activation scheme is particularly beneficial to the development of ultra-microporosity, compared to conventional preparation methodologies where carbonization and activation are performed separately.

Figure 4.11 shows the CO_2 adsorption profile and the cyclic adsorption/desorption performance obtained from TGA at 25 ^oC in simulated flue gas containing 15% CO_2 in N_2. It can be found that the best-performing KLK–1–600 carbon achieved an exceedingly high equilibrium capacity of 2.21 mmol-CO_2/g or 9.72 wt % at 25 ^oC and 15 kPa CO_2, which appears higher CO_2 uptake capacity than BET results due to dynamic TGA condition with the constant CO_2 partial pressures. It is also evident that the carbon showed a fast adsorption rate, with 90% of CO_2 equilibrium capacity completed in less than 3 min. Besides, the CO_2 adsorption was found to

be fully reversible and no obvious changes in CO_2 capacity were observed during the 50 cycles of continuous adsorption-desorption tests.

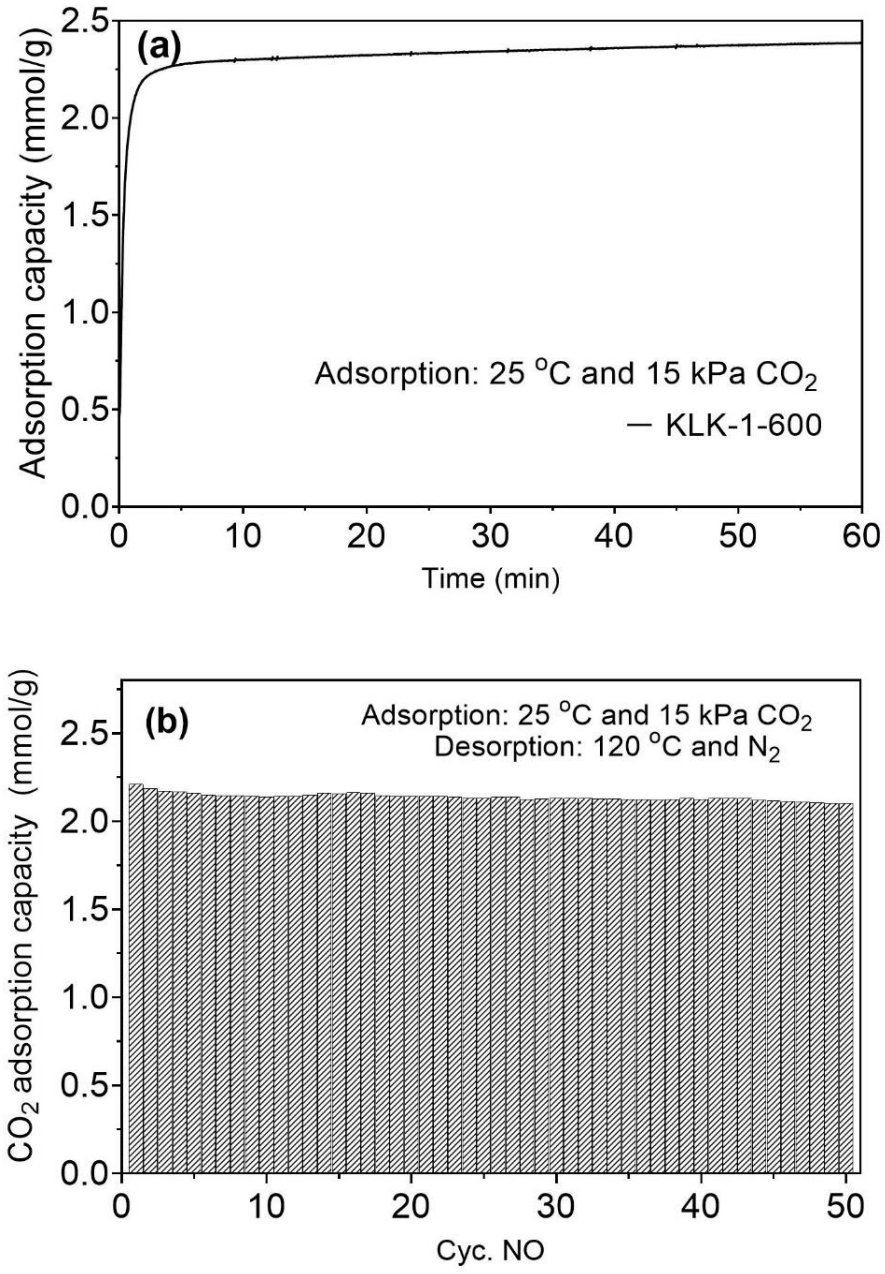


Figure 4.11 Dynamic CO_2 adsorption curve (a) and cyclic adsorption/desorption performance (b) of KLK–1–600 under simulated flue gas conditions containing 15% CO_2 in N_2. Adsorption temperature: 25 °C; Desorption temperature: 120 °C

4.2.5 Role of textural properties and surface chemistry in CO_2 adsorption

It is generally believed that both textural and surface chemical properties control the CO_2 adsorption of carbon materials, and numerous efforts have been dedicated to combine one or two together to bolster CO_2 capacity, particularly at low CO_2 partial pressures, although the significance of the role of surface chemistry remains a matter of debate (Sethia and Sayari, 2015, Pardakhti et al., 2019, Fujiki and Yogo, 2016, Seema et al., 2014). To date, most of the reported activated carbons for CO_2 capture involve nitrogen doping via either the use of N-containing carbon precursors or post-synthetic amination treatment to enhance CO_2 adsorption through mechanisms of acid-base interaction, quadrupolar interaction or hydrogen bonding interactions (Patel et al., 2013, Vaidhyanathan et al., 2010, Xing et al., 2012). For instance, Sethia and Sayari have developed nitrogen-rich (29.7 wt %) super adsorbent carbons and found that the best performing N-rich (22.3 wt %) carbon achieved an extraordinary capacity of 5.39 mmol/g at 25 ^oC and 100 kPa CO_2, but the CO_2 uptake was sharply reduced to ca. 1.7 mmol/g when adsorption took place in 15 kPa CO_2 at 25 ^oC (Sethia and Sayari, 2015). Langmuir modelling confirmed the importance of surface modification with nitrogen, notwithstanding the predominant role of ultra-microporosity. Similar findings are also obtained for other N-doped and sulphur-doped carbons, with CO_2 capacities being generally well below 1.7 mmol/g at 15 kPa CO_2 and 25 ^oC despite their high capacities (4.5 ~ 4.9 mmol/g) at 100 kPa CO_2 (Pardakhti et al., 2019, Fujiki and Yogo, 2016, Seema et al., 2014).

Despite the synthetic simplicity and no N-doping involved, it is evident that the kraft lignin-based carbons significantly outperform the reported ‘designer’ carbons and other biomass-derived carbons for CO_2 capture at low CO_2 partial pressures (Figure 4.10). This inspires us to further explore the relative role of the textural and chemical properties in CO_2 adsorption. Correlation attempts revealed that the CO_2 adsorption capacity of the lignin-based carbons was closely linked to the volume of narrow micropores smaller than 1 nm, whereas no clear relationship was obtained with the volume of larger pores (Figure 4.12). Particularly at a CO_2 partial

pressure of 15 kPa, the CO_2 adsorption at 0 ^oC showed the best linear relationship with the volume of narrow micropores smaller than 0.48 nm, (Figure 4.12a), while the pore size giving rise to the best correlation decreased to 0.44 nm when the adsorption took place at higher adsorption temperature of 25 ^oC, as shown in Figure 4.12b. The correlation coefficients (R^2) reached 0.96 for adsorption at 0 ^oC and 0.97 at 25 ^oC, respectively. At 100 kPa CO_2, the pore size best correlated to the CO_2 uptake was increased to 0.55 nm at 25 ^oC (R^2 = 0.80) and further to 1 nm when the adsorption took place at 0 ^oC (R^2 = 0.92), respectively, as shown in Figure 4.12(c, d). The above correlation results confirm the existence of critical pore sizes corresponding to CO_2 uptake by pore filling mechanism in activated carbons at different temperatures and partial pressures. While the findings agree well in general with previous investigations by Zhang et al and others, which found that CO_2 adsorption in ultra-micropores (≤0.7 nm) occurs via pore filling mechanism and the micropores with diameters smaller than 0.7 and 0.8 nm are mainly responsible for the high CO_2 uptake at 25 and 0 ^oC, respectively (Liu et al., 2017, Sethia and Sayari, 2015, Hu et al., 2011, Sevilla and Fuertes, 2011, Deng et al., 2015, Liu et al., 2019, Deng et al., 2014, Zhang et al., 2013b).

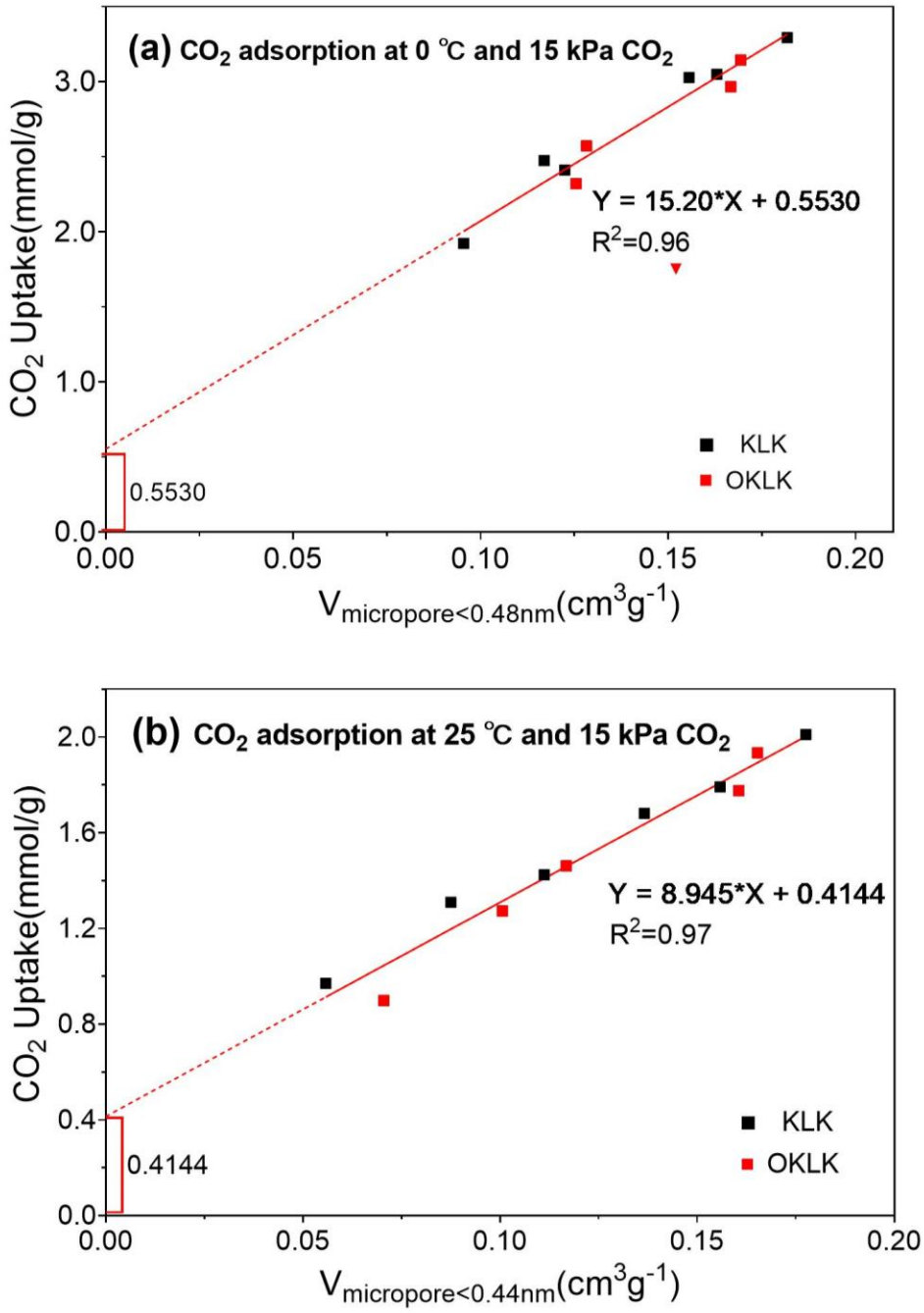


Figure 4.11 Relationship between CO_2 uptake and ultra-micropore volume of KL carbons (a) ≤0.48nm, 15 kPa CO_2 and 0 ^oC; (b)≤0.44 nm, 15 kPa CO_2 and 25 ^oC; (c) ≤1nm, 100 kPa CO_2 and 0 ^oC; (d) ≤0.55nm, 100 kPa CO_2 and 25 ^oC.

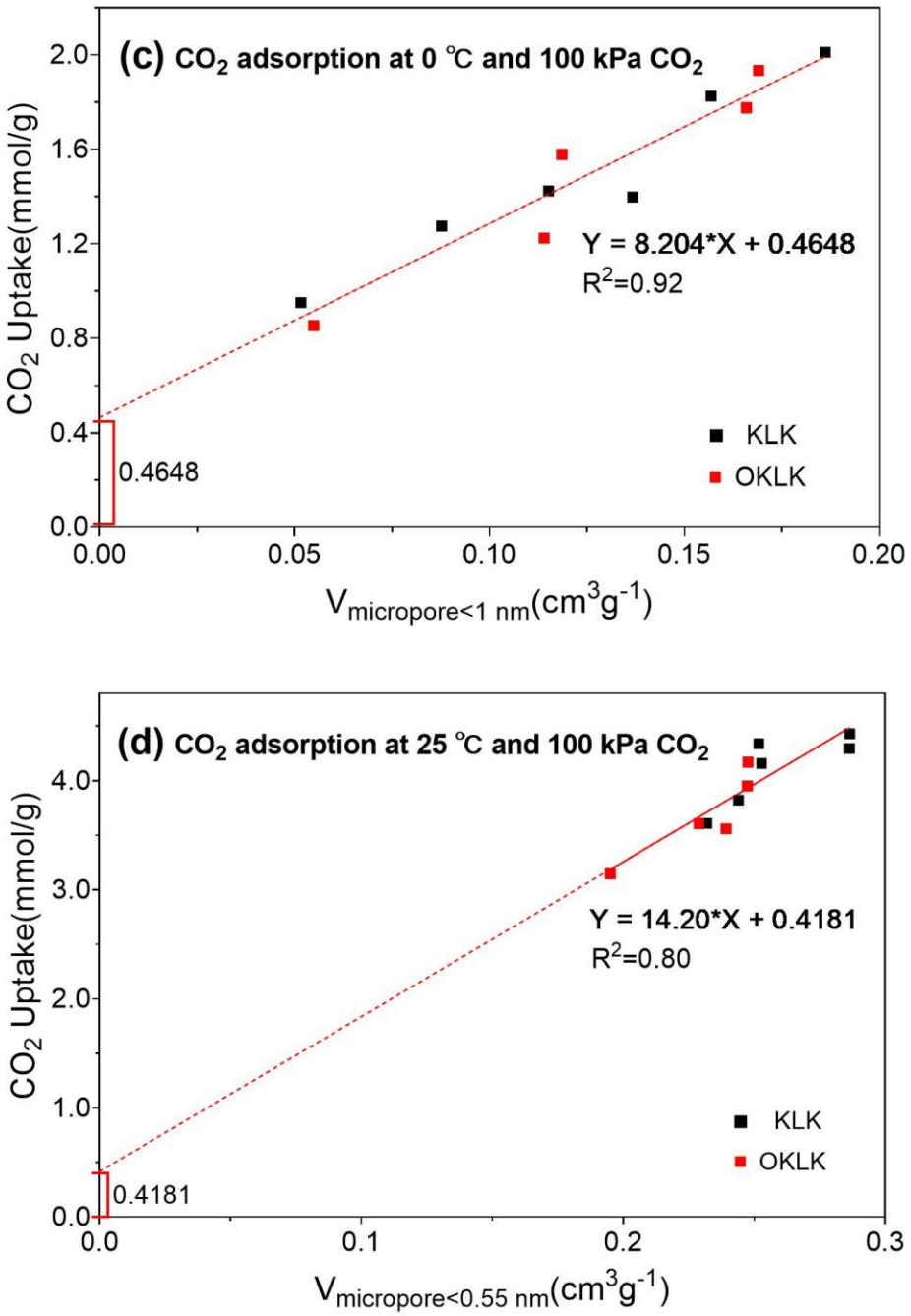


Figure 4.12 Relationship between CO_2 uptake and ultra-micropore volume of KL carbons (a) ≤0.48nm, 15 kPa CO_2 and 0 ^oC; (b)≤0.44 nm, 15 kPa CO_2 and 25 ^oC; (c) ≤1nm, 100 kPa CO_2 and 0 ^oC; (d) ≤0.55nm, 100 kPa CO_2 and 25 ^oC

However, it is apparent that the exceptional CO_2 uptake capacity of the carbons derived from kraft lignin cannot be fully accounted for by the micropore filling mechanism, as evidenced by the large y-axis intercepts observed in linear correlations (Figure 4.12). Specifically, the slope of the linear relations shows the variability of CO_2 adsorption with the volume of ultra-micropores under different adsorption conditions, while the magnitude of y-intercept corresponds to the excess CO_2 uptakes achieved by the kraft lignin-derived carbons via mechanisms that go beyond primary micropore filling, which is determined by the surface chemistry of the carbon materials. It was calculated by dividing the y-axis intercepts by the CO_2 adsorption capacity that the excess CO_2 uptake accounted for 20– 50% of the total CO_2 capacity of the kraft lignin carbons at 25 ^oC and 15 kPa CO_2 (Figure 4.12b), and the relative significance decreased to ca. 15~30% when the CO_2 adsorption took place at 0 ^oC and 15 kPa CO_2 (Figure 4.12a). The CO_2 adsorption behaviour of the lignin carbons indicates the vital role of surface chemistry in CO_2 capture. Given that the KLK/OKLK carbons are free of nitrogen, the excess CO_2 adsorption capacity was believed to be associated with the potassium (K)-modified surface chemistry of the Kraft lignin carbons during the process of the integrated carbonization-KOH activation. It was found in our previous investigations that KOH activation can give rise to the formation of intercalated potassium species deep into the matrices of the carbon framework structures, leading to the creation of extra-framework K cations (K^+) that favour CO_2 adsorption, particularly at low CO_2 partial pressures or high adsorption temperatures (Liu et al., 2017, Liu et al., 2015a, Yin et al., 2013). Figure 4.13a shows the XRD pattern of the microcrystalline structure for KLK-1-600 sample, confirming the presence of intercalated potassium in the prepared KLK/OKLK carbons, which occurred as the potassium survived the vigorous post-activation washing process with water. In addition, the SEM-EDX mapping obtained for KLK-1-600 (Figure 4.13b) reveals the extensive uniform distribution of the intercalated potassium species within the matrix of the KOH-activated lignin carbons.

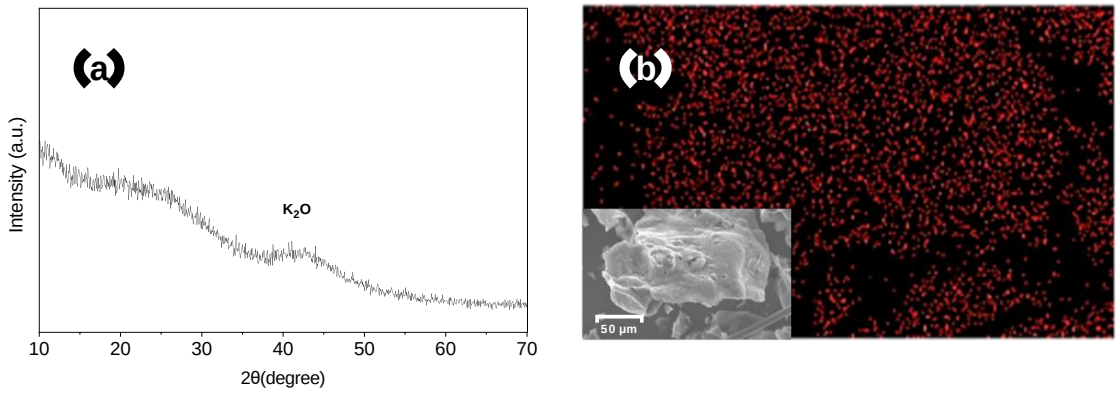


Figure 4.13 XRD patterns of KLK-1-600 carbon (a) and SEM-EDX element mapping of KLK-1-600

Table 4.5 shows the results of the XRF analysis of the residual potassium present in the KLK and OKLK carbons. As expected, the amount of potassium surviving the same excessive post-activation washing process was found to be disproportionately larger for all the carbon samples, varying from 2.39 to 6.11 wt %. An almost linear relationship with decent correlation coefficients (R^2=0.7) between the CO_2 uptake at 25 ^oC and 15 kPa and the density of intercalated potassium for lignin-derived carbon materials (Figure 4.14 Relationship between CO2 uptake and the density of intercalated potassium in the KLK and OKLK carbons), confirming the significant role of the potassium intercalation or its resultant extra-framework K^+ cations in the CO_2 adsorption. The presence of extra-framework ions, commonly found in zeolites and MOFs, is known to create strong local electric fields that can polarize adsorbate molecules and hence enhance the interaction of the adsorbate with the adsorption surface (Liu et al., 2015a, Liu et al., 2012b, Zhao et al., 2012). Similar phenomena can also take place strongly in carbon materials as found in previous work that the extra-framework ions due to potassium intercalation during controlled KOH activation can create strong surface electrostatic fields to polarize CO_2 molecular and serves as the additional forces in favour of CO_2 adsorption. Liu et al., 2020b found that the electric surface potential of potassium intercalated carbon samples was significantly greater than

that of the potassium free samples by as much as 153 ± 20 mV. As a results, the presence of the extra framework potassium ions gave rise to an increase in CO_2 uptake capacities by up to 44% at 25 ^oC and 15 kPa. Electrostatic forces, which are created by electrostatic fields that exist in the region surrounding extra-framework ions, are non-contact forces and can instantly polarise and selectively pull CO_2 molecules towards the surface due to the strong quadrupole polarizability of CO_2 molecules, thus leading to enhanced CO_2 adsorption via a combination of reinforced micropore filling and surface coverage with mono/multi-layer adsorption (Pulido et al., 2009, Valenzano et al., 2010). Therefore, the potassium-intercalated lignin carbon materials can be considered somewhat as zwitterionic material with widely distributed CO_2-polarising electrostatic nanodots.

Table 4.5 Chemical analysis by XRF of KLK and OKLK carbons

Sample	K (wt.%)
KLK-1-600	5.72
KLK-1-700	5.74
KLK-1-800	4.04
KLK-2-600	2.98
KLK-2-700	4.78
KLK-2-800	2.39
OKLK-1-600	5.72
OKLK-1-700	6.11
OKLK-2-600	3.15
OKLK-2-700	5.51

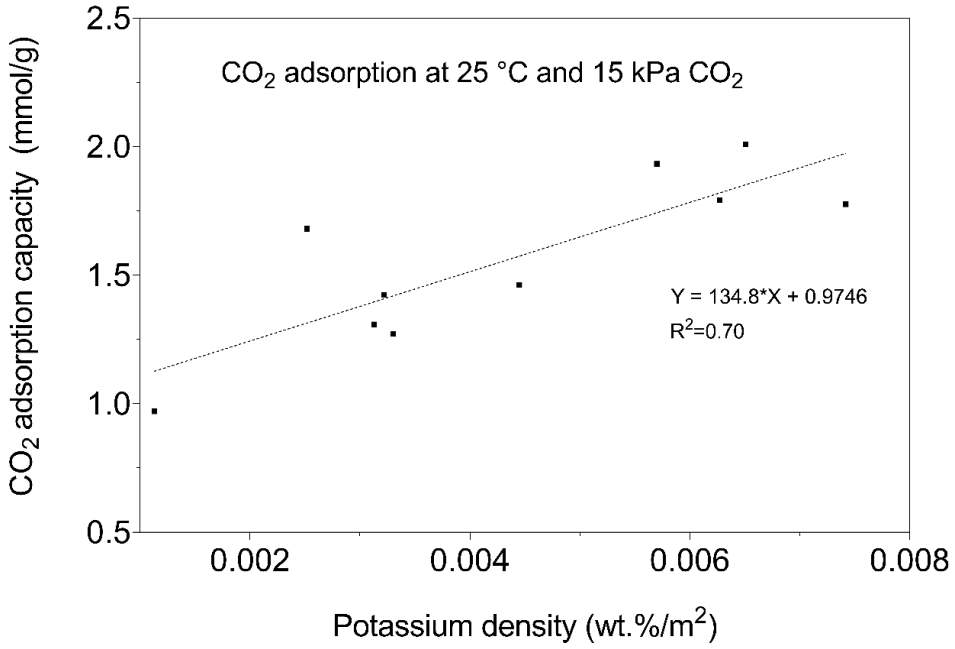


Figure 4.14 Relationship between CO_2 uptake and the density of intercalated potassium in the KLK and OKLK carbons

4.2.6 Heat of CO_2 adsorption

To further reveal the surface affinity of the lignin-derived carbons to CO_2 molecule, the isosteric heat of adsorption (Q_{st}) was calculated by using the Clausius-Clapeyron Equation. In this work, considering the heterogeneity of the carbon surface because of potassium intercalation, the dual-site Langmuir (DSL) model was used to fit the CO_2 adsorption isotherms of the carbons at 0 and 25 ^oC (Mason et al., 2011). By applying the Clausius-Clapeyron Equation to the DSL model, the pure gas Q_{st} can be calculated. The obtained Q_{st} as a function of the quantity of CO_2 adsorbed was shown in Figure 4.15 for the prepared activated carbons, with all the fitting results presented in Figure 4.7. The Q_{st} value for initial stages of adsorption (at a CO_2 uptake level of 0.01 mmol/g) has been widely accepted as being an indicator of the strength of interaction between the carbon surface and CO_2 molecules (Zhao et al., 2012). It was found that the initial Q_{st} of the KLK and OKLK carbons ranges from 29 to 43 kJ/mol, which is considerably higher than

those obtained for other carbon materials recently reported (Ashourirad et al., 2016, Rao et al., 2019, Rehman et al., 2021), indicating the enhanced surface affinity of the carbons to CO_2 molecules, which is clearly attributable to the presence of intercalated potassium. With the increase of CO_2 adsorption capacity, the strong adsorption sites became saturated, and the CO_2 was increasingly adsorbed onto weaker sites, leading to the decrease in Q_{st}. for all carbons. It is also noteworthy that the Q_{st}.of KLK carbons (KLK-600-1, KLK-700-1 and KLK-600-2) and OKLK carbons (OKLK-600-1 and OKLK-700-1) was still higher than 30 kJ/mol at late stages of adsorption, which was still much higher than those previously reported for biomass-based activated carbons (21 kJ/mol) (Li et al., 2019), phenolic resin derived carbons (25.7 kJ/mol)(Zhang et al., 2019c) and N-doped porous carbons (28.6 kJ/mol) (Ren et al., 2017). The above calculations highlight the critical role of intercalated potassium in bolstering the surface affinity of the lignin carbons to CO_2 molecules and therefore enhancing the adsorption capacity.

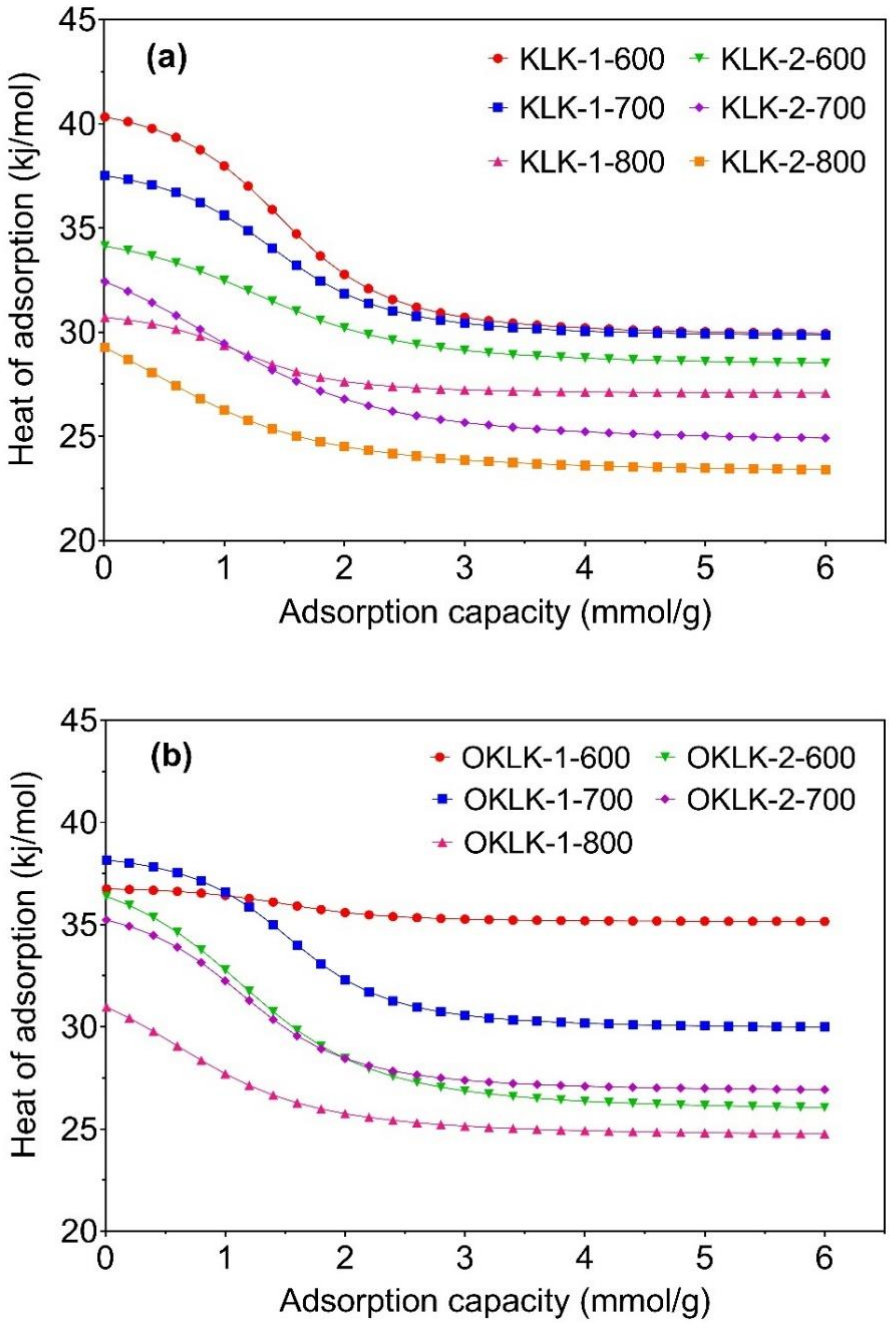


Figure 4.15 Isosteric heat of CO_2 adsorption calculated from the adsorption isotherms at 0 and 25 ^oC for (a) KLK carbons; (b) OKLK carbons

Table 4.6 Dual-Langmuir Fitting results

Sample	Temp (^{O}C)	q_A (mmol/g)	b_A (Pa^{-1})	q_B (mmol/g)	b_B (Pa^{-1})	E_A (kJ/mol)	$b_{0,A}$ (Pa^{-1})	E_B (kJ/mol)	$b_{0,B}$ (Pa^{-1})
KLK-1-600	0	1.56	1.46E-03	5.55	3.12E-05	41.33	1.80E-11	29.80	6.19E-11
	25	1.56	3.17E-04	5.55	1.04E-05				
KLK-1-700	0	6.41	2.18E-05	1.52	1.02E-03	29.76	4.42E-11	38.35	4.68E-11
	25	6.41	7.27E-06	1.52	2.47E-04				
KLK-1-800	0	1.24	7.30E-04	7.62	1.29E-05	31.14	8.02E-10	27.04	8.60E-11
	25	1.24	2.31E-04	7.62	4.73E-06				
KLK-2-600	0	8.10	1.70E-05	1.51	5.50E-04	28.39	6.30E-11	35.22	1.00E-10
	25	8.10	5.96E-06	1.51	1.50E-04				
KLK-2-700	0	11.75	9.12E-06	1.27	3.11E-04	24.70	1.71E-10	34.97	6.33E-11
	25	11.75	3.66E-06	1.27	8.54E-05				
KLK-2-800	0	16.54	5.27E-06	0.95	1.97E-04	23.25	1.87E-10	32.64	1.12E-10
	25	16.54	2.23E-06	0.95	5.90E-05				
OKLK-1-600	0	1.58	1.12E-03	4.91	2.74E-05	36.88	9.83E-11	35.14	5.17E-12
	25	1.58	2.87E-04	4.91	7.47E-06				
OKLK-1-700	0	6.18	2.22E-05	39.77	5.45E-13	39.77	5.45E-13	40.94	1.95E-11
	25	6.18	5.10E-06	39.77	5.45E-13				
OKLK-1-800	0	0.95	2.38E-04	10.25	7.25E-06	33.45	9.46E-11	24.66	1.39E-10
	25	0.95	6.91E-05	10.25	2.91E-06				
OKLK-2-600	0	7.18	1.25E-05	1.34	4.49E-04	25.87	1.40E-10	38.41	2.01E-11
	25	7.18	4.81E-06	1.34	1.08E-04				
OKLK-2-700	0	1.29	7.07E-04	8.76	1.22E-05	36.43	7.56E-11	26.83	8.95E-11
	25	1.29	1.84E-04	8.76	4.52E-06				

4.2.7 CO_2/N_2 selectivity

Selective CO_2 adsorption over N_2 is another key criterion for carbon materials in terms of CO_2 capture. In this work, the CO_2/N_2 selectivity of selected carbon samples was investigated, using the ideal adsorption solution theory (IAST) that has been employed as an effective model to evaluate the CO_2/N_2 selectivity of sorbent materials (Li et al., 2016, To et al., 2016). Table 4.7 shows the IAST CO_2/N_2 selectivity of selected lignin carbons for CO_2 adsorption in 15% CO_2/N_2 at an adsorption temperature of 25 ^oC. It can be found that the IAST CO_2/N_2 selectivity ranged from 22 to 38, which is significantly higher than many porous carbon materials reported to date (Demir et al., 2018, Yuan et al., 2019, Zhang et al., 2019a, Qezelsefloo et al., 2020). Among the lignin carbon materials prepared, the carbons prepared under mild conditions (600 ^oC with KOH/carbon ratio of 1 by mass) exhibited significantly higher IAST CO_2/N_2 selectivity, indicating that the importance of ultra-micropores (<0.5 nm) and potentially enhanced potassium intercalation.

Table 4.7 CO_2 uptake at 25 ^oC, 15 kPa CO_2 capacity and IAST CO_2/N_2 selectivity

Sample	CO_2 uptake (mmol/g)	IAST CO_2/N_2 selectivity
KLK-1-600	2.01	33
KLK-1-700	1.79	25
KLK-1-800	1.42	22
KLK-2-600	1.68	24
OKLK-1-600	1.78	38
OKLK-1-700	1.93	29
LHPC-700	1.10	22
PC-2-3	1.20	20
Zn-1500	1.50	26

4.3 Conclusion

Kraft lignin is an abundantly available renewable natural substance in biomass but is unwanted in many industrial processes like paper and ethanol production, giving rise to the production of lignin as waste in large quantities. In this investigation, the use of lignin waste to prepare high quality ultra-microporous bio-carbon materials or molecular sieves has been examined with success, using a novel integrated carbonization-activation process. Characterisations demonstrate that the bio-carbons derived from the pristine kraft lignin were almost exclusively ultra-microporous with pore sizes generally well below 1 nm, whereas those from the pre-oxidised lignin under mild conditions were found to have distinctive hierarchical ultra-micro/mesoporous structures with narrow bimodal pore size distributions. It was found that the effect of carbonization-KOH activation conditions (e.g. KOH/KL ratio, temperature and pre-oxidation treatment etc.) on the pore size distribution of the ultra-microporous lignin carbons was insignificant, despite the increased pore volume with increasing process severity and the formation of some levels of mesoporosity with pre-oxidation treatment. Potassium intercalation deep into the framework structures of the lignin carbons was also evident and varied considerably with the carbonization-activation conditions, leading to the formation of a wide range of extra-framework potassium cations that essentially transform the lignin carbons into a class of zwitterionic material with widely distributed highly polarising electrostatic nanodots. Applying the lignin-derived carbons to CO_2 adsorption at low CO_2 partial pressure demonstrates that the carbon materials possessed exceedingly high CO_2 uptake capacities of up to 2.01 mmol/g at 25 ^oC and 15 kPa CO_2 and outstanding CO_2/N_2 of up to 38, which is attributable to a combination of high ultra-microporosity and the abundance of extra-framework ions arising from the potassium intercalation achieved simultaneously during the integrated carbonization-activation process. The research provides unequivocal evidence of the important role of the surface chemistry of carbon materials in CO_2 adsorption, which can account for up to 50% of total CO_2 uptake for the lignin carbon materials.

Chapter 5
Hydrothermal Carbonization and Hydrochar-based functional carbon materials

5.1 Introduction

The manufacturing of activated carbon materials using lignocellulosic biomass has gained tremendous development in recent years but faces growing challenges in sourcing more sustainable suitable lignocellulosic biomass feedstock, which has been provided predominantly as forest waste. Therefore, there is a need and also a desire to explore non-forestry but still sustainable sources of biomass feedstock for more sustainable carbon materials production (Falco et al., 2013). Over recent years, hydrothermal carbonization (HTC) has emerged as a novel energy densification methodology to produce biocoal or hydrochar fuel from hard-to-process biomass waste, such as wet agricultural residues and bio-digestion waste. In this chapter, the use of HTC as a potential methodology to upgrade or improve the quality of biomass waste for making activated carbon materials has been examined.

Compared to traditional high-temperature carbonization through pyrolysis, HTC takes place in water under self-generated pressures at relatively mild temperatures (i.e., 180–250 ^{o}C), allowing the wet biomass to be processed directly without drying pre-treatment, which is usually a very energy-intensive process. In addition, during hydrothermal carbonization, a range of reactions can take place at varying significance, such as hydrolysis, dehydration, decarboxylation and even dehydroxylation and aromatisation reactions, leading to the formation of hydrochar with greatly increased energy density and improved carbonaceous texture (Jain et al., 2016). Therefore, HTC can potentially serve as a technology platform which can convert unfavourable biomass feedstock to suitable precursor feedstock for quality carbon materials manufacturing. A few studies have demonstrated that HTC hydrochars can be used to produce high-performing carbon materials for CO_2 adsorption. Sevilla and Fuertes (2011) employed KOH activation to produce functional carbon materials from hydrochar and found that the hydrochar-based carbon materials showed extremely high CO_2 uptake of 4.8 mmol/g at 25 ^{o}C and a CO_2 partial pressure of 100 kPa (1 bar). Coromina et al. (2016) also found that

the porous carbons prepared with KOH activation from using the HTC hydrochar of Jujun grass and Camellia japonica via hydrothermal carbonization, and the carbons activated at KOH/hydrochar ratio of 2 exhibited CO_2 uptakes of up to 5.0 mmol/g at 25 ^oC and 100 kPa of CO_2. However, the HTC hydrochar-based activated carbons were generally found to have low CO_2 adsorption capacities at low CO_2 partial pressures due to weak surface affinity of the carbons to CO_2 molecules, with CO_2 uptake capacity being generally well below 1.5 mmol/g at 25 ^oC and 15 kPa (Coromina et al., 2016, Goel et al., 2021, Rashidi and Yusup, 2016). In this investigation, the synthesis of ultra-microporous functional carbon materials from using the HTC hydrochar derived from eucalyptus biomass at different HTC temperatures has been investigated, and the effect of HTC and KOH activation conditions on the surface textural properties and related CO2 adsorption performance of the hydrochar-based carbon materials were examined comprehensively.

5.2 Results and discussion

5.2.1 Physicochemical properties of biomass and hydrochars

The physicochemical properties of raw EU and derived hydrochar are summarized in Table 5.1. Based on the proximate analysis results, the raw EU exhibited 83.13 wt% of VM and 16.87 wt% of FC. A decrease in the VM content and a corresponding increase in fixed carbon were found in hydrochar as the HTC temperature increased, with the lowest VM value of 50.61 wt% and highest FC content of 47.51 wt% obtained for hydrochar prepared at 260 ^oC. During the HTC process, it is well-established that cellulose and hemicellulose fragments undergo condensation and polymerization with increasing HTC temperature, resulting in carbonaceous polymers with relatively low volatile content due to cross-linking (Lynam et al., 2015, Zhuang et al., 2019). Thus, the increased fixed carbon and decreased volatile matter found in hydrochar produced at higher temperatures was expected.

Table 5.1 Physicochemical properties of raw EU and derived hydrochar

		EU	EUHC22	EUHC26
Proximate analysis (wt%)				
Moisture		5.28	2.74	1.13
Volatile matter		83.13	63.77	50.61
Fixed carbon		16.87	32.40	47.51
Ash		1.19	1.09	0.75
Ultimate analysis (wt%)				
C		49.25± 0.05	60.75± 0.08	69.47± 0.13
H		5.91± 0.01	5.29± 0.11	4.99± 0.03
N		0.29± 0.02	0.42± 0.01	0.48± 0.02
O		43.36± 0.06	32.45± 0.19	24.31± 0.14
Atomic ratio	H/C	1.44	1.04	0.86
	O/C	0.66	0.40	0.26
Yield (wt%)			64.44	52.89

The ultimate analysis shows that the carbon content of hydrochars is appreciably higher than that of raw EU and increased notably with an increase of HTC temperature, reaching a maximum of 70 wt % for the hydrochar prepared at 260 ^{o}C. Meanwhile, the oxygen and hydrogen contents generally decrease with increasing HTC temperature, indicating the transformation of the biomass into a highly condensed solid char product. The variation in the elemental composition of raw EU and hydrochars was also analysed via a Van Krevelen diagram as shown in Figure 5.1, which allows for the delineation of the reaction pathways. It can be found from the diagram that the evolution of the H/C-O/C atomic ratios from raw EU to hydrochars was predominantly governed by the dehydration process

combined with a minor extent of the decarboxylation process, which was consistent with that previously reported in the hydrothermal transformation of other lignocellulosic biomass materials (Cai et al., 2016, Gao et al., 2016, Zhuang et al., 2019). For comparison, the atomic ratios of other typical substances (biomass, peat, lignite, and coal) are also presented in Table 5.1. It is noticeable that the reduction of H/C-O/C atomic ratios of hydrochar as a consequence of the hydrothermal process gave rise to the maturation tendency of biomass to coal-like material, with EUHC22 failing within the region of peat and EUHC26 being comparable to the lignite-like product. Furthermore, a rapid decrease in the hydrochar yield by 12 % from 64.44% (EUHC22) to 52.89% (EUHC26) was observed as the HTC temperature increased from 220 to 260 ^{o}C, which was associated with the intensified decomposition reactions at higher HTC temperatures.

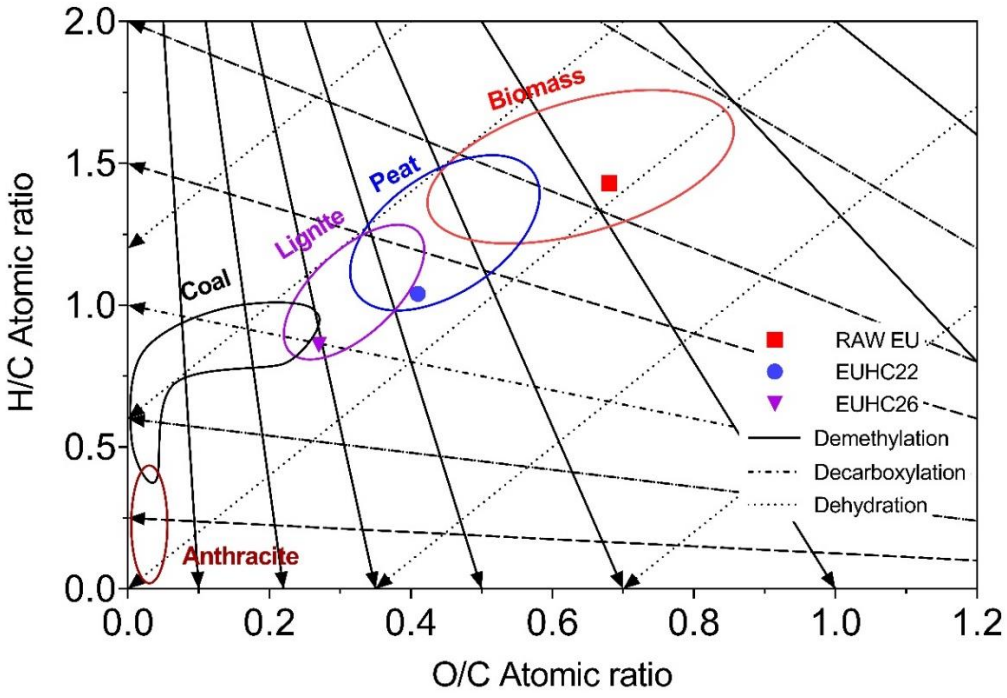


Figure 5.1 Van Krevelen diagram of raw EU and hydrochars at different carbonization temperatures

It is well known that the surface functional groups of hydrochar play a critical role in promoting chemical activation (Sevilla et al., 2011a, Jain et al., 2016). The FT-IR spectra of raw EU and hydrochars prepared at different HTC temperatures are shown in Figure 5.2. It can be noticed that the FT-IR spectra of raw EU and their derived hydrochar products exhibited distinguishable differences, confirming the occurrence of chemical transformation during the HTC process. The transmittance peaks at 3340 cm^{-1} and 1030 cm^{-1} were respectively assigned to O–H stretching vibrations in hydroxyl and carbonyl groups and alcohol C−O stretching vibrations (Zhang et al., 2018). Both peaks were observed in raw EU and hydrochar, while the intensities were weakened with the increase of HTC temperature from 220 to 260 ^{o}C, which was presumably due to the dehydration reaction that occurred during HTC. The result was consistence with the evolution of H/C-O/C atomic ratios based on the Van Krevelen diagram. On the other hand, the peaks at 2930-2843 cm^{-1} were attributed to the C−H stretching in aliphatic and aromatic structures. Peaks at 1600-1450 cm^{-1} and 875-750 cm^{-1} were ascribed to the C=C and C-H stretching in aromatic groups, respectively (Chen et al., 2018, Guo et al., 2015, Samaksaman et al.). These peaks were found to become more intense with the increase in HTC temperature, indicating the aromatization reaction was enhanced. Simultaneously, the peaks at 1700 cm^{-1} and 1210 cm^{-1} respectively denoting the C=O and C−O−C groups increased with the increasing HTC temperature, implying the growth of oxygen functional groups on the surface of the EUHC26 hydrochar (Guo et al., 2015, He et al., 2013).

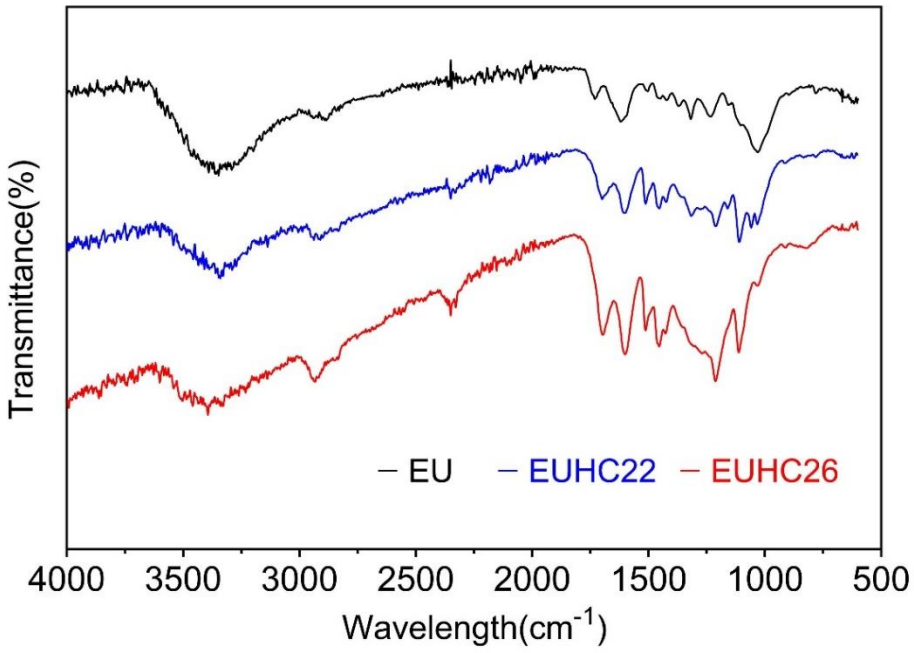


Figure 5.2 FT-IR spectra of raw EU and the hydrochars prepared at different HTC temperatures

5.2.2 Textural properties of EU-derived activated carbons

The N_2 sorption isotherms for the activated carbons prepared from using raw EU and their derived hydrochars under different activation conditions are depicted in Figure 5.3. It can be found that all carbon samples possess a steep and large N_2 uptake at a low relative pressure region of well below 0.1, indicating the prominent microporous nature of prepared carbons. In specific, the isotherm of EU derived activated carbon without hydrothermal treatment prepared at 600 ^oC and KOH/EU mass ratio of 1 belongs to the typical type I isotherm, indicating that the sample has a narrow pore size distribution in the micropore range. By contrast, it can be found that all the EU derived activated carbons prepared through hydrothermal carbonization exhibited a combination of type I and type IV isotherms according to the IUPAC classification (Figure 5.3) (Thommes et al., 2015). The narrow knee at low relative pressures ($P/P_0 < 0.1$) as characteristic of type I isotherm denoted the significant presence of micropores, while the observed hysteresis loops with variable amounts at relatively high pressure given by type IV isotherm indicated

the wider pore size distributions ranging from micro to mesoporous structures. The hysteresis in the isotherms well accorded with the Type H4 loop, which means that the mesopores were narrow slit-like pores. The emergence of a hysteresis loop associated with the development of mesoporosity is clearly attributed to the introduction of HTC treatment, which intensified the etching effect by the intercalated potassium as a result of KOH activation process.

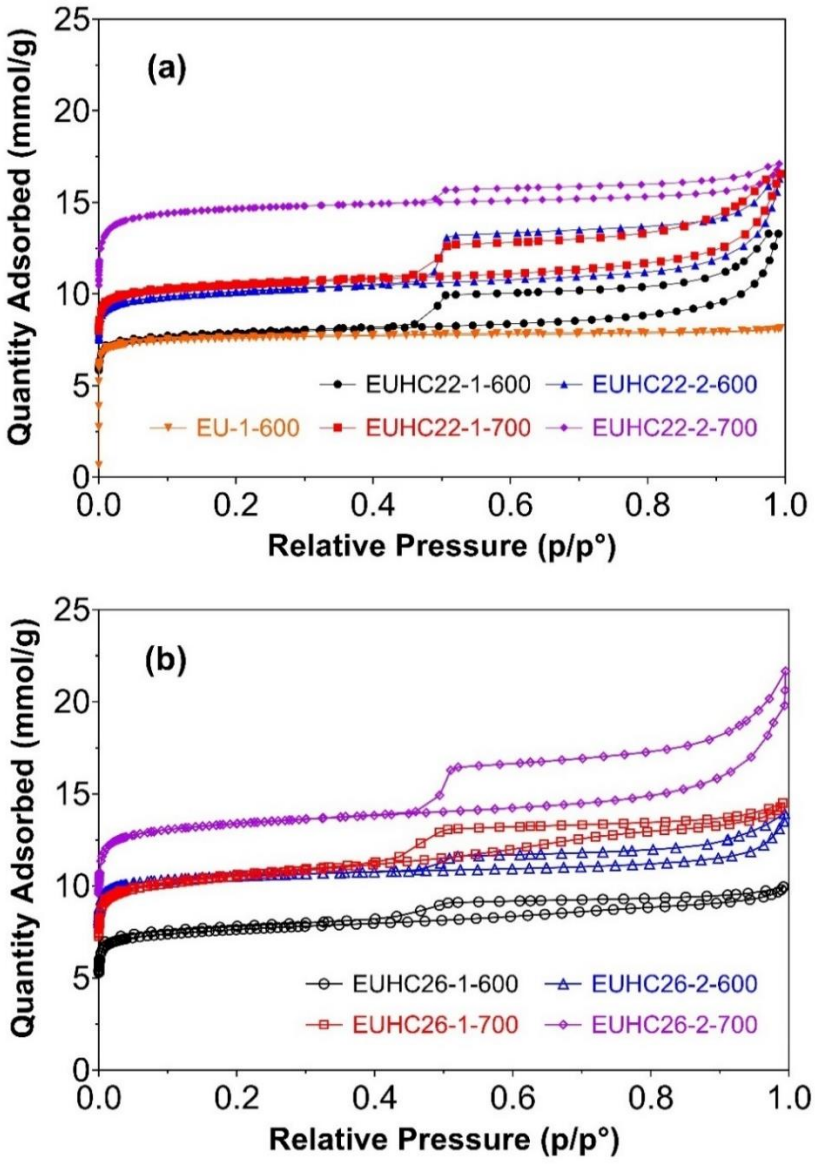


Figure 5.3 N_2 sorption isotherms obtained at -196 ºC for EU and EUHC derived carbons prepared at different HTC temperatures and activation conditions

Table 5.2 summarizes the overall textural properties of the carbon samples derived from raw EU and EUHC hydrochars.

Table 5.2 Textural properties of prepared carbon samples

Sample	S_{BET} (m^2/g)	V_{total} (cm^3/g)	V_{micro} (cm^3/g)	$V_{micro<0.7nm}$ (cm^3/g)	$V_{micro<0.40nm}$ (cm^3/g)	V_{micro}/V_{total}
EUHC22-1-600	699	0.435	0.247	0.213	0.154	57
EUHC22-1-700	943	0.538	0.337	0.289	0.149	63
EUHC22-2-600	903	0.522	0.321	0.269	0.160	61
EUHC22-2-700	1328	0.542	0.477	0.380	0.114	88
EUHC26-1-600	675	0.324	0.241	0.197	0.159	74
EUHC26-1-700	922	0.471	0.323	0.259	0.150	69
EUHC26-2-600	952	0.432	0.343	0.305	0.144	79
EUHC26-2-700	1198	0.640	0.423	0.343	0.128	66
EU-1-600	687	0.267	0.252	0.217	0.128	94

The results showed that the textural properties of carbons derived from the eucalyptus hydrochar were mainly determined by the activation temperature, KOH/EUHC mass ratio and HTC temperature. It can be seen that the BET surface area and total pore volume of EUHC22-derived carbons substantially increased from 699 to 1328 m^2/g and 0.435 to 0.542 cm^3/g, respectively, when the activation temperature increased from 600 to 700 ^oC and KOH/EUHC mass ratio from 1 to 2. Moreover, EUHC26 derived carbons followed a similar trend as EUHC22 derived carbons, with the BET surface area and total pore volume increasing from 675 to 1198 m^2/g and 0.324 to 0.640 cm^3/g, respectively. In addition, it appears that the HTC temperature has minimal effect on the BET surface area of EUHC22- and EUHC26-derived carbons prepared under the same activation conditions, whereas the total pore volume of carbons obtained from using lower HTC temperature of 220 ^oC was generally higher than those of carbons prepared at higher HTC temperature of 260 ^oC except for EUHC26-2-700. It is presumably because of a higher degree of aromatization of the hydrochars prepared at a higher temperature that gave rise to the enhanced chemical stability and structure order of hydrochars,

leading to a diminished KOH etching effect on porosity development in carbon samples (Falco et al., 2013). More importantly, through the introduction of HTC treatment, the total pore volumes of EUHC-derived carbons were significantly higher than that of the carbon prepared by using pristine EU without HTC treatment under the same activation protocols (600^{o}C and KOH/EU ratio of 1), with 63% and 21% increase in total pore volume from 0.267 cm^3/g to 0.435 and 0.324 cm^3/g for EUHC22-1-600 and EUHC26-1-600, respectively, despite their nearly identical BET surface areas. The enhancement of porosity is potentially due to the rise in oxygen functional group levels resulting from HTC treatment that facilitated the intercalation of potassium ions and resulted in efficient chemical activation (Sevilla and Fuertes, 2011, Falco et al., 2013, Jain et al., 2015). The micropore volume of all the EUHC carbons was found to be mainly influenced by the activation temperature and KOH/EUHC mass ratio rather than the HTC temperature. As the severity of the KOH activation process increased, the micropore volume of carbons continuously increased, with the highest micropore volume of EUHC22-2-700 reaching 0.477 cm^3/g, accounting for approximately 90% of the total pore volume. A similar trend was observed in terms of the variation of ultra-micropore volume (<0.7 nm), with the ultra-micropore volume of EUHC22 carbons and EUHC26 carbons increased from 0.213 to 0.380 cm^3/g and 0.197 to 0.343 cm^3/g, respectively, when the activation temperature increased from 600 to 700 ^{o}C and KOH/EUHC mass ratio from 1 to 2. Among all the prepared carbons, EUHC22-2-700 has the highest volume of ultra-micropore of 0.380 cm^3/g. The pore size distribution calculated from N_2 and CO_2 adsorption isotherms using the NLDFT model demonstrated that all the EUHC-derived carbons are predominantly ultra-microporous with the pore sizes centred at 0.37 nm, 0.53 nm, and 1.2 nm, with the relative significance of the ultra-microporosity is mainly influenced by the activation temperature and KOH/EUHC mass ratio (Figure 5.4). In specific, as the activation temperature and KOH/EU mass ratio increased, the pore volume of the smaller micropores centred at 0.37 nm decreased whilst those of the larger micropores centred at 0.53 nm increased continuously, highlighting the pore widening effect with increasing severity of KOH activation.

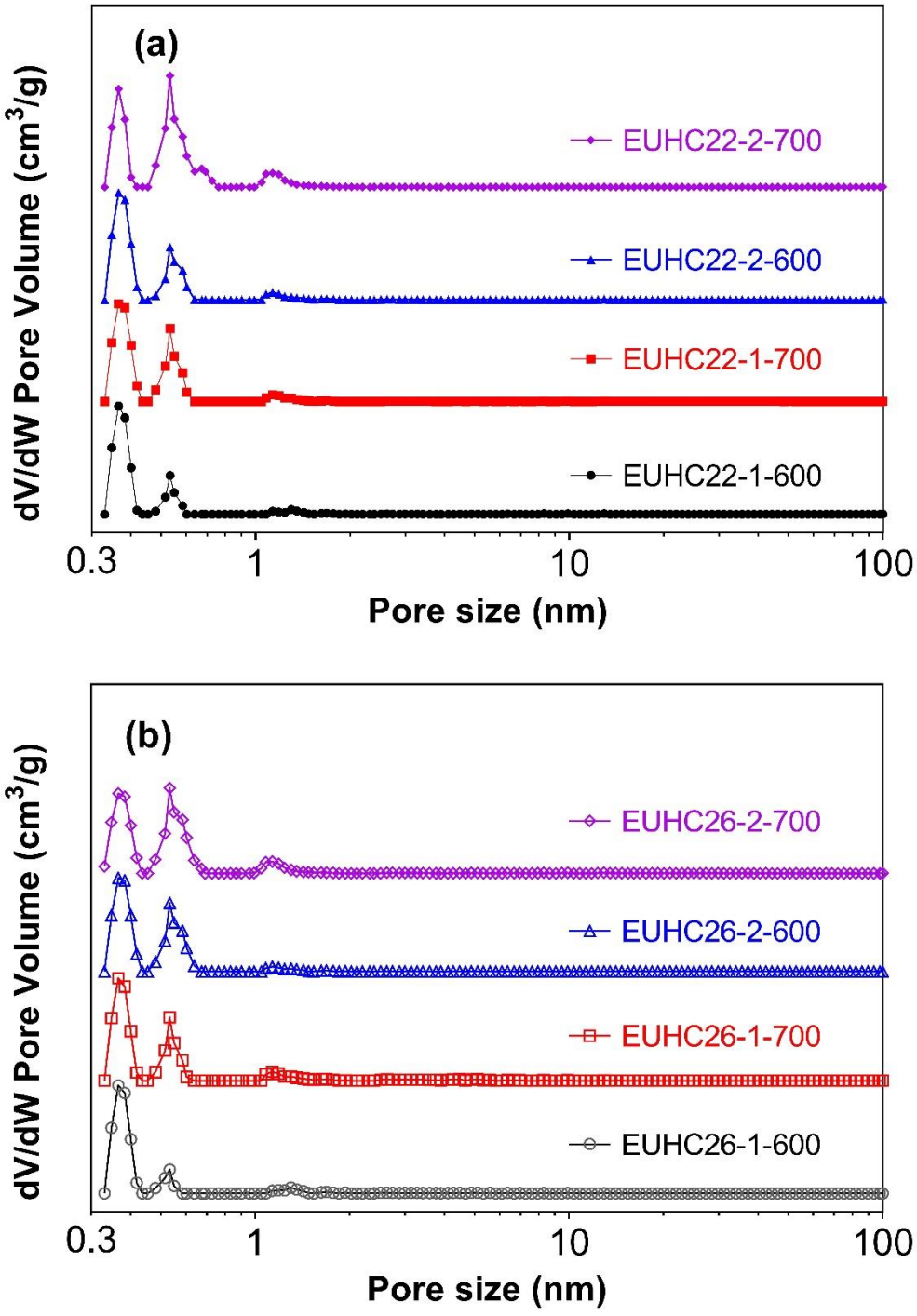


Figure 5.4 Pore size distributions for EUHC samples from KOH activation with different activation temperature and KOH/EUHC mass ratios

5.2.3 Morphology of EU-derived hydrochar and EUHC carbons

Figure 5.5 shows the morphology of eucalyptus-derived hydrochar and carbon samples prepared at different HTC and activation temperatures. SEM images of hydrochar samples reveal the presence of a large fraction of microspheres, which are presumably generated as a result of the decomposition of cellulose during hydrothermal carbonization (Sevilla et al., 2011a, Sevilla and Fuertes, 2009b). These microspheres are also found to be mixed with irregular particles derived from the preserved skeleton of the non-saccharide components of wood (i.e. lignin) due to their high chemical stability (Sevilla et al., 2011b).

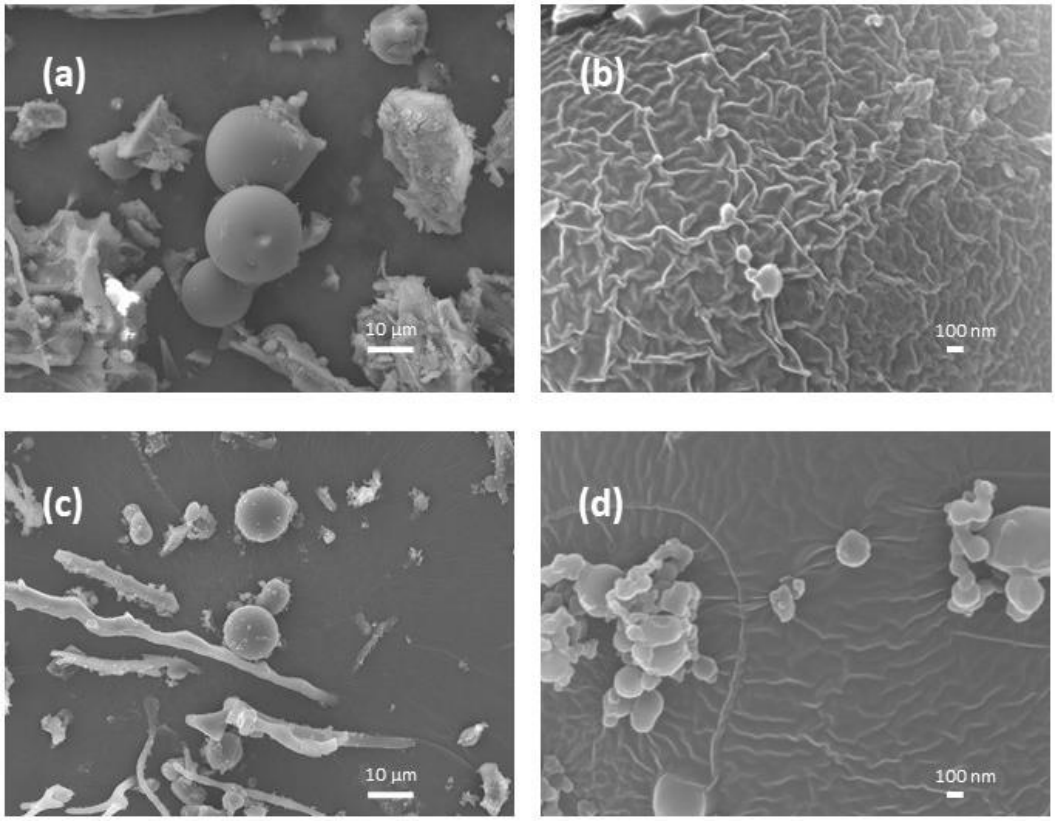


Figure 5.5 SEM images of hydrochars prepared under different HTC temperature: (a)(b) hydrochar prepared at 220 ºC; (c)(d) hydrochar prepared at 260 ºC

The morphology of EUHC-derived activated carbons prepared at different KOH activation protocols was presented in Figure 5.6. It can be found from Figure 5.6 (a,b,e,f) that both EUHC22 and EUHC26-derived carbon samples prepared at the mild activation conditions (600 ^{o}C and KOH/EUHC ratio of 1) retain the typical morphology of their parent hydrochars, i.e. a mixture of irregular and microspherical particles agglomerated with widely distributed fine cavities. While the appearance of a highly porous texture emerged in the carbon matrix is due to the pore expansion via KOH activation. Furthermore, Figure 5.6 (c,d,g,h) shows that the increase of activation temperature from 600 to 700 ^{o}C and KOH/EUHC ratio from 1 to 2 resulted in a drastic morphological transformation of carbon samples, with the collapse of microspheres and the formation of irregularly shaped particles with large conchoidal cavities and smooth surfaces. The macro-structures of such carbon samples appeared to be more porous, and the cavities became significantly widened due to the more pronounced levels of carbon-consuming activation activities. In addition, a laxer and more fragmented macrostructure was observed for EUHC22-2-700 compared to EUHC26-2-700, indicating the enhanced etching process occurred on hydrochar prepared at a lower HTC temperature.

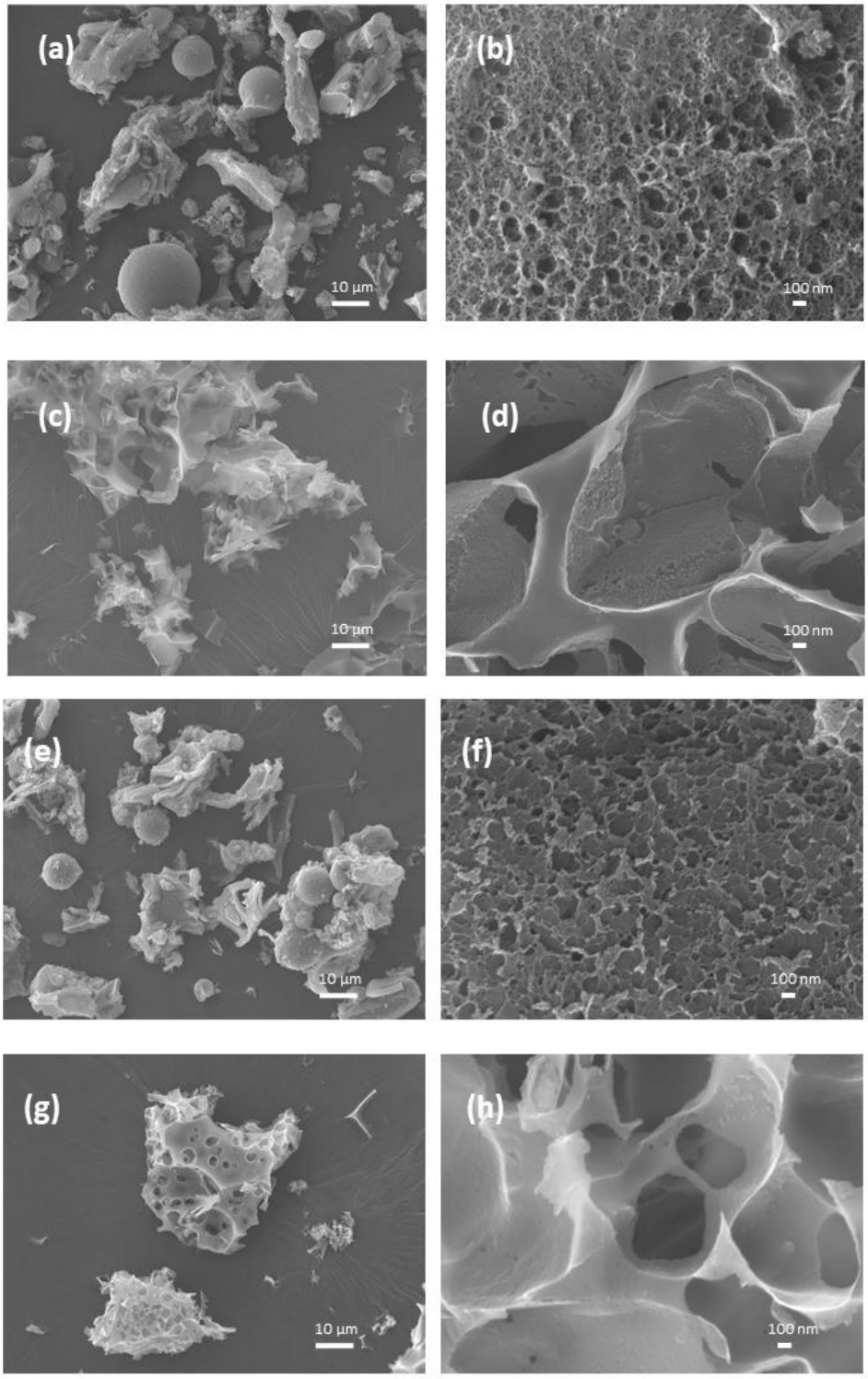


Figure 5.6 SEM images of EUHC26 and EUHC26-derived carbons prepared under different KOH activation protocols: (a)(b) EUHC22-1-600; (c) (d) EUHC22-2-700; (e)(f) EUHC26-1-600; (g)(h) EUHC26-2-700

The XRD patterns of EUHC22-1-600 and EUHC26-1-600 were shown in Figure 5.7 to further investigate the effect of HTC temperature on the graphitization degree of carbons. The two broad peaks in both carbon samples corresponded to the (002) and (100) diffraction patterns of amorphous graphitic carbon (Wang et al., 2012). Additionally, some shift appeared from the peak at the angles of 31° (EUHC26-1-600) to 26° (EUHC22-1-600), indicating the accelerated intercalation of K^+ ions into carbon skeleton for etching occurred for hydrochar prepared at lower HTC temperature, which consequently affected the graphene interlayer distance in the frameworks (Huang et al., 2019a).

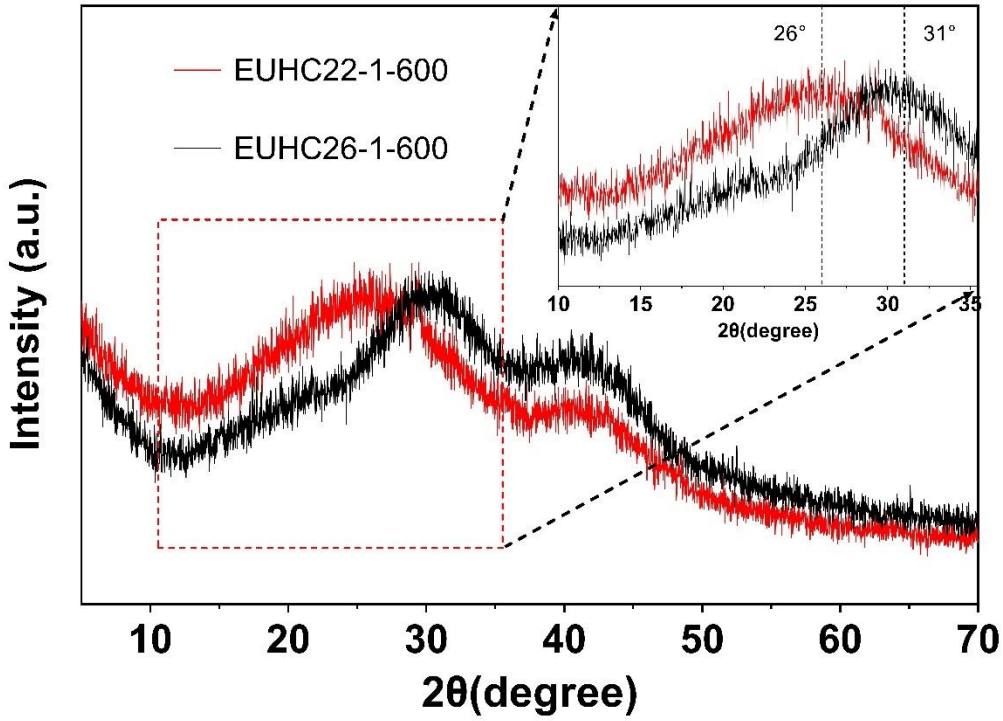


Figure 5.7 Representative XRD patterns of EUHC22-1-600 and EUHC26-1-600

5.2.4 CO_2 adsorption properties of EUHC-derived carbons

Figure 5.8 shows the CO_2 isotherms at 0 °C and 25 °C for EU- and EUHC-derived carbon samples. In the case of carbon samples prepared via HTC, the CO_2 adsorption performance was found to be mainly affected by the activation temperature and KOH/EUHC mass ratio rather than the HTC temperature.

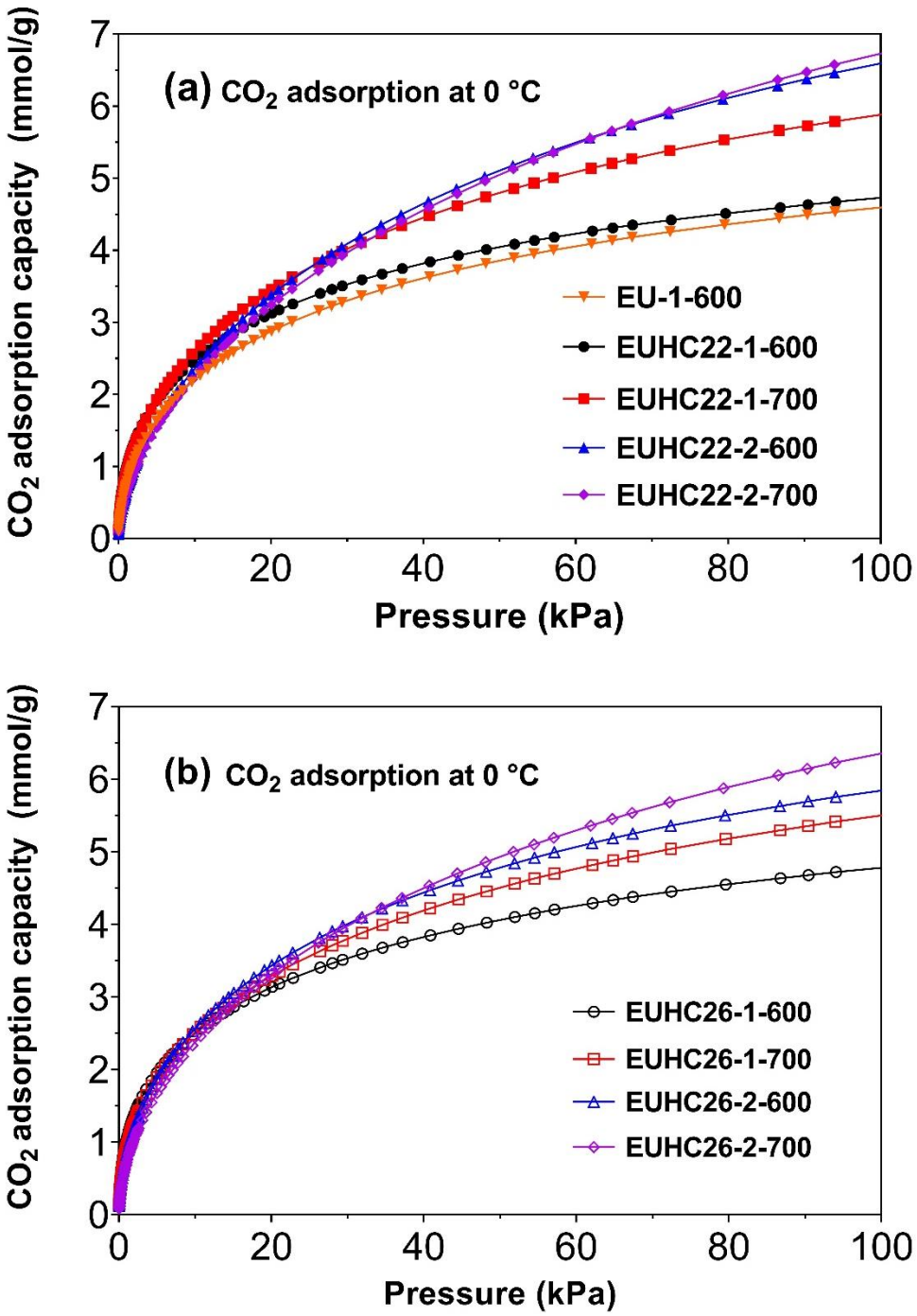


Figure 5.8 CO_2 adsorption isotherms EU- and EUHC22-derived carbons at (a) 0 °C (c) 25 °C and EUHC26-derived carbons at (b) 0 °C (d) 25 °C.

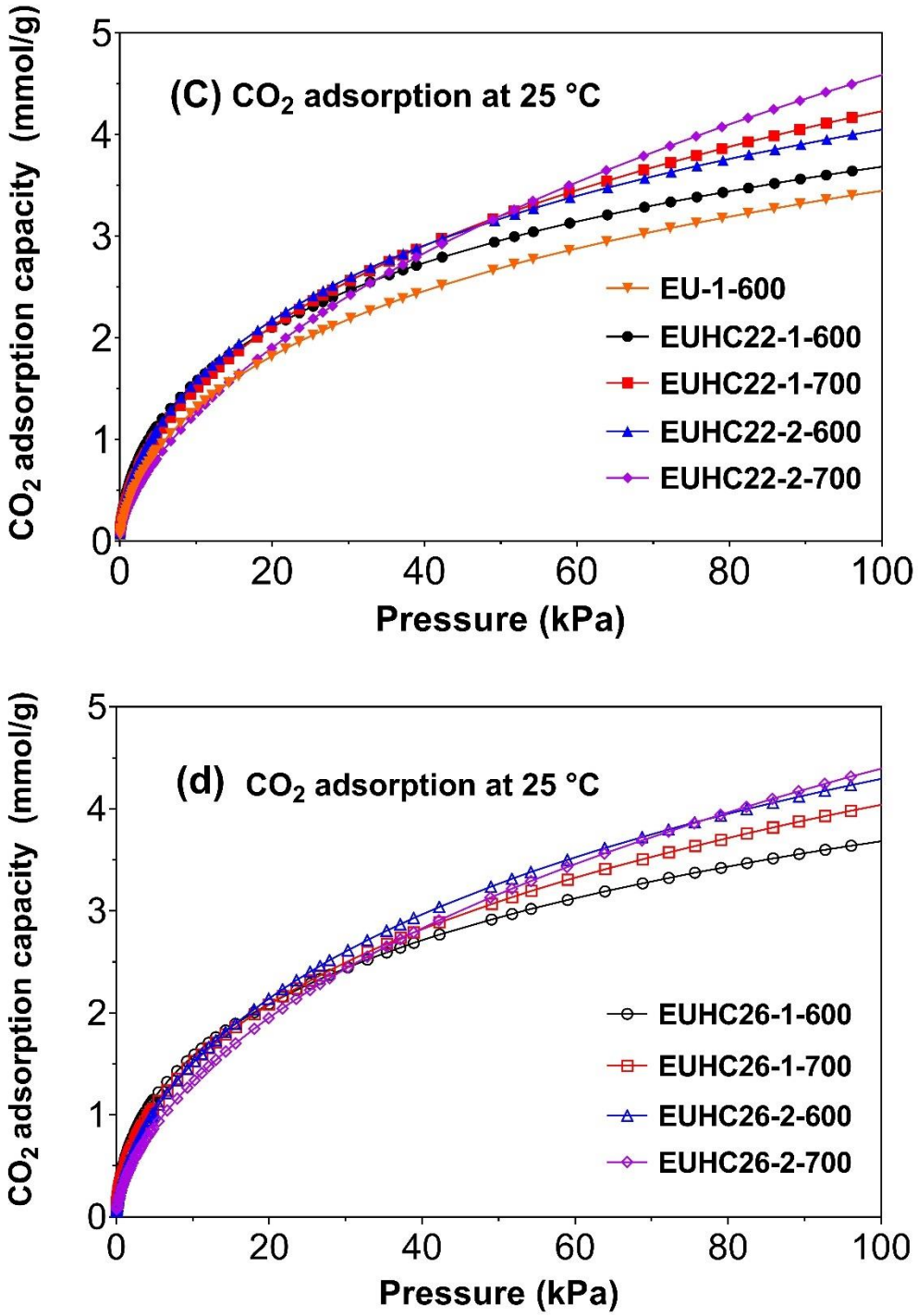


Figure 5.8 CO_2 adsorption isotherms EU- and EUHC22-derived carbons at (a) 0 °C (c) 25 °C and EUHC26-derived carbons at (b) 0 °C (d) 25 °C

In terms of activated carbons prepared under the HTC temperature of 220 ^{o}C, the CO_2 adsorption capacity substantially increased from 4.73 and 3.68 mmol/g to 6.73 and 4.59 mmol/g at 0 and 25 ^{o}C and 100 kPa, respectively, with the increasing KOH/EUHC mass ratio from 1 to 2 and activation temperature from 600 to 700 ^{o}C (Figure 5.8 a,c). By following a similar tendency as EUHC22 carbons, the CO_2 uptakes of EUHC26 carbons at 100 kPa were found to be overall comparable to those of EUHC22 carbons prepared at the same KOH activation protocol, with the highest CO_2 adsorption capacity reaching 6.35 and 4.40 mmol/g at 0 and 25 ^{o}C, respectively (Figure 5.8 b,d). It is evident that the CO_2 uptake of samples at 100 kPa generally followed the ranking of ultra-micropore volume, which is consistent with the findings of previous studies that CO_2 was preferable to be adsorbed in pores smaller than 1 nm at 100 kPa (Li et al., 2022b, Liu et al., 2020c). Among all the carbons, EUHC22-2-700 achieved the highest CO_2 adsorption capacity of 6.73 mmol/g at 0 ^{o}C and 100 kPa, which represents one of the best-performing biomass derived carbons via hydrothermal carbonization reported so far (Table 5.4). When the CO_2 partial pressure decreased to a low region of 15 kPa, it appeared that the variation of CO_2 adsorption capacity of both EUHC22- and EUHC26-derived carbons against the activation temperature and KOH/EUHC mass ratio was inconspicuous under mild activation conditions. At a CO_2 pressure of 15 kPa, sample EUHC22-2-600 exhibited superior high CO_2 adsorption capacities of 3.12 mmol/g and 1.91 mmol/g at 0 ^{o}C and 25 ^{o}C, respectively, which outperform most activated carbons and are even higher than some MOFs and porous organic polymers (Table 5.4). However, the CO_2 adsorption capacities of EUHC22 and EUHC26 carbons prepared at high severity of activation conditions (activation temperature = 700 ^{o}C; KOH/EUHC = 2:1) drastically decreased to 1.61 mmol/g and 1.66 mmol/g at 25 ^{o}C and 15 kPa, respectively, which is due to the reduction of ultra-microporosity as a result of enhanced KOH activation. It is noteworthy that the CO_2 capacities of EUHC derived carbons were generally higher than that of EU derived carbon prepared at the same activation conditions. Particularly at 25 ^{o}C and 15 kPa, the CO_2 uptake of EUHC22-1-600 (1.87 mmol/g) was approx. 20%

higher than that of EU-1-600 (1.59 mmol/g), which can be associated with the higher volume of ultra-micropores (<0.40 nm) in EUHC22-1-600.

However, the CO_2 uptake of EUHC carbons especially at low CO_2 partial pressure cannot be fully explained by the general textural properties as shown in Table 5.2. For instance, the EUHC22-2-700 carbon, which has the largest ultra-micropore volume of 0.380 cm^3/g, was found to have the highest CO_2 uptakes at 0 and 25 ^oC and a CO_2 pressure of 100 kPa but with the lowest CO_2 uptake of only 1.61 mmol/g at 25 ^oC and 15 kPa CO_2, amongst all carbon materials prepared. In sharp contrast, the EUHC26-1-600 carbon, which had the smallest ultra-micropore volume of 0.197 cm^3/g, was able to achieve a significantly higher adsorption capacity of 1.86 mmol/g in the same adsorption conditions.

Table 5.3 CO_2 adsorption capacity of EU- and EUHC-derived carbons

Sample	CO_2 uptake capacity, mmol-CO_2/g-ads			
	0 ^oC		25 ^oC	
	15 kPa	100 kPa	15 kPa	100 kPa
EUHC22-1-600	2.83	4.73	1.87	3.68
EUHC22-1-700	3.08	5.88	1.84	4.23
EUHC22-2-600	3.12	5.54	1.91	4.05
EUHC22-2-700	2.79	6.73	1.61	4.59
EUHC26-1-600	2.86	4.78	1.86	3.68
EUHC26-1-700	2.95	5.50	1.83	4.05
EUHC26-2-600	3.05	5.85	1.86	4.29
EUHC26-2-700	3.00	6.35	1.66	4.40
EU-1-600	2.58	4.59	1.59	3.45

In addition to the high CO_2 uptake capacity, the EUHC carbons also exhibited fast CO_2 adsorption kinetics with superior cyclic adsorption-desorption performance. Figure 5.9 displays the dynamic CO_2 adsorption profile and the cyclic adsorption/desorption performance for EUHC22-2-600, which was measured with TGA at 25 ^oC in a simulated flue gas containing 15% CO_2 in N_2. The selected carbon sample exhibited fast adsorption kinetics, with 90% of CO_2 equilibrium capacity completed in less than 4 min. Besides, the 50 cycles of continuous adsorption-desorption tests showed no obvious changes in CO_2 capacity, highlighting the superior adsorption reversibility and durability of carbons for practical applications.

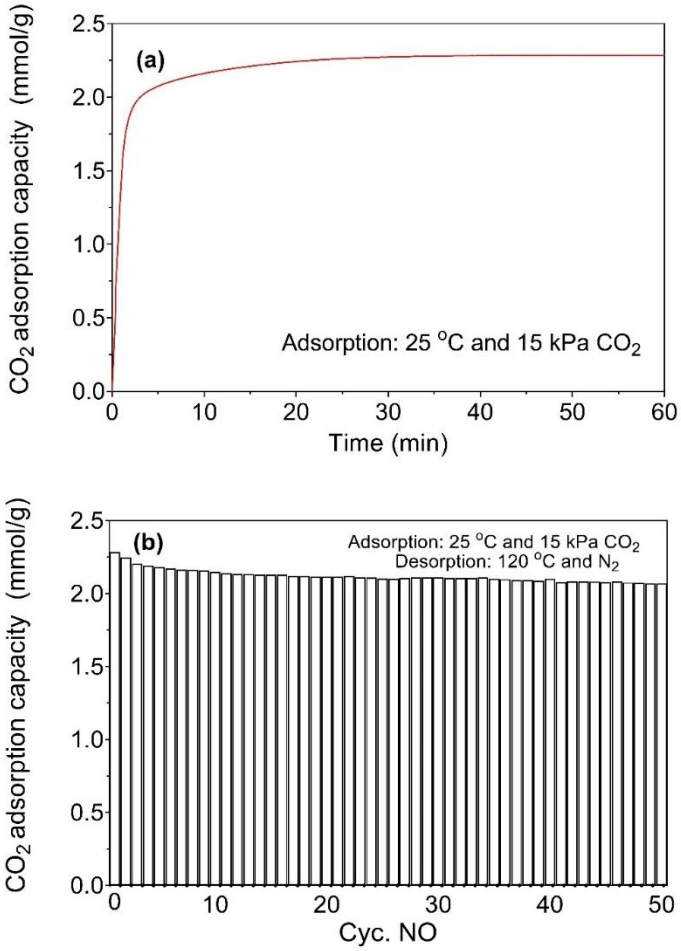


Figure 5.9 CO_2 adsorption curve and cyclic performance of selected samples (flue gases: 15% CO_2 + 85% N_2; adsorption temperature: 25^oC; desorption temperature: 120^oC)

Table 5.4 CO_2 adsorption capacity of biomass-derived activated carbon via hydrothermal carbonization

Precursor	Hydrothermal Temperature (°C)	CO_2 adsorption capacity				Refs
		15 kPa		100 kPa		
		0 °C	25 °C	0 °C	25 °C	
Eucalyptus wood	220	3.12	1.91	6.73	4.59	This work
Garlic peel	200	2.25	1.35	6.25	4.22	(Huang et al., 2019b)
Grass cuttings	N/A	1.92	1.05	4.02	2.75	(Hao et al., 2013)
Empty fruit bunch	250	1.75	1.25	5.23	3.71	(Parshetti et al., 2015)
Olive mill waste	200	1.55	1.19	3.52	3.00	(Gonzalez and Manya, 2020)
Jujun grass	250	N/A	1.50	N/A	4.90	(Coromina et al., 2016)
Camellia japonica	250	N/A	1.50	N/A	5.00	(Coromina et al., 2016)
Waste cornstalk	180	2.05	1.05	6.13	3.97	(Li et al., 2021)
Licorice residue	270	2.43	1.18	6.74	3.89	(Zhou et al., 2022)
Lotus stem	180	1.45	1.15	6.17	3.85	(Wu et al., 2018)
Tobacco stem	180	2.05	1.19	4.75	3.29	(Ma et al., 2022)
Tobacco stalk	220	2.58	1.34	6.64	4.30	(Huang et al., 2021)
Eucalyptus sawdust	230–250	2.00	1.25	6.60	4.80	(Sevilla and Fuertes, 2011)
Pinecones	220	1.55	1.45	3.20	2.90	(Kishibayev et al., 2021)
Metal–Triazolate Frameworks	N/A	2.90	1.80	4.46	3.34	(Shi et al., 2020)
Benzoxazole-based polymers	N/A	1.55	1.25	4.32	2.75	(Rabbani et al., 2017)

5.2.5 Role of textural properties and surface chemistry in CO_2 adsorption

It has been investigated in many studies that the narrow micropores can effectively strengthen the interaction between CO_2 molecules and carbon surface at the adsorption interface as a result of the superposition of the van der Waals forces imposed by the adjacent pore walls (Ashourirad et al., 2016, Liu et al., 2017, He et al., 2016). The overall CO_2 adsorption capacity of activated carbons was found to be closely related to the volume of pores with the critical pore size that varies with the CO_2 partial pressure and adsorption temperature. Therefore, the pore size effect over the CO_2 uptake capacity was also investigated in this chapter by plotting the cumulative volume of micropore less than a specific pore size against the CO_2 sorption capacity of carbon samples under different temperatures and CO_2 partial pressure (Figure 5.10). It can be observed in Figure 5.10a that the pores smaller than 0.7 nm are mainly responsible for CO_2 adsorption at 0 ^oC and 100 kPa, whereas the major contribution of CO_2 uptake originated from pores with diameters less than 0.6 nm when adsorption temperature increased to 25 ^oC as shown in Figure 5.10b. At a lower CO_2 partial pressure of 15 kPa, the unique pore size giving rise to the best correlation decreased significantly to 0.52 nm and 0.40 nm at 0 ^oC and 25 ^oC, respectively (Figure 5.10 (c,d)). The results revealed that the threshold pore in determining the CO_2 adsorption performance decreases with increasing adsorption temperature or decreasing CO_2 partial pressures, which agrees well with previous findings on carbon materials (Liu et al., 2017, Sevilla et al., 2013, Sethia and Sayari, 2015, Liu et al., 2019, Presser et al., 2011).

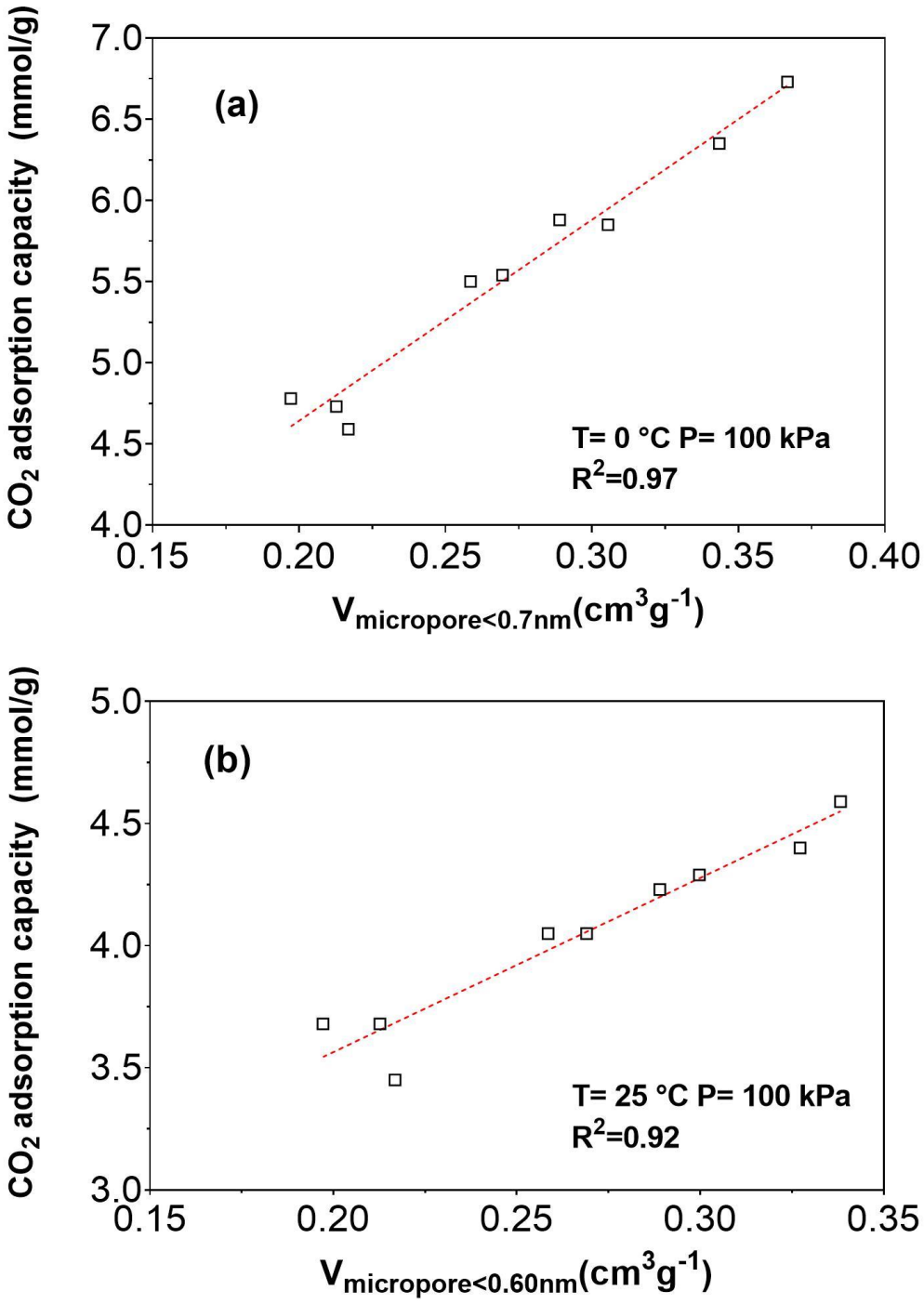


Figure 5.10 Relationship between CO_2 uptake and ultra-micropore volume of the EUHC-derived carbons: (a) 100 kPa CO_2 and 0 ^oC; (b) 100 kPa CO_2 and 25 ^oC; (c) 15 kPa CO_2 and 0 ^oC; (d) 15 kPa CO_2 and 25 ^oC

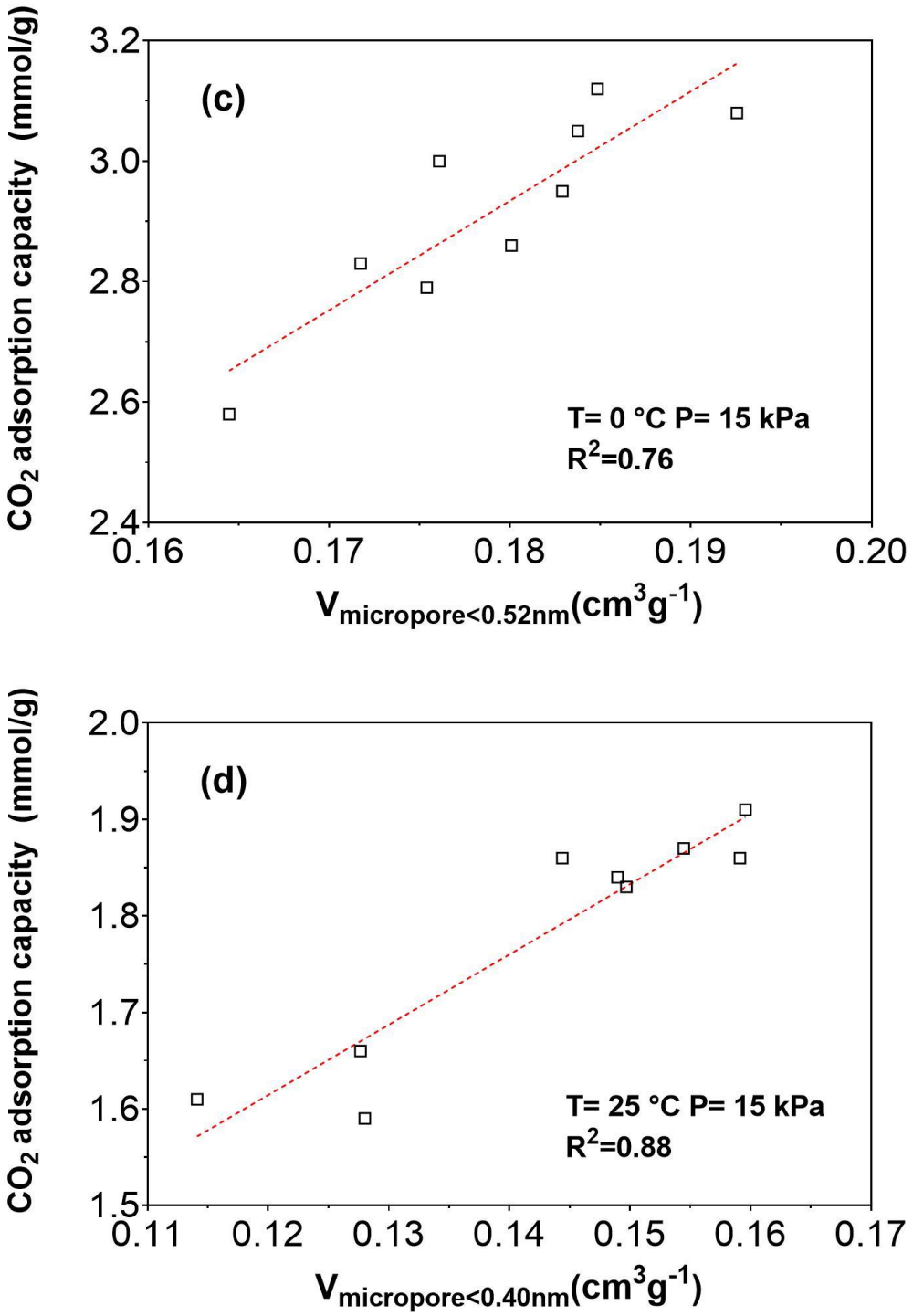


Figure 5.10 Relationship between CO_2 uptake and ultra-micropore volume of the EUHC-derived carbons: (a) 100 kPa CO_2 and 0 ^oC; (b) 100 kPa CO_2 and 25 ^oC; (c) 15 kPa CO_2 and 0 ^oC; (d) 15 kPa CO_2 and 25 ^oC

An examination of the literature shows that particularly at low CO_2 partial pressures, the CO_2 adsorption performance of the EUHC carbons greatly outperformed other biomass derived activated carbons and porous materials such as MOFs and zeolites reported so far (Table 5.4). It is evident that the superior CO_2 adsorption capacity of the EUHC-derived carbons at low CO_2 partial pressures cannot be only attributed to the contribution of ultra-micropore volumes, since other previously reported carbon materials possess relatively higher ultra-micropore volumes but own lower CO_2 uptake capacity at low CO_2 partial pressures. For instance, licorice-derived carbons achieved higher ultra-micropore volumes (0.495-0.671 cm^3/g) but performed much lower CO_2 adsorption capacities (0.68-1.18 mmol/g) than that of EUHC22-2-600 (1.91 mmol/g) at 25 ^oC and 15 kPa (Zhou et al., 2022).

Given that the EUHC-derived carbons are non-nitrogen doped, the carbon surface chemistry modified during the KOH activation process is assumed as another potential factor in promoting the CO_2 adsorption of prepared carbon samples. It has been demonstrated in our previous studies that the KOH activation gave rise to the intercalation of potassium species in the carbon framework, creating strongly bound potassium surface complexes presumably in the form of $O^{-\delta}$–$K^{+\delta}$ or extra-framework K^+ cations (Liu et al., 2015a, Liu et al., 2012b, Zhao et al., 2012). Consequently, the extra-framework K^+ cations presented in the carbon matrices can form strong local electric fields that are able to polarize CO_2 molecules and hence provide either additional active adsorption sites and/or enhance the interaction of the CO_2 molecules with the adsorption surface (Liu et al., 2017, Zhao et al., 2012). In this context, XRF analysis conducted for EUHC carbons demonstrated that all the samples contained a certain amount of potassium, varying from 3.30 to 8.76 wt% (Table 5.5). Figure 5.11 showed that the CO_2 uptakes at 25 ^oC and 15 kPa were closely correlated with the density of intercalated potassium (R^2=0.71). It is believed that a sound amount of potassium survived the extensive washing process and was deeply intercalated into the carbon skeleton in the form of extra framework cations K^+ ions, which is mainly responsible for the enhanced surface affinity to CO_2.

Table 5.5 Chemical analysis by XRF of EUHC carbons

Sample	K (wt.%)
EUHC22-1-600	8.23
EUHC22-1-700	7.92
EUHC22-2-600	8.29
EUHC22-2-600	3.30
EUHC26-1-600	7.20
EUHC26-1-700	8.76
EUHC26-2-600	5.77
EUHC26-2-700	5.55

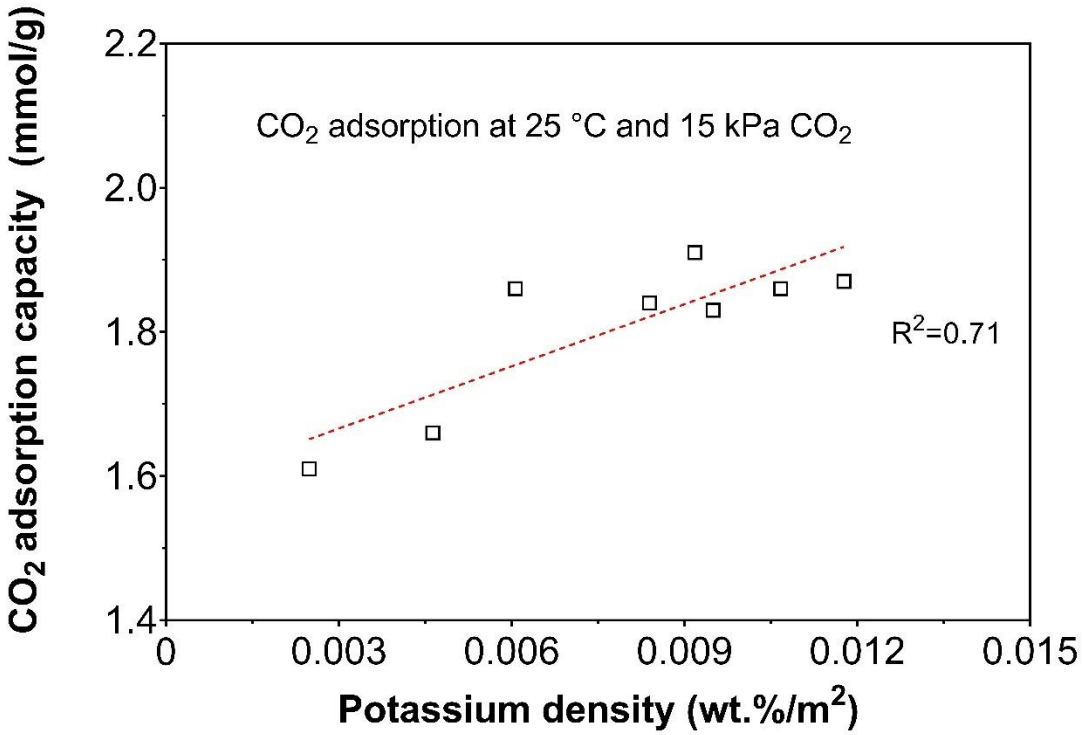


Figure 5.11 Relationship between CO_2 uptake and the density of intercalated potassium in the EUHC carbons.

5.2.6 Heat of CO_2 adsorption

To investigate the strength of interaction between CO_2 and the carbon surface of the prepared carbon samples, the isosteric heat (Q_{st}) of CO_2 adsorption was calculated from the CO_2 adsorption isotherms at 0 and 25 ^oC by using the Clausius-Clapeyron Equation. In consideration of the surface heterogeneity of the activated carbons created upon potassium intercalation, the dual-site Langmuir (DSL) equation was used in this work to fit adsorption isotherms and therefore the pure gas Q_{st} can be calculated by applying the Clausius-Clapeyron Equation to the DSL model. Hence, the interaction strength between CO_2 molecules and the carbon surface of activated carbons can be unveiled from the initial Q_{st} value at zero CO_2 coverage (0.01 mmol/g). Figure 5.12 shows the plots of Q_{st} as a function of CO_2 capacity for all the carbon samples. It can be found that the initial Q_{st} values of EUHC22 carbons vary between 31.1 and 37.8 kJ/mol, whereas EUHC26 carbons have high initial Q_{st} values ranging from 34.0 to 41.2 kJ/mol, which were higher than those obtained from nitrogen-doped activated carbon materials, porous polymers and even some MOFs (Zhou et al., 2022, Ma et al., 2018, Rabbani et al., 2017). Aside from the contribution of well-developed ultra-microporosity, the great improvement of the initial Q_{st} can be associated with the modified surface chemistry resulting from intercalated potassium in the form of highly polarizing extra-framework K^+ ions. Most notably, the initial Q_{st} values of carbon samples prepared via HTC were much higher than that of carbon without HTC treatment, which demonstrated the significant role of HTC in optimizing the textural properties and surface chemistry of carbon materials, thus leading to the consolidated interaction force between the carbon and the CO_2 molecules.

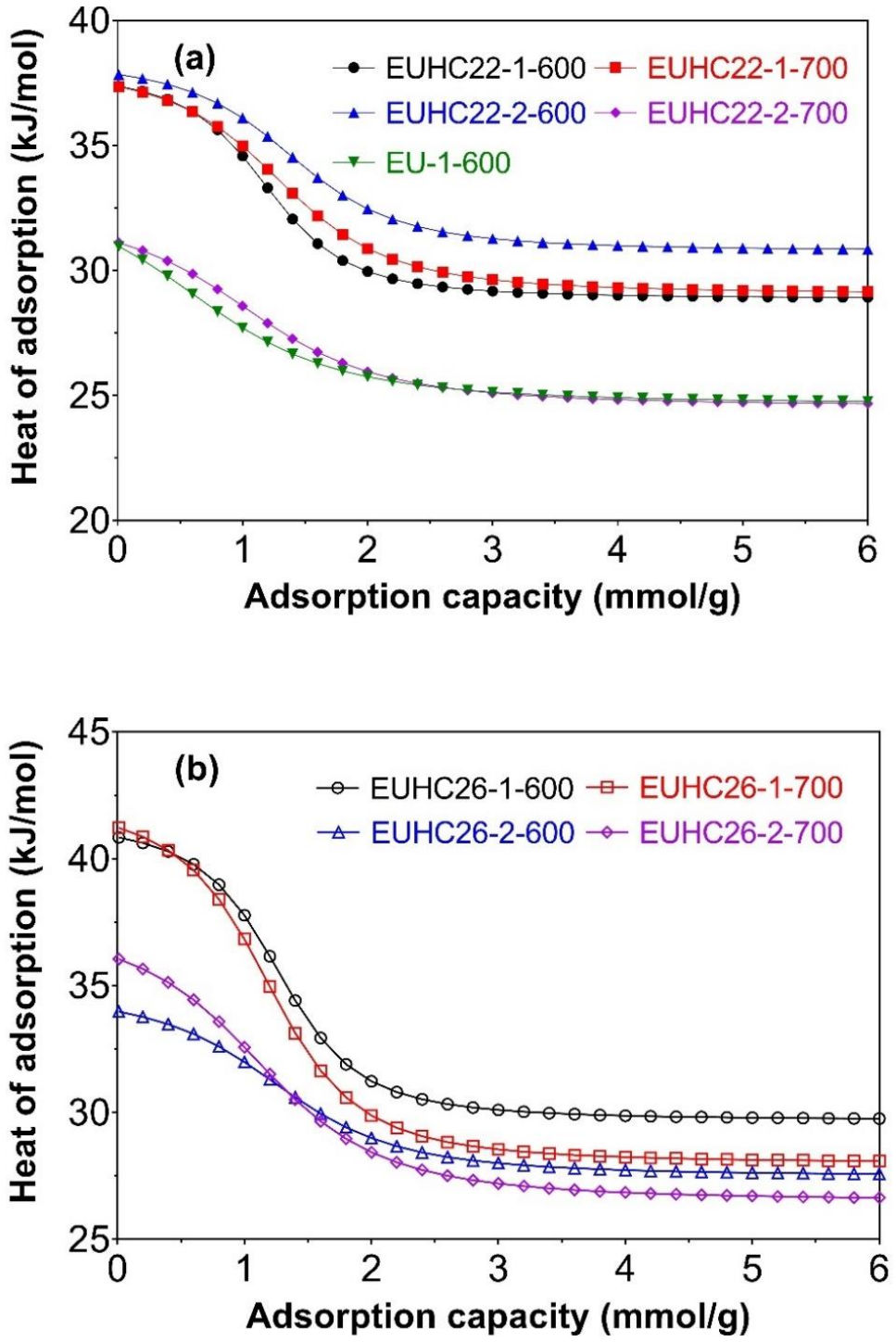


Figure 5.12 Isosteric heat of CO_2 adsorption calculated from the adsorption isotherms at 0 and 25 ^oC: (a) EUHC22 carbons; (b) EUHC26 carbons

5.2.7 CO_2/N_2 selectivity

In the development of activated carbon materials for carbon capture from flue gas, CO_2 selectivity needs to be taken into consideration aside from CO_2 uptake. Table 5.6 represents the IAST selectivity of CO_2/N_2 for EUHC carbons calculated by recording single-component isotherms of CO_2 and N_2 at 25 ^oC and 100 kPa, and then dividing the amount of adsorbed CO_2 at 15 kPa by the amount of adsorbed N_2 at 85 kPa according to the Equation 3.8. Therefore, the CO_2/N_2 adsorption selectivity of carbon samples in 15/85 mixture gases ranged from 20 to 35, with the EUHC22-2-600 sample having the highest selectivity value of 35, which is comparable to or higher than many kinds of porous carbons reported so far (He et al., 2021, Wang et al., 2020a, Li et al., 2017a). In comparison to the best performing kraft lignin derived carbons as discussed in Chapter 4, the carbon sample prepared via hydrothermal carbonization (EUHC22-2-600) had higher CO_2 selectivity despite the lower CO_2 adsorption capacity, indicating its higher ability to preferentially adsorb CO_2.

Table 5.6 CO_2 uptake at 25 ^oC, 15 kPa and IAST CO_2/N_2 selectivity

Sample	CO_2 uptake (mmol/g)	IAST CO_2/N_2 selectivity
EUHC22-1-600	1.87	33
EUHC22-1-700	1.84	25
EUHC22-2-600	1.91	35
EUHC22-2-700	1.61	20
EUHC26-1-600	1.86	33
EUHC26-1-700	1.83	27
EUHC26-2-600	1.86	27
EUHC26-2-700	1.66	21
KLK-1-600	2.01	33
OKLK-1-700	1.93	29

5.3 Conclusion

This chapter describes the synthesis of abundant and low-cost biomass wastes-based activated carbon adsorbents for effective CO_2 capture at flue gas conditions. The activated carbon was produced from eucalyptus waste through the sustainable HTC treatment followed by KOH activation. It appears that the HTC treatment tends to deliver desirable properties (e.g. high concentration of oxygenated functional groups) to hydrochar that are beneficial to promote chemical activation efficacy, leading to a higher porosity of hydrochar-derived carbons compared to that of samples without HTC treatment. With further increase of HTC temperature, the hydrochar was endowed with reinforced chemical stability and structure order due to the occurrence of enhanced aromatization reaction. The synthesized EUHC derived carbons are characterized by a high level of ultra-microporosity and unique surface chemistry, with EUHC22-2-600 processing the highest volume of narrow micropores (<0.40 nm) of 0.160 cm^3/g, resulting in a compelling high CO_2 uptake of 1.91 mmol/g at 25 ^oC and 15 kPa. It is also noteworthy that, under the same activation conditions, the carbon samples subjected to the pre-treatment of HTC exhibited up to 20% higher CO_2 adsorption capacity at 25 ^oC and 15 kPa than that of carbon prepared without HTC treatment. In addition, the intercalation of potassium species also played a key role in CO_2 adsorption and selectivity at low partial pressures by means of escalating the surface affinity towards CO_2 molecules. In this regard, our findings suggest that the involvement of HTC treatment in the KOH activation of biomass waste can be an effective approach to produce activated carbon materials with tailored textural properties and surface chemistry for CO_2 capture at flue gas conditions.

Chapter 6

FUNCTIONAL CARBON MATERIALS FROM HYDROTHERMAL CO-CARBONIZATION OF BIOMASS AND POLYVINYL CHLORIDE PLASTIC WASTE AND PERFORMANCE EVALUATION FOR CO_2 ADSORPTION

6.1 Introduction

In the previous chapter, HTC has been demonstrated as an effective means to convert biomass wastes to porous carbon materials with enhanced CO_2 adsorption properties. Apart from the conventional biomass wastes, appropriate HTC substrates may also include other organic solid wastes from municipal or industrial activities (Deb-Choudhury et al., 2014, Zhang et al., 2016b, Wang et al., 2019, Poerschmann et al., 2015, Zhao et al., 2018c). At present, polyvinyl chloride (PVC) remains one of the most abundant waste materials in building and construction, automotive, pipe and cable, bottles and packaging industries, inducing devastating environmental hazards associated with chlorine during its disposal by either landfill or incineration (Sadat-Shojai and Bakhshandeh, 2011). It has been proved that the organic chlorine in PVC could be effectively converted into inorganic water-soluble chlorine via HTC treatment (Kubatova et al., 2002, Poerschmann et al., 2015). As illustrated in Chapter 2, chlorine can be released from PVC by dechlorination reactions with the -OH nucleophilic substitution using water molecules as nucleophiles or dehydrochlorination reactions with HCl elimination. Thus, co-HTC of lignocellulosic biomass and PVC has been investigated in many studies to improve the dechlorination efficiency since the hydroxyl ions (−OH) supplied by the intermediate products (e.g. phenols and furfurals) of lignocellulose hydrolysis could enhance the substitution of the Cl bond in PVC (Shen et al., 2017, Lu et al., 2020a). However, most of the current work is aimed either at optimizing the synergistic effect on the dechlorination efficiency or producing hydrochar as a clean solid fuel. Considering the high carbon content, abundance, and low cost of PVC plastics, the conversion of PVC wastes into porous carbon materials has been considered not only as a potential recycling strategy but also as a means for valuable end-of-pipe product manufacture. To the best of our knowledge, no investigation has been carried out to use hydrochar from the hydrothermal co-carbonization (co-HTC) of biomass and PVC wastes for the production of activated carbons. In this Chapter, a series of activated carbons were prepared through co-HTC of biomass and PVC wastes followed by the KOH activation under different

conditions, with the physicochemical properties of hydrochars and textural and CO_2 adsorption properties of activated carbons being evaluated accordingly.

6.2 Results and discussion

6.2.1 Physicochemical properties of precursors and hydrochar

The physicochemical properties of the precursor materials (PVC, cellulose and kraft lignin) and their derived hydrochars are characterized by the ultimate analysis, proximate analysis and FT-IR analysis. Based on the proximate analysis as shown in Table 6.1, it can be seen that both physical and chemical properties of hydrochars were significantly altered through the hydrothermal treatment process. Prior to HTC, the raw PVC material showed volatile matters (VM) of 67.87 wt% and fixed carbon (FC) of 11.36 wt% as well as a notably high ash content of 20.67 wt% consisting of mainly calcium carbonate. Besides, CE was characterized by high VM content (92.38 wt%) and low FC content (4.22 wt%), whereas KL had relatively high FC content of 35.28 wt% and low VM content of 58.60 wt%. The hydrothermal treatment of PVC gave rise to an increase in fixed carbon of hydrochar, with the FC content consistently increasing from 12.94 to 29.17 wt% with the HTC temperature increased from 220 to 260 ^oC. Meanwhile, a 15.5 wt% increase in volatile matters was observed for PVC derived hydrochar obtained at the HTC temperature of 220 ^oC, which is associated with the large decrease in ash content from 20.67 to 3.17 wt% and chlorine content from 52.02 to 33.11 wt% (Table 6.2). The appreciable reduction of ash in hydrochar is presumably attributed to the reaction between the decomposed organochlorine in the form of HCl and the calcium carbonate ($CaCO_3$) in PVC, leading to the leaching of metal additive in the form of water-soluble calcium chloride ($CaCl_2$) (Wei et al., 2022). When the HTC temperature increased to 240 and 260 ^oC, the VM content decreased to 64.95 and 64.34 wt%, respectively, indicating the escalating degree of devolatilization as a result of recondensation reaction at higher HTC temperature. The hydrochars prepared from co-HTC treatment of PVC and biomass followed a similar trend as

PVC derived hydrochars. While the FC content of PVC/CE derived hydrochars was generally higher than that of PVC derived hydrochars produced at the same HTC temperature, varying from 15.84 to 35.15 wt% with the HTC temperature ranging from 220 to 260 ^{o}C, and the VM content decreased from 81.08 to 58.03 wt% correspondingly. Besides, co-hydrochars derived from KL and PVC possess the highest fixed carbon content in the range of 38.86 to 46.76 wt% and less volatile matters (43.29 - 57.04 wt%), which is ascribed to the high FC content in the raw KL as well as the aromatic structure of KL that is more reluctant to liquefaction (Wu et al., 2017).

Table 6.1 Proximate analysis of precursor materials and hydrochar samples

Sample	Proximate Analysis (wt%)			
	Moisture	**FC**	**VM**	**Ash**
PVC	0.11	11.36	67.87	20.67
CE	3.40	4.22	92.38	0.00
KL	3.29	35.28	58.60	2.31
PHC22	0.53	12.94	83.37	3.17
PHC24	0.74	26.60	64.95	7.71
PHC26	1.08	29.17	64.34	5.42
CEPHC22	0.54	15.84	81.08	2.55
CEPHC24	1.42	30.22	63.38	4.98
CEPHC26	1.90	35.15	58.03	4.92
KLPHC22	1.15	38.86	57.04	2.95
KLPHC24	1.96	41.65	48.41	7.98
KLPHC26	1.04	46.78	43.29	8.89

Additionally, as shown in Figure 6.1, the hydrochar yield was found to be affected by the HTC temperature and the type of feedstock used (the yields of hydrochar derived from cellulose and kraft lignin were also examined for comparison).

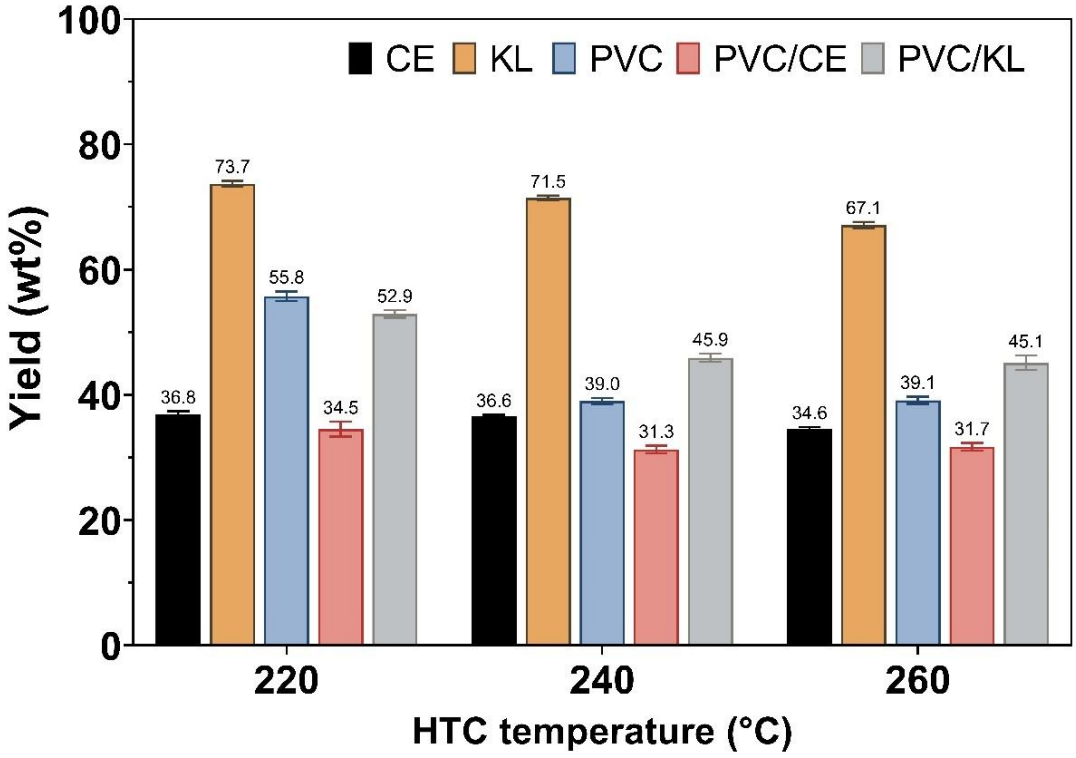


Figure 6.1 Yield of hydrochar derived from different feedstocks under different HTC temperature

As the HTC temperature increased from 220 to 240 ^{o}C, the yield of PVC hydrochar decreased rapidly from 55.8 to 39.0 wt%, which is mainly due to the dechlorination of PVC and formation of double bonds in polyene sequences (-(CH=CH)$_{n}$-) (Takeshita et al., 2004). When the HTC temperature further increased to 260 ^{o}C, polyene is first decomposed followed by the formation of hydrochar through the aromatization and polymerization of the decomposition products, leading to the barely changed solid yield (39.1 wt%). The co-hydrochars derived from PVC and biomass experienced a similar downward trend, where the hydrochar yields for PVC co-carbonized with CE and KL decreased from 34.5 to 31.7 wt% and 52.9 to 45.1 wt%, respectively, as the HTC temperature increased from 220 to 260 ^{o}C. It is also noteworthy that the yields of all co-hydrochars were considerably lower than the yields of the combination of hydrochar derived from each component. For

example, compared to the yield (55.3 wt%) of the combination of PVC and KL derived hydrochar prepared at 240 ^{o}C that is calculated by taking the average of each component derived hydrochar yield (39.0 wt% and 71.5 wt%), the yield (45.9 wt%) of co-hydrochar derived from PVC and KL was much lower. It might be inferred that the HCl produced from PVC dehydrochlorination can act as a catalyst to boost the hydrolysis of biomass material whilst the formation of hydroxyl radicals from the dehydration and demethylation of biomass could promote nucleophilic substitution reaction of PVC chlorine to release more HCl, resulting the lower product yield of co-hydrochar (Jiang et al., 2015, Ma et al., 2019a, Huang et al., 2019c).

The ultimate analysis of precursor materials and hydrochar samples is shown in Table 6.2. It is obvious that the carbon content of all hydrochar samples increased with increasing HTC temperature, indicating that the increased temperature enhanced the carbonization degree of hydrochars due to the hydrolysis, dehydration, and decarboxylation reactions during the HTC process (Li et al., 2020b). Specifically, the co-hydrochars derived from PVC and biomass prepared at 220 ^{o}C generally had higher carbon content (54.42 and 67.68 wt%) than that of PVC derived hydrochars (45.01 wt%), whereas no significant difference in their carbon contents was observed at HTC temperature over 240 ^{o}C. Interestingly, unlike the oxygen content of co-hydrochar decreased with the increasing HTC temperature due to the enhanced hydrolysis, dehydration, and decarboxylation of biomass fragments, the oxygen content of PVC derived hydrochar increased with an increase in HTC temperature, which could be attributable to the gradual −OH substitution of -Cl in the PVC (Ma et al., 2019a).

Table 6.2 XRF and Ultimate analysis of raw materials and hydrochar samples

Sample	Ultimate Analysis (dry basis)/wt%				XRF wt%	H/C	O/C
	C	H	N	O*	Cl		
PVC	22.95± 0.04	4.30± 0.09	0.06± 0.01	0	52.02	-	-
CE	42.82± 0.16	6.35± 0.13	0.14± 0.05	50.70± 0.16	0	1.78	0.89
KL	62.55± 0.13	5.28± 0.10	0.45± 0.01	29.41± 0.15	0	1.01	0.35
PHC22	45.01± 0.22	6.00± 0.17	0.18± 0.00	12.53± 0.25	33.11	1.60	0.21
PHC24	67.22± 0.65	6.59± 0.23	0.20± 0.00	13.08± 0.75	5.20	1.18	0.15
PHC26	71.65± 0.44	6.38± 0.11	0.23± 0.01	15.58± 0.43	0.74	1.07	0.16
CEPHC22	54.42± 0.34	6.18± 0.15	0.34± 0.10	17.55± 0.38	18.96	1.36	0.24
CEPHC24	71.81± 0.14	6.25± 0.05	0.33± 0.02	14.12± 0.16	2.51	1.04	0.15
CEPHC26	75.69± 0.16	6.50± 0.07	0.28± 0.02	11.72± 0.22	0.89	1.03	0.12
KLPHC22	67.68± 0.26	6.04± 0.10	0.42± 0.02	21.14± 0.20	1.77	1.07	0.23
KLPHC24	71.26± 0.16	5.63± 0.07	0.44± 0.00	11.81± 0.21	2.88	0.95	0.12
KLPHC26	72.44± 0.28	5.43± 0.13	0.44± 0.03	11.04± 0.38	1.76	0.90	0.11

Values are means of triplicates and ± is the standard deviation, * : by difference

The Van Krevelen diagram of the feedstock and hydrochar samples is given in Figure 6.2 to depict the chemical changes that occurred during the hydrothermal treatment. Being different from the reaction path of biomass (eucalyptus wood) as elaborated in Chapter 5, the hydrothermal evolution pathways of PVC and PVC/biomass feedstocks did not show significant decarbonization reactions in the Van Krevelen diagram. This was mainly due to the lower O and higher Cl contents of PVC that led to the occurrence of dechlorination reactions in the HTC, resulting in the unique reaction path of PVC in the HTC. In addition, the continuous decrease of H/C and O/C with the increasing HTC temperature indicated the aromaticity of the hydrochar increased, with higher HTC temperature promoting the formed hydrochars toward coal-like materials. Meanwhile, it was found that all co-hydrochars derived from PVC and biomass had higher carbonization degrees than

PVC derived hydrochar produced at the same HTC temperature, indicating the dehydration and decarboxylation were further promoted during co-HTC of PVC with biomass.

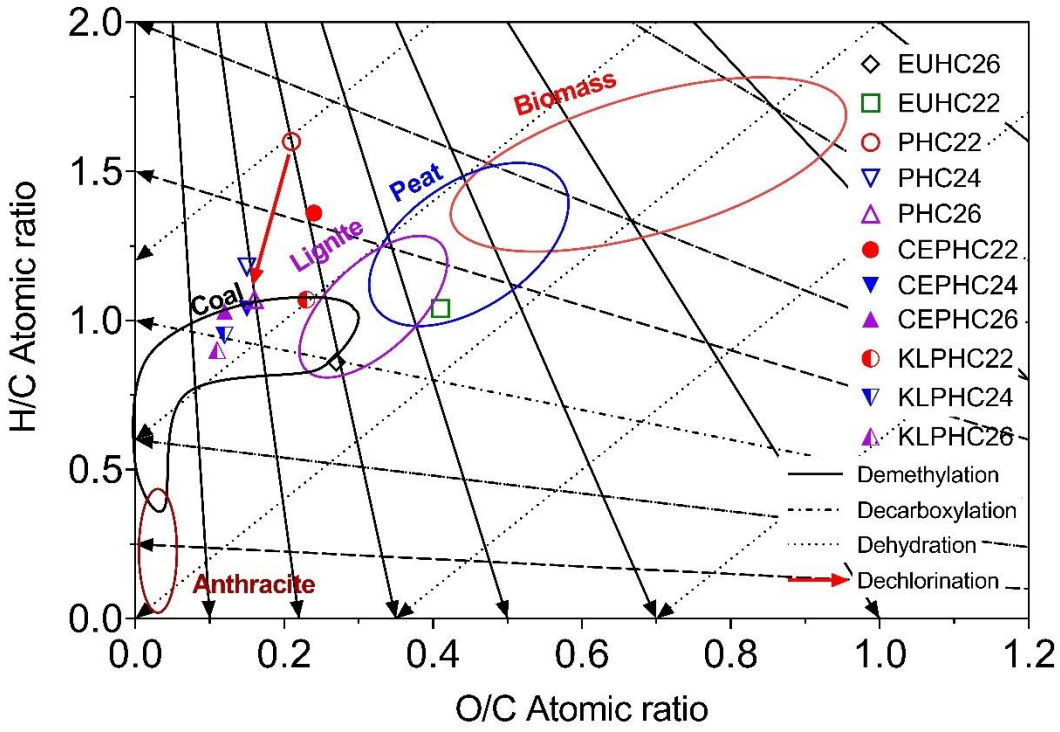


Figure 6.2 The Van Krevelen diagram of feedstocks and hydrochar samples

Studies have shown that organic chlorine in PVC could be effectively converted to inorganic chlorine via the HTC process in subcritical water (Kubatova et al., 2002, Poerschmann et al., 2015). Hence, the dechlorination efficiency (DE) of PVC in HTC is vital for the valorisation of hydrochar in the production of activated carbon. Figure 6.3 shows the dechlorination efficiency of PVC through HTC and co-HTC with biomass materials, which is calculated based on the XRF analysis results. It is evident that the HTC temperature and feedstock play important roles in the removal of chlorine from PVC. The hydrothermal carbonization of PVC at the HTC temperature of 220 ^{o}C gave rise to a relatively low DE of 64.5%. As the HTC temperature further increased to 240 ^{o}C and 260 ^{o}C, the DE of PVC increased to 96.1% and 99.4%, respectively. Meanwhile, the addition of biomass (CE and KL)

appeared to enhance the dechlorination efficiency of PVC in the co-HTC process, especially at the mild condition. Through the co-HTC of PVC with cellulose, the DE of PVC increased to 74.9% at the HTC temperature of 220 ^{o}C. Furthermore, replacing cellulose with kraft lignin greatly improved the chlorine removal from PVC during the co-HTC process, with the DE of PVC increased by 50% to achieve 96.40% at the HTC temperature of 220 ^{o}C. It is because of the aromatic structure of lignin which could provide excessive free -OH bonds from its hydrolysed phenolic substances during the HTC process and thus accelerating the dechlorination of PVC (Lu et al., 2020b, Shen et al., 2017). However, as the HTC temperature increased to 260 ^{o}C, the DE of PVC by the addition of KL appeared to be reduced, implying the insoluble lignin fragments that coated on the PVC surface may hinder the substitution of –Cl in PVC (Zhang et al., 2023b). The results are found to be consistent with previous studies, confirming the synergistic effect of lignocellulosic biomass on the enhancement of the PVC dechlorination in the co-HTC process, where the dehydration and demethylation of biomass led to the formation of hydroxyl groups and thus promoting the substitution of –Cl in PVC (Xue et al., 2022a, Huang et al., 2019c). Considering the preferential effect on dechlorination of PVC, co-HTC of biomass and PVC wastes holds a great potential to convert PVC waste into high-quality carbon precursors.

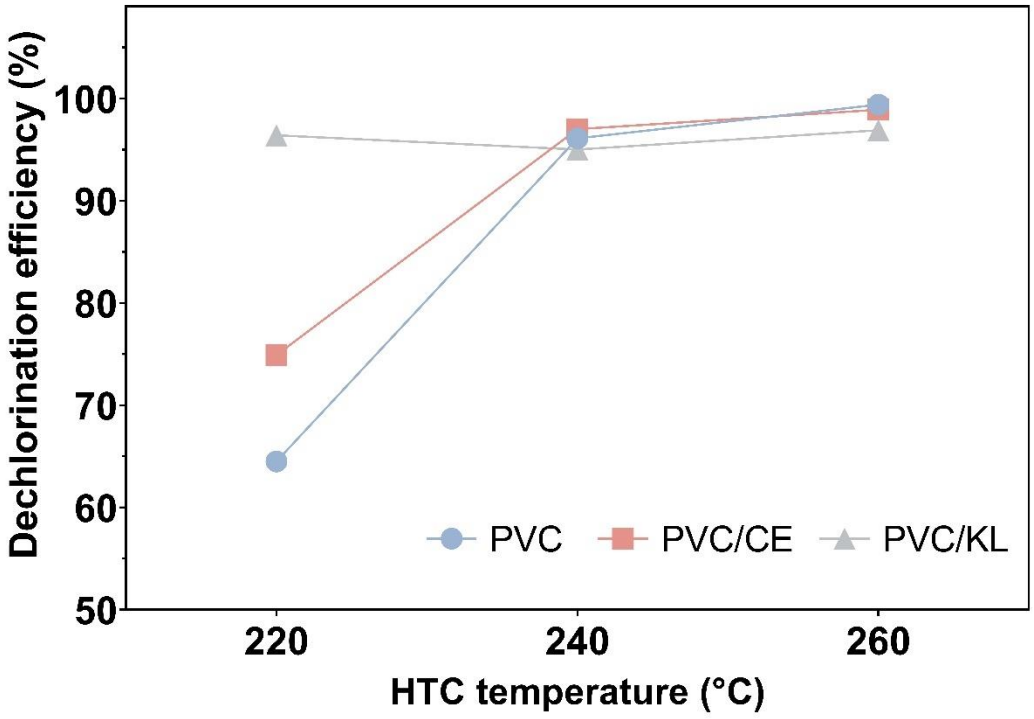


Figure 6.3 Dechlorination efficiency of PVC through HTC and co-HTC with biomass materials at different HTC temperatures

In order to further understand the chemical structural changes caused by the HTC, the surface functional groups of feedstocks and hydrochars were analysed by using FTIR. As displayed in Figure 6.4, considerable differences were observed over the feedstocks and HTC temperature, confirming the occurrence of chemical transformation during the HTC process.

1. The band at 1415 cm^{-1} in the spectra of PVC can be attributed to the C–H bending from –CHCl–, where the significant weakening of this peak intensity in all PVC and PVC/biomass hydrochars indicated that the skeletal carbon chain of PVC was destroyed as a result of dechlorination reaction. In addition, the decrease in the peaks at 875 cm^{-1} (corresponding to C–Cl stretching vibration in the halogenated alkane) confirmed that part of the chlorine had been removed during the HTC process (Yao and Ma, 2017, Zhang et al., 2019b).

2. The broad band around 3300 cm^{-1} in the biomass components (cellulose and lignin) was assigned to –OH stretching vibration in hydroxyl or carboxyl groups. The absorption peaks at 1030 cm^{-1} could be attributed to C–O bonds contained in the alcohol group of cellulose and the methoxy group of lignin (Xue et al., 2022b). It was clear that the –OH and C–O in the PVC/CE and PVC/KL hydrochars were consumed, which is indicative of the dehydration and/or substitution dechlorination that occurred as the HTC progressed.
3. Distinctions were also observed between hydrochars derived from using different feedstocks in terms of their surface functionality. Compared to the PVC hydrochar, the band at approximately 1720 cm^{-1} corresponded to the vibration of C=O (carboxyl and lactone) became more intense in the hydrochars. implying that substitution reactions by hydroxyl functional groups occurred during co-HTC, forming unstable intermediates, which then underwent oxidation or intramolecular dehydration to form a more stable structure (Xue et al., 2022b). However, this band completely disappeared in the PVC/KL hydrochars. While the peaks occurring at 1265-1210 cm^{-1} were only found in PVC/KL hydrochars, indicating that the formation of carbonyl C=O and ether C–O as a result of condensation reactions of the aromatic structures of kraft lignin during the co-HTC process (Zhang et al., 2023a).

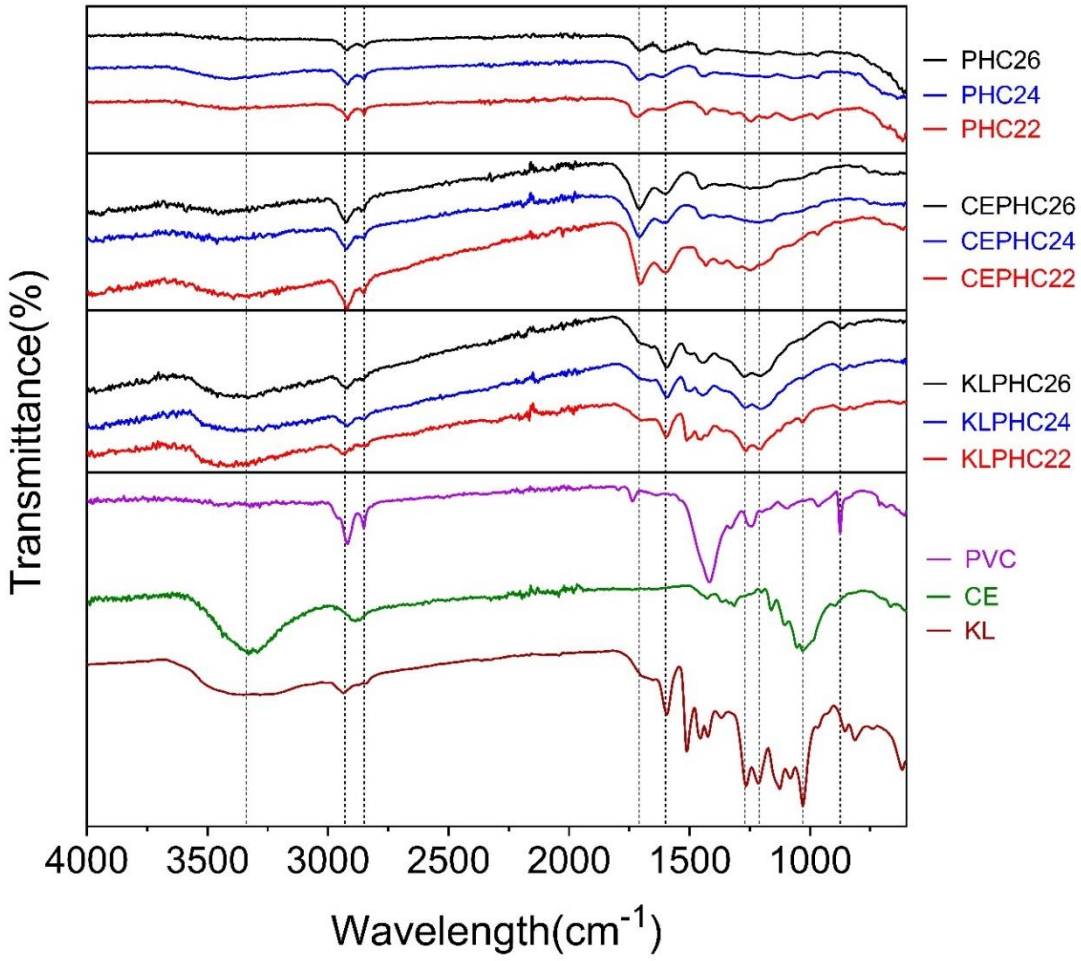


Figure 6.4 FT-IR spectra of feedstocks and hydrochar samples

6.2.2 Textural properties of activated carbons

Figure 6.5 shows the nitrogen isotherms of PVC derived carbons prepared from the protocol of hydrothermal carbonization followed by KOH activation under different conditions of HTC temperature varying from 240 to 260 ^{o}C, activation temperature ranging from 600 to 800 ^{o}C and KOH/PHC mass ratio from 1 to 2. It can be clearly seen that the nitrogen adsorption isotherms of all PHC derived carbons belong to Type I isotherms which are characterized by the large sharp N_2 uptake at low relative pressures below 0.1 followed by virtually horizontal plateaus at high relative pressures, indicating the extraordinary microporosity of PHC carbons. In addition, the emergence of narrow hysteresis loops at high relative

pressures suggests the presence of mesopores in both PHC24- and PHC26-derived carbons prepared at a higher KOH/PHC mass ratio of 2 or higher activation temperature of 800 ^{o}C. The hysteresis loops in the isotherms were found to be similar to Type H4, which is characteristic of narrow slit-like mesopores.

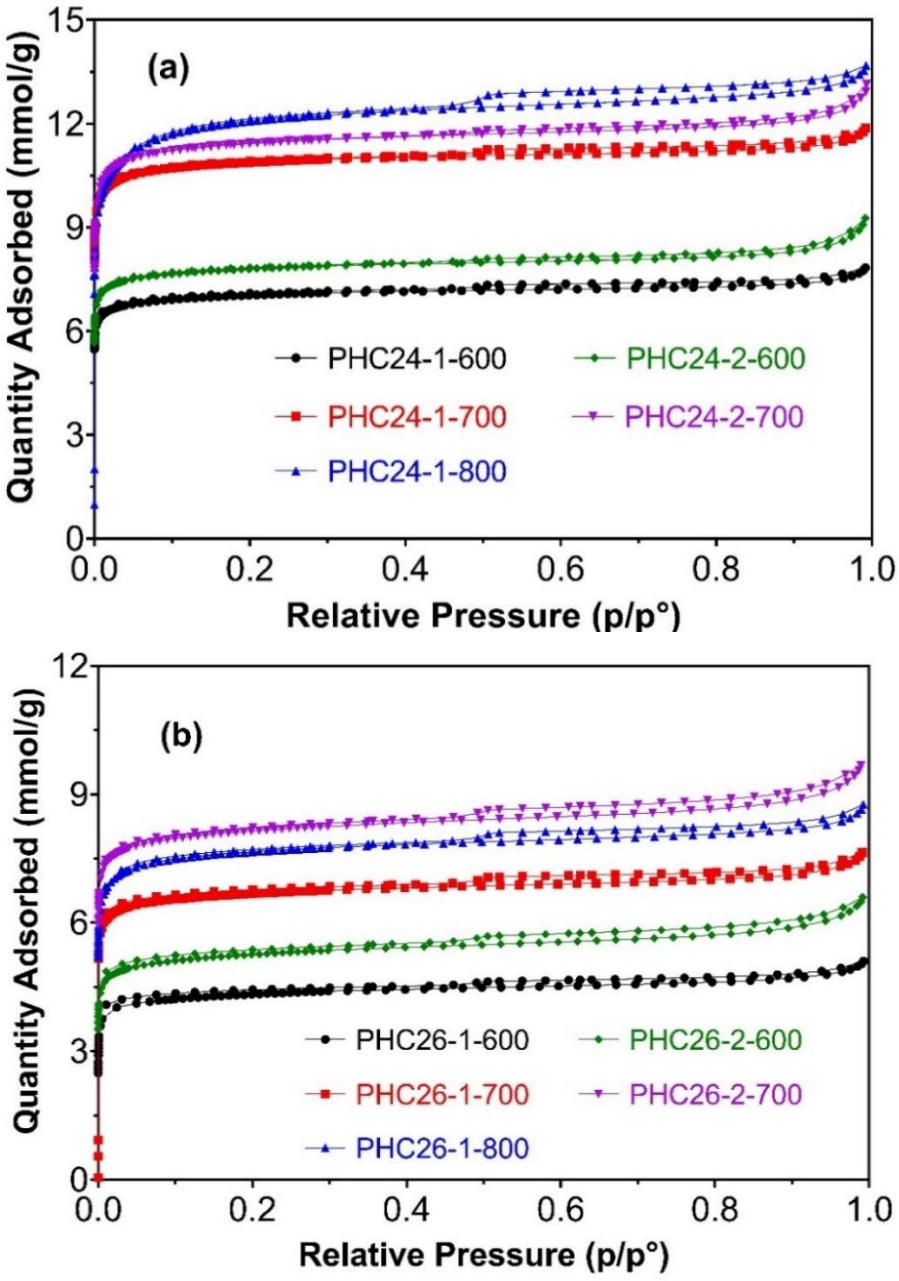


Figure 6.5 N_2 adsorption isotherms obtained at -196 ^{o}C for activated carbons derived from PVC under different HTC and activation conditions: (a) PHC24 carbons; (b) PHC26 carbons

Figure 6.6 presents the N_2 adsorption isotherms for activated carbons derived from PVC/CE and PVC/KL via co-HTC treatment. A similar trend with that of PVC-derived carbons was observed in the isotherms of carbons derived from hydrochars prepared by co-hydrothermal carbonization of cellulose and PVC, with all the isotherms being Type I isotherms, indicating the highly microporous nature. In terms of the carbons derived from PVC and KL via co-HTC, most of the samples, except for KLPHC26-1-600, showed a combination of Type I and Type IV isotherms with the large sharp uptake at low relative pressure followed by variable significant amounts of hysteresis at higher relative pressures, being indicative of micropore dominant structure with the pore size distributions ranging from micro to mesopores in the carbons. The appearance of a distinct type IV hysteresis loop suggested the presence of slit-like mesopores in the carbons.

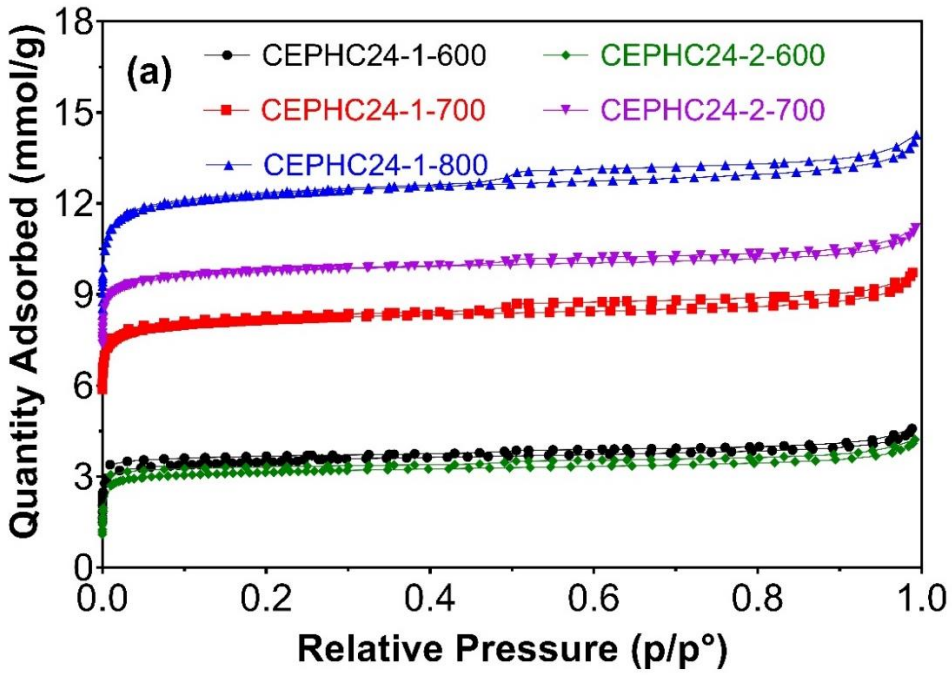


Figure 6.6 N_2 adsorption isotherms obtained at -196 °C for activated carbons derived from biomass and PVC under different HTC and activation conditions: (a) CEPHC24 carbons; (b) CEPHC26 carbons; (c) KLPHC24 and KLPHC26 carbons

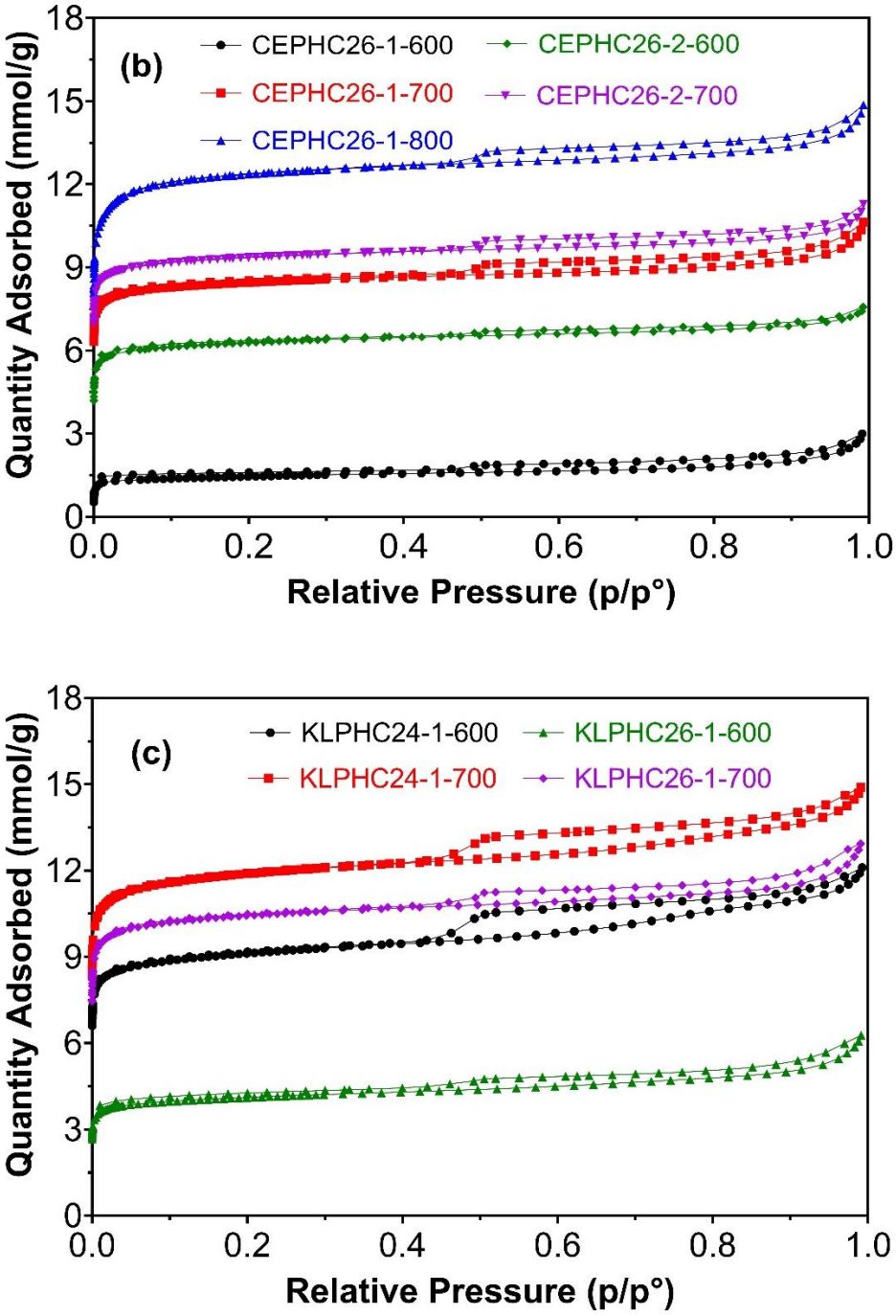


Figure 6.6 N_2 adsorption isotherms obtained at -196 °C for activated carbons derived from biomass and PVC under different HTC and activation conditions: (a) CEPHC24 carbons; (b) CEPHC26 carbons; (c) KLPHC24 and KLPHC26 carbons

The detailed textural properties of PVC derived carbon samples are listed in Table 6.3 and their pore size distributions are shown in Figure 6.7.

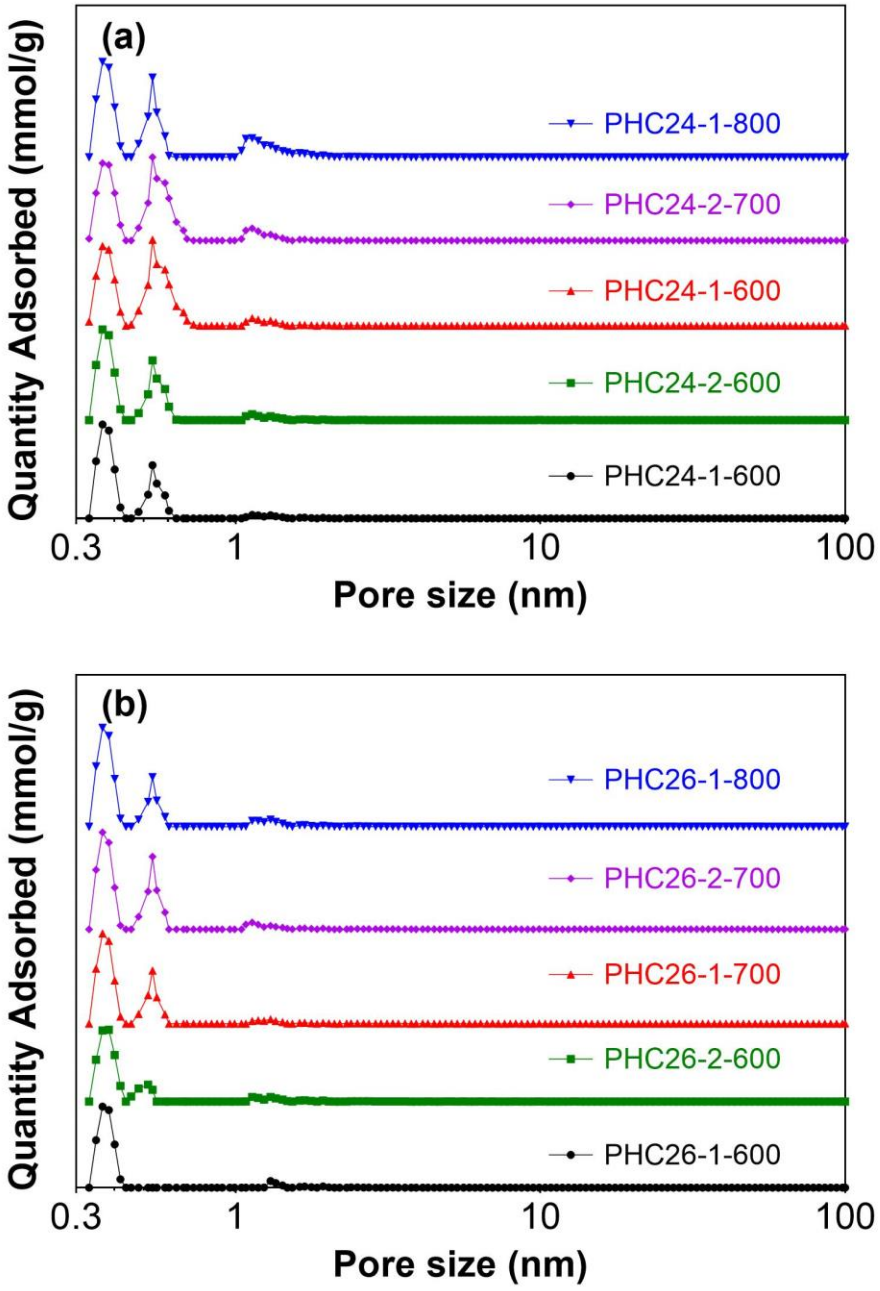


Figure 6.7 Pore size distributions (PSDs) of PVC-derived carbons via different HTC temperatures：(a) samples prepared at HTC temperature of 240 ºC; (b) samples prepared at HTC temperature of 260 ºC

Table 6.3 Specific surface areas, pore structure parameters of activated carbon derived from PVC hydrochars via different HTC temperatures

Sample	S_{BET}, m^2/g	V_{total}, cm^3/g	V_{micro}, cm^3/g	$V_{micro<0.7\ nm}$, cm^3/g	$V_{micro<0.40\ nm}$, cm^3/g	V_{micro}/V_{total}	$V_{micro<0.7\ nm}/V_{micro}$
PHC24-1-600	638	0.255	0.232	0.205	0.119	91	88
PHC24-1-700	991	0.379	0.356	0.310	0.106	94	87
PHC24-1-800	1058	0.439	0.392	0.235	0.121	89	60
PHC24-2-600	705	0.298	0.256	0.219	0.115	86	86
PHC24-2-700	1034	0.412	0.372	0.300	0.103	90	81
PHC26-1-600	383	0.165	0.139	0.110	0.107	84	79
PHC26-1-700	604	0.249	0.220	0.191	0.117	88	87
PHC26-1-800	687	0.284	0.251	0.197	0.128	88	78
PHC26-2-600	467	0.215	0.171	0.135	0.099	80	79
PHC26-2-700	732	0.316	0.267	0.225	0.122	84	84

At a given HTC temperature of 240 ^oC, the BET surface area and total pore volume of PVC derived carbons increased from 638 to 1058 m^2/g and 0.255 to 0.439 cm^3/g, respectively, when the activation temperature increased from 600 to 800 ^oC and the KOH/PHC mass ratio increased from 1 to 2. Likewise, the textural properties of carbon samples from using PVC derived hydrochars prepared at a higher HTC temperature of 260 ^oC experienced a similar effect from the activation conditions, with the BET surface area and total pore volume increased from 383 to 732 m^2/g and 0.139 to 0.267 cm^3/g with an increase of BET surface area and KOH/PHC mass ratio from 600 to 800 ^oC and 1 to 2, respectively. However, the higher HTC temperature appeared to induce the high aromaticity and low polarity (low H/C and O/C) in the hydrochar that inhibit the development of porosity of activated carbons, which can be reflected by the lower BET surface area and smaller total pore volume of PHC26 carbons compared to those of PHC24 carbons (Zhu et al., 2015). Additionally, the PHC-derived activated carbons were characterized by micropore-

dominant porous structure, with the microporosity accounting for up to 94% and 88% of the total porosity for PHC24 and PHC26 carbons, respectively. Meanwhile, the pore size distribution of PHC carbons obtained by applying the NLDFT method on their nitrogen isotherms at -196 ^{o}C and CO_2 isotherms at 0 ^{o}C are shown in Figure 6.7. It can be found that the microporosity was consisted mostly of ultra-micropores with pore diameter centred at 0.37 and 0.53 nm, which represents up to 88% of the total porosity.

Table 6.4 Specific surface areas, pore structure parameters of activated carbon derived from blended PVC/CE and PVC/KL via co-HTC at different conditions

Sample	$S_{BET,}$ m^2/g	V_{total}, cm^3/g	V_{micro}, cm^3/g	$V_{micro<0.7 nm}$, cm^3/g	$V_{micro<0.40 nm}$, cm^3/g	V_{micro}/V_{total}	$V_{micro<0.7nm}/V_{micro}$
PVC/CE carbon							
CEPHC24-1-600	306	0.150	0.113	0.113	0.111	75	100
CEPHC24-1-700	737	0.316	0.265	0.211	0.171	84	80
CEPHC24-1-800	1112	0.452	0.400	0.321	0.131	88	80
CEPHC24-2-600	279	0.136	0.093	0.090	0.087	69	97
CEPHC24-2-700	885	0.360	0.320	0.285	0.133	89	89
CEPHC26-1-600	124	0.093	0.065	0.065	0.065	70	100
CEPHC26-1-700	764	0.339	0.274	0.234	0.161	81	85
CEPHC26-1-800	1104	0.469	0.398	0.295	0.133	85	74
CEPHC26-2-600	558	0.244	0.203	0.158	0.137	83	78
CEPHC26-2-700	845	0.359	0.304	0.260	0.161	85	86
PVC/KL carbon							
KLPHC24-1-600	812	0.393	0.290	0.247	0.137	74	85
KLPHC24-1-700	1061	0.479	0.379	0.312	0.130	79	82
KLPHC26-1-600	362	0.205	0.125	0.123	0.114	61	98
KLPHC26-1-700	938	0.417	0.337	0.284	0.151	81	84

Table 6.4 summarises the surface textural properties of carbon samples derived from PVC and biomass via co-HTC at different HTC temperatures. In general, the textural structure parameters of activated carbons obtained via co-HTC are significantly influenced by the activation conditions (activation temperature and KOH/co-hydrochar mass ratio), HTC temperature and the type of feedstock used. In terms of the PVC/CE derived activated carbons at HTC temperature of 240 ^{o}C, the surface area and total pore volume substantially increased from 279 to 1112 m^2/g and 0.136 to 0.452 cm^3/g, respectively, as the activation temperature increased from 600 to 800 ^{o}C and KOH/co-hydrochar mass ratio increasing from 1 to 2, indicating an enhanced KOH activation effect. A similar trend was observed for the carbons obtained via a higher HTC temperature of 260 ^{o}C, with BET surface area and total pore volume considerably increased from 124 to 1104 m^2/g and 0.093 to 0.469 cm^3/g with the increasing severity of activation conditions. However, the HTC temperature appeared to have no distinct effect on the textural properties of PVC/CE derived carbons prepared at higher activation temperatures of 700 and 800 ^{o}C, which can be revealed by the almost identical surface area and total pore volume of CEPHC26 to that of CEPHC24 carbons. The result is likely to be associated with the similar degree of aromaticity and polarity in their parent hydrochars that resulted in the similar KOH etching effect. Moreover, it is noticeable that the KOH activation gave rise to the formation of highly micropore-dominant structure in all the PVC/CE co-hydrochar derived carbon samples, with the microporosity accounting for 69-89% and 70-85% of total pore volume for CEPHC24- and CEPHC26-derived carbons, respectively. In addition, the pore size distribution of PVC/CE derived carbons calculated by the combination of N_2 isotherm and CO_2 isotherms at 0 ^{o}C were illustrated in Figure 6.8 (a,b). It is evident that all the carbon samples are micropore-dominant structures with pore size centred at 0.37 and 0.53 nm while the relative significance of different micropores is mainly varied with the activation temperature and KOH/CEPHC mass ratio. At a lower activation temperature of 600 ^{o}C, the carbon samples experienced different KOH/CEPHC mass ratios and HTC temperatures followed unimodal distribution, with pore size centred at 0.37 nm. The increase in activation temperature and

KOH/CEPHC mass ratio led to the emergence of a bimodal pore size distribution, with the volume of micropores centred at 0.53 nm increased with the increasing severity of activation conditions, indicating that the formation of larger micropores due to the progressive pore widening effect led by the reinforced activation activity.

Interestingly, the substitution of KL for CE in co-hydrochar preparation with PVC appeared to generate a more developed porosity in PVC/KL derived carbons than that of PVC/CE derived carbons produced at the same HTC and activation temperature regardless of the higher aromaticity of their parent hydrochar materials, with the surface area and total pore volume varying from 362 to 1061 m^2/g and 0.205 to 0.479 cm^3/g, respectively. It was believed that the presence of insoluble lignin prohibited the aggregation of co-hydrochar particles that may allow the more pronounced KOH etching to occur (Lu et al., 2020). Besides, the development of porosity in the chemically activated carbons could also be affected by the oxygen functional groups in the hydrochar precursor (Jain et al., 2016). According to the FT-IR results, weak acidic functionalities (such as carbonyl and ether) presented in the PVC/KL co-hydrochars, which will be thermally decomposed to CO, thus resulting in higher porosity in the activated carbons (Lillo-Rodenas et al., 2003, Kim et al., 2019). The PVC/KL co-hydrochar derived carbon samples otherwise were still characterized by high microporosity, with the microporosity contributing 74-79% and 61-81% of the total pore volume of KLPHC24- and KLPHC26-derived carbons, respectively. The pore size distribution of KLPHC carbons (Figure 6.8 c) shows that the carbon samples prepared at a lower activation temperature of 600 ^oC exhibited narrower microporosities with ultra-micropores (0.37 nm and 0.53 nm) being dominant. The increase in activation temperature led to the increased volume of micropores centred at 0.53 and 1.2 nm, indicating the formation of larger micropores with broader size distribution in the carbons.

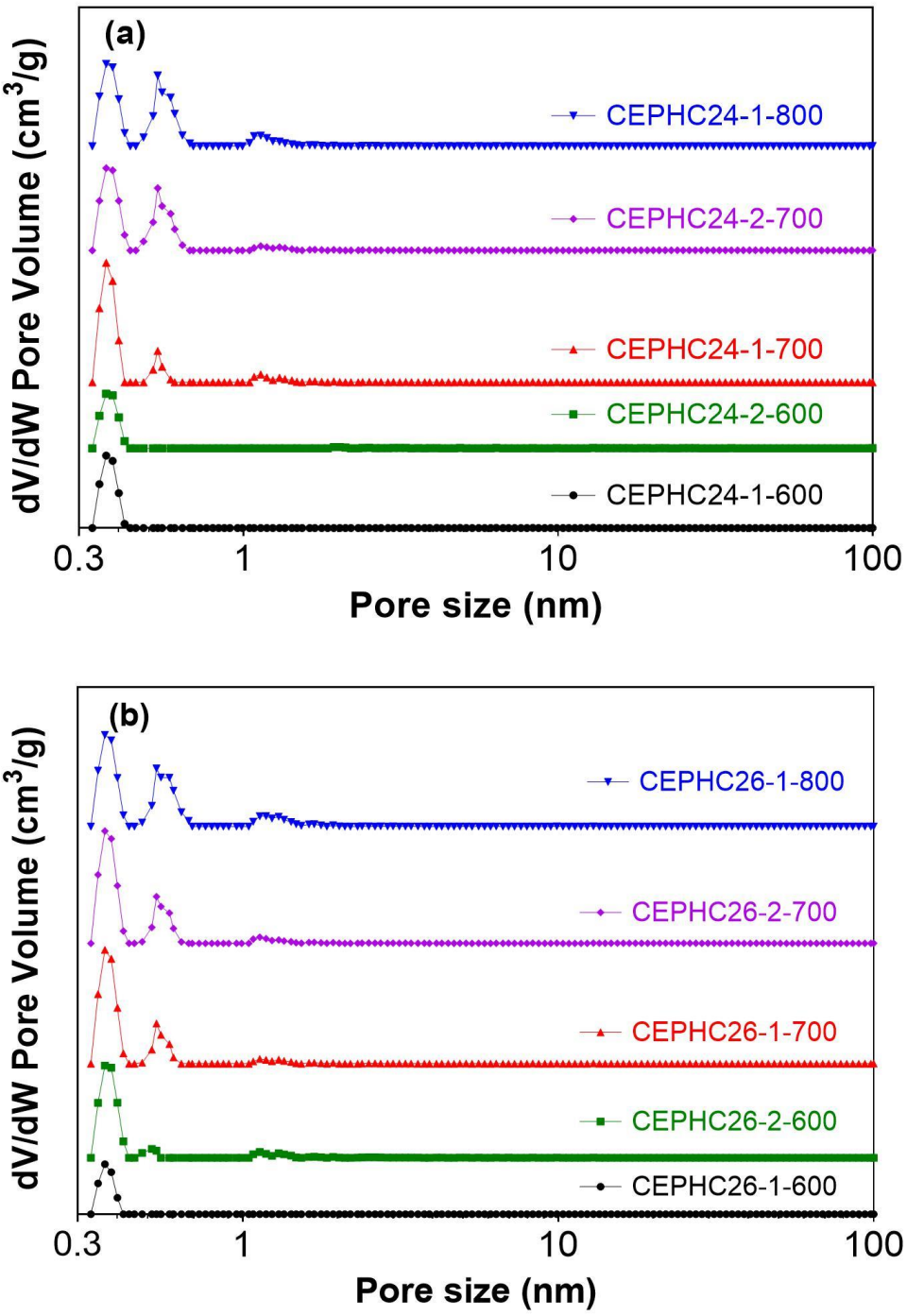


Figure 6.8 Pore size distributions (PSDs) of CEPHC and KLPHC-derived carbons; (a) CEPHC24 carbons; (b) CEPHC26 carbons; (c) KLPHC carbons

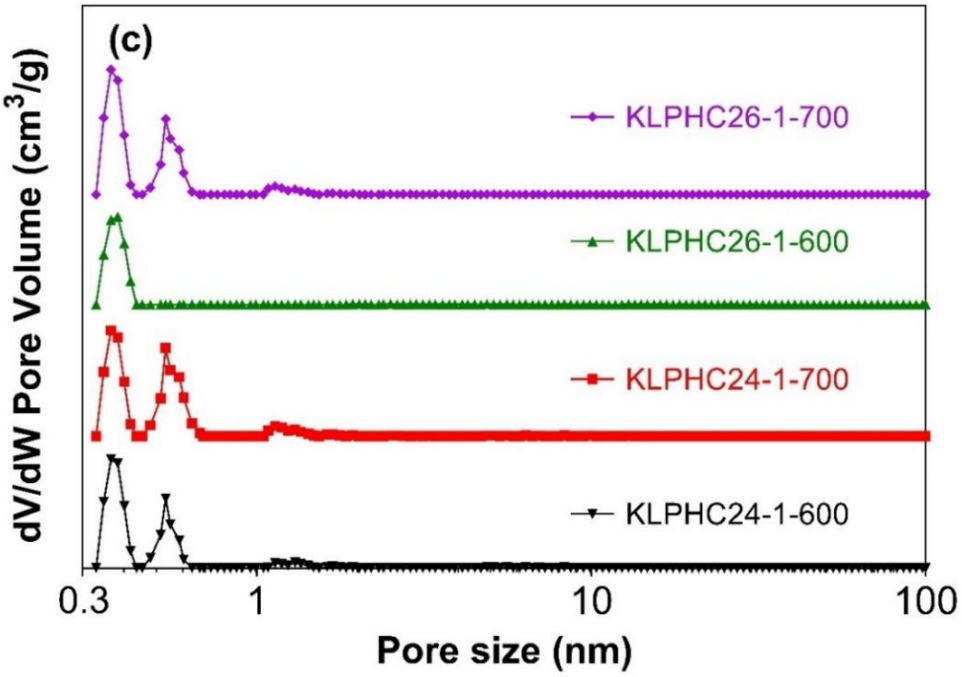


Figure 6.8 Pore size distributions (PSDs) of CEPHC and KLPHC-derived carbons; (a) CEPHC24 carbons; (b) CEPHC26 carbons; (c) KLPHC carbons

6.2.3 Morphology of hydrochar and activated carbons

Figure 6.9 shows the morphology of hydrochar samples derived from PVC, blended PVC/CE and PVC/KL under different HTC temperatures. It is apparent that the hydrochars subjected to the different HTC scenarios exhibited significant differences in terms of surface topography. Under the HTC temperature of 220 ^{o}C, the PVC substrates in all hydrochar samples were partially destructed, with irregular depressions and fragmentary pores being created due to the dechlorination, whereas the co-hydrochar samples involved the agglomeration of cellulose and lignin hydrolysates on the PVC chars (Figure 6.9 (a,d,g)). It is noticeable that large amounts of spherical microparticles existed in the KLPHC22, which is presumably due to the existence of π–π interactions of the aromatic rings between lignin molecules that led to the formation of nanospheres (Xiong et al., 2017, Wikberg et al., 2015). As the HTC temperature increased to 240 and 260 ^{o}C,

the structure of PVC fractions in hydrochars became more porous with the increasing HTC temperature due to the enhanced dechlorination and decomposition reactions that occurred (Figure 6.9 (b,c,e,f,h,i)). Besides, the co-HTC with the addition of PVC at higher temperatures promoted further decomposition of cellulose into smaller fragments, while the spherical hydrochars derived from lignin still remained and attached as an integral part of co-hydrochars.

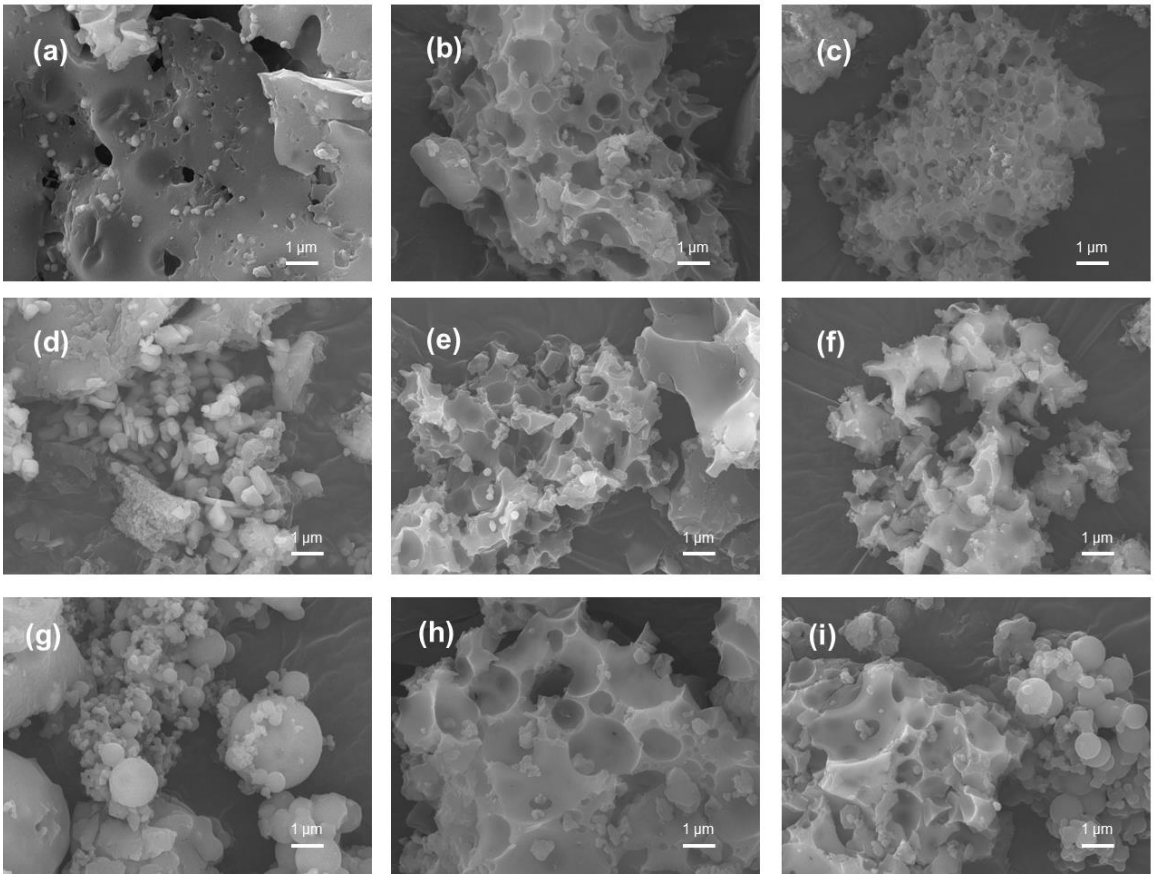


Figure 6.9 SEM images of hydrochars; (a) PHC22; (b) PHC24; (c) PHC26; (d) CEPHC22; (e) CEPHC24; (f) CEPHC26; (g) KLPHC22; (h) KLPHC24; (i) KLPHC26

The morphology of PVC hydrochar and PVC/biomass co-hydrochar derived activated carbons is presented in Figure 6.10. Apparently, KOH activation led to the pronounced loose structure in the activated carbon samples compared to their parent hydrochars, with the carbon morphology varying substantially with the

activation severity, type of feedstocks and HTC temperature. In specific, the CEPHC24-1-600 and KLPHC24-1-600 appeared to exhibit denser structures compared to PHC24-1-600 samples, which is presumably attributable to the agglomerated structure of co-hydrochars that prevent the KOH etching at the mild activation condition. However, all the activated carbons prepared at higher activation temperatures showed broadly distributed irregular voids and well-developed porous networks, indicating the enhanced KOH etching effect caused by the severe activation condition.

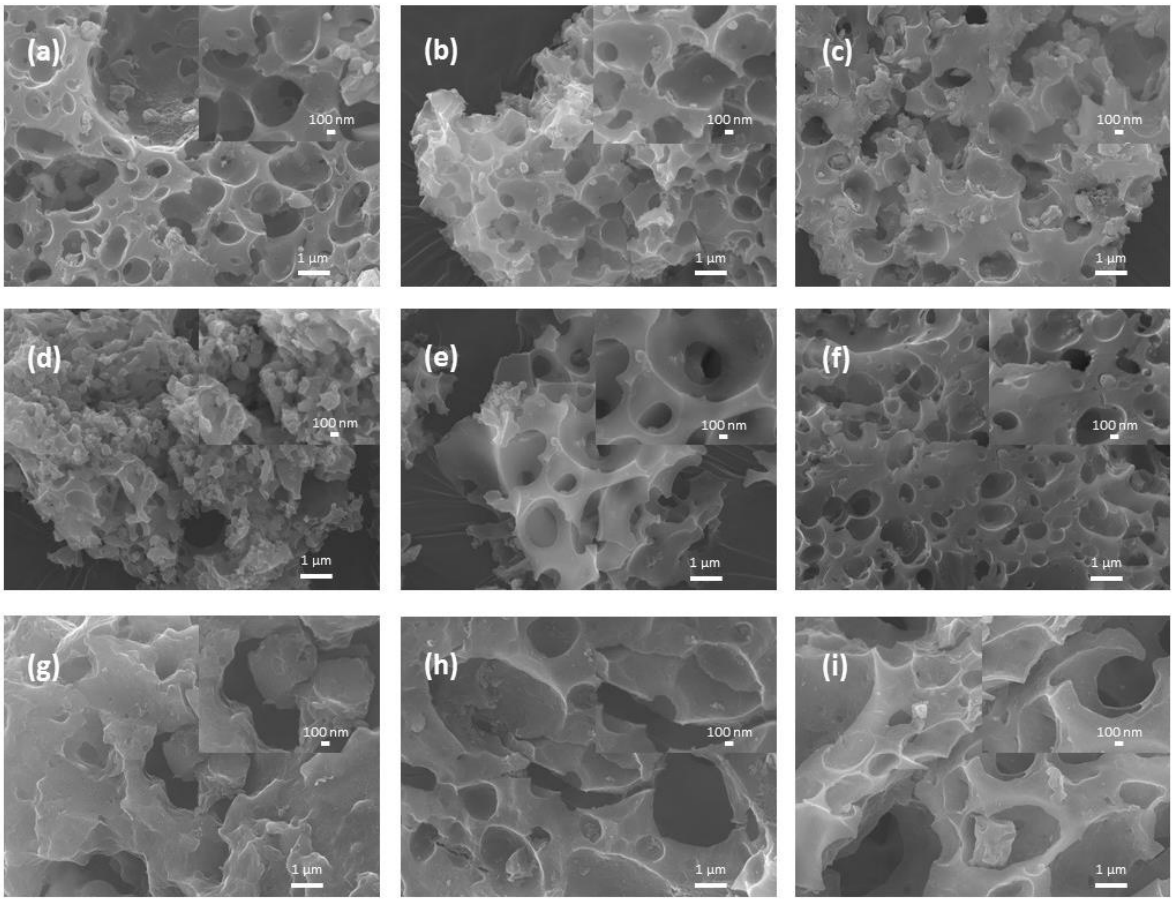


Figure 6.10 SEM images of hydrochars derived carbons; (a) PHC24-1-600; (b) PHC24-1-700; (c) PHC26-1-700; (d) CEPHC24-1-600; (e) CEPHC24-1-700; (f) CEPHC26-1-700; (d) KLPHC24-1-600; (e) KLPHC24-1-700; (f) KLPHC26-1-700

6.2.4 CO_2 adsorption properties of PVC-derived carbons prepared via HTC

The CO_2 adsorption isotherms of carbon samples derived from PVC hydrochars were investigated at 0 ^oC and 25 ^oC up to 100 kPa (Figure 6.11). Clearly, the CO_2 uptake of the prepared samples was affected by the activation temperature, amount of KOH used and HTC temperature. At CO_2 partial pressure of 100 kPa, the CO_2 adsorption capacity of PHC24-derived carbons at 0 ^oC and 25 ^oC increased from 4.22 to 5.47 mmol/g and 3.15 to 3.68 mmol/g, respectively, when the activation temperature increased from 600 to 700 ^oC at a given KOH/PHC mass ratio of 1. While increasing activation temperature from 700 to 800 ^oC and KOH/PHC mass ratio from 1 to 2 led to a decrease in CO_2 adsorption capacity. In contrast, the CO_2 uptake of PHC26-derived carbons consistently increased from 3.17 to 4.68 mmol/g and 2.42 to 3.41 mmol/g at 0 ^oC and 25 ^oC, respectively, with the increasing activation severity. However, the CO_2 performance of PHC26 samples prepared at higher HTC temperature of 260 ^oC is overall lower than that of PHC24 carbons produced at an HTC temperature of 240 ^oC. According to Table 6.3, the CO_2 adsorption capacity of carbon samples prepared at different activation conditions generally increases with the increasing ultra-micropore volume ($V_{micro<0.7\ nm}$), indicating the governance of ultra-micropore volume on the CO_2 adsorption capacity. At a low CO_2 partial pressure of 15 kPa, no obvious difference was observed for PHC24-derived carbon in terms of CO_2 uptake, with PHC24-1-800 exhibiting the highest CO_2 adsorption capacity of 2.46 and 1.53 mmol/g at 0 ^oC and 25 ^oC, respectively. As for the PHC26-derived carbons, the CO_2 adsorption capacity at 15 kPa CO_2 followed a similar trend as that at 100 kPa CO_2, with PHC-1-800 reaching the highest CO_2 uptake of 1.59 mmol/g at 25 ^oC among all the PVC-derived carbons prepared via HTC. The variation of CO_2 uptake capacity with the adsorption temperature and CO_2 partial pressure appeared to be associated with the ultra-micropores with a specific pore size that was produced at different HTC and activation protocols.

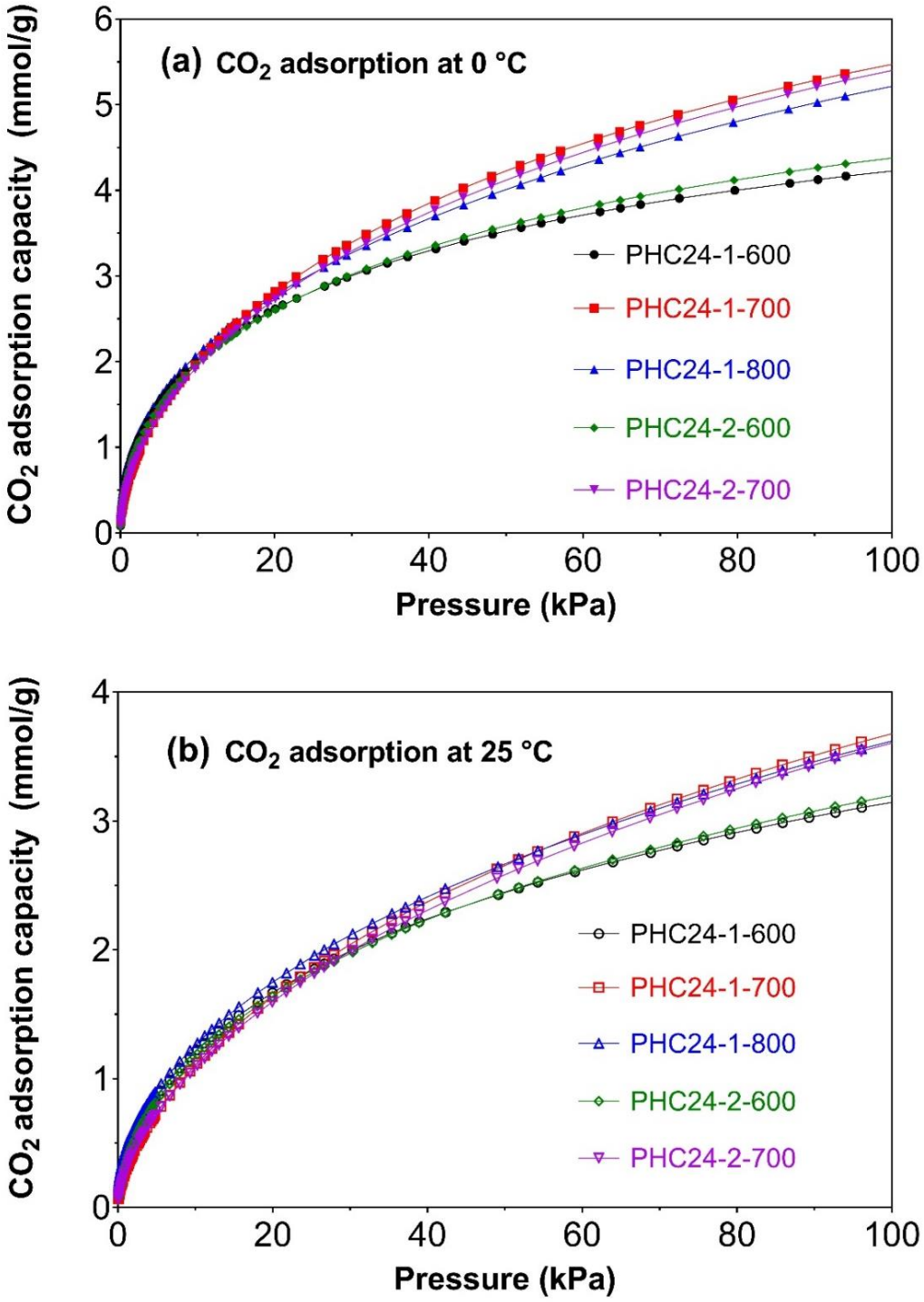


Figure 6.11 CO_2 adsorption profiles of PHC24-derived carbons at: (a) 0 ºC (b) 25 ºC and PHC26-derived carbons at (c) 0 ºC (d) 25 ºC.

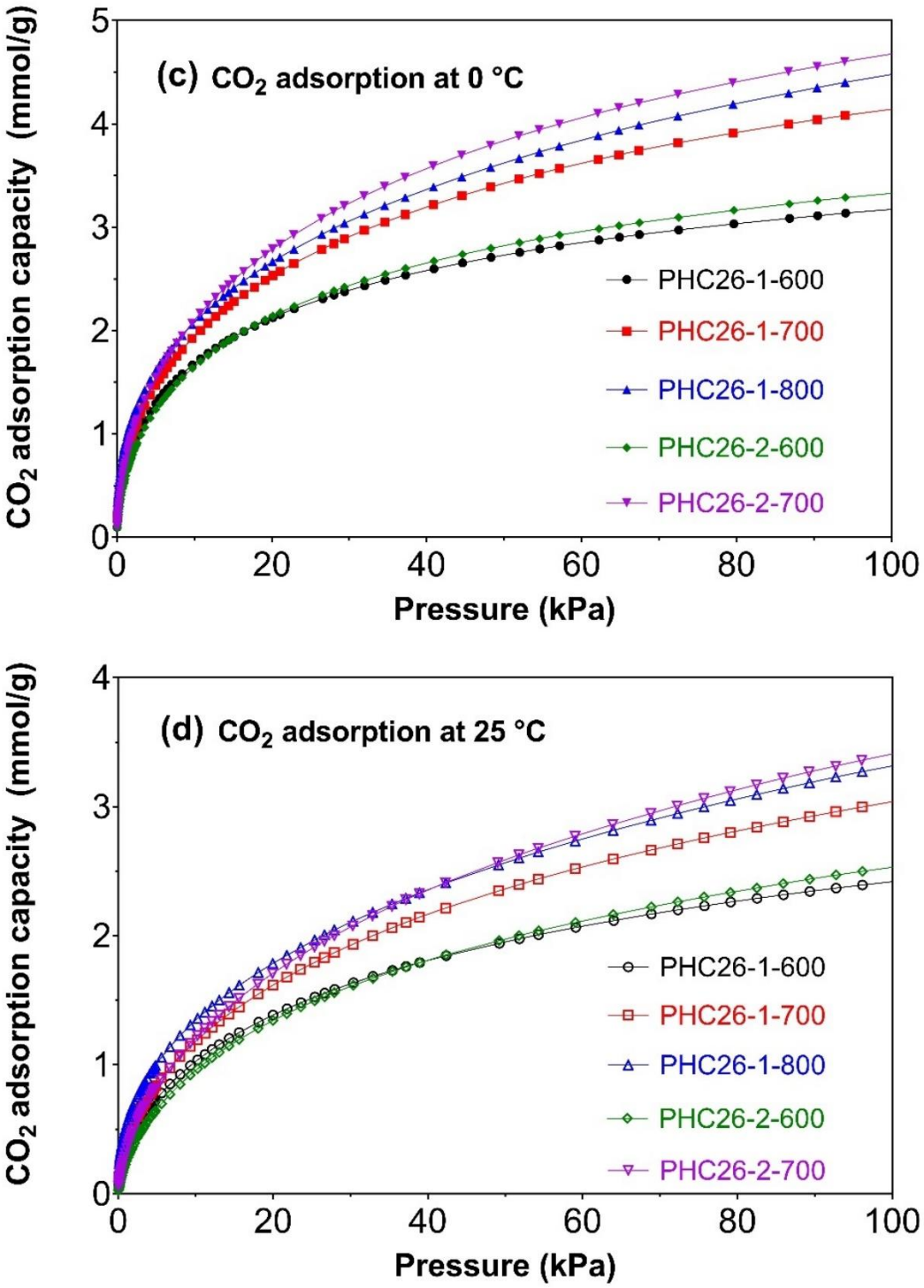


Figure 6.11 CO_2 adsorption profiles of PHC24-derived carbons at: (a) 0 ºC (b) 25 ºC and PHC26-derived carbons at (c) 0 ºC (d) 25 ºC.

Table 6.5 CO_2 adsorption capacity of PHC-derived carbons

Sample	CO_2 uptake capacity, mmol-CO_2/g-ads			
	0 °C		25 °C	
	15 kPa	100 kPa	15 kPa	100 kPa
PHC24-1-600	2.35	4.22	1.46	3.15
PHC24-1-700	2.45	5.47	1.39	3.68
PHC24-1-800	2.46	5.21	1.53	3.62
PHC24-2-600	2.33	4.38	1.43	3.19
PHC24-2-700	2.38	5.40	1.36	3.60
PHC26-1-600	1.93	3.17	1.23	2.42
PHC26-1-700	2.28	4.14	1.42	3.04
PHC26-1-800	2.41	4.48	1.59	3.31
PHC26-2-600	1.93	3.33	1.17	2.53
PHC26-2-700	2.49	4.68	1.49	3.41

The CO_2 adsorption performance of co-hydrochar (CEPHC and KLPHC)-derived activated carbons were also evaluated by their CO_2 adsorption isotherms measured at 0 °C and 25 °C (Figure 6.12). It is evident that the CO_2 uptakes of carbon samples were influenced by both activation/HTC temperature, KOH/hydrochar mass ratio and feedstock to a differential extent. As shown in Figure 6.12 (a,b), when the activation temperature increased from 600 to 800 °C at a given KOH/CEPHC mass ratio of 1, the CO_2 adsorption capacity of CEPHC24 carbons at 100 kPa CO_2 sharply increased from 3.67 to 6.07 mmol/g and 2.98 to 4.19 mmol/g, respectively at 0 °C and 25 °C. The CO_2 capacities of CEPHC26 carbons followed a similar trend as CEPHC24 carbons, with the CO_2 uptake at 100 kPa varying from 3.45 to 5.66 mmol/g and 2.77 to 3.91 mmol/g at 0 °C and 25 °C, respectively (Figure 6.12 c,d). However, being different from the CO_2 uptakes of PHC26 carbons which are all lower than those of PHC24 carbons prepared at the same activation conditions, the CO_2 adsorption capacity of CEPHC26-2-600 is

higher than that of CEPHC24-2-600 with its much higher ultra-micropore volume ($V_{micro<0.7\ nm}$) than CEPHC24-2-600. A slight discrepancy is observed with regard to the variation of CO_2 adsorption of CEPHC carbons at low CO_2 partial pressure region (Figure 6.12 (a,c)). For instance, the carbon samples produced at mild activation conditions (activation temperature = 700 ^oC and KOH/CEPHC mass ratio = 1) exhibited much higher CO_2 adsorption capacities of 3.03 and 2.98 mmol/g at 0 ^oC, respectively. When the adsorption temperature was increased to 25 ^oC, CEPHC24-1-700 achieved the highest adsorption capacity of 2.00 mmol/g at 15 kPa, which is 44% higher than that of PVC hydrochar-derived carbon obtained at the same activation conditions. Given that the micropore volume and ultra-micropore volume of CEPHC24-1700 are much lower than PHC24-1-700, the significant improvement in CO_2 uptake of the co-hydrochar derived carbon at 15 kPa CO_2 and 25 ^oC is presumably due to the presence of a large volume of fine micropore ($V_{micro<0.4\ nm}$) with critical pore size. Moreover, the CO_2 adsorption profiles of KLPHC carbons also implied the potential relevance between CO_2 uptake and ultra-micropore volume, with KLPHC24-1-700 having the second largest volume of ultra-micropore exhibiting the second highest CO_2 adsorption capacity of 5.85 mmol/g at 0 ^oC and 100 kPa CO_2.

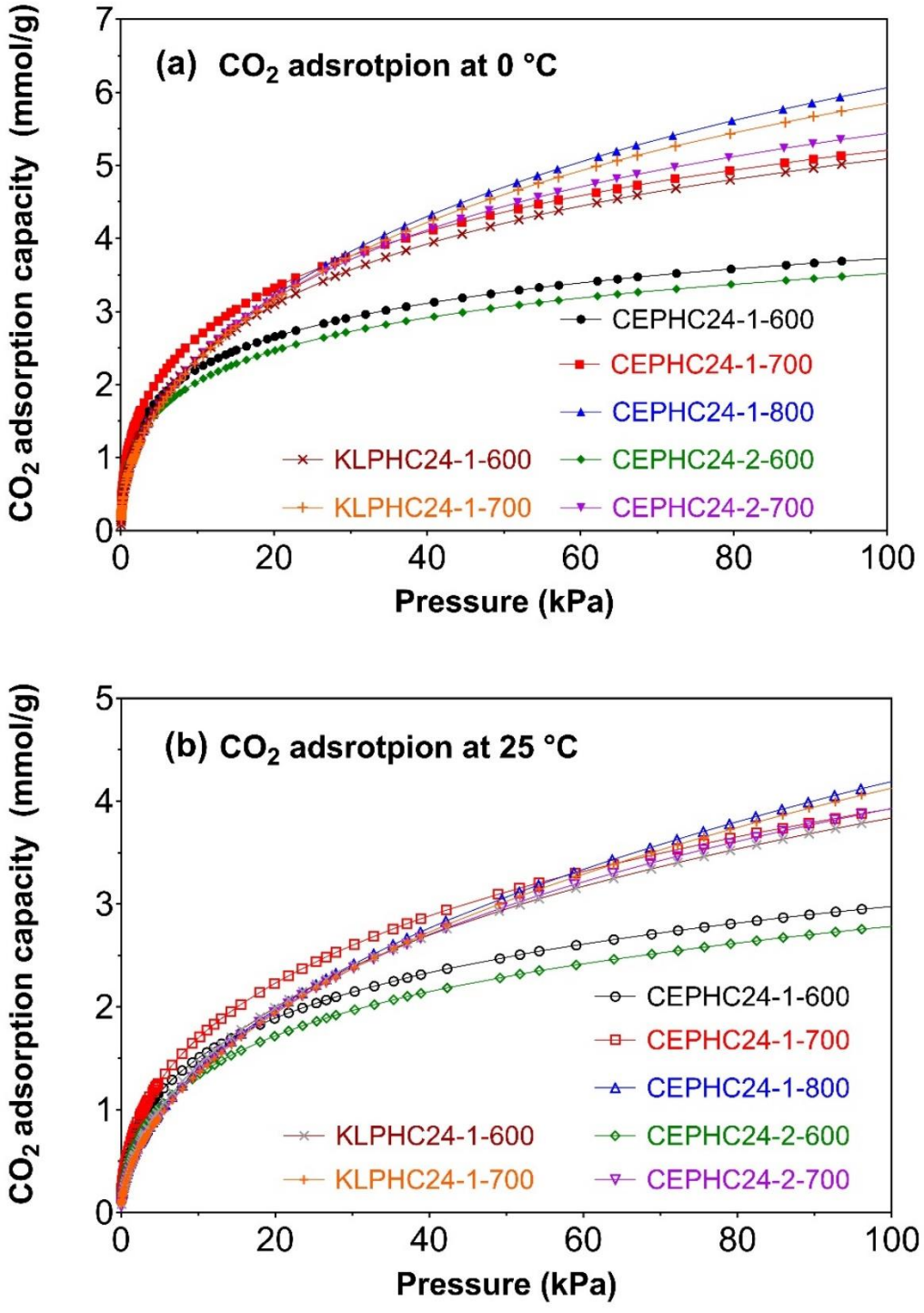


Figure 6.12 CO_2 adsorption profiles of CEPHC24- and KLPHC24-derived carbons at: (a) 0 °C (b) 25 °C and PHC26-derived carbons at (c) 0 °C (d) 25 °C.

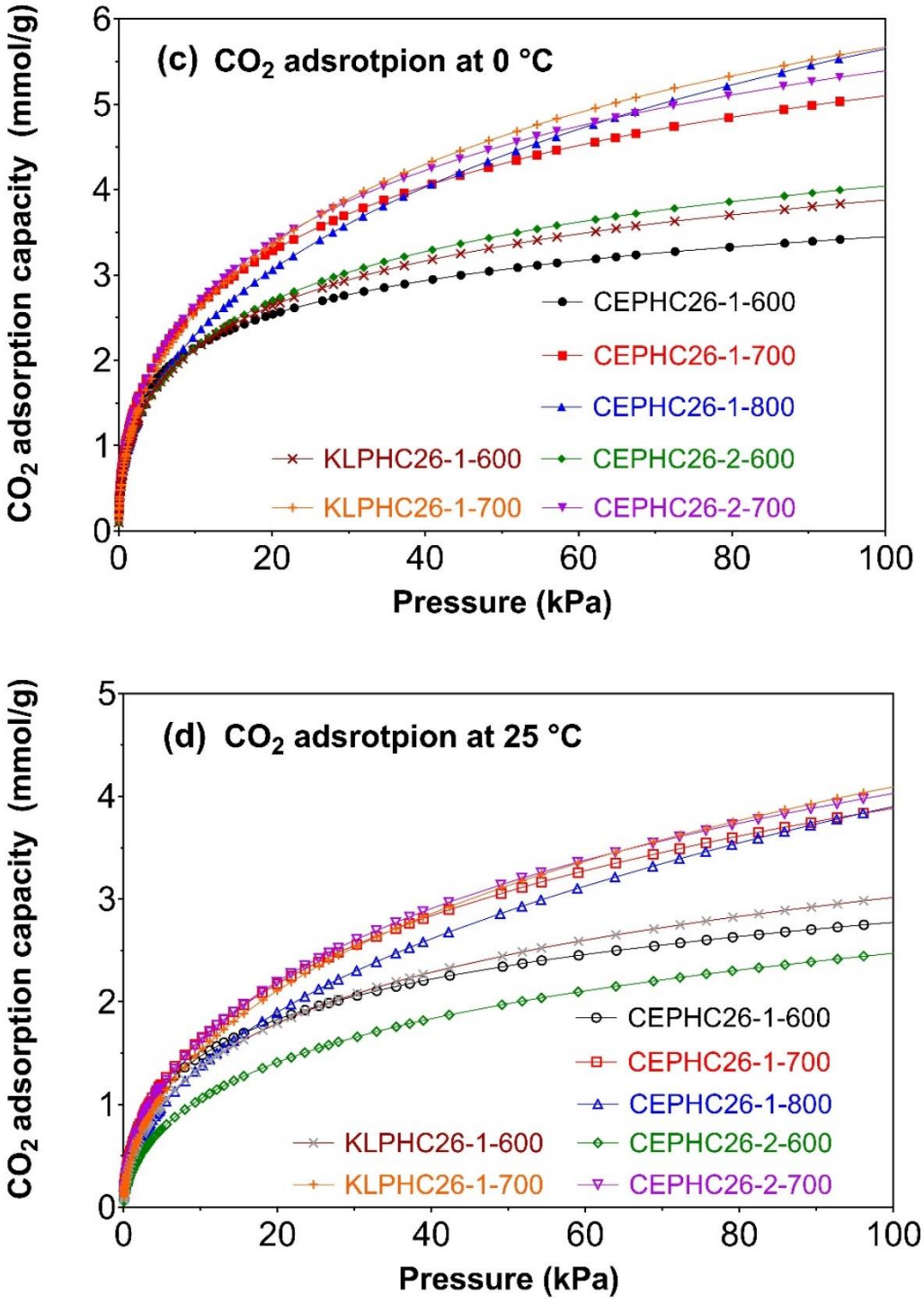


Figure 6.12 CO_2 adsorption profiles of CEPHC24- and KLPHC24-derived carbons at: (a) 0 °C (b) 25 °C and PHC26-derived carbons at (c) 0 °C (d) 25 °C.

Table 6.6 CO_2 adsorption capacity of CEPHC- and KLPHC-derived carbons

Sample	CO_2 uptake capacity, mmol-CO_2/g-ads			
	0 °C		25 °C	
	15 kPa	100 kPa	15 kPa	100 kPa
CEPHC carbons				
CEPHC24-1-600	2.46	3.67	1.69	2.98
CEPHC24-1-700	3.03	5.20	2.00	3.93
CEPHC24-1-800	2.77	6.07	1.71	4.19
CEPHC24-2-600	2.28	3.52	1.55	2.79
CEPHC24-2-700	2.82	5.44	1.69	3.93
CEPHC26-1-600	2.37	3.45	1.68	2.77
CEPHC26-1-700	2.98	5.10	1.94	3.88
CEPHC26-1-800	2.72	5.66	1.66	3.91
CEPHC26-2-600	2.47	4.04	1.26	2.47
CEPHC26-2-700	3.03	5.35	1.94	4.05
KLPHC carbons				
KLPHC24-1-600	2.77	5.09	1.74	3.84
KLPHC24-1-700	2.79	5.85	1.67	4.12
KLPHC26-1-600	2.42	3.88	1.61	3.02
KLPHC26-1-700	3.00	5.67	1.85	4.09

6.2.5 Role of textural properties and surface chemistry in CO_2 adsorption

In order to investigate the factors provoking the enhancement of CO_2 adsorption capacity, the relationships between the CO_2 uptake and textural properties and surface chemistry were further evaluated. The correlation between CO_2 adsorption capacity at 15 kPa and 100 kPa for the co-hydrochar-derived carbons and the volume of pores smaller than a specific pore size were analyzed in Figure 6.13. It can be observed that CO_2 adsorption capacity at 0 °C and 100 kPa was almost

linear with the volume of micropores smaller than 0.7 nm, with a high correlation coefficient (R^2 = 0.98). When the adsorption temperature increased to 25 ^oC, the unique pore size giving rise to the best correlation decreased to 0.6 nm at 100 kPa CO_2 (R^2 = 0.97). Similar linear relationships were also obtained at a lower CO_2 partial pressure of 15 kPa, whereas the CO_2 uptake at 0 ^oC and 25 ^oC gave the best correlation with the volume of micropores smaller than 0.52 nm (R^2 = 0.87) and 0.37 nm (R^2 = 0.76) respectively. It is well known that the ultra-micropores could enhance the adsorption potential due to the superposition of the strong Van der Waals force produced by the adjacent walls of ultra-micropores, with the adsorption potential being inversely proportional to the pore radius and decreases with the pore width (Everett and Powl, 1976). Therefore, the critical pore size of ultra-micropore becomes much smaller to provide a sufficient force to keep the CO_2 molecules in the pores when a stronger interaction force is needed during the adsorption at a higher temperature or a lower CO_2 partial pressure (Sevilla et al., 2013, Ashourirad et al., 2016, Liu et al., 2022). However, it is noteworthy that the CEPHC26-1-600 sample with the lowest ultra-microporosity still possessed a relatively high CO_2 uptake, especially at low partial pressure, which reached 1.68 mmol/g at 25 ^oC and 15 kPa CO_2, which outperformed many other samples with higher ultra-microporosity. Apparently, other factors besides textural properties have contributed to the adsorption. Many studies have demonstrated that the existence of surface heteroatom-containing groups is capable of changing the electrostatics of the surface, which could enhance the affinity to CO_2 molecules (Lahijani et al., 2018, Hosseini et al., 2015, Liu et al., 2020a). Given that all the co-hydrochar derived carbon samples are non-nitrogen-doped, the augmented CO_2 adsorption ability is very likely to be linked with the surface chemistry of activated carbons that being modified by the intercalated potassium during the KOH activation and remaining metal additives from the parent hydrochar.

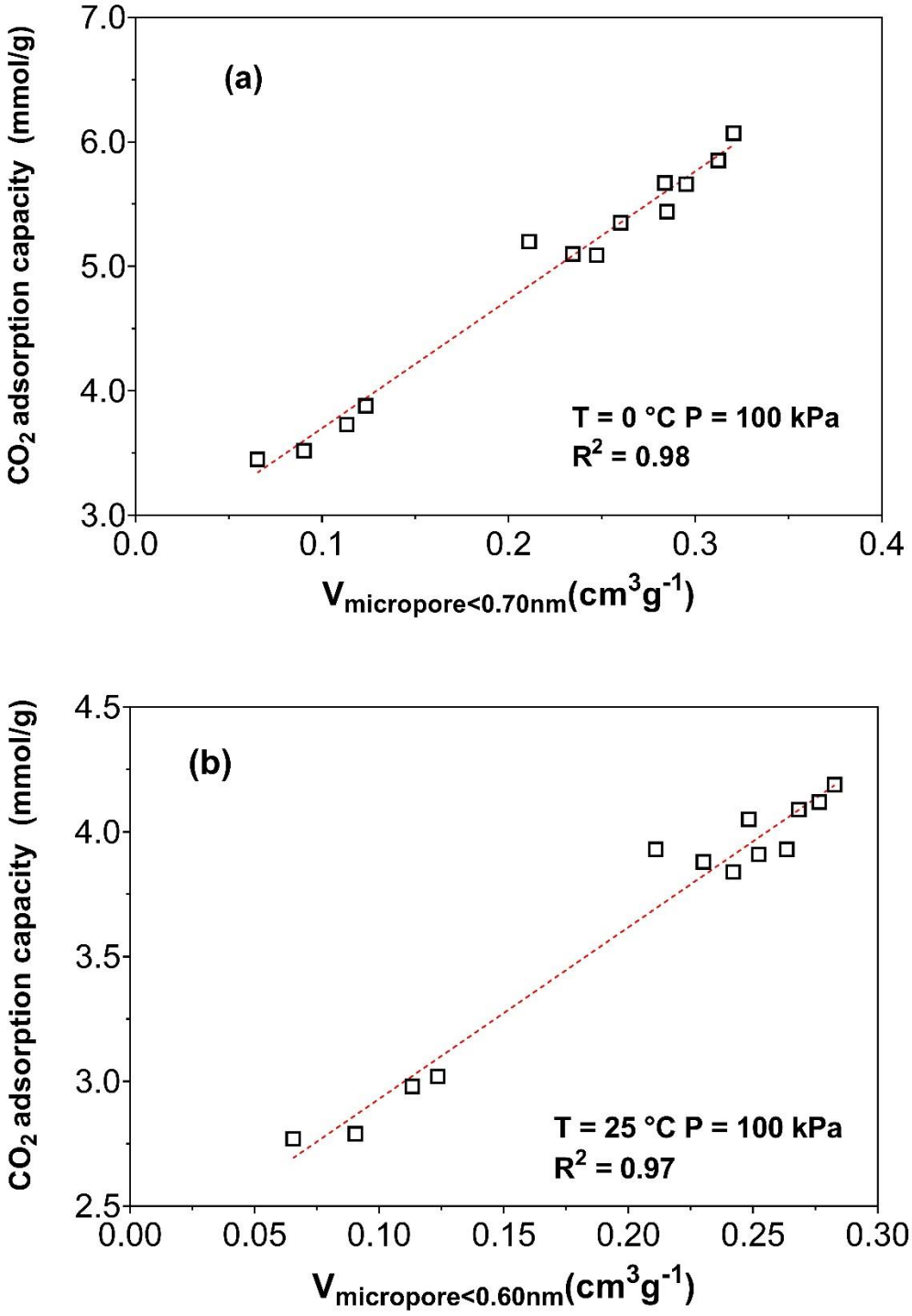


Figure 6.13 Relationship between CO_2 uptake and ultra-micropore volume of the CEPHC and KLPHC-derived carbons: (a) 100 kPa CO_2 and 0 ^oC; (b) 100 kPa CO_2 and 25 ^oC; (c) 15 kPa CO_2 and 0 ^oC; (d) 15 kPa CO_2 and 25 ^oC

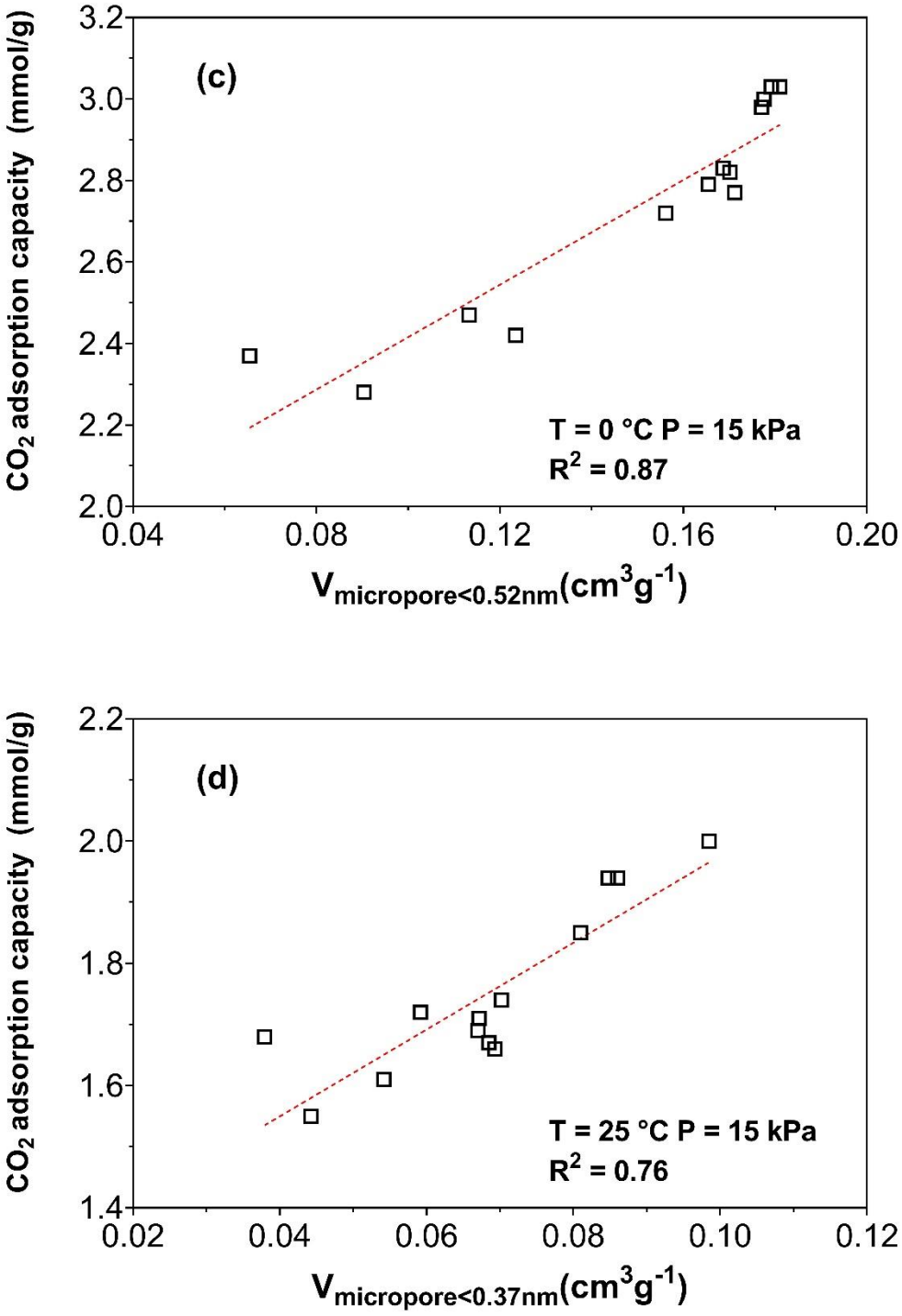


Figure 6.13 Relationship between CO_2 uptake and ultra-micropore volume of the CEPHC and KLPHC-derived carbons: (a) 100 kPa CO_2 and 0 °C; (b) 100 kPa CO_2 and 25 °C; (c) 15 kPa CO_2 and 0 °C; (d) 15 kPa CO_2 and 25 °C

Table 6.7 shows the XRF results of the hydrochars and their-derived activated carbons. It can be found that K and Ti are the primary compositions of the remaining species in the activated carbons, which represent up to 86% of the total ash content. It appears that the enhanced CO_2 uptake capacity of the prepared carbon materials at the lower CO_2 partial pressure region is irrelevant to the content of titanium, which even hindered the adsorption of CO_2. As for the PVC derived carbons which possessed higher levels of titanium content of up to 11.03 wt%, their CO_2 adsorption capacities at 15 kPa CO_2 were overall lower than those of PVC/CE and PVC/KL derived carbons. Therefore, other chemical composition should be taken into account to evaluate the enhanced CO_2 adsorption capacity. Given that all the hydrochars and co-hydrochars contain no potassium, the varying amounts of potassium presented in their derived carbons apparently originated from the introduction of intercalated potassium through the KOH activation. Figure 6.15 presents the XRD patterns of selected carbon samples, the peak at ca. 45º can be ascribed to K_2O, confirming the presence of intercalated potassium in the prepared co-hydrochar derived activated carbons (Liu et al, 2015). It has been investigated in the previous Chapters that the exposed potassium on the surface of activated carbons acts like the extra framework cations in the same manner seen in MOFs and zeolites, reinforcing the delocalization of charge and the polarity of the surface, and therefore increasing the surface affinity to CO_2 molecules. For example, the CEPHC26-1-600 sample which exhibited the highest level of potassium content (12.26 wt%) still achieved high CO_2 uptake of 1.68 mmol/g at 25 ^oC and 15 kPa. Considering its lowest ultra-micropore (<0.40 nm) volume of 0.065 cm^3/g, the excessive CO_2 adsorption capacity was explicitly attributed to the enhanced affinity to CO_2 due to the presence of extra framework K^+ ions. The distribution of the potassium of selected carbon samples obtained from the SEM-EDX mapping was depicted in Figure 6.14. As can be seen from the image of elemental mapping, the potassium intercalation via KOH activation resulted in relatively even distributions of K with no obvious segregation, implying that the incorporated K was highly dispersed throughout the carbon samples.

Table 6.7 Chemical analysis by XRF of CEPHC and KLPHC carbons

Sample	K (wt%)	Ti (wt%)	Sample	K (wt%)	Ti (wt%)
CEPHC24	0	3.42	PHC24	0	3.84
CEPHC26	0	2.95	PHC26	0	2.95
CEPHC24-1-600	13.98	6.27	PHC24-1-600	7.45	9.27
CEPHC24-1-700	11.76	5.43	PHC24-1-700	4.39	9.93
CEPHC24-1-800	6.72	6.76	PHC24-1-800	8.81	11.03
CEPHC24-2-600	10.89	6.41	PHC24-2-600	7.78	10.30
CEPHC24-2-700	4.41	4.62	PHC24-2-700	6.49	11.50
CEPHC26-1-600	12.26	5.31	PHC26-1-600	7.38	7.40
CEPHC26-1-700	9.03	5.46	PHC26-1-700	8.97	7.57
CEPHC26-1-800	9.15	6.06	PHC26-1-800	10.87	9.53
CEPHC26-2-600	7.28	5.93	PHC26-2-600	6.63	6.79
CEPHC26-2-700	7.85	5.03	PHC26-2-700	7.02	6.87
KLPHC24	0	2.87			
KLPHC26	0	3.34			
KLPHC24-1-600	5.89	2.72			
KLPHC24-1-700	5.93	4.15			
KLPHC26-1-600	9.17	3.48			
KLPHC26-1-700	6.93	3.80			

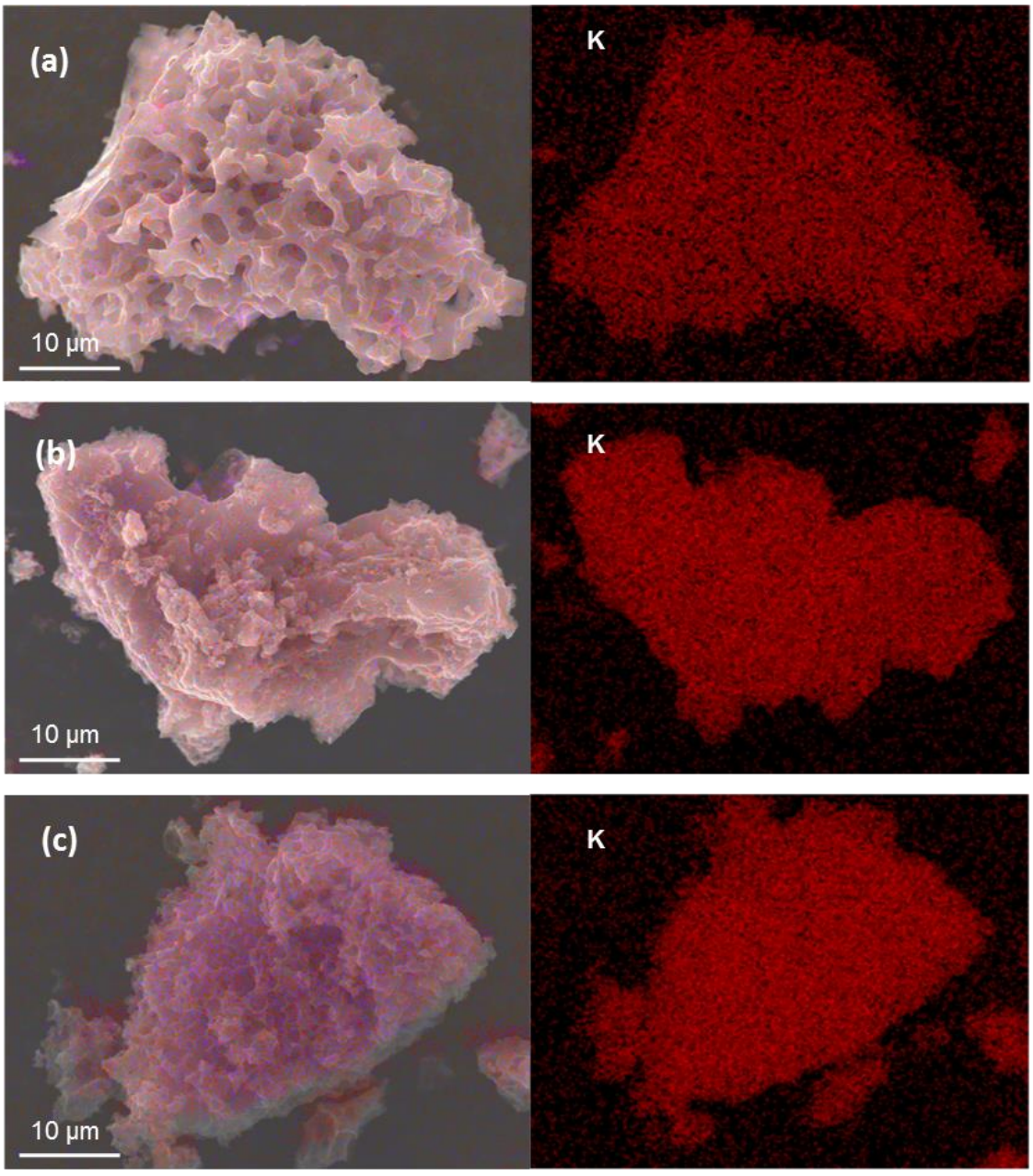


Figure 6.14 SEM images of potassium mapping: (a) PHC24-1-700, (b) CEPHC24-1-700, (c) KLPHC24-1-700

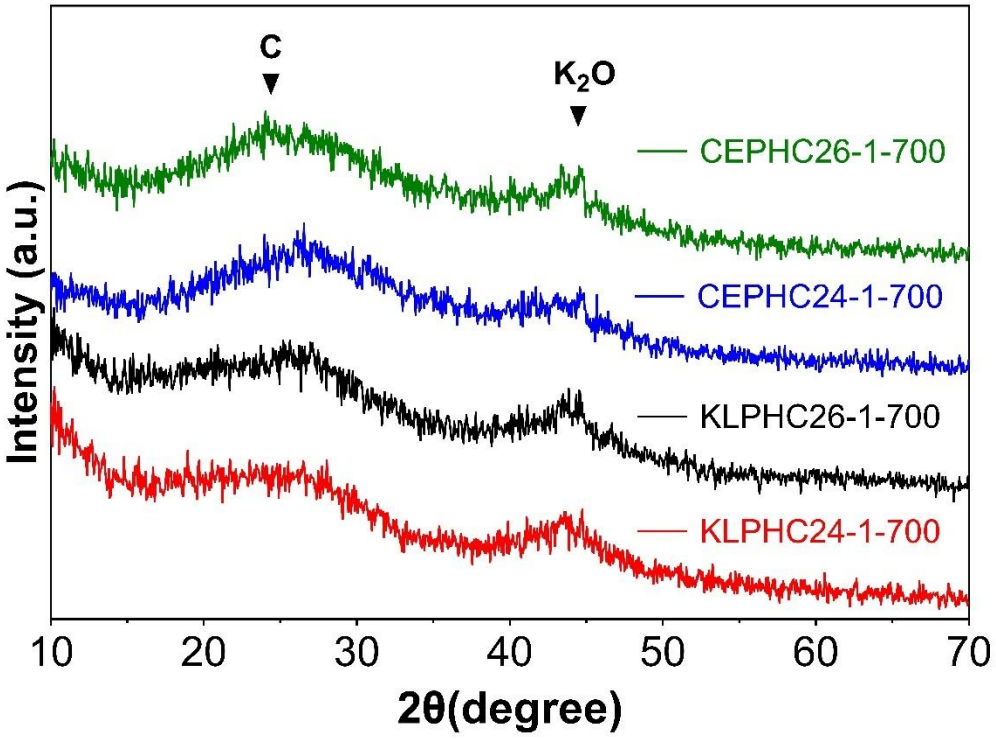


Figure 6.15 XRD pattern of selected carbon samples

6.2.6 Heat of CO_2 adsorption

The heat of CO_2 adsorption serves as a significant thermodynamic parameter in characterizing the adsorption behaviour of an adsorbent and evaluating the interaction strength between CO_2 and the carbon surface. In this study, the isosteric heats (Q_{st}) of CO_2 adsorption on all carbon samples were calculated from the CO_2 adsorption isotherms measured at 0 and 25 ^oC via the Clausius-Clapeyron equation to reveal the surface affinity of carbon towards CO_2 molecules. In addition, the dual-site Langmuir equation was applied to fit the adsorption isotherms of carbon samples considering the heterogeneity of surface induced by the potassium intercalation. Figure 6.17 a illustrates the initial Q_{st} for both PHC- and CEPHC/KLPHC-derived carbons calculated at a CO_2 uptake level of 0.01 mmol/g. Generally, the initial Q_{st} values for the CEPHC carbons (38-49 kJ/mol) are substantially higher than those of PHC (33-43 kJ/mol) and KLPHC carbons (36-41 kJ/mol) obtained at the same conditions. It is also noteworthy that the initial Q_{st}

values of CEPHC carbons are even higher than those of N-doped porous carbons (38 kJ/mmol) (Rao et al., 2019) and MOFs materials (38 kJ/mol) (Chen et al., 2019), indicating the existence of strong interaction force between CO_2 and the adsorbent. Figure 6.17 b showed the Q_{st} curves of prepared carbons over the whole range of CO_2 adsorption capacity, where the Q_{st} remained at a high level at CO_2 uptake up to 1 mmol/g and gradually decreased to a constant value with the increasing adsorption of CO_2. Notably, the Q_{st} value of CEPHC24-1-600 and CEPHC24-1-700 could still achieve >30 kJ/mol at late stages of adsorption, indicating that the exposed potassium on the surface can effectively enhance the surface affinity while the improvement of overall affinity or heat of adsorption mainly came from their higher potassium contents. The higher level of Q_{st} stands for a relatively stronger affinity of co-hydrochar derived carbons towards CO_2, which is beneficial for the removal of CO_2 from gas mixtures.

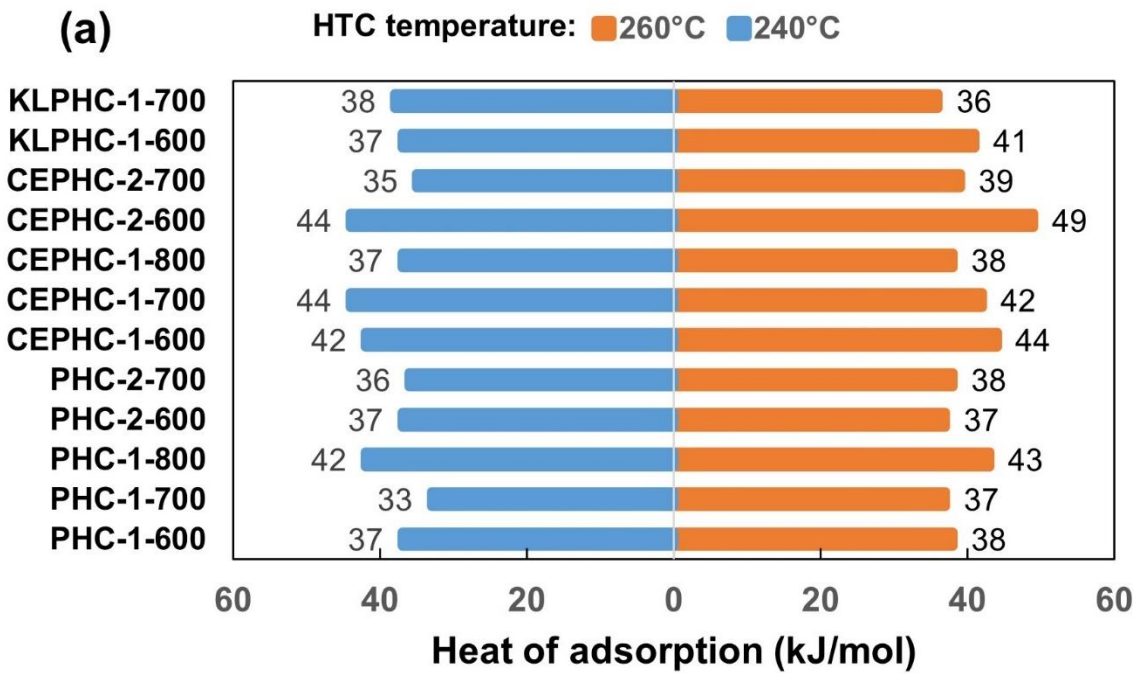


Figure 6.16 (a) Fitted isosteric adsorption heat at a CO_2 uptake level of 0.01 mmol/g for all the carbon samples; (b) Fitted isosteric adsorption heat of selected carbon samples as a function of absolute CO_2 loading using dual-site Langmuir model

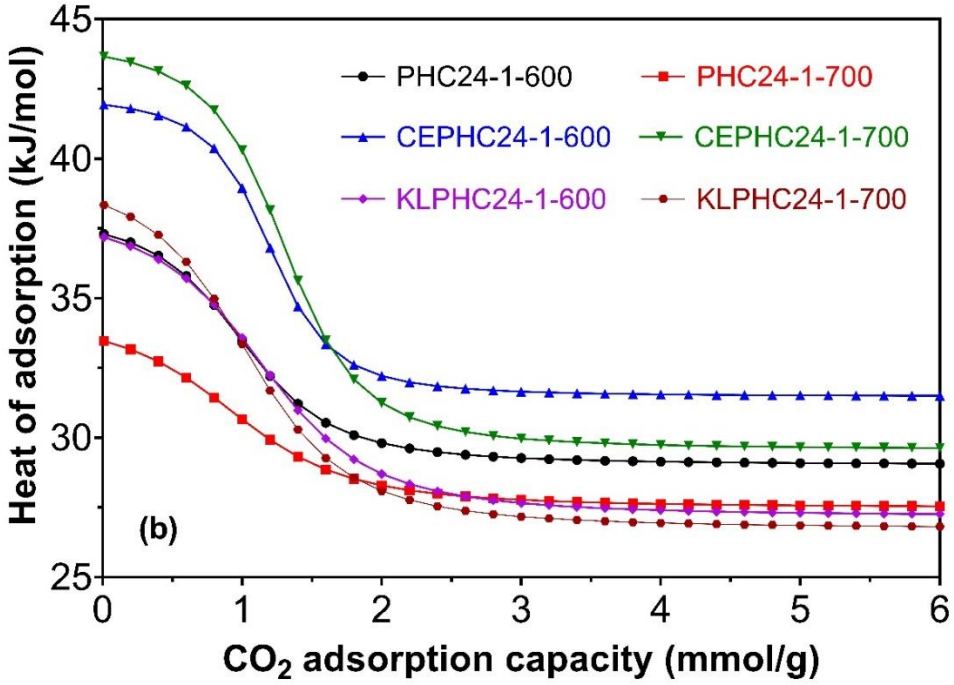


Figure 6.17 (a) Fitted isosteric adsorption heat at a CO_2 uptake level of 0.01 mmol/g for all the carbon samples; (b) Fitted isosteric adsorption heat of selected carbon samples as a function of absolute CO_2 loading using dual-site Langmuir model

6.3 Conclusion

In conclusion, we have valorised biomass and plastic wastes (PVC) into value-added activated carbon materials via an integrated co-hydrothermal treatment-chemical activation protocol for CO_2 capture. Our results showed that the dechlorination of PVC and removal of inorganics were simultaneously achieved through HTC treatment, with the addition of lignocellulosic biomass (cellulose and lignin) could significantly improve the dechlorination efficiency by up to 50% at a relatively mild HTC temperature of 220 ^{o}C. The positive synergistic effect in the co-HTC of biomass and PVC wastes appeared to improve the physiochemical properties of hydrochar in favour of producing highly ultra-microporous activated carbons via KOH activation. By controlling the synthetic conditions such as HTC

temperature, activation temperature and KOH/hydrochar mass ratio, the CEPHC24-1-700 from using the co-hydrochar derived from cellulose and PVC possessed the largest ultra-micropore volume (<0.40 nm) of 0.171 cm^3/g, which was 61% higher than that of PVC derived carbons prepared under the same activation protocol. The advanced textural properties gave rise to the outstanding CO_2 adsorption performance at lower CO_2 partial pressure, with the CO_2 uptake capacity increased by 44% compared with PVC carbon and achieved 2.00 mmol/g at flue gas conditions (15 kPa CO_2 and 25 ^oC). Further characterization of the surface chemistry of carbon samples by using XRF and SEM-EDX confirmed the contribution of the extra-framework potassium cations to the enhanced surface affinity to CO_2 molecules. This work provides an innovative and sustainable strategy to convert biomass and PVC wastes to effective CO_2 sorbents via the coupling of co-HTC and KOH activation.

Chapter 7

CONCLUSION AND FUTURE RESEARCH

7.1 General discussion

In this PhD project, miscellaneous solid wastes including biomass wastes (kraft lignin, eucalyptus wood and cellulose) and plastic wastes (PVC) have been selected as the low-cost and easily accessible precursor materials to produce advanced carbon materials through sustainable pre-treatment (pre-oxidation/hydrothermal carbonization) followed by KOH activation. To be specific, kraft lignin was converted to activated carbons through an easily integrated carbonization-activation process, while eucalyptus wood and PVC wastes underwent a two-stage method of hydrothermal carbonization and chemical activation to produce carbon materials. Besides, PVC wastes were further hydrothermally co-carbonized with cellulose and kraft lignin followed by chemical activation to fabricate the activated carbon composites. As explained in chapter 4 to 6, the preparation of carbon samples towards the specific CO_2 adsorption targets requires optimized activation conditions (activation temperature and KOH/precursor mass ratio) that varied with the precursor and pre-treatment methods (pre-oxidation and hydrothermal carbonization) selected. The analysis results indicated that both ultra-microporosity and surface chemistry played a critical role in developing effective CO_2 adsorbent materials, particularly for post-combustion scenarios. This section will discuss not only the effect of pre-treatment on the physiochemical properties of carbon precursors but also the effect of activation conditions and carbon precursors on the development of porosity and surface chemistry of prepared carbon samples as well as the CO_2 adsorption performance.

7.1.1 Effect of pre-treatment on the physiochemical properties of carbon precursors derived from different raw feedstocks

The physiochemical properties of carbon precursors after different pre-treatment processes and their raw materials are listed in Table 7.1. It can be found that pre-treatment by either pre-oxidation or hydrothermal carbonization gave rise to an increase in fixed carbon content and a decrease in volatile matter for biomass

wastes (kraft lignin and eucalyptus wood). Plastic wastes (PVC) had experienced different evolution under hydrothermal carbonization in terms of their volatile matter, which showed an increase at HTC temperature of 220 ^{o}C followed by a decrease as temperature increased due to the preliminary large ash reduction and gradual removal of organic chlorine. Additionally, co-HTC of biomass wastes with PVC was found to significantly promote the dechlorination of PVC, especially at low HTC temperature, with the addition of different types of biomass precursors (cellulose and kraft lignin) offering different degrees of dechlorination efficiency. For example, the chlorine content of CEPHC22 and KLPHC22 co-hydrochar obtained at HTC temperature of 220 ^{o}C is 18.96 wt% and 1.77 wt%, respectively, representing 74.3% and 96.4% of dechlorination efficiency. The results are higher than that of single PVC being hydrothermally carbonized at the same conditions (64.6%), with lignin having a higher synergistic effect on chlorine removal of PVC.

Table 7.1 Physiochemical properties of raw materials and their derived samples after different pre-treatment methods

Sample	Proximate Analysis (wt%)			Atomic ratio		XRF (wt%)
	FC	VM	Ash	H/C	O/C	Cl
KL	35.28	58.60	2.31	1.01	0.35	-
OKL	45.00	49.83	2.45	0.65	0.41	-
EU	16.87	83.13	1.19	1.43	0.68	-
EUHC22	34.07	65.93	1.48	1.04	0.41	-
EUHC26	48.09	51.91	1.30	0.76	0.27	-
PVC	11.36	67.87	20.67	-	-	52.02
PHC22	12.94	83.37	3.17	1.60	0.21	33.11
PHC24	26.60	64.95	7.71	1.18	0.15	5.20
PHC26	29.17	64.34	5.42	1.07	0.16	0.74
CEPHC22	15.84	81.08	2.55	1.36	0.24	18.96
CEPHC24	30.22	63.38	4.98	1.04	0.15	2.51
CEPHC26	35.15	58.03	4.92	1.03	0.12	0.89
KLPHC22	38.86	57.04	2.95	1.07	0.23	1.77
KLPHC24	41.65	48.41	7.98	0.95	0.12	2.88
KLPHC26	46.78	43.29	8.89	0.90	0.11	1.76

7.1.2 Effect of activation conditions and carbon precursors on the textural properties of activated carbon samples

The textural properties of selected carbon samples from using different precursors and preparation conditions were presented in Table 7.2. The results indicated that activated temperature and KOH/precursor mass ratio significantly affect the textural characteristics of carbon samples prepared via different pre-treatments. As illustrated in Chapter 4, the carbons derived from kraft lignin showed a clear augmentation in surface area and total pore volume with an increased activation temperature and KOH/KL mass ratio. Moreover, the pre-oxidized lignin derived carbons prepared especially at the low KOH/KL ratio of 1 and high activation temperature possessed higher total pore volume and more developed mesoporosity, which is mainly attributed to etched structure and formed oxygen-bearing functional groups of precursors that promote the pore widening effect during the KOH activation process. The pre-treatment of biomass wastes by hydrothermal carbonization also had significant contributions to the development of porosity in the activated carbons. As shown in Table 7.2, the biomass (eucalyptus wood) derived activated carbon prepared via HTC exhibited higher total pore volume (0.435 cm^3/g) compared to the carbon obtained at the same activation condition (600 ^oC and KOH/precursor=1:1) without HTC treatment (0.267 cm^3/g), which can be ascribed to the enriched oxygen functional groups in hydrochar that are beneficial to facilitate chemical activation. In addition, the EU hydrochars prepared at different HTC temperatures showed differences in KOH activation under the same conditions, with the activated carbons produced at a lower HTC temperature generally having higher total pore volume. It can also be found in Chapter 7 that PVC derived carbons came to a similar trend. The reason might be associated with the lower degree of aromatization of hydrochars obtained at a lower HTC temperature, which is in favour of KOH etching and thus led to the development of porosity during the activation process. Meanwhile, co-HTC of PVC with different types of biomass wastes appeared to result in distinctions in terms of the textural properties of the final activated carbon composites, with the surface

area, total pore volume and volume of ultra-micropores of PVC/ lignin derived carbons are overall higher than PVC/cellulose carbons. This result could be explained by the unique presence of CO-releasing functional groups in the PVC/lignin hydrochars that help to create more pores with KOH activation.

Table 7.2 Textural properties and CO_2 adsorption capacities of selected carbon samples from using different precursors

Sample	S_{BET} (m^2/g)	V_{total} (cm^3/g)	V_{micro}, cm^3/g	$V_{micro<0.7\ nm}$, cm^3/g	CO_2 adsorption capacity (mmol/g)	
					25 °C	0 °C
					15 kPa	100 kPa
KLK-1-600	878	0.372	0.320	0.278	2.01	5.84
KLK-1-800	1255	0.554	0.466	0.275	1.79	5.55
KLK-2-700	1528	0.598	0.557	0.377	1.31	6.86
OKLK-1-800	1109	0.785	0.397	0.195	0.90	5.24
EU-1-600	687	0.267	0.252	0.217	1.59	4.59
EUHC22-1-600	699	0.435	0.247	0.213	1.87	4.73
EUHC22-1-700	943	0.538	0.337	0.289	1.84	5.88
EUHC26-1-600	675	0.324	0.241	0.197	1.86	4.78
EUHC26-1-700	922	0.471	0.323	0.259	1.83	5.50
PHC24-1-700	991	0.379	0.356	0.310	1.39	5.47
PHC26-1-700	604	0.249	0.220	0.191	1.42	4.14
CEPHC24-1-700	737	0.316	0.265	0.211	2.00	5.20
CEPHC26-1-700	764	0.339	0.274	0.234	1.94	5.10
KLPHC24-1-700	1061	0.479	0.379	0.312	1.67	5.85
KLPHC26-1-700	938	0.417	0.337	0.284	1.85	5.67

7.1.3 CO_2 adsorption performance

The CO_2 adsorption capacities of selected carbon samples at different conditions are given in Table 7.1. It can be found that the CO_2 adsorption capacities at 0 ^oC and 100 kPa tended to correspond with variations in the ultra-micropore volume. Sample KLK-2-700, which possessed the highest ultra-micropore volume, exhibited the highest CO_2 adsorption capacity of 6.86 mmol/g, while PHC26-1-700 with the lowest volume of ultra-micropore had the lowest CO_2 uptake capacity. However, no obvious relationship was observed between the CO_2 adsorption capacity and ultra-micropore volume when CO_2 partial pressure decreased to 15 kPa and temperature increased to 25 ^oC. For example, sample CEPHC24-1-700 with a much lower ultra-micropore volume whilst having the second highest CO_2 adsorption capacity. The results revealed that the CO_2 adsorption performance at flue gas conditions could be associated with other factors, which inspires us to investigate the potential effect from the point of view of physisorption as well as chemisorption. Overall, the carbon materials produced in this study exhibited exceptional high CO_2 adsorption capacity, especially at low CO_2 partial pressure of 15 kPa, outperformed most biomass derived carbons, porous polymers and even some MOFs developed so far Table 7.3.

Table 7.3 The CO2 adsorption capacity of prepared carbons at flue gas conditions compared to the literature

Precursor	CO_2 adsorption capacity at 15 kPa CO_2 (mmol/g)		Reference
	25 °C	0 °C	
Kraft lignin	**2.01**	**3.29**	
Eucalyptus	**1.91**	**3.12**	**This work**
PVC/Biomass	**2.00**	**3.03**	
Cotton stalk	1.60	2.50	(Pramanik et al., 2021)
Lignin	1.65	2.85	(Saha et al., 2017)
Lumpy bracket	1.67	3.05	(Serafin et al., 2019)
Palm shells	1.70	2.60	(Ello et al., 2013b)
Garlic peel	1.35	2.25	(Huang et al., 2019b)
Grass cuttings	1.05	1.92	(Hao et al., 2013)
Empty fruit bunch	1.25	1.75	(Parshetti et al., 2015)
Olive mill waste	1.19	1.55	(Gonzalez and Manya, 2020)
Jujun grass	1.50	N/A	(Coromina et al., 2016)
Camellia japonica	1.50	N/A	(Coromina et al., 2016)
Waste cornstalk	1.05	2.05	(Li et al., 2021)
Licorice residue	1.18	2.43	(Zhou et al., 2022)
Lotus stem	1.15	1.45	(Wu et al., 2018)
Tobacco stem	1.19	2.05	(Ma et al., 2022)
Tobacco stalk	1.34	2.58	(Huang et al., 2021)
Eucalyptus sawdust	1.25	2.00	(Sevilla and Fuertes, 2011)
Pinecones	1.45	1.55	(Kishibayev et al., 2021)
Metal–Triazolate Frameworks	1.80	2.90	(Shi et al., 2020)

7.1.3.1 Effect of porosity on CO_2 adsorption

The porous structure or porosity of activated carbons serves as the predominant factor as a physical adsorbent in CO_2 adsorption. Therefore, the crucial step towards enabling their practical use lies in adjusting the porous structure of carbon materials to enhance their CO_2 adsorption capacity. In fact, the adsorption of CO_2 on activated carbon is primarily governed by the interaction force between the CO_2 molecule and carbon surface, which arises from the superposition of weak Van der Waals force generated by the two adjacent pore walls. More importantly, the strength of such interaction force is inversely proportional to the radius of the pore and diminishes as the width of the pore increases (Powl and Everett, 1976), which implies the presence of a critical pore size that can exactly retain the CO_2 molecule in the pores at a certain condition (temperature and CO_2 partial pressure). Hence, the critical pore size for post-combustion carbon capture was evaluated in this project. Figure 7.1 depicts the relationship between CO_2 uptake capacity and ultra-micropore volume at the simulated flue gas conditions (25 ^oC and 15 kPa CO_2) for carbon samples derived from different precursors and pre-treatment methods. As can be found from the linear fitting results, the CO_2 adsorption capacity at 25 ^oC and 15 kPa was best correlated with the ultra-micropore with the critical pore size in a range of 0.37-0.44 nm despite the different precursors or pre-treatment methods being used. Meanwhile, the correlation between CO_2 adsorption at other conditions and critical pore size as reported in Chapter 4 to Chapter 6 suggested that the critical pore size increased with the adsorption temperature decreased or CO_2 partial pressure increased. Our findings further corroborated that pores with a diameter less than 0.44 nm are more suitable for CO_2 adsorption at 25 ^oC and CO_2 partial pressure of 15 kPa. Combining with the analysis results of textural properties in the previous Chapters, it appeared that the carbon samples with higher ultra-micropore volume (<0.44 nm) were usually fabricated at mild KOH activation conditions, such as KLK-1-600, EUHC22-2-600 and CEPHC24-1-700. As for carbon samples prepared at more severe activation conditions (higher

temperature and KOH/precursor mass ratio), their ultra-micropore tended to be enlarged, with the pores centred at 0.37 nm continuously decreased and shifted to larger pores centred at 0.53 nm and 1.1 nm. The above results overall provided an effective strategy for designing CO_2-capturing adsorbents in different scenarios.

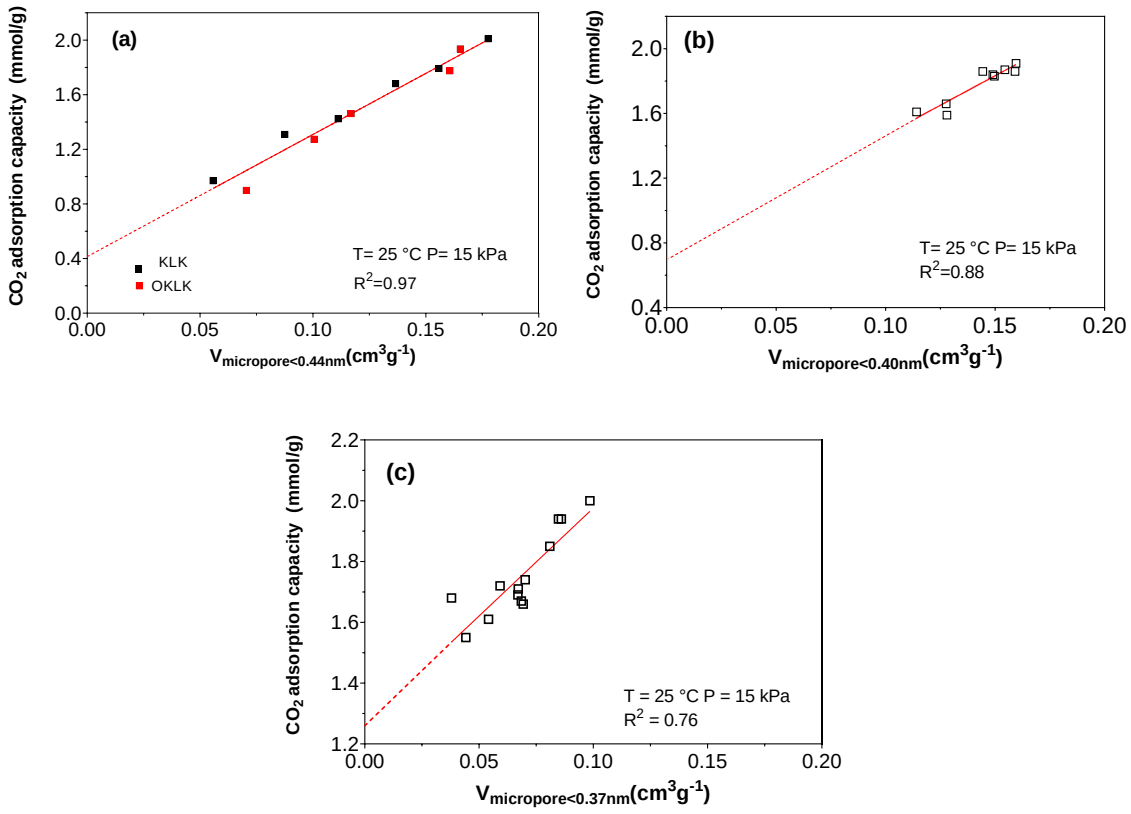


Figure 7.1 Relationship between CO_2 uptake and ultra-micropore volume of carbons at 25 ºC and 15 kPa CO_2: (a) kraft lignin derived carbon; (b) eucalyptus derived carbon via HTC; (c) PVC/cellulose and PVC/kraft lignin derived carbon via co-HTC

7.1.3.2 Effect of surface chemistry on CO_2 adsorption

Though good relationships between the appropriate pore size and CO_2 adsorption capacity were identified, the large y-axis intercepts of the above linear relations indicated that the exceptional CO_2 uptake cannot be solely attributed to the surface textural properties. It has been well-known that the extra-framework cations usually presented in MOFs and zeolites can create strong local electric fields that polarize adsorbate molecules and thereby increase the interaction between the adsorbate and the adsorption surface, with the magnitude of the effect determined by both the charge density of the extra-framework ions and the electric quadrupole of adsorbate (Liu et al., 2017). CO_2 is an acidic gas that possesses a very large electrical quadrupole moment (-1.43± 0.06 $\times 10^{-39}$ Cm^2), which is three times greater than the major component (N_2) ($-4.65\pm 0.08\times 10^{-40}$ Cm^2) in flue gas (RAAB, 1998), indicating that CO_2 molecules can be preferentially polarized in an electrostatic field. Given that all prepared carbon samples in this project were non-nitrogen doped, the great excess CO_2 uptake could be only ascribed to the strong preferential CO_2 polarization by the extra framework metal (K^+) cations that were formed as a result of potassium intercalation achieved during the KOH activation. The results as shown in Chapter 4 revealed that the surface chemistry contributed up to 50% of the total CO_2 uptake, with the CO_2 capacity at 25 ^oC and 15 kPa positively correlated with the density of intercalated potassium. Simultaneously, it appeared in Chapter 6 that the presence of other metals in the carbon matrices such as titanium showed negligible or even negative impact on CO_2 uptake, demonstrating the significant unique role of the extra-framework K^+ cations in the CO_2 adsorption.

Notably, unlike other carbon materials that are commonly modified by covalently incorporating heteroatom groups into the carbon framework to improve CO_2 adsorption, there was no strong covalent bond existing between potassium and carbon. The potassium intercalated into the carbon skeleton is mostly like the modification of adsorbent rather than the modification of the surface, where the

inner structure and chemical composition of precursor had a significant effect on the degree of intercalation aside from the activation conditions (KOH/precursor mass ratio and temperature) and post-activation washing protocol. Stated differently, the modified samples can be defined as a type of nanocomposite material.

Overall, the in-depth examination of the effect of porous structure and surface modification on CO_2 adsorption in this thesis has provided useful data and insights for the design of next-generation carbon-based adsorbents.

7.2 Conclusions

This PhD research project aimed to develop sustainable and innovative synthetic techniques to produce advanced carbon materials by using abundant and easily accessible feedstocks for post-combustion carbon capture. The major conclusions drawn from this study are as follows:

1) A facial one-step carbonization-activation synthetic approach was employed to prepare activated carbons by using the abundant underutilized kraft lignin wastes, with the pre-oxidation treatment of lignin additionally used to investigate the effect of precursor on the properties of final carbons. The textural characterization demonstrated that the pristine kraft lignin derived carbons exhibited exceptionally high ultra-microporosity accounting for up to 92% of the microporosity. With the introduction of pre-oxidation treatment, the resultant carbon samples prepared at mild activation conditions were found to have distinctive hierarchical ultra-micro/mesoporous structures mainly as a result of the etched structure and formed oxygen functional groups in the oxidized lignin that promote the pore widening effect. The application of lignin derived carbons for CO_2 capture at flue gas conditions (25 ^oC and 15 kPa) revealed that the prepared carbon materials possessed exceedingly high CO_2 uptake capacities of up to 2.01 mmol/g, as well as remarkable CO_2/N_2 selectivity of up to 38. In addition to the significant role played by high ultra-

microporosity in the excellent CO_2 adsorption performance, characterisations by XRF and EDX element mapping demonstrated the existence of extra framework potassium cations that also made a substantial contribution to CO_2 adsorption, accounting for up to 50% of the total CO_2 uptake.

2) Hydrothermal carbonization was utilized as a sustainable pre-treatment technique to convert the easily accessible eucalyptus wood wastes into “coal-like” precursors, with the subsequent KOH activation combined to produce porous carbon materials for CO_2 capture. By this means, the carbon sample exhibited a higher porosity than the carbon without HTC treatment due to the emergence of desired oxygen-containing functional groups that tend to promote chemical activation. Additionally, the role of HTC temperature was manifested as different levels of porosity in the derived activated carbons from KOH activation, where hydrochar with a higher aromatization degree generated at higher HTC temperature resulted in the decline of porosity in the derived carbons. By and large, the synthesized carbons via HTC were characterized by high ultra-microporosity, especially in pores smaller than 0.44 nm, along with large amounts of mesopores. The integration of hydrothermal carbonization in the synthesis process appeared to thrive in the development of high ultra-microporosity and the unique surface chemistry of samples, leading to much higher CO_2 uptakes, up to 6.73 mmol/g at 0 ^oC and 100 kPa and 1.91 mmol/g at 25 ^oC and 15 kPa. Particularly at the flue gas conditions (25 ^oC and 15 kPa), the activated carbon prepared with HTC treatment had approx. 20% more CO_2 adsorption capacity than the carbon without HTC.

3) The low-cost and hard-to-recycle polyvinyl chloride wastes were simultaneously recycled and converted to value-added carbon materials for CO_2 capture through an eco-friendly and innovative approach involving the preliminary hydrothermal carbonization either with or without the addition of

lignocellulosic biomass followed by chemical activation. Our results showed that the HTC treatment could effectively promote the dechlorination of PVC, with the highest dechlorination efficiency of 99.7% obtained at an HTC temperature of 260 ^{o}C. The employment of co-HTC of PVC with lignocellulosic biomass in this study also highlighted the significant synergistic effect on the enhancement of the PVC dechlorination especially at lower HTC temperature, with co-HTC of PVC with cellulose and kraft lignin at 220 ^{o}C gave rise to 80.7% and 96.4% dechlorination efficiency, respectively, which are much higher than that without biomass addition (64.6%). Through the regulation of synthetic parameters such as HTC temperature, activation temperature, and KOH/hydrochar mass ratio, the CEPHC24-1-700 derived co-hydrochars from using blended PVC/cellulose exhibited the largest ultra-micropore volume (<0.40 nm) of 0.171 cm^3/g. Together with the presence of unique surface chemistry, the carbon sample achieved a record high CO_2 uptake at flue gas conditions (up to 2 mmol/g at 25 ^{o}C and 15 kPa), which was 44% higher than that of PVC derived carbon prepared at the same activation conditions. Further characterization by XRF analysis indicated that the surface chemistry acting on the CO_2 adsorption mainly originated from the enhanced formation of extra framework potassium cations from KOH activation rather than other inherent metal additives in the precursors.

4) Overall, different biomass wastes derived carbon materials have shown fast CO_2 adsorption kinetics and superior adsorption reversibility. The dynamic CO_2 adsorption profiles obtained by TGA analysis showed that 90% of the CO_2 equilibrium capacity of kraft lignin derived carbons and eucalyptus wood derived carbons can be completed within 3 to 4 minutes. In addition, their CO_2 capacities also remained stable throughout the 50 cycles of continuous adsorption-desorption tests. The exceptional properties of the prepared carbon materials make them suitable for utilization in large-scale operations.

7.3 Future work

7.3.1 Advanced characterization of chemical properties of hydrochar

Hydrothermal carbonization has been employed as a sustainable and versatile pre-treatment method in this project to convert biomass and plastic wastes into high-quality hydrochars for the effective production of chemically activated carbon. It has proven that HTC bestowed the hydrochar with preferable chemical characteristics (i.e., the high concentration of oxygen functional groups and the low degree of aromatization), which were beneficial to improve the porosity of carbon samples prepared by chemical activation. The change of surface functional groups in the hydrochar was identified by FT-IR and the variation of atomic H/C ratio was also investigated by elemental analysis, with further textural properties of activation carbons demonstrating the influential impact of the resulting chemical properties on the porosity development of carbons. However, the more accurate qualitative-quantitative measurement of carbon and oxygen functional groups by X-ray photoelectron spectroscope (XPS) and ^{13}C solid-state nuclear magnetic resonance (NMR) are planned in future work to further confirm the contribution of the unique chemical structures in hydrochars to the porosity of their derived carbons.

7.3.2 Advanced characterization of potassium intercalated in carbon

In this project, KOH was selected as the activating agent to prepare advanced porous carbon materials for CO_2 capture. Our study rationalized the contribution of intercalated potassium to the enhancement of surface affinity to CO_2 molecules, which helps improve the CO_2 adsorption capacity, especially in post-combustion scenarios. The characterization by EDX element mapping identified the uniform distribution of potassium ions on the carbon surface, whilst XRF analysis quantified the potassium content in the carbon that enabled the establishment of a close relationship between potassium ions and adsorption capacity. Although the

experimental results verified the efficacy of potassium ions, additional characterization analyses of carbon samples are encouraged to directly support the change of surface chemistry due to the introduction of potassium. Given that the potassium presents in the carbon matrix in the form of extra framework cations, which changes the distribution of electrostatics fields and the charge of surface like the way in MOFs and zeolite, characterizations of carbon samples in the future by X-ray photoelectron spectroscope (XPS) or Electrostatic force microscopy (EFM) can provide useful information such as chemical state and the electronic state of the elements present as well as the electrostatic field to help understand the mechanism.

7.3.3 Improvement in preparation of PVC/biomass co-hydrochar derived carbon

Hydrothermal co-carbonization of polyvinyl chloride plastic and biomass wastes coupled with chemical activation has been proven as an efficient and innovative approach for the valorisation of waste materials into valuable CO_2 sorbents. The synergistic effect of different types of biomass precursors on the enhancement of the PVC dechlorination at a lower HTC temperature of 220 ^oC has been reported in Chapter 6. Therefore, future work can be extended to investigate the co-HTC of PVC with other abundant biomass wastes to achieve the optimum synergistic dechlorination efficiency that could offer hydrochar with preferable properties for the production of CO_2 adsorbent materials. In addition, optimization of synthetic conditions such as HTC temperature, HTC duration and activation time should also be considered in the next step of work.

7.3.4 The effect of water vapor and gas impurities on CO2 capture performance of carbon materials

Flue gas from a conventional power plant is usually composed of not only CO_2 and N_2 but also a certain number of impurities, such as H_2O, SO_2 and NO_x, which will affect the CO_2 adsorption performance of adsorbent. The hydrophobic nature of

activated carbon gives rise to a relatively low water uptake at low levels of humidity, which is advantageous for CO_2 capture in humid conditions. However, capillary condensation initiates with an increase in relative humidity, leading to a significant increase of water uptake under high humidity conditions and therefore decrementing the CO_2 adsorption/desorption performance of activated carbons. On the other hand, the presence of other gas impurities, such as SO_2 and NO_x, may also compete with CO_2 for adsorption sites, influencing the CO_2 adsorption/desorption. Since few studies have investigated the impact of high relative humidity and gas impurities on CO_2 capture using carbon materials so far, future work will focus on:

1) Evaluation of CO_2 adsorption performance of activated carbons under different levels of relative humidity and different concentrations of SO_2 and NO_x by using the fixed bed column system.

2) Modifying the carbon material through surface functionalization to enhance its selectivity for CO_2 over other gaseous components, potentially mitigating the impact of moisture and impurities.

References

ABD, A. A., OTHMAN, M. R. & KIM, J. 2021. A review on application of activated carbons for carbon dioxide capture: present performance, preparation, and surface modification for further improvement. Environmental Science and Pollution Research, 28, 43329-43364.

ACIKYILDIZ, M., GURSES, A. & KARACA, S. 2014. Preparation and characterization of activated carbon from plant wastes with chemical activation. Microporous and Mesoporous Materials, 198, 45-49.

ADELODUN, A. A., KIM, K. H., NGILA, J. C. & SZULEJKO, J. 2015. A review on the effect of amination pre-treatment for the selective separation of CO_2. Applied Energy, 158, 631-642.

AHMAD, A. A., AL-RAGGAD, M. & SHAREEF, N. 2021. Production of activated carbon derived from agricultural by-products via microwave-induced chemical activation: a review. Carbon Letters, 31, 957-971.

ALEX ZAPANTIS, N. A. A., IAN HAVERCROFT, RUTH IVORY-MOORE, MATT STEYN, XIAOLIANG YANG, RUTH GEBREMEDHIN, MOHAMMAD ABU ZAHRA, ERROL PINTO, DOMINIC RASSOOL, ERIC WILLIAMS, CHRIS CONSOLI, AND JOEY MINERVINI 2022. GLOBAL STATUS OF CCS 2022.

ALOTHMAN, Z., HABILA, M. & ALI, R. 2011. Preparation of activated carbon using the copyrolysis of agricultural and municipal solid wastes at a low carbonization temperature. carbon, 24, 67-72.

ANCA-COUCE, A. 2016. Reaction mechanisms and multi-scale modelling of lignocellulosic biomass pyrolysis. Progress in Energy and Combustion Science, 53, 41-79.

ANDLAR, M., REZIĆ, T., MARĐETKO, N., KRACHER, D., LUDWIG, R. & ŠANTEK, B. 2018. Lignocellulose degradation: An overview of fungi and fungal enzymes involved in lignocellulose degradation. Engineering in Life Sciences, 18, 768-778.

ANIRUDDHA, R., SREEDHAR, I. & REDDY, B. M. 2020. MOFs in carbon capture-past, present and future. Journal of CO_2 Utilization, 42.

ASHOURIRAD, B., ARAB, P., ISLAMOGLU, T., CYCHOSZ, K. A., THOMMES, M. & EL-KADERI, H. M. 2016. A cost-effective synthesis of heteroatom-doped porous carbons as efficient CO_2 sorbents. Journal of Materials Chemistry A, 4, 14693-14702.

ASHOURIRAD, B., SEKIZKARDES, A. K., ALTARAWNEH, S. & EL-KADERI, H. M. 2015. Exceptional Gas Adsorption Properties by Nitrogen-Doped Porous Carbons Derived from Benzimidazole-Linked Polymers. Chemistry of Materials, 27, 1349-1358.

AZADI, P., INDERWILDI, O. R., FARNOOD, R. & KING, D. A. 2013. Liquid fuels, hydrogen and chemicals from lignin: A critical review. Renewable & Sustainable Energy Reviews, 21, 506-523.

BACCILE, N., FALCO, C. & TITIRICI, M. M. 2014. Characterization of biomass and its derived char using C-13-solid state nuclear magnetic resonance. Green Chemistry, 16, 4839-4869.

BAE, T. H., HUDSON, M. R., MASON, J. A., QUEEN, W. L., DUTTON, J. J., SUMIDA, K., MICKLASH, K. J., KAYE, S. S., BROWN, C. M. & LONG, J. R. 2013. Evaluation of cation-exchanged zeolite adsorbents for post-combustion carbon dioxide capture. Energy & Environmental Science, 6, 128-138.

BAGHERI, N. & ABEDI, J. 2009. Preparation of high surface area activated carbon from corn by chemical activation using potassium hydroxide. Chemical Engineering Research & Design, 87, 1059-1064.

BAJWA, D. S., POURHASHEM, G., ULLAH, A. H. & BAJWA, S. G. 2019. A concise review of current lignin production, applications, products and their environmental impact. Industrial Crops and Products, 139, 11.

BARDHAN, M., NOVERA, T. M., TABASSUM, M., ISLAM, M. A. & HAMEED, B. H. 2021. Co-hydrothermal carbonization of different feedstocks to hydrochar as potential energy for the future world: A review. Journal of Cleaner Production, 298.

BEN-MANSOUR, R., HABIB, M. A., BAMIDELE, O. E., BASHA, M., QASEM, N. A. A., PEEDIKAKKAL, A., LAOUI, T. & ALI, M. 2016. Carbon capture by physical adsorption: Materials, experimental investigations and numerical modeling and simulations - A review. Applied Energy, 161, 225-255.

BERGE, N. D., RO, K. S., MAO, J. D., FLORA, J. R. V., CHAPPELL, M. A. & BAE, S. Y. 2011. Hydrothermal Carbonization of Municipal Waste Streams. Environmental Science & Technology, 45, 5696-5703.

BLAUWHOFF, P. M. M., VERSTEEG, G. F. & VANSWAAIJ, W. P. M. 1984. A STUDY ON THE REACTION BETWEEN CO_2 AND ALKANOLAMINES IN AQUEOUS-SOLUTIONS. Chemical Engineering Science, 39, 207-225.

BOUJIBAR, O., SOUIKNY, A., GHAMOUSS, F., ACHAK, O., DAHBI, M. & CHAFIK, T. 2018. CO_2 capture using N-containing nanoporous activated carbon obtained from argan fruit shells. Journal of Environmental Chemical Engineering, 6, 1995-2002.

BP 2022. Statistical review of world energy 2022. BP London, UK.

BRAZIL, T. R., GONCALVES, M., MAURO, S. O. & REZENDE, M. C. 2022. Sustainable process to produce activated carbon from Kraft lignin impregnated with H3PO4 using microwave pyrolysis. Biomass & Bioenergy, 156.

BREBU, M., TAMMINEN, T. & SPIRIDON, I. 2013. Thermal degradation of various lignins by TG-MS/FTIR and Py-GC-MS. Journal of Analytical and Applied Pyrolysis, 104, 531-539.

BRITO, M. J. P., VELOSO, C. M., SANTOS, L. S., BONOMO, R. C. F. & FONTAN, R. D. I. 2018. Adsorption of the textile dye Dianix (R) royal blue CC onto carbons obtained from yellow mombin fruit stones and activated with KOH and H3PO4: kinetics, adsorption equilibrium and thermodynamic studies. Powder Technology, 339, 334-343.

BRUNAUER, S., EMMETT, P. H. & TELLER, E. 1938. Adsorption of gases in multimolecular layers. Journal of the American chemical society, 60, 309-319.

BUI, M., ADJIMAN, C. S., BARDOW, A., ANTHONY, E. J., BOSTON, A., BROWN, S., FENNELL, P. S., FUSS, S., GALINDO, A., HACKETT, L. A., HALLETT, J. P., HERZOG, H. J., JACKSON, G., KEMPER, J., KREVOR, S., MAITLAND, G. C., MATUSZEWSKI, M., METCALFE, I. S., PETIT, C., PUXTY, G., REIMER, J., REINER, D. M., RUBIN, E. S., SCOTT, S. A., SHAH, N., SMIT, B., TRUSLER, J. P. M., WEBLEY, P., WILCOX, J. & MAC DOWELL, N. 2018. Carbon capture and storage (CCS): the way forward. Energy & Environmental Science, 11, 1062-1176.

BUNACIU, A. A., UDRIŞTIOIU, E. G. & ABOUL-ENEIN, H. Y. 2015. X-ray diffraction: instrumentation and applications. Critical reviews in analytical chemistry, 45, 289-299.

CAGNON, B., PY, X., GUILLOT, A., STOECKLI, F. & CHAMBAT, G. 2009. Contributions of hemicellulose, cellulose and lignin to the mass and the porous properties of chars and steam activated carbons from various lignocellulosic precursors. Bioresource Technology, 100, 292-298.

CAI, J. X., LI, B., CHEN, C. Y., WANG, J., ZHAO, M. & ZHANG, K. 2016. Hydrothermal carbonization of tobacco stalk for fuel application. Bioresource Technology, 220, 305-311.

CALVO-MUNOZ, E. M., GARCIA-MATEOS, F. J., ROSAS, J. M., RODRIGUEZ-MIRASOL, J. & CORDERO, T. 2016. Biomass Waste Carbon Materials as adsorbents for CO_2 Capture under Post-Combustion Conditions. Frontiers in Materials, 3.

CAO, X. Y., RO, K. S., LIBRA, J. A., KAMMANN, C. I., LIMA, I., BERGE, N., LI, L., LI, Y., CHEN, N., YANG, J., DENG, B. L. & MAO, J. D. 2013. Effects of Biomass Types and Carbonization Conditions on the Chemical Characteristics of Hydrochars. Journal of Agricultural and Food Chemistry, 61, 9401-9411.

CHAO, C., DENG, Y. M., DEWIL, R., BAEYENS, J. & FAN, X. F. 2021. Post-combustion carbon capture. Renewable & Sustainable Energy Reviews, 138.

CHEN, C., FENG, X., ZHU, Q., DONG, R., YANG, R., CHENG, Y. & HE, C. 2019. Microwave-assisted rapid synthesis of well-shaped MOF-74 (Ni) for CO_2 efficient capture. Inorganic chemistry, 58, 2717-2728.

CHEN, C., ZHANG, S., ROW, K. H. & AHN, W. S. 2017. Amine-silica composites for CO_2 capture: A short review. Journal of Energy Chemistry, 26, 868-880.

CHEN, J., YANG, J., HU, G. S., HU, X., LI, Z. M., SHEN, S. W., RADOSZ, M. & FAN, M. H. 2016. Enhanced CO_2 Capture Capacity of Nitrogen-Doped Biomass-Derived Porous Carbons. Acs Sustainable Chemistry & Engineering, 4, 1439-1445.

CHEN, X. F., MA, X. Q., PENG, X. W., LIN, Y. S. & YAO, Z. L. 2018. Conversion of sweet potato waste to solid fuel via hydrothermal carbonization. Bioresource Technology, 249, 900-907.

CHEN, X. G., JEYASEELAN, S. & GRAHAM, N. 2002. Physical and chemical properties study of the activated carbon made from sewage sludge. Waste Management, 22, 755-760.

CHENG, J., LIU, N., HU, L., LI, Y., WANG, Y. & ZHOU, J. 2019. Polyethyleneimine entwine thermally-treated Zn/Co zeolitic imidazolate frameworks to enhance CO_2 adsorption. Chemical Engineering Journal, 364, 530-540.

CHEUNG, O. & HEDIN, N. 2014. Zeolites and related sorbents with narrow pores for CO_2 separation from flue gas. Rsc Advances, 4, 14480-14494.

CHIANG, Y. C. & JUANG, R. S. 2017. Surface modifications of carbonaceous materials for carbon dioxide adsorption: A review. Journal of the Taiwan Institute of Chemical Engineers, 71, 214-234.

CHOI, W., PARK, J., KIM, C. & CHOI, M. 2021. Structural effects of amine polymers on stability and energy efficiency of adsorbents in post-combustion CO_2 capture. Chemical Engineering Journal, 408.

COROMINA, H. M., WALSH, D. A. & MOKAYA, R. 2016. Biomass-derived activated carbon with simultaneously enhanced CO_2 uptake for both pre and post-combustion capture applications. Journal of Materials Chemistry A, 4, 280-289.

CORREA, C. A., DE SANTI, C. R. & LECLERC, A. 2019. Green-PVC with full recycled industrial waste and renewably sourced content. Journal of Cleaner Production, 229, 1397-1411.

CORREA, C. R., NGAMYING, C., KLANK, D. & KRUSE, A. 2018. Investigation of the textural and adsorption properties of activated carbon from HTC and pyrolysis carbonizates. Biomass Conversion and Biorefinery, 8, 317-328.

CORREA, C. R., OTTO, T. & KRUSE, A. 2017a. Influence of the biomass components on the pore formation of activated carbon. Biomass & Bioenergy, 97, 53-64.

CORREA, C. R., STOLLOVSKY, M., HEHR, T., RAUSCHER, Y., ROLLI, B. & KRUSE, A. 2017b. Influence of the Carbonization Process on Activated Carbon Properties from Lignin and Lignin-Rich Biomasses. Acs Sustainable Chemistry & Engineering, 5, 8222-8233.

CUONG, D. V., LIU, N. L., NGUYEN, V. A. & HOU, C. H. 2019. Meso/micropore-controlled hierarchical porous carbon derived from activated biochar as a high-performance adsorbent for copper removal. Science of the Total Environment, 692, 844-853.

DANISH, M. & AHMAD, T. 2018. A review on utilization of wood biomass as a sustainable precursor for activated carbon production and application. Renewable & Sustainable Energy Reviews, 87, 1-21.

DE YUSO, A. M., RUBIO, B. & IZQUIERDO, M. T. 2014. Influence of activation atmosphere used in the chemical activation of almond shell on the characteristics and adsorption performance of activated carbons. Fuel Processing Technology, 119, 74-80.

DEB-CHOUDHURY, S., HAINES, S., HARLAND, D., CLERENS, S., VAN KOTEN, C. & DYER, J. 2014. Effect of Cooking on Meat Proteins: Mapping Hydrothermal Protein Modification as a Potential Indicator of Bioavailability. Journal of Agricultural and Food Chemistry, 62, 8187-8196.

DEMIR, M., TESSEMA, T. D., FARGHALY, A. A., NYANKSON, E., SARASWAT, S. K., AKSOY, B., ISLAMOGLU, T., COLLINSON, M. M., EL-KADERI, H. M. & GUPTA, R. B. 2018. Lignin-derived heteroatom-doped porous carbons for supercapacitor and CO_2 capture applications. International Journal of Energy Research, 42, 2686-2700.

DENG, S. B., HU, B. Y., CHEN, T., WANG, B., HUANG, J., WANG, Y. J. & YU, G. 2015. Activated carbons prepared from peanut shell and sunflower seed shell for high CO_2 adsorption. Adsorption-Journal of the International Adsorption Society, 21, 125-133.

DENG, S. B., WEI, H. R., CHEN, T., WANG, B., HUANG, J. & YU, G. 2014. Superior CO_2 adsorption on pine nut shell-derived activated carbons and the effective micropores at different temperatures. Chemical Engineering Journal, 253, 46-54.

DENIEL, M., HAARLEMMER, G., ROUBAUD, A., WEISS-HORTALA, E. & FAGES, J. 2016. Energy valorisation of food processing residues and model compounds by hydrothermal liquefaction. Renewable & Sustainable Energy Reviews, 54, 1632-1652.

DESSBESELL, L., PALEOLOGOU, M., LEITCH, M., PULKKI, R. & XU, C. 2020. Global lignin supply overview and kraft lignin potential as an alternative for petroleum-based polymers. Renewable & Sustainable Energy Reviews, 123.

DIAS, J. M., ALVIM-FERRAZ, M. C. M., ALMEIDA, M. F., RIVERA-UTRILLA, J. & SANCHEZ-POLO, M. 2007. Waste materials for activated carbon preparation and its use in aqueous-phase treatment: A review. Journal of Environmental Management, 85, 833-846.

DINDI, A., QUANG, D. V., VEGA, L. F., NASHEF, E. & ABU-ZAHRA, M. R. M. 2019. Applications of fly ash for CO_2 capture, utilization, and storage. Journal of CO_2 Utilization, 29, 82-102.

DING, M. L., FLAIG, R. W., JIANG, H. L. & YAGHI, O. M. 2019. Carbon capture and conversion using metal-organic frameworks and MOF-based materials. Chemical Society Reviews, 48, 2783-2828.

DINJUS, E., KRUSE, A. & TROGER, N. 2011. Hydrothermal Carbonization-1. Influence of Lignin in Lignocelluloses. Chemical Engineering & Technology, 34, 2037-2043.

DRAGE, T. C., SNAPE, C. E., STEVENS, L. A., WOOD, J., WANG, J. W., COOPER, A. I., DAWSON, R., GUO, X., SATTERLEY, C. & IRONS, R. 2012. Materials challenges for the development of solid sorbents for post-combustion carbon capture. Journal of Materials Chemistry, 22, 2815-2823.

DURMAZ, T. 2018. The economics of CCS: Why have CCS technologies not had an international breakthrough? Renewable and Sustainable Energy Reviews, 95, 328-340.

EL HADRI, N., QUANG, D. V., GOETHEER, E. L. & ZAHRA, M. R. A. 2017. Aqueous amine solution characterization for post-combustion CO_2 capture process. Applied Energy, 185, 1433-1449.

ELLO, A. S., DE SOUZA, L. K. C., TROKOUREY, A. & JARONIEC, M. 2013a. Coconut shell-based microporous carbons for CO_2 capture. Microporous and Mesoporous Materials, 180, 280-283.

ELLO, A. S., DE SOUZA, L. K. C., TROKOUREY, A. & JARONIEC, M. 2013b. Development of microporous carbons for CO_2 capture by KOH activation of African palm shells. Journal of CO_2 Utilization, 2, 35-38.

EVERETT, D. H. & POWL, J. C. 1976. Adsorption in slit-like and cylindrical micropores in the henry's law region. A model for the microporosity of carbons. Journal of the Chemical Society, Faraday Transactions 1: Physical Chemistry in Condensed Phases, 72, 619-636.

FABER, R., YAN, J. Y., STARK, F. & PRIESNITZ, S. 2011. Flue gas desulphurization for hot recycle Oxyfuel combustion: Experiences from the 30 MWth Oxyfuel pilot plant in Schwarze Pumpe. International Journal of Greenhouse Gas Control, 5, S210-S223.

FALCO, C., BACCILE, N. & TITIRICI, M. M. 2011. Morphological and structural differences between glucose, cellulose and lignocellulosic biomass derived hydrothermal carbons. Green Chemistry, 13, 3273-3281.

FALCO, C., MARCO-LOZAR, J. P., SALINAS-TORRES, D., MORALLON, E., CAZORLA-AMOROS, D., TITIRICI, M. M. & LOZANO-CASTELLO, D. 2013. Tailoring the porosity of chemically activated hydrothermal carbons: Influence of the precursor and hydrothermal carbonization temperature. Carbon, 62, 346-355.

FIERRO, V., TORNE-FERNANDEZ, V. & CELZARD, A. 2007. Methodical study of the chemical activation of Kraft lignin with KOH and NaOH. Microporous and Mesoporous Materials, 101, 419-431.

FOO, G. S., LEE, J. J., CHEN, C. H., HAYES, S. E., SIEVERS, C. & JONES, C. W. 2017. Elucidation of Surface Species through in Situ FTIR Spectroscopy of Carbon Dioxide Adsorption on Amine-Grafted SBA-15. Chemsuschem, 10, 266-276.

FOO, K. Y. & HAMEED, B. H. 2012. Potential of jackfruit peel as precursor for activated carbon prepared by microwave induced NaOH activation. Bioresource Technology, 112, 143-150.

FUJIKI, J. & YOGO, K. 2016. The increased CO_2 adsorption performance of chitosan-derived activated carbons with nitrogen-doping. Chemical Communications, 52, 186-189.

FUNKE, A. & ZIEGLER, F. 2010. Hydrothermal carbonization of biomass: A summary and discussion of chemical mechanisms for process engineering. Biofuels Bioproducts & Biorefining-Biofpr, 4, 160-177.

GAO, P., ZHOU, Y. Y., MENG, F., ZHANG, Y. H., LIU, Z. H., ZHANG, W. Q. & XUE, G. 2016. Preparation and characterization of hydrochar from waste eucalyptus bark by hydrothermal carbonization. Energy, 97, 238-245.

GAO, Y., YUE, Q., GAO, B. & LI, A. 2020. Insight into activated carbon from different kinds of chemical activating agents: A review. Science of the Total Environment, 746, 141094.

GHOLIDOUST, A., ATKINSON, J. D. & HASHISHO, Z. 2017. Enhancing CO_2 Adsorption via Amine-Impregnated Activated Carbon from Oil Sands Coke. Energy & Fuels, 31, 1756-1763.

GOEL, C., MOHAN, S. & DINESHA, P. 2021. CO_2 capture by adsorption on biomass-derived activated char: A review. Science of The Total Environment, 798, 149296.

GOLDSTEIN, J. I., NEWBURY, D. E., MICHAEL, J. R., RITCHIE, N. W., SCOTT, J. H. J. & JOY, D. C. 2017. Scanning electron microscopy and X-ray microanalysis, Springer.

GONZALEZ, B. & MANYA, J. J. 2020. Activated olive mill waste-based hydrochars as selective adsorbents for CO_2 capture under postcombustion conditions. Chemical Engineering and Processing-Process Intensification, 149.

GUNDOGDU, A., DURAN, C., SENTURK, H. B., SOYLAK, M., IMAMOGLU, M. & ONAL, Y. 2013. Physicochemical characteristics of a novel activated carbon produced from tea industry waste. Journal of Analytical and Applied Pyrolysis, 104, 249-259.

GUO, S. Q., DONG, X. Y., WU, T. T., SHI, F. J. & ZHU, C. X. 2015. Characteristic evolution of hydrochar from hydrothermal carbonization of corn stalk. Journal of Analytical and Applied Pyrolysis, 116, 1-9.

GUO, Y. F., TAN, C., SUN, J., LI, W. L., ZHANG, J. B. & ZHAO, C. W. 2020. Porous activated carbons derived from waste sugarcane bagasse for CO_2 adsorption. Chemical Engineering Journal, 381, 9.

HACK, J., MAEDA, N. & MEIER, D. M. 2022. Review on CO_2 Capture Using Amine-Functionalized Materials. Acs Omega, 7, 39520-39530.

HAO, W. M., BJORKMAN, E., LILLIESTRALE, M. & HEDIN, N. 2013. Activated carbons prepared from hydrothermally carbonized waste biomass used as adsorbents for CO_2. Applied Energy, 112, 526-532.

HAYASHI, J., HORIKAWA, T., TAKEDA, I., MUROYAMA, K. & ANI, F. N. 2002. Preparing activated carbon from various nutshells by chemical activation with K2CO3. Carbon, 40, 2381-2386.

HE, C., GIANNIS, A. & WANG, J. Y. 2013. Conversion of sewage sludge to clean solid fuel using hydrothermal carbonization: Hydrochar fuel characteristics and combustion behavior. Applied Energy, 111, 257-266.

HE, J. J., TO, J. W. F., PSARRAS, P. C., YAN, H. P., ATKINSON, T., HOLMES, R. T., NORDLUND, D., BAO, Z. N. & WILCOX, J. 2016. Tunable Polyaniline-Based Porous Carbon with Ultrahigh Surface Area for CO_2 Capture at Elevated Pressure. Advanced Energy Materials, 6.

HE, S., CHEN, G. Y., XIAO, H., SHI, G. B., RUAN, C. C., MA, Y. S., DAI, H. M., YUAN, B. H., CHEN, X. F. & YANG, X. B. 2021. Facile preparation of N-doped activated carbon produced from rice husk for CO_2 capture. Journal of Colloid and Interface Science, 582, 90-101.

HEIDARINEJAD, Z., DEHGHANI, M. H., HEIDARI, M., JAVEDAN, G., ALI, I. & SILLANPAA, M. 2020. Methods for preparation and activation of activated carbon: a review. Environmental Chemistry Letters, 18, 393-415.

HERAWAN, S. G., HADI, M. S., AYOB, M. R. & PUTRA, A. 2013. Characterization of Activated Carbons from Oil-Palm Shell by CO_2 Activation with No Holding Carbonization Temperature. Scientific World Journal.

HOEKMAN, S. K., BROCH, A. & ROBBINS, C. 2011. Hydrothermal Carbonization (HTC) of Lignocellulosic Biomass. Energy & Fuels, 25, 1802-1810.

HONG, S. M., YOON, H. J., CHOI, Y., CHO, Y. Z., MUN, S., POL, V. G. & LEE, K. B. 2020. Solving two environmental problems simultaneously: Scalable production of carbon microsheets from structured packing peanuts with tailored microporosity for efficient CO_2 capture. Chemical Engineering Journal, 379, 9.

HONICKE, I. M., SENKOVSKA, I., BON, V., BABURIN, I. A., BONISCH, N., RASCHKE, S., EVANS, J. D. & KASKEL, S. 2018. Balancing Mechanical Stability and Ultrahigh Porosity in Crystalline Framework Materials. Angewandte Chemie-International Edition, 57, 13780-13783.

HORNBOSTEL, M. D., BAO, J., KRISHNAN, G., NAGAR, A., JAYAWEERA, I., KOBAYASHI, T., SANJURJO, A., SWEENEY, J., CARRUTHERS, D., PETRUSKA, M. A. & DUBOIS, L. 2013. Characteristics of an advanced carbon sorbent for CO_2 capture. Carbon, 56, 77-85.

HOSSEINI, S., BAYESTI, I., MARAHEL, E., BABADI, F. E., ABDULLAH, L. C. & CHOONG, T. S. Y. 2015. Adsorption of carbon dioxide using activated carbon impregnated with Cu promoted by zinc. Journal of the Taiwan Institute of Chemical Engineers, 52, 109-117.

HU, X., RADOSZ, M., CYCHOSZ, K. A. & THOMMES, M. 2011. CO_2-Filling Capacity and Selectivity of Carbon Nanopores: Synthesis, Texture, and Pore-Size Distribution from Quenched-Solid Density Functional Theory (QSDFT). Environmental Science & Technology, 45, 7068-7074.

HU, X. E., LIU, L., LUO, X., XIAO, G., SHIKO, E., ZHANG, R., FAN, X., ZHOU, Y., LIU, Y. & ZENG, Z. 2020. A review of N-functionalized solid adsorbents for post-combustion CO_2 capture. Applied Energy, 260, 114244.

HUANG, F., LI, D. W., WANG, L., ZHANG, K., FU, L. L., GUO, Z. Y., LIANG, M., WANG, B., LUO, D. S. & LI, B. 2021. Rational introduction of nitridizing agent to hydrothermal carbonization for enhancing CO_2 capture performance of tobacco stalk-based porous carbons. Journal of Analytical and Applied Pyrolysis, 157.

HUANG, G.-G., LIU, Y.-F., WU, X.-X. & CAI, J.-J. 2019a. Activated carbons prepared by the KOH activation of a hydrochar from garlic peel and their CO_2 adsorption performance. New Carbon Materials, 34, 247-257.

HUANG, G. G., LIU, Y. F., WU, X. X. & CAI, J. J. 2019b. Activated carbons prepared by the KOH activation of a hydrochar from garlic peel and their CO_2 adsorption performance. New Carbon Materials, 34, 247-257.

HUANG, N., ZHAO, P., GHOSH, S. & FEDYUKHIN, A. 2019c. Co-hydrothermal carbonization of polyvinyl chloride and moist biomass to remove chlorine and inorganics for clean fuel production. Applied Energy, 240, 882-892.

IEA 2022, Carbon Capture, Utilisation and Storage, IEA, Paris https://www.iea.org/reports/carbon-capture-utilisation-and-storage-2

IEA 2023, CO_2 Emissions in 2022, IEA, Paris https://www.iea.org/reports/co2-emissions-in-2022

IPCC 2023. AR6 Synthesis Report: Climate Change 2023. Geneva, Switzerland: Intergovernmental panel on climate change IPCC.

JAIN, A., BALASUBRAMANIAN, R. & SRINIVASAN, M. P. 2015. Tuning hydrochar properties for enhanced mesopore development in activated carbon by hydrothermal carbonization. Microporous and Mesoporous Materials, 203, 178-185.

JAIN, A., BALASUBRAMANIAN, R. & SRINIVASAN, M. P. 2016. Hydrothermal conversion of biomass waste to activated carbon with high porosity: A review. Chemical Engineering Journal, 283, 789-805.

JANSEN, D., GAZZANI, M., MANZOLINI, G., VAN DIJK, E. & CARBO, M. 2015. Pre-combustion CO_2 capture. International Journal of Greenhouse Gas Control, 40, 167-187.

JIANG, Z., YI, J., LI, J., HE, T. & HU, C. 2015. Promoting effect of sodium chloride on the solubilization and depolymerization of cellulose from raw biomass materials in water. ChemSusChem, 8, 1901-1907.

JIAO, J., CAO, J., XIA, Y. & ZHAO, L. 2016. Improvement of adsorbent materials for CO_2 capture by amine functionalized mesoporous silica with worm-hole framework structure. Chemical Engineering Journal, 306, 9-16.

JIN, Z. H., WANG, B. D., MA, L., FU, P. B., XIE, L. L., JIANG, X. & JIANG, W. J. 2020. Air pre-oxidation induced high yield N-doped porous biochar for improving toluene adsorption. Chemical Engineering Journal, 385.

KANG, S. M., LI, X. H., FAN, J. & CHANG, J. 2012. Characterization of Hydrochars Produced by Hydrothermal Carbonization of Lignin, Cellulose, D-Xylose, and Wood Meal. Industrial & Engineering Chemistry Research, 51, 9023-9031.

KANNICHE, M., GROS-BONNIVARD, R., JAUD, P., VALLE-MARCOS, J., AMANN, J.-M. & BOUALLOU, C. 2010a. Pre-combustion, post-combustion and oxy-combustion in thermal power plant for CO_2 capture. Applied Thermal Engineering, 30, 53-62.

KANNICHE, M., GROS-BONNIVARD, R., JAUD, P., VALLE-MARCOS, J., AMANN, J. M. & BOUALLOU, C. 2010b. Pre-combustion, post-combustion and oxy-combustion in thermal power plant for CO_2 capture. Applied Thermal Engineering, 30, 53-62.

KHALIFA, O., ALKHATIB, I. I., BAHAMON, D., ALHAJAJ, A., ABU-ZAHRA, M. R. & VEGA, L. F. 2022. Modifying absorption process configurations to improve their performance for Post-Combustion CO_2 capture–What have we learned and what is still Missing? Chemical Engineering Journal, 430, 133096.

KHAN, T. A., SAUD, A. S., JAMARI, S. S., AB RAHIM, M. H., PARK, J. W. & KIM, H. J. 2019. Hydrothermal carbonization of lignocellulosic biomass for carbon rich material preparation: A review. Biomass & Bioenergy, 130.

KIM, J. H., HWANG, S. Y., PARK, J. E., LEE, G. B., KIM, H., KIM, S. & HONG, B. U. 2019. Impact of the oxygen functional group of nitric acid-treated activated carbon on KOH activation reaction. Carbon Letters, 29, 281-287.

KIM, M. J., CHOI, S. W., KIM, H., MUN, S. & LEE, K. B. 2020a. Simple synthesis of spent coffee ground -based microporous carbons using K 2 CO 3 as an activation agent and their application to CO 2 capture. Chemical Engineering Journal, 397.

KIM, M. J., CHOI, S. W., KIM, H., MUN, S. & LEE, K. B. 2020b. Simple synthesis of spent coffee ground -based microporous carbons using K 2 CO 3 as an activation agent and their application to CO 2 capture. Chemical Engineering Journal, 397, 11.

KISHIBAYEV, K. K., SERAFIN, J., TOKPAYEV, R. R., KHAVAZA, T. N., ATCHABAROVA, A. A., ABDUAKHYTOVA, D. A., IBRAIMOV, Z. T. & SRENSCEK-NAZZAL, J. 2021. Physical and chemical properties of activated carbon synthesized from plant wastes and shungite for CO_2 capture. Journal of Environmental Chemical Engineering, 9.

KNEZEVIC, D., VAN SWAAIJ, W. P. M. & KERSTEN, S. R. A. 2009. Hydrothermal Conversion of Biomass: I, Glucose Conversion in Hot Compressed Water. Industrial & Engineering Chemistry Research, 48, 4731-4743.

KOMAKI, A., GOTOU, T., UCHIDA, T., YAMADA, T., KIGA, T. & SPERO, C. 2014. Operation Experiences of Oxyfuel Power Plant in Callide Oxyfuel Project. 12th International Conference on Greenhouse Gas Control Technologies, Ghgt-12, 63, 490-496.

KOOHESTANIAN, E. & SHAHRAKI, F. 2021. Review on principles, recent progress, and future challenges for oxy-fuel combustion CO_2 capture using compression and purification unit. Journal of Environmental Chemical Engineering, 9.

KUBATOVA, A., LAGADEC, A. J. M. & HAWTHORNE, S. B. 2002. Dechlorination of lindane, dieldrin, tetrachloroethane, trichloroethene, and PVC in subcritical water. Environmental Science & Technology, 36, 1337-1343.

KUMAR, A. & JENA, H. M. 2015. High surface area microporous activated carbons prepared from Fox nut (Euryale ferox) shell by zinc chloride activation. Applied Surface Science, 356, 753-761.

KUMAR, A. & JENA, H. M. 2016. Preparation and characterization of high surface area activated carbon from Fox nut (Euryale ferox) shell by chemical activation with H3PO4. Results in Physics, 6, 651-658.

LAHIJANI, P., MOHAMMADI, M. & MOHAMED, A. R. 2018. Metal incorporated biochar as a potential adsorbent for high capacity CO_2 capture at ambient condition. Journal of CO_2 Utilization, 26, 281-293.

LANDERS, J., GOR, G. Y. & NEIMARK, A. V. 2013. Density functional theory methods for characterization of porous materials. Colloids and Surfaces a-Physicochemical and Engineering Aspects, 437, 3-32.

LANGMUIR, I. 1918. The adsorption of gases on plane surfaces of glass, mica and platinum. Journal of the American Chemical society, 40, 1361-1403.

LEE, J. S., KIM, J. H., KIM, J. T., SUH, J. K., LEE, J. M. & LEE, C. H. 2002. Adsorption equilibria of CO_2 on zeolite 13X and zeolite X/Activated carbon composite. Journal of Chemical and Engineering Data, 47, 1237-1242.

LEE, S. Y. & PARK, S. J. 2015. A review on solid adsorbents for carbon dioxide capture. Journal of Industrial and Engineering Chemistry, 23, 1-11.

LENG, L. J., XIONG, Q., YANG, L. H., LI, H., ZHOU, Y. Y., ZHANG, W. J., JIANG, S. J., LI, H. L. & HUANG, H. J. 2021. An overview on engineering the surface area and porosity of biochar. Science of the Total Environment, 763, 18.

LEUNG, D. Y. C., CARAMANNA, G. & MAROTO-VALER, M. M. 2014. An overview of current status of carbon dioxide capture and storage technologies. Renewable & Sustainable Energy Reviews, 39, 426-443.

LI, B. & LI, K. 2019. Effect of nitric acid pre-oxidation concentration on pore structure and nitrogen/oxygen active decoration sites of ethylenediamine-modified biochar for mercury (II) adsorption and the possible mechanism. Chemosphere, 220, 28-39.

LI, B. W., HU, J. C., XIONG, H. & XIAO, Y. 2020a. Application and Properties of Microporous Carbons Activated by ZnCl2: Adsorption Behavior and Activation Mechanism. Acs Omega, 5, 9398-9407.

LI, D., CHEN, Y. L., ZHENG, M., ZHAO, H. F., ZHAO, Y. F. & SUN, Z. C. 2016. Hierarchically Structured Porous Nitrogen-Doped Carbon for Highly Selective CO_2 Capture. Acs Sustainable Chemistry & Engineering, 4, 298-304.

LI, D. W., MA, T. F., ZHANG, R. L., TIAN, Y. Y. & QIAO, Y. Y. 2015a. Preparation of porous carbons with high low-pressure CO_2 uptake by KOH activation of rice husk char. Fuel, 139, 68-70.

LI, D. W., ZHOU, J. J., ZHANG, Z. B., LI, L. J., TIAN, Y. Y., LU, Y. M., QIAO, Y. Y., LI, J. H. & WEN, L. 2017a. Improving low-pressure CO_2 capture performance of N-doped active carbons by adjusting flow rate of protective gas during alkali activation. Carbon, 114, 496-503.

LI, H., EDDAOUDI, M., GROY, T. L. & YAGHI, O. M. 1998. Establishing microporosity in open metal-organic frameworks: Gas sorption isotherms for Zn(BDC) (BDC = 1,4-benzenedicarboxylate). Journal of the American Chemical Society, 120, 8571-8572.

LI, H., EDDAOUDI, M., O'KEEFFE, M. & YAGHI, O. M. 1999. Design and synthesis of an exceptionally stable and highly porous metal-organic framework. Nature, 402, 276-279.

LI, J., ZHAO, P., LI, T., LEI, M., YAN, W. & GE, S. 2020b. Pyrolysis behavior of hydrochar from hydrothermal carbonization of pinewood sawdust. Journal of Analytical and Applied Pyrolysis, 146, 104771.

LI, J. X., MICHALKIEWICZ, B., MIN, J. K., MA, C. D., CHEN, X. C., GONG, J., MIJOWSKA, E. & TANG, T. 2019. Selective preparation of biomass-derived porous carbon with controllable

pore sizes toward highly efficient CO_2 capture. Chemical Engineering Journal, 360, 250-259.

LI, K., ZHANG, D. Q., NIU, X. J., GUO, H. F., YU, Y. Y., TANG, Z. H., LIN, Z. & FU, M. L. 2022a. Insights into CO_2 adsorption on KOH-activated biochars derived from the mixed sewage sludge and pine sawdust. Science of the Total Environment, 826.

LI, M. & XIAO, R. 2019. Preparation of a dual Pore Structure Activated Carbon from Rice Husk Char as an Adsorbent for CO_2 Capture. Fuel Processing Technology, 186, 35-39.

LI, M. B., LIU, X., SUN, C. G., STEVENS, L. & LIU, H. 2022b. Synthesis and characterization of advanced bio-carbon materials from Kraft lignin with enhanced CO_2 capture properties. Journal of Environmental Chemical Engineering, 10.

LI, S. J., HAN, K. H., LI, J. X., LI, M. & LU, C. M. 2017b. Preparation and characterization of super activated carbon produced from gulfweed by KOH activation. Microporous and Mesoporous Materials, 243, 291-300.

LI, X. F., XU, Q., FU, Y. & GUO, Q. X. 2014. Preparation and characterization of activated carbon from Kraft lignin via KOH activation. Environmental Progress & Sustainable Energy, 33, 519-526.

LI, Y., ZHANG, T., WANG, Y. G. & WANG, B. B. 2021. Transformation of waste cornstalk into versatile porous carbon adsorbent for selective CO_2 capture and efficient methanol adsorption. Journal of Environmental Chemical Engineering, 9.

LI, Y. X., ZHANG, X., YANG, R. G., LI, G. Y. & HU, C. W. 2015b. The role of H3PO4 in the preparation of activated carbon from NaOH-treated rice husk residue. Rsc Advances, 5, 32626-32636.

LI, Z., LIU, P., OU, C. J. & DONG, X. C. 2020c. Porous Metal-Organic Frameworks for Carbon Dioxide Adsorption and Separation at Low Pressure. Acs Sustainable Chemistry & Engineering, 8, 15378-15404.

LI, Z. Y., GAO, X. Y., WU, L., WANG, K. W. & KOBAYASHI, N. 2017c. Preparation of activated carbons from poplar wood by chemical activation with KOH. Journal of Porous Materials, 24, 193-202.

LIANG, Q., LIU, Y., CHEN, M., MA, L., YANG, B., LI, L. & LIU, Q. 2020. Optimized preparation of activated carbon from coconut shell and municipal sludge. Materials Chemistry and Physics, 241, 122327.

LIANG, Z. W., RONGWONG, W., LIU, H. L., FU, K. Y., GAO, H. X., CAO, F., ZHANG, R., SEMA, T., HENNI, A., SUMON, K., NATH, D., GELOWITZ, D., SRISANG, W., SAIWAN, C., BENAMOR,

A., AL-MARRI, M., SHI, H. C., SUPAP, T., CHAN, C., ZHOU, Q., ABU-ZAHRA, M., WILSON, M., OLSON, W., IDEM, R. & TONTIWACHWUTHIKUL, P. 2015. Recent progress and new developments in post-combustion carbon-capture technology with amine based solvents. International Journal of Greenhouse Gas Control, 40, 26-54.

LIAO, P. Q., CHEN, X. W., LIU, S. Y., LI, X. Y., XU, Y. T., TANG, M. N., RUI, Z. B., JI, H. B., ZHANG, J. P. & CHEN, X. M. 2016. Putting an ultrahigh concentration of amine groups into a metal-organic framework for CO_2 capture at low pressures. Chemical Science, 7, 6528-6533.

LILLO-RODENAS, M. A., CAZORLA-AMOROS, D. & LINARES-SOLANO, A. 2003. Understanding chemical reactions between carbons and NaOH and KOH - An insight into the chemical activation mechanism. Carbon, 41, 267-275.

LIM, G., LEE, K. B. & HAM, H. C. 2016. Effect of N-Containing Functional Groups on CO_2 Adsorption of Carbonaceous Materials: A Density Functional Theory Approach. Journal of Physical Chemistry C, 120, 8087-8095.

LIN, L., MENG, Y., JU, T., HAN, S., MENG, F., LI, J., DU, Y., SONG, M., LAN, T. & JIANG, J. 2023. Characteristics, application and modeling of solid amine adsorbents for CO_2 capture: A review. Journal of Environmental Management, 325, 116438.

LIN, Y. S., GE, Y., XIAO, H. M., HE, Q., WANG, W. H. & CHEN, B. M. 2020. Investigation of hydrothermal co-carbonization of waste textile with waste wood, waste paper and waste food from typical municipal solid wastes. Energy, 210.

LIN, Y. S., MA, X. Q., PENG, X. W. & YU, Z. S. 2017. Hydrothermal carbonization of typical components of municipal solid waste for deriving hydrochars and their combustion behavior. Bioresource Technology, 243, 539-547.

LIU, H., LIU, B., LIN, L. C., CHEN, G. J., WU, Y. Q., WANG, J., GAO, X. T., LV, Y. N., PAN, Y., ZHANG, X. X., ZHANG, X. R., YANG, L. Y., SUN, C. Y., SMIT, B. & WANG, W. C. 2014. A hybrid absorption-adsorption method to efficiently capture carbon. Nature Communications, 5.

LIU, H., ZHANG, J., BAO, N., CHENG, C., REN, L. & ZHANG, C. L. 2012a. Textural properties and surface chemistry of lotus stalk-derived activated carbons prepared using different phosphorus oxyacids: Adsorption of trimethoprim. Journal of Hazardous Materials, 235, 367-375.

LIU, J., THALLAPALLY, P. K., MCGRAIL, B. P. & BROWN, D. R. 2012b. Progress in adsorption-based CO_2 capture by metal-organic frameworks. Chemical Society Reviews, 41, 2308-2322.

LIU, J. J., SUN, N. N., SUN, C. G., LIU, H., SNAPE, C., LI, K. X., WEI, W. & SUN, Y. H. 2015a. Spherical potassium intercalated activated carbon beads for pulverised fuel CO_2 post-combustion capture. Carbon, 94, 243-255.

LIU, R. S., SHI, X. D., WANG, C. T., GAO, Y. Z., XU, S., HAO, G. P., CHEN, S. Y. & LU, A. H. 2021. Advances in Post-Combustion CO_2 Capture by Physical Adsorption: From Materials Innovation to Separation Practice. Chemsuschem, 14, 1428-1471.

LIU, W. J., JIANG, H. & YU, H. Q. 2015b. Thermochemical conversion of lignin to functional materials: a review and future directions. Green Chemistry, 17, 4888-4907.

LIU, X., LIU, J., SUN, C., LIU, H., WANG, W., SMITH, E., JIANG, L., CHEN, X. & SNAPE, C. 2020a. Design and development of 3D hierarchical ultra-microporous CO 2-sieving carbon architectures for potential flow-through CO 2 capture at typical practical flue gas temperatures. Journal of Materials Chemistry A, 8, 17025-17035.

LIU, X., LIU, J. J., SUN, C. G., LIU, H., WANG, W. L., SMITH, E., JIANG, L., CHEN, X. Y. & SNAPE, C. 2020b. Design and development of 3D hierarchical ultra-microporous CO_2-sieving carbon architectures for potential flow-through CO(2)capture at typical practical flue gas temperatures. Journal of Materials Chemistry A, 8, 17025-17035.

LIU, X., SUN, C. G., LIU, H., TAN, W. H., WANG, W. L. & SNAPE, C. 2019. Developing hierarchically ultra-micro/mesoporous biocarbons for highly selective carbon dioxide adsorption. Chemical Engineering Journal, 361, 199-208.

LIU, X., SUN, Y., LIU, J. J., SUN, C. G., LIU, H., XUE, Q., SMITH, E. & SNAPE, C. 2017. Potassium and Zeolitic Structure Modified Adsorbent Materials from a Renewable Fe Surface Chemistry for CO_2 Capture Ultra-microporous edstock with Favourable. Acs Applied Materials & Interfaces, 9, 26826-26839.

LIU, X., WANG, S. B., SUN, C. G., LIU, H., STEVENS, L., DWOMOH, P. K. & SNAPE, C. 2020c. Synthesis of functionalized 3D microporous carbon foams for selective CO_2 capture. Chemical Engineering Journal, 402, 11.

LIU, X., YANG, F. M., LI, M. B., WANG, S. B. & SUN, C. G. 2022. From polyvinyl chloride waste to activated carbons: the role of occurring additives on porosity development and gas adsorption properties. Science of the Total Environment, 833.

LIU, Y., LI, K. & SUN, G. 2010a. Effect of precursor preoxidation on the structure of phenolic resin-based activated carbon spheres. Journal of Physics and Chemistry of Solids, 71, 453-456.

LIU, Y., LI, K. X. & SUN, G. H. 2010b. Effect of precursor preoxidation on the structure of phenolic resin-based activated carbon spheres. Journal of Physics and Chemistry of Solids, 71, 453-456.

LIU, Y. Y. & WILCOX, J. 2012. Effects of Surface Heterogeneity on the Adsorption of CO_2 in Microporous Carbons. Environmental Science & Technology, 46, 1940-1947.

LIU, Z., ZHANG, Z., JIA, Z. J., ZHAO, L., ZHANG, T. T., XING, W., KOMARNENI, S., SUBHAN, F. & YAN, Z. F. 2018. New strategy to prepare ultramicroporous carbon by ionic activation for superior CO_2 capture. Chemical Engineering Journal, 337, 290-299.

LOWELL, S., SHIELDS, J. E., THOMAS, M. A. & THOMMES, M. 2006. Characterization of porous solids and powders: surface area, pore size and density, Springer Science & Business Media.

LU, X., MA, X., CHEN, X., YAO, Z. & ZHANG, C. 2020a. Co-hydrothermal carbonization of polyvinyl chloride and corncob for clean solid fuel production. Bioresource technology, 301, 122763.

LU, X. L., MA, X. Q., CHEN, X. F., YAO, Z. L. & ZHANG, C. Y. 2020b. Co-hydrothermal carbonization of polyvinyl chloride and corncob for clean solid fuel production. Bioresource Technology, 301.

LU, X. W., FLORA, J. R. V. & BERGE, N. D. 2014. Influence of process water quality on hydrothermal carbonization of cellulose. Bioresource Technology, 154, 229-239.

LU, X. W., JORDAN, B. & BERGE, N. D. 2012. Thermal conversion of municipal solid waste via hydrothermal carbonization: Comparison of carbonization products to products from current waste management techniques. Waste Management, 32, 1353-1365.

ĽUDMILA, H., MICHAL, J., ANDREA, Š. & ALEŠ, H. 2015. Lignin, potential products and their market value. Wood Res, 60, 973-986.

LYNAM, J. G., REZA, M. T., YAN, W., VASQUEZ, V. R. & CORONELLA, C. J. 2015. Hydrothermal carbonization of various lignocellulosic biomass. Biomass Conversion and Biorefinery, 5, 173-181.

MA, D., FENG, Q., CHEN, B., CHENG, X., CHEN, K. & LI, J. 2019a. Insight into chlorine evolution during hydrothermal carbonization of medical waste model. Journal of hazardous materials, 380, 120847.

MA, D. C., FENG, Q. G., CHEN, B. Q., CHENG, X., CHEN, K. & LI, J. 2019b. Insight into chlorine evolution during hydrothermal carbonization of medical waste model. Journal of Hazardous Materials, 380.

MA, X. C., LI, L. Q., CHEN, R. F., WANG, C. H., LI, H. L. & WANG, S. B. 2018. Heteroatom-doped nanoporous carbon derived from MOF-5 for CO_2 capture. Applied Surface Science, 435, 494-502.

MA, X. C., WU, Y., FANG, M. O. E., LIU, B. G., CHEN, R. F., SHI, R., WU, Q. D., ZENG, Z. & LI, L. Q. 2022. In-situ activated ultramicroporous carbon materials derived from waste biomass for CO_2 capture and benzene adsorption. Biomass & Bioenergy, 158.

MA, Z. Q., SUN, Q. F., YE, J. W., YAO, Q. F. & ZHAO, C. 2016. Study on the thermal degradation behaviors and kinetics of alkali lignin for production of phenolic-rich bio-oil using TGA-FTIR and Py-GC/MS. Journal of Analytical and Applied Pyrolysis, 117, 116-124.

MACDERMID-WATTS, K., PRADHAN, R. & DUTTA, A. 2021. Catalytic hydrothermal carbonization treatment of biomass for enhanced activated carbon: a review. Waste and Biomass Valorisation, 12, 2171-2186.

MAHAJAN, S. & LAHTINEN, M. 2022. Recent Progress in Metal-organic Frameworks (MOFs) for CO_2 Capture At Different Pressures. Journal of Environmental Chemical Engineering, 108930.

MALGHANI, S., GLEIXNER, G. & TRUMBORE, S. E. 2013. Chars produced by slow pyrolysis and hydrothermal carbonization vary in carbon sequestration potential and greenhouse gases emissions. Soil Biology & Biochemistry, 62, 137-146.

MANYA, J. J., GONZALEZ, B., AZUARA, M. & ARNER, G. 2018. Ultra-microporous adsorbents prepared from vine shoots-derived biochar with high CO_2 uptake and CO_2/N-2 selectivity. Chemical Engineering Journal, 345, 631-639.

MARSH, H., YAN, D. S., OGRADY, T. M. & WENNERBERG, A. 1984. FORMATION OF ACTIVE CARBONS FROM COKES USING POTASSIUM HYDROXIDE. Carbon, 22, 603-611.

MASEL, R. I. 1996. Principles of adsorption and reaction on solid surfaces, John Wiley & Sons.

MASON, J. A., SUMIDA, K., HERM, Z. R., KRISHNA, R. & LONG, J. R. 2011. Evaluating metal-organic frameworks for post-combustion carbon dioxide capture via temperature swing adsorption. Energy & Environmental Science, 4, 3030-3040.

MENG, F. Z., MENG, Y., JU, T. Y., HAN, S. Y., LIN, L. & JIANG, J. G. 2022. Research progress of aqueous amine solution for CO_2 capture: A review. Renewable & Sustainable Energy Reviews, 168.

METZ, B., DAVIDSON, O., DE CONINCK, H., LOOS, M. & MEYER, L. 2005. IPCC special report on carbon dioxide capture and storage, Cambridge: Cambridge University Press.

MILLWARD, A. R. & YAGHI, O. M. 2005. Metal-organic frameworks with exceptionally high capacity for storage of carbon dioxide at room temperature. Journal of the American Chemical Society, 127, 17998-17999.

MODAK, A. & JANA, S. 2019. Advancement in porous adsorbents for post-combustion CO_2 capture. Microporous and Mesoporous Materials, 276, 107-132.

MOLLER, M., NILGES, P., HARNISCH, F. & SCHRODER, U. 2011. Subcritical Water as Reaction Environment: Fundamentals of Hydrothermal Biomass Transformation. Chemsuschem, 4, 566-579.

MOOD, S. H., GOLFESHAN, A. H., TABATABAEI, M., JOUZANI, G. S., NAJAFI, G., GHOLAMI, M. & ARDJMAND, M. 2013. Lignocellulosic biomass to bioethanol, a comprehensive review with a focus on pre-treatment. Renewable & Sustainable Energy Reviews, 27, 77-93.

MOURA, P. A. S., BEZERRA, D. P., VILARRASA-GARCIA, E., BASTOS-NETO, M. & AZEVEDO, D. C. S. 2016. Adsorption equilibria of CO_2 and CH4 in cation-exchanged zeolites 13X. Adsorption-Journal of the International Adsorption Society, 22, 71-80.

MUKHERJEE, A., OKOLIE, J. A., ABDELRASOUL, A., NIU, C. & DALAI, A. K. 2019. Review of post-combustion carbon dioxide capture technologies using activated carbon. Journal of Environmental Sciences, 83, 46-63.

MUNIANDY, L., ADAM, F., MOHAMED, A. R. & NG, E. P. 2014. The synthesis and characterization of high purity mixed microporous/mesoporous activated carbon from rice husk using chemical activation with NaOH and KOH. Microporous and Mesoporous Materials, 197, 316-323.

MUSA, U., CASTRO-DIAZ, M., UGUNA, C. N. & SNAPE, C. E. 2022. Effect of process variables on producing biocoals by hydrothermal carbonization of pine Kraft lignin at low temperatures. Fuel, 325.

NAGAI, Y., SMITH, R. L., INOMATA, H. & ARAI, K. 2007. Direct observation of polyvinylchloride degradation in water at temperatures up to 500 degrees C and at pressures up to 700 MPa. Journal of Applied Polymer Science, 106, 1075-1086.

NASRAZADANI, S. & HASSANI, S. 2016. Modern analytical techniques in failure analysis of aerospace, chemical, and oil and gas industries. Handbook of materials failure analysis with case studies from the oil and gas industry, 39-54.

NAYAK, A., BHUSHAN, B., GUPTA, V. & SHARMA, P. 2017. Chemically activated carbon from lignocellulosic wastes for heavy metal wastewater remediation: Effect of activation conditions. Journal of colloid and interface science, 493, 228-240.

NEMITALLAH, M. A., HABIB, M. A., BADR, H. M., SAID, S. A., JAMAL, A., BEN-MANSOUR, R., MOKHEIMER, E. M. A. & MEZGHANI, K. 2017. Oxy-fuel combustion technology: current status, applications, and trends. International Journal of Energy Research, 41, 1670-1708.

NOR, N. M., LAU, L. C., LEE, K. T. & MOHAMED, A. R. 2013. Synthesis of activated carbon from lignocellulosic biomass and its applications in air pollution control—a review. Journal of Environmental Chemical Engineering, 1, 658-666.

NWAOHA, C., IDEM, R., SUPAP, T., SAIWAN, C., TONTIWACHWUTHIKUL, P., RONGWONG, W., AL-MARRI, M. J. & BENAMOR, A. 2017. Heat duty, heat of absorption, sensible heat and heat of vaporization of 2-Amino-2-Methyl-1-Propanol (AMP), Piperazine (PZ) and Monoethanolamine (MEA) tri-solvent blend for carbon dioxide (CO_2) capture. Chemical Engineering Science, 170, 26-35.

OGUNGBENRO, A. E., QUANG, D. V., AL-ALI, K. & ABU-ZAHRA, M. R. M. 2017. Activated carbon from date seeds for CO_2 capture applications. 13th International Conference on Greenhouse Gas Control Technologies, Ghgt-13, 114, 2313-2321.

OGUNGBENRO, A. E., QUANG, D. V., AL-ALI, K. A., VEGA, L. F. & ABU-ZAHRA, M. R. M. 2020. Synthesis and characterization of activated carbon from biomass date seeds for carbon dioxide adsorption. Journal of Environmental Chemical Engineering, 8.

OKADA, K., YAMAMOTO, N., KAMESHIMA, Y. & YASUMORI, A. 2003. Porous properties of activated carbons from waste newspaper prepared by chemical and physical activation. Journal of Colloid and Interface Science, 262, 179-193.

OKMAN, I., KARAGöZ, S., TAY, T. & ERDEM, M. 2014. Activated carbons from grape seeds by chemical activation with potassium carbonate and potassium hydroxide. Applied Surface Science, 293, 138-142.

OLABI, A. G., OBAIDEEN, K., ELSAID, K., WILBERFORCE, T., SAYED, E. T., MAGHRABIE, H. M. & ABDELKAREEM, M. A. 2022. Assessment of the pre-combustion carbon capture contribution into sustainable development goals SDGs using novel indicators. Renewable & Sustainable Energy Reviews, 153.

OLIVARES-MARIN, M., FERNANDEZ-GONZALEZ, C., MACIAS-GARCIA, A. & GOMEZ-SERRANO, V. 2012. Preparation of activated carbon from cherry stones by physical activation in air. Influence of the chemical carbonization with H2SO4. Journal of Analytical and Applied Pyrolysis, 94, 131-137.

OSMAN, A. I., HEFNY, M., MAKSOUD, M., ELGARAHY, A. M. & ROONEY, D. W. 2021. Recent advances in carbon capture storage and utilisation technologies: a review. Environmental Chemistry Letters, 19, 797-849.

PAPARI, S., BAMDAD, H. & BERRUTI, F. 2021. Pyrolytic Conversion of Plastic Waste to Value-Added Products and Fuels: A Review. Materials, 14.

PARDAKHTI, M., JAFARI, T., TOBIN, Z., DUTTA, B., MOHARRERI, E., SHEMSHAKI, N. S., SUIB, S. & SRIVASTAVA, R. 2019. Trends in Solid Adsorbent Materials Development for CO_2 Capture. Acs Applied Materials & Interfaces, 11, 34533-34559.

PARSHETTI, G. K., CHOWDHURY, S. & BALASUBRAMANIAN, R. 2015. Biomass derived low-cost microporous adsorbents for efficient CO_2 capture. Fuel, 148, 246-254.

PATEL, H. A., JE, S. H., PARK, J., CHEN, D. P., JUNG, Y., YAVUZ, C. T. & COSKUN, A. 2013. Unprecedented high-temperature CO_2 selectivity in N-2-phobic nanoporous covalent organic polymers. Nature Communications, 4, 8.

PATRóN, G. D. & RICARDEZ-SANDOVAL, L. 2022. An integrated real-time optimization, control, and estimation scheme for post-combustion CO_2 capture. Applied Energy, 308, 118302.

PETRESCU, L., BONALUMI, D., VALENTI, G., CORMOS, A.-M. & CORMOS, C.-C. 2017. Life Cycle Assessment for supercritical pulverized coal power plants with post-combustion carbon capture and storage. Journal of Cleaner Production, 157, 10-21.

PETROVIC, B., GORBOUNOV, M. & SOLTANI, S. M. 2022. Impact of surface functional groups and their introduction methods on the mechanisms of CO_2 adsorption on porous carbonaceous adsorbents. Carbon Capture Science & Technology, 100045.

PEVIDA, C., DRAGE, T. & SNAPE, C. 2008a. Silica-templated melamine–formaldehyde resin derived adsorbents for CO_2 capture. Carbon, 46, 1464-1474.

PEVIDA, C., PLAZA, M. G., ARIAS, B., FERMOSO, J., RUBIERA, F. & PIS, J. J. 2008b. Surface modification of activated carbons for CO_2 capture. Applied Surface Science, 254, 7165-7172.

PLAZA, M. G., THURECHT, K. J., PEVIDA, C., RUBIERA, F., PIS, J. J., SNAPE, C. E. & DRAGE, T. C. 2013. Influence of oxidation upon the CO_2 capture performance of a phenolic-resin-derived carbon. Fuel Processing Technology, 110, 53-60.

POERSCHMANN, J., WEINER, B., WOSZIDLO, S., KOEHLER, R. & KOPINKE, F. D. 2015. Hydrothermal carbonization of poly(vinyl chloride). Chemosphere, 119, 682-689.

POWL, J. & EVERETT, D. 1976. Adsorption in slit-like and cylindrical micropores in the Henry's law region. J. Chem. Soc., Faraday Trans, 1, 72.

PRAHAS, D., KARTIKA, Y., INDRASWATI, N. & ISMADJI, S. 2008. Activated carbon from jackfruit peel waste by H3PO4 chemical activation: Pore structure and surface chemistry characterization. Chemical Engineering Journal, 140, 32-42.

PRAMANIK, P., PATEL, H., CHAROLA, S., NEOGI, S. & MAITI, S. 2021. High surface area porous carbon from cotton stalk agro-residue for CO_2 adsorption and study of techno-economic viability of commercial production. Journal of CO_2 Utilization, 45, 12.

PRESSER, V., MCDONOUGH, J., YEON, S. H. & GOGOTSI, Y. 2011. Effect of pore size on carbon dioxide sorption by carbide derived carbon. Energy & Environmental Science, 4, 3059-3066.

PULIDO, A., NACHTIGALL, P., ZUKAL, A., DOMINGUEZ, I. & CEJKA, J. 2009. Adsorption of CO_2 on Sodium-Exchanged Ferrierites: The Bridged CO_2 Complexes Formed between Two Extraframework Cations. Journal of Physical Chemistry C, 113, 2928-2935.

QEZELSEFLOO, E., KHALILI, S., JAHANSHAHI, M. & PEYRAVI, M. 2020. Adsorptive removal of CO_2 on Nitrogen-doped porous carbon derived from polyaniline: Effect of chemical activation. Materials Chemistry and Physics, 239.

QUAN, C., SU, R. R. & GAO, N. B. 2020. Preparation of activated biomass carbon from pine sawdust for supercapacitor and CO_2 capture. International Journal of Energy Research, 44, 4335-4351.

RAAB, C. G. D. I. R. 1998. Measurement of the electric quadrupole moments of CO_2, CO, N2, Cl2 and BF3. Molecular Physics, 93, 49-56.

RABBANI, M. G., ISLAMOGLU, T. & EL-KADERI, H. M. 2017. Benzothiazole- and benzoxazole-linked porous polymers for carbon dioxide storage and separation. Journal of Materials Chemistry A, 5, 258-265.

RAGANATI, F., ALFE, M., GARGIULO, V., CHIRONE, R. & AMMENDOLA, P. 2019. Kinetic study and breakthrough analysis of the hybrid physical/chemical CO_2 adsorption/desorption behavior of a magnetite-based sorbent. Chemical Engineering Journal, 372, 526-535.

RAGANATI, F., MICCIO, F. & AMMENDOLA, P. 2021. Adsorption of carbon dioxide for post-combustion capture: a review. Energy & Fuels, 35, 12845-12868.

RAJAPAKSHA, A. U., CHEN, S. S., TSANG, D. C. W., ZHANG, M., VITHANAGE, M., MANDAL, S., GAO, B., BOLAN, N. S. & OK, Y. S. 2016. Engineered/designer biochar for contaminant

removal/immobilization from soil and water: Potential and implication of biochar modification. Chemosphere, 148, 276-291.

RAMBABU, N., RAO, B., SURISETTY, V. R., DAS, U. & DALAI, A. K. 2015. Production, characterization, and evaluation of activated carbons from de-oiled canola meal for environmental applications. Industrial Crops and Products, 65, 572-581.

RAO, L. L., LIU, S. F., WANG, L. L., MA, C. D., WU, J. Y., AN, L. Y. & HU, X. 2019. N-doped porous carbons from low-temperature and single-step sodium amide activation of carbonized water chestnut shell with excellent CO_2 capture performance. Chemical Engineering Journal, 359, 428-435.

RASHIDI, N. A. & YUSUP, S. 2016. An overview of activated carbons utilization for the post-combustion carbon dioxide capture. Journal of CO_2 Utilization, 13, 1-16.

RAYMUNDO-PINERO, E., AZAIS, P., CACCIAGUERRA, T., CAZORLA-AMOROS, D., LINARES-SOLANO, A. & BEGUIN, F. 2005. KOH and NaOH activation mechanisms of multiwalled carbon nanotubes with different structural organisation. Carbon, 43, 786-795.

REHMAN, A., HEO, Y. J., NAZIR, G. & PARK, S. J. 2021. Solvent-free, one-pot synthesis of nitrogen-tailored alkali-activated microporous carbons with an efficient CO_2 adsorption. Carbon, 172, 71-82.

REHMAN, A. & PARK, S.-J. 2020. From chitosan to urea-modified carbons: Tailoring the ultra-microporosity for enhanced CO_2 adsorption. Carbon, 159, 625-637.

REN, X., GUO, J., LI, S. & CHANG, J. 2020. Thermogravimetric analysis–Fourier transform infrared spectroscopy study on the effect of extraction pre-treatment on the pyrolysis properties of eucalyptus wood waste. ACS omega, 5, 23364-23371.

REN, X. M., LI, H., CHEN, J., WEI, L. J., MODAK, A., YANG, H. Q. & YANG, Q. H. 2017. N-doped porous carbons with exceptionally high CO_2 selectivity for CO_2 capture. Carbon, 114, 473-481.

REZA, M. T., ROTTLER, E., HERKLOTZ, L. & WIRTH, B. 2015. Hydrothermal carbonization (HTC) of wheat straw: Influence of feedwater pH prepared by acetic acid and potassium hydroxide. Bioresource Technology, 182, 336-344.

RUIZ, B., PARRA, J. á., PAJARES, J. & PIS, J. 2006. Effect of coal pre-oxidation on the optical texture and porosity of pyrolysis chars. Journal of analytical and applied pyrolysis, 75, 27-32.

SADAT-SHOJAI, M. & BAKHSHANDEH, G. R. 2011. Recycling of PVC wastes. Polymer Degradation and Stability, 96, 404-415.

SAHA, B. B., JRIBI, S., KOYAMA, S. & EL-SHARKAWY, I. I. 2011. Carbon dioxide adsorption isotherms on activated carbons. Journal of Chemical & Engineering Data, 56, 1974-1981.

SAHA, D., VAN BRAMER, S. E., ORKOULAS, G., HO, H. C., CHEN, J. H. & HENLEY, D. K. 2017. CO_2 capture in lignin-derived and nitrogen-doped hierarchical porous carbons. Carbon, 121, 257-266.

SAIDUR, R., ABDELAZIZ, E. A., DEMIRBAS, A., HOSSAIN, M. S. & MEKHILEF, S. 2011. A review on biomass as a fuel for boilers. Renewable & Sustainable Energy Reviews, 15, 2262-2289.

SAKA, C. 2012. BET, TG-DTG, FT-IR, SEM, iodine number analysis and preparation of activated carbon from acorn shell by chemical activation with ZnCl2. Journal of Analytical and Applied Pyrolysis, 95, 21-24.

SAMAKSAMAN, U., PATTARAPRAKORN, W., NERAMITTAGAPONG, A. & KANCHANATIP, E. Solid fuel production from macadamia nut shell: effect of hydrothermal carbonization conditions on fuel characteristics. Biomass Conversion and Biorefinery.

SAMANTA, A., ZHAO, A., SHIMIZU, G. K. H., SARKAR, P. & GUPTA, R. 2012. Post-Combustion CO_2 Capture Using Solid Sorbents: A Review. Industrial & Engineering Chemistry Research, 51, 1438-1463.

SANCHEZ-SANCHEZ, A., SUAREZ-GARCIA, F., MARTINEZ-ALONSO, A. & TASCÓN, J. M. 2014. Influence of porous texture and surface chemistry on the CO_2 adsorption capacity of porous carbons: acidic and basic site interactions. ACS Applied Materials & Interfaces, 6, 21237-21247.

SEEMA, H., KEMP, K. C., LE, N. H., PARK, S. W., CHANDRA, V., LEE, J. W. & KIM, K. S. 2014. Highly selective CO_2 capture by S-doped microporous carbon materials. Carbon, 66, 320-326.

SERAFIN, J., BACA, M., BIEGUN, M., MIJOWSKA, E., KALENCZUK, R. J., SRENSCEK-NAZZAR, J. & MICHALKIEWICZ, B. 2019. Direct conversion of biomass to nanoporous activated biocarbons for high CO_2 adsorption and supercapacitor applications. Applied Surface Science, 497, 19.

SERAFIN, J., NARKIEWICZ, U., MORAWSKI, A. W., WROBEL, R. J. & MICHALKIEWICZ, B. 2017. Highly microporous activated carbons from biomass for CO_2 capture and effective micropores at different conditions. Journal of CO_2 Utilization, 18, 73-79.

SETHIA, G. & SAYARI, A. 2015. Comprehensive study of ultra-microporous nitrogen-doped activated carbon for CO_2 capture. Carbon, 93, 68-80.

SEVILLA, M., DIEZ, N. & FUERTES, A. B. 2021. More Sustainable Chemical Activation Strategies for the Production of Porous Carbons. Chemsuschem, 14, 94-117.

SEVILLA, M. & FUERTES, A. B. 2009a. Chemical and Structural Properties of Carbonaceous Products Obtained by Hydrothermal Carbonization of Saccharides. Chemistry-a European Journal, 15, 4195-4203.

SEVILLA, M. & FUERTES, A. B. 2009b. The production of carbon materials by hydrothermal carbonization of cellulose. Carbon, 47, 2281-2289.

SEVILLA, M. & FUERTES, A. B. 2011. Sustainable porous carbons with a superior performance for CO_2 capture. Energy & Environmental Science, 4, 1765-1771.

SEVILLA, M. & FUERTES, A. B. 2013. A general and facile synthesis strategy towards highly porous carbons: carbonization of organic salts. Journal of Materials Chemistry A, 1, 13738-13741.

SEVILLA, M. & FUERTES, A. B. 2016. A Green Approach to High-Performance Supercapacitor Electrodes: The Chemical Activation of Hydrochar with Potassium Bicarbonate. Chemsuschem, 9, 1880-1888.

SEVILLA, M., FUERTES, A. B. & MOKAYA, R. 2011a. High density hydrogen storage in superactivated carbons from hydrothermally carbonized renewable organic materials. Energy & Environmental Science, 4, 1400-1410.

SEVILLA, M., MACIA-AGULLO, J. A. & FUERTES, A. B. 2011b. Hydrothermal carbonization of biomass as a route for the sequestration of CO_2: Chemical and structural properties of the carbonized products. Biomass & Bioenergy, 35, 3152-3159.

SEVILLA, M., PARRA, J. B. & FUERTES, A. B. 2013. Assessment of the Role of Micropore Size and N-Doping in CO_2 Capture by Porous Carbons. Acs Applied Materials & Interfaces, 5, 6360-6368.

SHAFEEYAN, M. S., DAUD, W., HOUSHMAND, A. & SHAMIRI, A. 2010. A review on surface modification of activated carbon for carbon dioxide adsorption. Journal of Analytical and Applied Pyrolysis, 89, 143-151.

SHAHKARAMI, S., DALAI, A. K. & SOLTAN, J. 2016. Enhanced CO_2 Adsorption Using MgO-Impregnated Activated Carbon: Impact of Preparation Techniques. Industrial & Engineering Chemistry Research, 55, 5955-5964.

SHANG, J. B., LIN, J. & ZHAO, G. J. 2018. Preparation and Characterization of Wood-based Pre-oxidized Precursors and Activated Carbon Microspheres. Bioresources, 13, 7983-7997.

SHELDON, R. A. 2014. Green and sustainable manufacture of chemicals from biomass: state of the art. Green Chemistry, 16, 950-963.

SHEN, W., LI, Z. & LIU, Y. 2008. Surface chemical functional groups modification of porous carbon. Recent Patents on Chemical Engineering, 1, 27-40.

SHEN, Y. F. 2020. A review on hydrothermal carbonization of biomass and plastic wastes to energy products. Biomass & Bioenergy, 134.

SHEN, Y. F., YU, S. L., GE, S., CHEN, X. M., GE, X. L. & CHEN, M. D. 2017. Hydrothermal carbonization of medical wastes and lignocellulosic biomass for solid fuel production from lab-scale to pilot-scale. Energy, 118, 312-323.

SHER, F., PANS, M. A., SUN, C. G., SNAPE, C. & LIU, H. 2018. Oxy-fuel combustion study of biomass fuels in a 20 kW(th) fluidized bed combustor. Fuel, 215, 778-786.

SHI, Z. L., TAO, Y., WU, J. S., ZHANG, C. Z., HE, H. L., LONG, L. L., LEE, Y. J., LI, T. & ZHANG, Y. B. 2020. Robust Metal-Triazolate Frameworks for CO_2 Capture from Flue Gas. Journal of the American Chemical Society, 142, 2750-2754.

SHUKLA, P. R. 2022. Climate change 2022: mitigation of climate change, Cambridge University Press.

SIEGELMAN, R. L., KIM, E. J. & LONG, J. R. 2021. Porous materials for carbon dioxide separations. Nature Materials, 20, 1060-1072.

SING, K. S. 1985. Reporting physisorption data for gas/solid systems with special reference to the determination of surface area and porosity (Recommendations 1984). Pure and applied chemistry, 57, 603-619.

SINGH, G., RUBAN, A. M., GENG, X. & VINU, A. 2023. Recognizing the potential of K-salts, apart from KOH, for generating porous carbons using chemical activation. Chemical Engineering Journal, 451, 139045.

SINGH, H. M., KOTHARI, R., GUPTA, R. & TYAGI, V. V. 2019. Bio-fixation of flue gas from thermal power plants with algal biomass: Overview and research perspectives. Journal of Environmental Management, 245, 519-539.

SPIGARELLI, B. P. & KAWATRA, S. K. 2013. Opportunities and challenges in carbon dioxide capture. Journal of CO_2 Utilization, 1, 69-87.

STARNES, W. H. 2012. How and to what extent are free radicals involved in the nonoxidative thermal dehydrochlorination of poly(vinyl chloride)? Journal of Vinyl & Additive Technology, 18, 71-75.

STARNES, W. H. & GE, X. L. 2004. Mechanism of autocatalysis in the thermal dehydrochlorination of poly(vinyl chloride). Macromolecules, 37, 352-359.

SUBRAMANIAM, M., SATISH, S., SOLOMON, J. M. & SATHYAMURTHY, R. 2020. Numerical and experimental investigation on capture of CO_2 and other pollutants from an SI engine using the physical adsorption technique. Heat Transfer, 49, 2943-2960.

SUN, F., LIU, X., GAO, J. H., PI, X. X., WANG, L. J., QU, Z. B. & QIN, Y. K. 2016. Highlighting the role of nitrogen doping in enhancing CO_2 uptake onto carbon surfaces: a combined experimental and computational analysis. Journal of Materials Chemistry A, 4, 18248-18252.

SUN, M. Z., GU, Q. F., HANIF, A., WANG, T. Q. & SHANG, J. 2019. Transition metal cation-exchanged SSZ-13 zeolites for CO_2 capture and separation from N-2. Chemical Engineering Journal, 370, 1450-1458.

TAKESHITA, Y., KATO, K., TAKAHASHI, K., SATO, Y. & NISHI, S. 2004. Basic study on treatment of waste polyvinyl chloride plastics by hydrothermal decomposition in subcritical and supercritical regions. The Journal of supercritical fluids, 31, 185-193.

TANG, X. H., SONG, M., LEI, Y. & WANG, X. 2017. Comparison and application of different component municipal solid wastes based carbon on adsorption of carbon dioxide. International Journal of Green Energy, 14, 135-140.

THEO, W. L., LIM, J. S., HASHIM, H., MUSTAFFA, A. A. & HO, W. S. 2016. Review of pre-combustion capture and ionic liquid in carbon capture and storage. Applied Energy, 183, 1633-1663.

THOMMES, M. & CYCHOSZ, K. A. 2014. Physical adsorption characterization of nanoporous materials: progress and challenges. Adsorption-Journal of the International Adsorption Society, 20, 233-250.

THOMMES, M., KANEKO, K., NEIMARK, A. V., OLIVIER, J. P., RODRIGUEZ-REINOSO, F., ROUQUEROL, J. & SING, K. S. W. 2015. Physisorption of gases, with special reference to the evaluation of surface area and pore size distribution (IUPAC Technical Report). Pure and Applied Chemistry, 87, 1051-1069.

TIAN, W. J., ZHANG, H. Y., SUN, H. Q., TADE, M. O. & WANG, S. B. 2018. One-step synthesis of flour-derived functional nanocarbons with hierarchical pores for versatile environmental applications. Chemical Engineering Journal, 347, 432-439.

TIAN, Y. Y. & ZHU, G. S. 2020. Porous Aromatic Frameworks (PAFs). Chemical Reviews, 120, 8934-8986.

TIRYAKI, B., YAGMUR, E., SANFORD, A. & AKTAS, Z. 2014. Comparison of activated carbon produced from natural biomass and equivalent chemical compositions. Journal of Analytical and Applied Pyrolysis, 105, 276-283.

TITIRICI, M. M., ANTONIETTI, M. & BACCILE, N. 2008. Hydrothermal carbon from biomass: a comparison of the local structure from poly- to monosaccharides and pentoses/hexoses. Green Chemistry, 10, 1204-1212.

TITIRICI, M. M., WHITE, R. J., FALCO, C. & SEVILLA, M. 2012. Black perspectives for a green future: hydrothermal carbons for environment protection and energy storage. Energy & Environmental Science, 5, 6796-6822.

TO, J. W. F., HE, J. J., MEI, J. G., HAGHPANAH, R., CHEN, Z., KUROSAWA, T., CHEN, S. C., BAE, W. G., PAN, L. J., TOK, J. B. H., WILCOX, J. & BAO, Z. N. 2016. Hierarchical N-Doped Carbon as CO_2 Adsorbent with High CO_2 Selectivity from Rationally Designed Polypyrrole Precursor. Journal of the American Chemical Society, 138, 1001-1009.

TOPRAK, A. & KOPAC, T. 2017. Carbon Dioxide Adsorption Using High Surface Area Activated Carbons from Local Coals Modified by KOH, NaOH and ZnCl2 Agents. International Journal of Chemical Reactor Engineering, 15.

TRAVIS, W., GADIPELLI, S. & GUO, Z. X. 2015. Superior CO_2 adsorption from waste coffee ground derived carbons. Rsc Advances, 5, 29558-29562.

UNDAVALLI, V. K., LING, C. & KHANDELWAL, B. 2021. Impact of alternative fuels and properties on elastomer compatibility. Aviation Fuels. Elsevier.

UNUR, E. 2013. Functional nanoporous carbons from hydrothermally treated biomass for environmental purification. Microporous and Mesoporous Materials, 168, 92-101.

ÜNVEREN, E. E., MONKUL, B. Ö., SARıOĞLAN, Ş., KARADEMIR, N. & ALPER, E. 2017. Solid amine sorbents for CO_2 capture by chemical adsorption: A review. Petroleum, 3, 37-50.

VAGNER, C., FINQUENEISEL, G., ZIMNY, T., BURG, P., GRZYB, B., MACHNIKOWSKI, J. & WEBER, J. V. 2003. Characterization of the surface properties of nitrogen-enriched carbons by inverse gas chromatography methods. Carbon, 41, 2847-2853.

VAIDHYANATHAN, R., IREMONGER, S. S., SHIMIZU, G. K. H., BOYD, P. G., ALAVI, S. & WOO, T. K. 2010. Direct Observation and Quantification of CO_2 Binding Within an Amine-Functionalized Nanoporous Solid. Science, 330, 650-653.

VAKHARIA, V., SALIM, W., WU, D. Z., HAN, Y., CHEN, Y. X., ZHAO, L. & HO, W. S. W. 2018. Scale-up of amine-containing thin-film composite membranes for CO_2 capture from flue gas. Journal of Membrane Science, 555, 379-387.

VALENZANO, L., CIVALLERI, B., CHAVAN, S., PALOMINO, G. T., AREAN, C. O. & BORDIGA, S. 2010. Computational and Experimental Studies on the Adsorption of CO, N-2, and CO_2 on Mg-MOF-74. Journal of Physical Chemistry C, 114, 11185-11191.

VERDEGAAL, W. M., WANG, K. C., SCULLEY, J. P., WRIEDT, M. & ZHOU, H. C. 2016. Evaluation of Metal-Organic Frameworks and Porous Polymer Networks for CO_2-Capture Applications. Chemsuschem, 9, 636-643.

VITILLO, J. G., SMIT, B. & GAGLIARDI, L. 2017. Introduction: Carbon Capture and Separation. Chemical Reviews, 117, 9521-9523.

W JOHN THOMAS, F. & CRITTENDEN, B. 1998. Adsorption technology and design, Butterworth-Heinemann.

WANG, H. F., LI, X. H., CUI, Z. Y., FU, Z. R., YANG, L. J., LIU, G. H. & LI, M. H. 2020a. Coffee grounds derived N enriched microporous activated carbons: Efficient adsorbent for post-combustion CO_2 capture and conversion. Journal of Colloid and Interface Science, 578, 491-499.

WANG, J., WANG, F. N., DUAN, H. M., LI, Y., XU, J. M., HUANG, Y. Q., LIU, B. & ZHANG, T. 2020b. Polyvinyl Chloride-Derived Carbon Spheres for CO_2 Adsorption. Chemsuschem, 13, 6426-6432.

WANG, J. T., CHEN, H. C., ZHOU, H. H., LIU, X. J., QIAO, W. M., LONG, D. H. & LING, L. C. 2013. Carbon dioxide capture using polyethylenimine-loaded mesoporous carbons. Journal of Environmental Sciences, 25, 124-132.

WANG, J. Y., YUAN, X. Z., DENG, S., ZENG, X. L., YU, Z., LI, S. J. & LI, K. X. 2020c. Waste polyethylene terephthalate (PET) plastics-derived activated carbon for CO_2 capture: a route to a closed carbon loop. Green Chemistry, 22, 3836-3845.

WANG, L. P., CHANG, Y. Z. & LI, A. M. 2019. Hydrothermal carbonization for energy-efficient processing of sewage sludge: A review. Renewable & Sustainable Energy Reviews, 108, 423-440.

WANG, R., WANG, P., YAN, X., LANG, J., PENG, C. & XUE, Q. 2012. Promising porous carbon derived from celtuce leaves with outstanding supercapacitance and CO_2 capture performance. ACS applied materials & interfaces, 4, 5800-5806.

WANG, X., WANG, D. Y., SONG, M. J., XIN, C. L. & ZENG, W. L. 2017. Tetraethylenepentamine-Modified Activated Semicoke for CO_2 Capture from Flue Gas. Energy & Fuels, 31, 3055-3061.

WEI, H. R., DENG, S. B., HU, B. Y., CHEN, Z. H., WANG, B., HUANG, J. & YU, G. 2012. Granular Bamboo-Derived Activated Carbon for High CO_2 Adsorption: The Dominant Role of Narrow Micropores. Chemsuschem, 5, 2354-2360.

WEI, M. Q., YU, Q. B., MU, T. T., HOU, L. M., ZUO, Z. L. & PENG, J. Y. 2016. Preparation and characterization of waste ion-exchange resin-based activated carbon for CO_2 capture. Adsorption-Journal of the International Adsorption Society, 22, 385-396.

WEI, Y. Y., FAKUDZE, S., ZHANG, Y. M., MA, R., SHANG, Q. Q., CHEN, J. Q., LIU, C. G. & CHU, Q. L. 2022. Co-hydrothermal carbonization of pomelo peel and PVC for production of hydrochar pellets with enhanced fuel properties and dechlorination. Energy, 239.

WEN, G. D., WANG, B. L., WANG, C. X., WANG, J., TIAN, Z. J., SCHLOGL, R. & SU, D. S. 2017. Hydrothermal Carbon Enriched with Oxygenated Groups from Bio-mass Glucose as an Efficient Carbocatalyst. Angewandte Chemie-International Edition, 56, 600-604.

WEN, H. M., LIAO, C. J., LI, L. B., ALSALME, A., ALOTHMAN, Z., KRISHNA, R., WU, H., ZHOU, W., HU, J. & CHEN, B. L. 2019. A metal-organic framework with suitable pore size and dual functionalities for highly efficient post-combustion CO_2 capture. Journal of Materials Chemistry A, 7, 3128-3134.

WIKBERG, H., OHRA-AHO, T., PILEIDIS, F. & TITIRICI, M.-M. 2015. Structural and morphological changes in kraft lignin during hydrothermal carbonization. ACS Sustainable Chemistry & Engineering, 3, 2737-2745.

WILBERFORCE, T., OLABI, A., SAYED, E. T., ELSAID, K. & ABDELKAREEM, M. A. 2021. Progress in carbon capture technologies. Science of The Total Environment, 761, 143203.

WU, Q., YU, S., HAO, N., WELLS JR, T., MENG, X., LI, M., PU, Y., LIU, S. & RAGAUSKAS, A. J. 2017. Characterization of products from hydrothermal carbonization of pine. Bioresource technology, 244, 78-83.

WU, X. X., ZHANG, C. Y., TIAN, Z. W. & CAI, J. J. 2018. Large-surface-area carbons derived from lotus stem waste for efficient CO_2 capture. New Carbon Materials, 33, 252-260.

XIAO, M., LIU, H., IDEM, R., TONTIWACHWUTHIKUL, P. & LIANG, Z. 2016. A study of structure–activity relationships of commercial tertiary amines for post-combustion CO_2 capture. Applied energy, 184, 219-229.

XING, W., LIU, C., ZHOU, Z. Y., ZHANG, L., ZHOU, J., ZHUO, S. P., YAN, Z. F., GAO, H., WANG, G. Q. & QIAO, S. Z. 2012. Superior CO_2 uptake of N-doped activated carbon through hydrogen-bonding interaction. Energy & Environmental Science, 5, 7323-7327.

XIONG, F., HAN, Y., WANG, S., LI, G., QIN, T., CHEN, Y. & CHU, F. 2017. Preparation and formation mechanism of size-controlled lignin nanospheres by self-assembly. Industrial crops and products, 100, 146-152.

XU, C., ARANCON, R. A. D., LABIDI, J. & LUQUE, R. 2014a. Lignin depolymerisation strategies: towards valuable chemicals and fuels. Chemical Society Reviews, 43, 7485-7500.

XU, J. Z., CHEN, L. Z., QU, H. Q., JIAO, Y. H., XIE, J. X. & XING, G. G. 2014b. Preparation and characterization of activated carbon from reedy grass leaves by chemical activation with H3PO4. Applied Surface Science, 320, 674-680.

XUE, Y., BAI, L., CHI, M., XU, X., CHEN, Z., YU, K. & LIU, Z. 2022a. Co-hydrothermal carbonization of pre-treatment lignocellulose biomass and polyvinyl chloride for clean solid fuel production: Hydrochar properties and its formation mechanism. Journal of Environmental Chemical Engineering, 10, 106975.

XUE, Y. X., BAI, L., CHI, M. S., XU, X. L., TAI, L. Y., CHEN, Z., YU, K. C. & LIU, Z. 2022b. Co-hydrothermal carbonization of lignocellulose biomass and polyvinyl chloride: The migration and transformation of chlorine. Chemical Engineering Journal, 446.

YADAV, S. & MONDAL, S. S. 2022. A review on the progress and prospects of oxy-fuel carbon capture and sequestration (CCS) technology. Fuel, 308.

YAKOUT, S. M. & EL-DEEN, G. S. 2016. Characterization of activated carbon prepared by phosphoric acid activation of olive stones. Arabian Journal of Chemistry, 9, S1155-S1162.

YANG, P. P., RAO, L. L., ZHU, W. Q., WANG, L. L., MA, R., CHEN, F. Y., LIN, G. R. & HU, X. 2020. Porous Carbons Derived from Sustainable Biomass via a Facile One-Step Synthesis Strategy as Efficient CO_2 Adsorbents. Industrial & Engineering Chemistry Research, 59, 6194-6201.

YAO, Z. & MA, X. 2017. A new approach to transforming PVC waste into energy via combined hydrothermal carbonization and fast pyrolysis. Energy, 141, 1156-1165.

YAO, Z. L. & MA, X. Q. 2018. Characteristics of co-hydrothermal carbonization on polyvinyl chloride wastes with bamboo. Bioresource Technology, 247, 302-309.

YIN, G. J., LIU, Z. Y., LIU, Q. Y. & WU, W. Z. 2013. The role of different properties of activated carbon in CO_2 adsorption. Chemical Engineering Journal, 230, 133-140.

YORGUN, S. & YILDIZ, D. 2015. Preparation and characterization of activated carbons from Paulownia wood by chemical activation with H3PO4. Journal of the Taiwan Institute of Chemical Engineers, 53, 122-131.

YOUNAS, M., REZAKAZEMI, M., DAUD, M., WAZIR, M. B., AHMAD, S., ULLAH, N., INAMUDDIN & RAMAKRISHNA, S. 2020a. Recent progress and remaining challenges in post-combustion CO_2 capture using metal-organic frameworks (MOFs). Progress in Energy and Combustion Science, 80.

YOUNAS, M., REZAKAZEMI, M., DAUD, M., WAZIR, M. B., AHMAD, S., ULLAH, N. & RAMAKRISHNA, S. 2020b. Recent progress and remaining challenges in post-combustion CO_2 capture using metal-organic frameworks (MOFs). Progress in Energy and Combustion Science, 80, 100849.

YU, J. M., XIE, L. H., LI, J. R., MA, Y. G., SEMINARIO, J. M. & BALBUENA, P. B. 2017. CO_2 Capture and Separations Using MOFs: Computational and Experimental Studies. Chemical Reviews, 117, 9674-9754.

YU, X., LIU, S., LIN, G., YANG, Y., ZHANG, S., ZHAO, H., ZHENG, C. & GAO, X. 2019. Promotion effect of KOH surface etching on sucrose-based hydrochar for acetone adsorption. Applied Surface Science, 496, 143617.

YUAN, H. R., CHEN, J., LI, D. N., CHEN, H. B. & CHEN, Y. 2019. 5 Ultramicropore-rich renewable porous carbon from biomass tar with excellent adsorption capacity and selectivity for CO_2 capture. Chemical Engineering Journal, 373, 171-178.

ZAKZESKI, J., BRUIJNINCX, P. C. A., JONGERIUS, A. L. & WECKHUYSEN, B. M. 2010. The Catalytic Valorisation of Lignin for the Production of Renewable Chemicals. Chemical Reviews, 110, 3552-3599.

ZHANG, C. M., SONG, W., MA, Q. L., XIE, L. J., ZHANG, X. C. & GUO, H. 2016a. Enhancement of CO_2 Capture on Biomass-Based Carbon from Black Locust by KOH Activation and Ammonia Modification. Energy & Fuels, 30, 4181-4190.

ZHANG, J., CHEN, Y. H., XIA, X., FU, B. B., LIN, C. J., JIA, G. C., CUI, X., LIU, F., ZHAO, P. T. & LI, Y. M. 2023a. Co-hydrothermal carbonization of polyvinyl chloride and lignocellulose biomasses for chlorine and inorganics removal. Waste Management, 156, 198-207.

ZHANG, J., ZHANG, L., LIN, C., WANG, C., ZHAO, P. & LI, Y. 2023b. Co-hydrothermal carbonization of polyvinyl chloride and lignocellulose biomasses: Influence of biomass feedstock on fuel properties and combustion behaviors. Science of The Total Environment, 161532.

ZHANG, J. H., LIN, Q. M. & ZHAO, X. R. 2014. The Hydrochar Characters of Municipal Sewage Sludge Under Different Hydrothermal Temperatures and Durations. Journal of Integrative Agriculture, 13, 471-482.

ZHANG, L., ZHOU, B., DUAN, P. G., WANG, F. & XU, Y. P. 2016b. Hydrothermal conversion of scrap tire to liquid fuel. Chemical Engineering Journal, 285, 157-163.

ZHANG, P. X., ZHONG, Y., DING, J., WANG, J., XU, M., DENG, Q., ZENG, Z. L. & DENG, S. G. 2019a. A new choice of polymer precursor for solvent-free method: Preparation of N-enriched porous carbons for highly selective CO_2 capture. Chemical Engineering Journal, 355, 963-973.

ZHANG, X., WU, J., YANG, H. P., SHAO, J. G., WANG, X. H., CHEN, Y. Q., ZHANG, S. H. & CHEN, H. P. 2016c. Preparation of nitrogen-doped microporous modified biochar by high temperature CO_2-NH3 treatment for CO_2 adsorption: effects of temperature. Rsc Advances, 6, 98157-98166.

ZHANG, X., ZHANG, L. & LI, A. 2019b. Co-hydrothermal carbonization of lignocellulosic biomass and waste polyvinyl chloride for high-quality solid fuel production: Hydrochar properties and its combustion and pyrolysis behaviors. Bioresource technology, 294, 122113.

ZHANG, X. J., ZHANG, L. & LI, A. M. 2018. Eucalyptus sawdust derived biochar generated by combining the hydrothermal carbonization and low concentration KOH modification for hexavalent chromium removal. Journal of Environmental Management, 206, 989-998.

ZHANG, X. S., TIAN, X. D., SONG, Y., WU, J. R., YANG, T. & LIU, Z. J. 2022. Boosting Zn-ion storage capacity of pitch coke-based activated carbon via pre-oxidation assisted KOH activation strategy. Microporous and Mesoporous Materials, 333.

ZHANG, Z., LUO, D., LUI, G., LI, G. R., JIANG, G. P., CANO, Z. P., DENG, Y. P., DU, X. J., YIN, S., CHEN, Y. F., ZHANG, M. H., YAN, Z. F. & CHEN, Z. W. 2019c. In-situ ion-activated carbon nanospheres with tunable ultramicroporosity for superior CO_2 capture. Carbon, 143, 531-541.

ZHANG, Z., ZHOU, J., XING, W., XUE, Q., YAN, Z., ZHUO, S. & QIAO, S. Z. 2013a. Critical role of small micropores in high CO 2 uptake. Physical chemistry chemical physics, 15, 2523-2529.

ZHANG, Z. B., LEI, Y. Q., LI, D. W., ZHAO, J. W., WANG, Y. K., ZHOU, G. Y., YAN, C. W. & HE, Q. X. 2020. Sudden heating of H3PO4-loaded coconut shell in CO_2 flow to produce super activated carbon and its application for benzene adsorption. Renewable Energy, 153, 1091-1099.

ZHANG, Z. S., ZHOU, J., XING, W., XUE, Q. Z., YAN, Z. F., ZHUO, S. P. & QIAO, S. Z. 2013b. Critical role of small micropores in high CO_2 uptake. Physical Chemistry Chemical Physics, 15, 2523-2529.

ZHAO, B. & SU, Y. 2014. Process effect of microalgal-carbon dioxide fixation and biomass production: a review. Renewable and Sustainable Energy Reviews, 31, 121-132.

ZHAO, H. Y., LUO, X. N., ZHANG, H. J., SUN, N. N., WEI, W. & SUN, Y. H. 2018a. Carbon-based adsorbents for post-combustion capture: a review. Greenhouse Gases-Science and Technology, 8, 11-36.

ZHAO, P. Y., ZHANG, G. J., YAN, H. Y. & ZHAO, Y. Q. 2021a. The latest development on amine functionalized solid adsorbents for post-combustion CO_2 capture: Analysis review. Chinese Journal of Chemical Engineering, 35, 17-43.

ZHAO, X., ZHAN, L., XIE, B. & GAO, B. 2018b. Products derived from waste plastics (PC, HIPS, ABS, PP and PA6) via hydrothermal treatment: Characterization and potential applications. Chemosphere, 207, 742-752.

ZHAO, X. Y., ZHAN, L., XIE, B. & GAO, B. 2018c. Products derived from waste plastics (PC, HIPS, ABS, PP and PA6) via hydrothermal treatment: Characterization and potential applications. Chemosphere, 207, 742-752.

ZHAO, Y. F., LIU, X., YAO, K. X., ZHAO, L. & HAN, Y. 2012. Superior Capture of CO_2 Achieved by Introducing Extra-framework Cations into N-doped Microporous Carbon. Chemistry of Materials, 24, 4725-4734.

ZHAO, Z. N., MA, C. D., CHEN, F. Y., XU, G. Z., PANG, R. X., QIAN, X. Y., SHAO, J. W. & HU, X. 2021b. Water caltrop shell-derived nitrogen-doped porous carbons with high CO_2 adsorption capacity. Biomass & Bioenergy, 145, 10.

ZHOU, Y. B., TAN, P., HE, Z. Q., ZHANG, C., FANG, Q. Y. & CHEN, G. 2022. CO_2 adsorption performance of nitrogen-doped porous carbon derived from licorice residue by hydrothermal treatment. Fuel, 311.

ZHU, R., YU, Q. F., LI, M., ZHAO, H., JIN, S. X., HUANG, Y. W., FAN, J. & CHEN, J. 2021. Analysis of factors influencing pore structure development of agricultural and forestry waste-derived activated carbon for adsorption application in gas and liquid phases: A review. Journal of Environmental Chemical Engineering, 9.

ZHU, X., LIU, Y., QIAN, F., ZHOU, C., ZHANG, S. & CHEN, J. 2015. Role of hydrochar properties on the porosity of hydrochar-based porous carbon for their sustainable application. ACS Sustainable Chemistry & Engineering, 3, 833-840.

ZHUANG, X. Z., ZHAN, H., SONG, Y. P., HE, C., HUANG, Y. Q., YIN, X. L. & WU, C. Z. 2019. Insights into the evolution of chemical structures in lignocellulose and non-lignocellulose biowastes during hydrothermal carbonization (HTC). Fuel, 236, 960-974.

Appendix A

Table A1 Sample labels and synthesis conditions for prepared hydrochars

Sample label	Precursor	HTC temperature (°C)	Precursor/water mass ratio	Residence time (h)
EUHC22	Eucalyptus wood	220	1:5	3
EUHC26		260		
PHC22	PVC	220	1:25	6
PHC24		240		
PHC26		260		
CEPHC22	PVC/Cellulose	220		
CEPHC24		240		
CEPHC26		260		
KLPHC22	PVC/Kraft lignin	220		
KLPHC22		240		
KLPHC22		260		

Table A2 Sample labels and synthesis conditions for prepared activated carbons

Sample label	Precursor	Pre-treatment	Activation temperature (ºC)	KOH/Precursor mass ratio
KLK-1-600	Kraft lignin	n/a	600	1
KLK-1-700			700	1
KLK-1-800			800	1
KLK-2-600			600	2
KLK-2-700			700	2
OKLK-1-600		Pre-oxidation	600	1
OKLK-1-700			700	1
OKLK-1-800			800	1
OKLK-2-600			600	2
OKLK-2-700			700	2
EU-1-600	Eucalyptus wood	n/a	600	1
EUHC22-1-600		Hydrothermal carbonization	600	1
EUHC22-1-700			700	1
EUHC22-2-600			600	2
EUHC22-2-700			700	2
EUHC26-1-600			600	1
EUHC26-1-700			700	1
EUHC26-2-600			600	2
PHC24-1-600	PVC	Hydrothermal carbonization	700	2
PHC24-1-700			700	1
PHC24-1-800			800	1
PHC24-2-600			600	2
PHC24-2-600			700	2
PHC26-1-600			600	1
PHC26-1-700			700	1
PHC26-1-800			800	1
PHC26-2-600			600	2
PHC26-2-700			700	2

Table A2 Sample labels and synthesis conditions for prepared activated carbons

Sample label	Precursor	Pre-treatment	Activation temperature (°C)	KOH/Precursor mass ratio
CEPHC24-1-600	PVC/Cellulose	Hydrothermal co-carbonization	600	1
CEPHC24-1-700			700	1
CEPHC24-1-800			800	1
CEPHC24-2-600			600	2
CEPHC24-2-700			700	2
CEPHC26-1-600			600	1
CEPHC26-1-700			700	1
CEPHC26-1-800			800	1
CEPHC26-2-600			600	2
CEPHC26-2-700			700	2
KLPHC22-1-600	PVC/Kraft lignin		600	1
KLPHC22-1-700			700	1
KLPHC26-1-600			600	1
KLPHC26-1-700			700	1

Appendix B

List of publications

1. LI, M. B., LIU, X., SUN, C. G., STEVENS, L. & LIU, H. 2022b. Synthesis and characterization of advanced bio-carbon materials from Kraft lignin with enhanced CO_2 capture properties. Journal of Environmental Chemical Engineering, 10.

2. YANG, F., LIU, X., LI, M., UGUNA, C., WANG, W. & SUN, C. 2023. Polyvinyl chloride (PVC) derived microporous carbons prepared via hydrothermal dechlorination and potassium hydroxide activation for efficient CO_2 capture. Renewable and Sustainable Energy Reviews, 180, 113279.

3. SANI, S., LIU, X., LI, M., STEVENS, L. & SUN, C. 2023. Synthesis and characterization of three-dimensional interconnected large-pore mesoporous cellular lignin carbon materials and their potential for CO_2 capture. Microporous and Mesoporous Materials, 347, 112334.

4. BAI, F., LIU, X., LIU, Y., LI, M., SANI, S., GUO, W. & SUN, C. 2023. CO_2 capture from dilute sources using triamine functionalized MCF silica at ambient temperature. Microporous and Mesoporous Materials, 349, 112370.

5. LIU, X., YANG, F., LI, M., WANG, S. & SUN, C. 2022. From polyvinyl chloride waste to activated carbons: the role of occurring additives on porosity development and gas adsorption properties. Science of The Total Environment, 833, 154894.

6. LIU, X., YANG, F., LI, M., SUN, C. & WU, Y. 2022a. Development of cost-effective PCM-carbon foam composites for thermal energy storage. Energy Reports, 8, 1696-1703.